

---

# Epitaxial Growth and Oxidation of Thin Gold and Ruthenium Films

---

Epitaktisches Wachstum und Oxidation von dünnen Gold- und  
Rutheniumfilmen

Genehmigte Dissertation  
zur Erlangung des Doktorgrades der Naturwissenschaften  
-Dr. rer. nat.-  
am Fachbereich Biologie und Chemie  
der Justus-Liebig-Universität Gießen

von

Daniel Wolfgang Langsdorf  
aus Rockenberg

Gießen, 2015



Dekan / Dean:

Prof. Dr. Volker Wissemann

1. Gutachter / 1st Reviewer:

Prof. Dr. Herbert Over

2. Gutachter / 2nd Reviewer:

Prof. Dr. Bernd Smarsly



Die vorliegende Arbeit wurde in der Zeit von März 2011 bis August 2015 am Physikalisch-Chemischen Institut der Justus-Liebig-Universität Gießen unter der Leitung von Prof. Dr. Herbert Over durchgeführt.

„Ich erkläre: Ich habe die vorliegende Dissertation selbstständig und ohne unerlaubte fremde Hilfe und nur mit den Hilfen angefertigt, die ich in der Dissertation angegeben habe. Alle Textstellen, die durch wörtlich oder sinngemäß aus veröffentlichten Schriften entnommen sind, und alle Angaben, die auf mündliche Auskünften beruhen, sind als solche kenntlich gemacht. Bei den von mir durchgeführten und in der Dissertation erwähnten Untersuchungen habe ich die Grundsätze guter wissenschaftliche Praxis, wie sie in der „Satzung der Justus-Liebig-Universität Gießen zur Sicherung guter wissenschaftlicher Praxis“ niedergelegt sind, eingehalten.“

Daniel Langsdorf

# Abstract

In the present work the growth and redox behavior of thin Au islands or films with various thicknesses (two to five layers) deposited on Ru(0001) was studied by x-ray photoelectron spectroscopy (XPS) and scanning tunneling microscopy (STM). By exposure of atomic oxygen at room temperature, small oxidized gold nanoparticles are formed by the fragmentation of the metallic gold islands or film. For smaller exposures of atomic oxygen (< 80 L) only the gold islands are attacked, while the Ru(0001) surface is unharmed. With increasing thickness of the Au islands (or film), the rate of the Au oxide/Au nanoparticle formation and the number of formed nanoparticles decreases, while their size increases. To describe the thickness dependent oxidation and fragmentation process of the gold islands (or films), a shoveling mechanism is proposed where oxidized gold atoms are shoveled from the gold-ruthenium interface to the rim of the gold islands (films). The catalytic activity of these nanoparticles was investigated by CO oxidation experiments at room temperature. However no activity has been observed. Only the reduction of the Au oxide/Au nanoparticles occurs, while the shape and dispersion of the nanoparticles on the surface is retained.

This change on the morphologies of the gold islands (or films) upon their oxidation or reduction is elucidated in the context of the theory of heterogeneous nucleation and epitaxial growth. Based on Young's equation in particular, the energy contributions of the interface energy, the strain energy and the surface free energies of the deposited material and the substrate are related to the growth behavior and the resulting morphology.

In the second part of the present work the growth and redox behavior of metallic ruthenium structures on Au(111) were studied. Again the resulting morphologies upon oxidation and reduction of ruthenium are elucidated by the energy relation given by Young's equation. The deposition of ruthenium on the Au(111) surface leads to three dimensional growth of metallic ruthenium islands. These islands merge to a rough ruthenium film. By exposure of oxygen at 680 K the merged ruthenium islands rearrange to a rather flat ruthenium film with a unique perforated morphology. XPS measurements indicate that this perforated film is stabilized by a chemisorbed oxygen phase. By using typical Ru(0001) single crystal oxidation conditions (680 K,  $5 \cdot 10^{-5}$  mbar  $O_2$ , 30 min) the ruthenium islands on Au(111) do only form a covering film of  $RuO_2$  if the former metallic ruthenium islands had a critical thickness of 10 monolayers Ru.  $RuO_2$  structures bound to the Au(111) surface are assumed to be not stable, so a metallic ruthenium buffer layer between the oxide and the gold substrate is necessary. To describe the transformation of the three dimensional Ru islands to the perforated ruthenium

film with a chemisorbed oxygen phase, a mechanism is proposed based on the energy relation given by Young's equation.

Finally a brief literature overview of other growth systems is given to further evaluate the general applicability of Young's equation.

# Zusammenfassung

In dieser Arbeit wurde das Wachstums- und Redoxverhalten dünner Goldschichten (Inseln oder Filme) mittels Röntgenphotoelektronenspektroskopie (engl. x-ray photoelectron spectroscopy, XPS) und Rastertunnelmikroskopie (RTM, engl. scanning tunneling microscopy, STM) untersucht, welche auf einer Ru(0001)-Einkristalloberfläche abgeschieden worden sind. Durch das Dosieren von atomarem Sauerstoff bei Raumtemperatur werden die dünnen Goldschichten aufgebrochen und in kleine oxidierte Nanopartikel umgewandelt. Dabei ist die vorherige Dicke der Goldschicht entscheidend für die resultierende Morphologie der geformten Nanopartikel. Generell werden aus sehr dünnen Goldschichten (zwei Goldlagen) sehr viele kleinere oxidierte Goldnanopartikel geformt, während bei dickeren Goldschichten ( $\geq$  vier Goldlagen) deutlich weniger Partikel geformt werden, welche aber deutlich größer sind. Außerdem ist die Geschwindigkeit, mit der die Partikel geformt werden, für dünnere Goldschichten deutlich höher als bei dickeren Schichten. Um diesen dickenabhängigen Oxidationsprozess von Goldschichten zu beschreiben, wurde ein sogenannter Schaufelmechanismus (engl. shoveling process) vorgeschlagen, der den Schlüsselschritt der Fragmentierung, nämlich das Hinaufbefördern (Schaufeln) einzelner Goldatome von der Gold-Ruthenium-Grenzfläche zu der Oberseite der Goldinsel, demonstriert. Um ein mögliche katalytische Aktivität der oxidierten Nanopartikel nachzuweisen, wurden CO-Oxidationsexperimente bei Raumtemperatur durchgeführt. Jedoch konnte bisher nur nachgewiesen werden, dass die Partikel, selbst unter stark oxidierenden Bedingungen, von dem Reaktionsgemisch reduziert werden. Die Dispersion und Morphologie der Nanopartikel bleibt bei diesen Reduktionsbedingungen erhalten.

Die beobachteten Morphologien, sowie deren Veränderungen durch Zugabe von atomarem Sauerstoff, wurden mit Hilfe des allgemeinen Modells der heterogenen Nukleation und des epitaktischen Wachstums beschrieben. Basierend auf der Youngschen Gleichung ist es möglich das Benetzungsverhalten eines abgeschiedenen Materials (Adsorbat) anhand verschiedener Grenzflächenenergien zu beschreiben. Diese beinhalten die Oberflächenenergien des abgeschiedenen Materials (Adsorbats) und des Substrats sowie die Grenzflächenenergie zwischen diesen beiden Materialien. Bei unterschiedlichen Gitterparametern von Substrat und Adsorbat muss zudem noch die Verspannungsenergie berücksichtigt werden.

Im zweiten Teil dieser Arbeit wird das Wachstums- und Redoxverhalten dünner Rutheniumschichten auf einer Au(111)-Einkristalloberfläche beschrieben. Wird metallisches

Ruthenium auf der Goldoberfläche abgeschieden, kommt es zum dreidimensionalen Inselwachstum, welches, durch Zusammenwachsen der einzelnen Inseln, in einem rauen metallischen Film endet (zum Beispiel nach Abscheiden von 4 Monolagen Ru). Wiederum ist das Hinzudosieren von Sauerstoff maßgeblich verantwortlich für eine starke morphologische Änderung des abgeschiedenen Rutheniums. Bei typischen Ru(0001)-Einkristall Oxidationsbedingungen (680 K,  $5 \cdot 10^{-5}$  mbar O<sub>2</sub>, 30 min) wird die raue, metallische Rutheniumschicht umgeformt in einen glatten löchrigen Rutheniumfilm. XPS Messungen zeigen, dass dieser löchrige Rutheniumfilm durch eine chemisorbierte Sauerstoffphase stabilisiert wird. Damit ein deckendes RuO<sub>2</sub> gebildet werden kann, muss die Dicke der rauen Rutheniumschicht erhöht werden (typisch 10 Monolagen). Das impliziert, dass eine metallische Rutheniumschicht vonnöten ist, welche als Pufferlage zwischen dem gebildeten RuO<sub>2</sub> und der Goldoberfläche liegt, da angenommen wird, dass ein RuO<sub>2</sub>-film nicht stabil ist, wenn er direkt an eine Goldoberfläche gebunden ist. Um die Umwandlung der dreidimensional zusammengewachsenen Rutheniuminseln zu einem deckenden löchrigen Rutheniumfilm mit einer chemisorbierten Sauerstoffphase beschreiben zu können, wird ein Mechanismus vorgeschlagen. Dieser basiert auf den Beobachtungen in den Experimenten sowie den energetischen Verhältnissen, welche in der Youngschen Gleichung gegeben sind. Abschließend wird die generelle Anwendbarkeit der Youngschen Gleichung anhand verschiedener Beispiele in der Literatur validiert.



# Contents

|  |           |
|--|-----------|
| <b>1. Introduction and Motivation</b>                              | <b>1</b>  |
| 1.1 Brief introduction into the field of gold catalysis            | 1         |
| 1.2 Oxidation of gold surfaces                                     | 4         |
| <b>2. Experimental setup and applied methods</b>                   | <b>9</b>  |
| 2.1 The STM chamber setup  | 9         |
| 2.2 The thermal gas cracker  | 14        |
| 2.3 Electron beam evaporator                                       | 16        |
| 2.4 Scanning tunneling microscopy (STM)                            | 18        |
| 2.5 X-ray photoelectron spectroscopy (XPS)                         | 23        |
| <b>3. Epitaxial growth and nucleation theory</b>                   | <b>27</b> |
| 3.1 Homogeneous nucleation   | 28        |
| 3.2 Heterogeneous nucleation                                       | 32        |
| 3.3 Epitaxial growth   | 34        |
| 3.3.1 Ideal growth near thermodynamic equilibrium                  | 34        |
| 3.3.2 Interface energy and strain energy                           | 39        |
| 3.3.3 Growth far away from thermodynamic equilibrium               | 44        |
| <b>4. Oxidation of Au(111) by atomic oxygen</b>                    | <b>49</b> |
| <b>5. Deposition of Au on Ru(0001)</b>                             | <b>55</b> |
| 5.1 Gold deposited on ruthenium surfaces – General Considerations  | 58        |
| 5.1.1 Gold deposited on oxygen precovered Ru(0001)                 | 62        |
| 5.1.2 Gold deposited on oxygen free Ru(0001)                       | 67        |
| 5.1.3 Gold deposited on RuO <sub>2</sub> (110)                     | 70        |
| 5.2 Redox chemistry of thin gold islands                           | 75        |
| 5.2.1 Oxidation at room temperature by atomic oxygen               | 75        |
| 5.2.2 Au oxide/Au nanoparticle reduction and Au island reformation | 79        |
| 5.3 Thickness dependent oxidation of gold islands                  | 82        |

|   |            |
|---|------------|
| 5.3.1 Incremental oxidation of three layered gold islands                           | 84         |
| 5.3.2 Incremental oxidation of four layered gold islands                            | 86         |
| 5.3.3 Statistic evaluation of the gold nanoparticle height                          | 88         |
| 5.3.4 Oxidation of thick Au islands grown on RuO <sub>2</sub> (110)                 | 90         |
| 5.4 Oxidation of gold films   | 92         |
| 5.4.1 Oxidation of thin gold films by atomic oxygen                                 | 92         |
| 5.4.2 Thickness dependent oxidation of gold films                                   | 96         |
| 5.5 Proposed mechanism for the fragmentation process of thin gold islands and films | 98         |
| 5.6 Activity of the oxidized gold nanoparticles                                     | 101        |
| 5.6.1 Transient activity of the oxidized gold nanoparticles                         | 101        |
| 5.6.1 CO oxidation by the oxidized gold nanoparticles                               | 106        |
| 5.7 Conclusion considering the growth and oxidation of Au on Ru(0001)               | 111        |
| <b>6. Deposition of Ru on Au(111)</b>   | <b>113</b> |
| 6.1 Deposition of ruthenium on Au(111) in vacuum                                    | 117        |
| 6.2 Oxidation of ruthenium islands by molecular oxygen                              | 121        |
| 6.2.1 Formation of a perforated ruthenium film                                      | 121        |
| 6.2.2 Formation of RuO <sub>2</sub> (110) by oxidation of 10 ML Ru/Au(111)          | 126        |
| 6.2.3 Thermal stability of the perforated ruthenium film                            | 131        |
| 6.3 Proposed mechanism for the formation of the perforated Ru film                  | 134        |
| 6.4 Conclusion considering the growth and oxidation of Ru on Au(111)                | 137        |
| <b>7. Inhibition of the Ru(0001) oxidation by gold islands</b>                      | <b>140</b> |
| <b>8. Brief survey about growth behaviors in the literature</b>                     | <b>148</b> |
| 8.1 Deposition of metals on TiO <sub>2</sub>  | 154        |
| 8.2 Growth of RuO <sub>2</sub> on TiO <sub>2</sub> (110)                            | 157        |
| 8.3 Formation of RuO <sub>2</sub> (110) by oxidation of Ru(0001)                    | 160        |
| 8.4 Summary and conclusion  | 167        |
| <b>9. References</b>  | <b>169</b> |

|  |            |
|--|------------|
| <b>10. Appendices</b>  | <b>188</b> |
| A: Theory of the heterogeneous nucleation                      | 188        |
| B: Basic elastic theory – strain energy and dislocation energy | 194        |
| C: Blueprint of the used Ru(0001) and Au(111) single crystals  | 202        |
| D: Danksagung  | 203        |



# 1. Introduction and Motivation

## 1.1 Brief introduction into the field of gold catalysis

Heterogeneous catalysis today is of central interest for the chemical industry. Estimations predict that about 80 % of all commercially produced chemical products involve catalysts (mainly heterogeneous catalysts) at some stage in the process of their manufacture.<sup>[1]</sup> In 2005 catalyzed processes generated about 900 billion US Dollar in products worldwide.<sup>[2]</sup> Especially the platinum group metals and their oxides are used in manifold industrial applications, e.g. oxidation catalysts in exhaust emission or fuel cells.<sup>[3-8]</sup> Therefore research in catalysis is a major field in applied science to further improve the already applied catalytic processes.

Due to the high complexity of the catalytic systems under real process conditions in industry, model systems are generally used to study one or two of the most important aspects of the system. To account for this well defined metal surfaces (i.e. single crystal surfaces) under controlled reaction conditions (usually HV to UHV-conditions)<sup>1</sup>, i.e. single elementary reactions of the more complex reaction mechanism are investigated. By such surface science studies it is possible to design clear cut experiments to investigate and improve the properties of the catalyst systematically.

Generally, the development of equally active and selective catalysts is of great interest. Starting from the same reactant, activation energies for different reaction paths may sometimes differ by less than 1 eV in the field of heterogeneous catalysis<sup>[9]</sup>, thus making it difficult to accomplish a combination of high catalytic activity and selectivity by noble metal catalysts.<sup>[10,11]</sup>

Since the discovery of catalytically active and selective gold nanoparticle catalysts by Haruta et al. manifold research was performed in the field of gold catalysis.<sup>[12-14]</sup> The unique catalytic activity and selectivity of gold catalysts is described in various review articles within the last two decades.<sup>[15-19]</sup> Using the CO oxidation as a model reaction in surface science, different properties have been proclaimed to be responsible for the high activity of the gold nanoparticle catalysts. These properties are the following: the gold *nanosize effect*<sup>[20-29]</sup>, *influence of the substrate* at the interface<sup>[25,27,30-32]</sup>, *electronic effects* like charge transfer<sup>[20,21,33-37]</sup> and the *oxidation state* of the gold nanoparticle.<sup>[16,17,27,38-42]</sup>

---

<sup>1</sup> HV: High vacuum regime:  $10^{-9} - 10^{-3}$  mbar. UHV: Ultra-high vacuum regime:  $10^{-12} - 10^{-9}$  mbar.

- The *nanosize effect* of gold nanoparticles towards CO oxidation is displayed by an increase in reactivity with decreasing size of the gold nanoparticles, with the highest reactivity at a cluster size of 2 nm.<sup>[20-27]</sup> Gold nanoparticles larger than this 2 nm have shown less catalytic activity towards CO oxidation for a broad operating pressure range of O<sub>2</sub> and CO: experiments conducted at UHV conditions<sup>[20,23,24]</sup> and at ambient pressures (mbar region).<sup>[27]</sup> Beside the size of the nanoparticles the morphology of the gold catalyst is equally important.<sup>[25,26,28,29]</sup> The group of Goodman et al. described a flat gold bilayer film on the TiO<sub>2</sub>(110)/Mo(112) surface that is as active as deposited gold nanoparticle catalysts. This activity is explained by the unique structure of the gold bilayer, which consists of a high number of undercoordinated gold atoms.<sup>[20-22,28]</sup>
- *The influence of the substrate* towards the reactivity has also been elucidated: Gold nanoparticles deposited at reducible metal oxides (e.g. TiO<sub>2</sub>, CeO<sub>2</sub>) show a higher catalytic activity than nanoparticles deposited on non-reducible metal oxides (e.g. Al<sub>2</sub>O<sub>3</sub>, SiO<sub>2</sub>).<sup>[25,27,30-32,43]</sup> Experiments and calculations showed that oxygen defects in the metal oxide substrate at the interface perimeter sites facilitate the O<sub>2</sub> adsorption and dissociation during the CO oxidation.<sup>[44-47]</sup> The interplay between oxygen vacancies and undercoordinated gold atoms at these perimeter sites are assumed to be responsible for the high activity of gold.<sup>[41,48,49]</sup>
- *Electronic effects* like the charge transfer from the gold valence orbitals to the  $\pi^*$  molecular orbital (LUMO)<sup>2</sup> of O<sub>2</sub> is also a central aspect in the catalytic activity of gold.<sup>[20,21,33-37]</sup> An increased electron density in gold atoms induced by charge transfer from the underlying substrate to the gold atoms, again supports the influence of the underlying substrate.<sup>[20,21,33-35]</sup> Also the morphology of the gold catalyst is of importance in this context. Charge transfer from the substrate to undercoordinated gold atoms is assumed to be crucial for the O<sub>2</sub> splitting and therefore for the gold activity.<sup>[20,21,36,37]</sup>
- The *oxidation state* of gold during the CO oxidation is probably the most controversial issue. Besides Au(0), Au(I) and Au(III) also anionic gold has been reported to be responsible for the high catalytic activity.<sup>[16,17,27,38-42]</sup> It has been pointed out that the oxidation of gold using atomic oxygen enhances the catalytic activity, with chemisorbed oxygen on metallic gold being more active than a surface gold oxide species.<sup>[16,27,31,38-40]</sup> In contrast, partially oxidized gold particles have

---

<sup>2</sup> LUMO: Lowest unoccupied molecular orbital

been reported to be the active species during CO oxidation.<sup>[17,41,42]</sup> So even for oxidized gold species the most active one for CO oxidation has not been clearly identified yet.

Altogether, manifold research was carried out to clarify the influence of each of these properties on the high catalytic activity of gold nanocatalysts. Despite this intensive work the most active gold species for the CO oxidation remains still elusive. However, the dissociation of O<sub>2</sub> is concordantly determined as the crucial step in CO oxidation due to the generally high dissociation energy of O<sub>2</sub> on gold.<sup>[16,24,33,34,50]</sup> Undercoordinated gold atoms are determined to play a key role in oxidation reactions<sup>[20,21,26,28,29,33,34,36,44,51-53]</sup> because the dissociation energy of O<sub>2</sub> gets significantly lowered.<sup>[44,50,54]</sup>

The availability of undercoordinated gold atoms is also important for CO. Compared to (atomically) flat gold single crystal surfaces, it was shown that CO predominantly binds to undercoordinated gold atoms at highly stepped surfaces due to a higher binding energy.<sup>[52,53,55]</sup> It is pointed out that the overall interaction between the gold catalyst and the CO depends less on the size of the gold nanoparticles but more on the total number of undercoordinated gold atoms.<sup>[53]</sup>

In summary, the catalytic activity of gold catalysts correlates to the availability of undercoordinated gold atoms. Besides a well chosen morphology of gold catalysts (e.g. small gold nanoparticles with size of 2 nm or the gold bilayer system), the oxidation of gold also leads to a higher number of undercoordinated gold atoms.<sup>[36,39,40,51,56-61]</sup>

## 1.2 Oxidation of gold surfaces

Bulk gold is known as one of the least reactive chemical elements. The oxidation of gold using molecular oxygen can hardly be achieved and harsh oxidation conditions are necessary like very high temperatures (usually 500 – 800 °C) and oxygen pressures (up to 1 bar).<sup>[56,62-65]</sup> Quite contrary is the oxidation behavior of gold towards atomic oxygen. By dosing atomic oxygen towards a gold surface it is possible to oxidize gold at lower temperatures (below 200 K).<sup>[66,67]</sup> Even at very low temperatures as 28 K, gold oxide on Au(110) has been formed by electron bombardment of physisorbed oxygen layers.<sup>[68,69]</sup> Recent studies showed that a catalytic inactive gold single crystal surface can be activated by oxidation of atomic oxygen.<sup>[16,30,40,60,66,67,70]</sup> Although the oxidized gold surfaces revealed a higher activity towards CO oxidation and a higher O<sub>2</sub> dissociation probability, it is not clear whether the oxidized gold surface can sustain a catalytic cycle in oxidation reactions, thus only proving a transient activity so far.<sup>[40,51,66]</sup>

The oxidation of gold single crystal surfaces has been investigated using a large variety of atomic oxygen sources, i.e. exposure of ozone, thermal dissociation of O<sub>2</sub> using hot filaments, O<sup>+</sup> sputtering, radiofrequency-generated plasma source, coadsorption of NO<sub>2</sub> and H<sub>2</sub>O and electron bombardment of NO<sub>2</sub>.<sup>[16,32,36,58,59,64,66,70,71-77]</sup> Depending on the source of atomic oxygen, the oxidation of the gold surface can change significantly, leading to different morphologies and oxidized gold species.<sup>[16,55]</sup>

Friend et al. systematically investigated and characterized several oxidized gold species that are formed during the oxidation of a Au(111) single crystal surface by exposure of ozone at 200 and 400 K, respectively.<sup>[66]</sup> At 200 K and lower oxygen coverages (< 0.5 ML) a chemisorbed oxygen phase is formed with the oxygen sitting in the 3-fold hollow sites of the Au(111) surface. At higher coverages (> 1 ML) a three-dimensional bulk oxide phase is formed alongside with subsurface oxygen. If the oxidation of the Au(111) surface is done at 400 K, a two-dimensional surface oxide is formed instead of a chemisorbed oxygen phase.<sup>[66]</sup> Further investigations showed that oxidation of Au(111) at different temperatures and dosages of atomic oxygen leads to coexisting phases of surface oxide, chemisorbed oxygen and subsurface oxygen species.<sup>[39,57]</sup> The surface oxide is preferentially formed at higher temperatures and higher oxygen exposures, while the chemisorbed oxygen phase is usually prepared at lower temperatures and oxygen dosages.<sup>[39,57]</sup>

The oxidation of the Au(111) surface can be briefly summarized in the following steps: Fracturing of the herringbone superstructure towards the linear arrangement of the

herringbone soliton walls, extraction of single gold atoms from the surface and roughening of the surface accompanied by further accumulation of undercoordinated gold atoms on the surface.<sup>[36,39,40,51,57-61]</sup> The adsorbed atomic oxygen has shown to stabilize undercoordinated gold atoms that are formed during the oxidation of gold surfaces.<sup>[36,61]</sup> This explains the roughening of gold surfaces during oxidation, especially if no gold oxides are formed.

The undercoordinated gold atoms, which are released from the gold surface, form mobile AuO<sub>2</sub> species that either diffuse across the surface or rearrange to structures like the surface oxide on Au(111).<sup>[39,57]</sup> The mobile AuO<sub>2</sub> species has been investigated by DFT, and a linear O-Au-O<sup>[78]</sup> as well as an angulated O-Au-O<sup>[38,39,57]</sup> as the mobile precursor structure have been proposed.

The oxidation of the Au(110) and Au(100) surfaces is similar to the oxidation of Au(111), if thermally cracked oxygen or O<sub>2</sub> sputtering is used as source of atomic oxygen.<sup>[50,60,65,68,69,79]</sup>

In summary: The oxidation leads to the removal of the surface reconstruction of the Au(110) and Au(100) surfaces, which is followed by the extraction of single gold atoms and the formation of various oxidized gold structures. Depending on the amount of dosed atomic oxygen a chemisorbed oxygen phase, a surface oxide, subsurface oxygen and bulk oxygen can be produced.<sup>[68]</sup> The importance of the atomic oxygen source becomes evident, if ozone is used to oxidize the Au(100) surface. Because the O<sub>3</sub> molecule cannot dissociate on the Au(100) surface, no chemisorbed oxygen phase or oxide formation has been observed.<sup>[55]</sup>

In general, from all metastable bulk gold oxide structures the well described Au<sub>2</sub>O<sub>3</sub><sup>[80,81]</sup> is known to be the most stable one.<sup>[36,63]</sup>

The stability of Au<sub>2</sub>O<sub>3</sub> critically depends on the environment of the oxide.<sup>[68,72,73,80,82]</sup> It easily decomposes by either applying higher temperatures (> 390 K)<sup>[63,68]</sup> or exposing the oxide to air for several hours<sup>[72]</sup>. Calculations and experiments were conducted to solve the pathway of the oxide decomposition, because decomposition products like Au<sub>2</sub>O are considered to be a reactive species in oxidation reactions.<sup>[80]</sup>

The thermal decomposition of oxidized gold surfaces is summarized in table 1.2-1 showing the differently formed gold-oxygen species and the correlating desorption temperatures, obtained from thermal desorption spectroscopy (TDS) experiments.

**Table 1.2-1: TDS data for the thermal decomposition of various oxidized gold surfaces in literature.**

| Oxidation conditions   | Formed oxidized gold species        | TDS: $T_{max}$ | Reference |
|--|-------------------------------------|----------------|-----------|
| <i>Au(111), O<sub>2</sub> at high T and p</i>                        | Bulk Au <sub>2</sub> O <sub>3</sub> | 413 K          | 62,63     |
| <i>Au(111), NO<sub>2</sub>, e<sup>-</sup> bombardement</i>           | chemisorbed oxygen                  | 550 K          | 51        |
| <i>Au(111), O<sub>2</sub> sputtering</i>                             | Au <sub>2</sub> O <sub>3</sub>      | 390 K          | 68        |
|  | chemisorbed oxygen                  | 590 K          | 68        |
| <i>Au(111), multilayer O<sub>2</sub>, e<sup>-</sup> bombardement</i> | Surface gold oxide                  | 490 K          | 69        |
|  | chemisorbed oxygen                  | 590 K          | 69        |
| <i>Au(111), ozone</i>  | chemisorbed oxygen                  | 520-550 K      | 71        |
| <i>Au(111), ozone</i>  | chemisorbed oxygen                  | 560 K          | 55        |
|  | chem. O from lifted herringbone     | 590 K          | 55        |
| <i>Au(111), thermally cracked O<sub>2</sub></i>                      | chemisorbed oxygen                  | 505-535 K      | 79        |
| <i>Au(211), ozone</i>  | chemisorbed oxygen from terraces    | 515-530 K      | 56        |
|  | chemisorbed oxygen from steps       | 540 K          | 56        |
| <i>Au(311), ozone</i>  | chemisorbed oxygen                  | 560 K          | 55        |
| <i>Au(100), O<sub>2</sub> sputtering</i>                             | chemisorbed oxygen                  | 460 K          | 60        |
|  | chem. O at undercoordinated Au      | 550 K          | 60        |
|  | subsurface oxygen                   | 620 K          | 60        |
|  | bulk oxygen                         | 720 K          | 60        |
| <i>Au(100), thermally cracked O<sub>2</sub></i>                      | chemisorbed oxygen                  | 470 K          | 79        |
| <i>Au(110), O<sub>2</sub> sputtering</i>                             | Surface oxide                       | 415 K          | 50,68     |
|  | chemisorbed oxygen                  | 545 K          | 50,68     |
|  | subsurface oxygen                   | 620 K          | 50,68     |
|  | bulk oxygen                         | 750 K          | 50,68     |

**Table 1.2-1:** *continued from previous page*

| Oxidation conditions  | Formed oxidized gold species | TDS: $T_{max}$ | Reference |
|---|------------------------------|----------------|-----------|
| <i>Au(110), thermally cracked <math>O_2</math></i>            | chemisorbed oxygen           | 590 K          | 65        |
| <i>Polycrystalline Au, thermally cracked <math>O_2</math></i> | chemisorbed oxygen           | 670 K          | 83        |

Besides the oxidation of single crystal surfaces the oxidation of gold nanoparticles deposited on reducible metal oxides has been investigated.<sup>[32,64,70]</sup> It could be shown that both the formation and the thermal stability of the  $Au_2O_3$  on gold nanoparticles correlates with the size of the gold particle.<sup>[32,74]</sup> The oxidation rate of smaller nanoparticles is usually higher but the stability of gold oxide decreases with decreasing size nanoparticle.<sup>[32,70,74]</sup> An exception are the  $Au_{55}$  nanoparticles that show an inertness towards oxygen plasma.<sup>[74]</sup> Nanoparticles larger than  $Au_{55}$  (~ 1.4 nm) are stated to form a core shell structure containing of a gold oxide shell covering the metallic core upon oxidation in oxygen plasma.<sup>[74]</sup> In addition to the nanoparticle size, the supporting material (e.g.  $TiO_2$ ) is also important for the stability of the formed gold oxide shell. For instance, defects or vacancies in the supporting reducible metal oxide induce the reduction of the oxide shell by oxygen transfer from the gold oxide to the support.<sup>[32,64]</sup>

As described before oxidized gold surfaces show a high activity towards CO oxidation.<sup>[30,40,60,66,70]</sup> Based on these investigations oxidized gold catalysts have already been used to study other oxidation reactions like the partial oxidation of propene, the selective oxidation of styrene or oxidative coupling reactions.<sup>[39,79,84-88]</sup>

The purpose of this dissertation is to investigate the morphology of (ultra-)thin gold and ruthenium structures and their morphologic changes upon oxidation and reduction at variable temperatures. These morphologic changes will then be elucidated on the basis of the heterogeneous nucleation and epitaxial growth theories.

In the first part of this dissertation the growth of thin gold islands and films was thoroughly investigated by scanning tunneling microscopy (STM) and photoelectron spectroscopy (XPS). Gold was deposited by physical vapor deposition (PVD) on a Ru(0001) single crystal surface, which was chosen as the substrate. A well-defined epitaxial growth of gold, with [111] orientation, on the ruthenium substrate occurs due to the small lattice misfit between Au(111) and Ru(0001). Therefore Au grown on Ru(0001) is an ideal model system to study the morphologic changes of thin gold structures under oxygen exposure and to compare their resulting morphology to the literature, i.e. oxidized Au(111) surfaces. The oxidation was

accomplished by using atomic oxygen from a thermal gas cracker as the oxygen source. Within these experiments, the surface was always kept at room temperature due to the thermal instability of oxidized gold structures. After oxidation of the thin gold islands (and films) the redox chemistry of the oxidized gold was investigated by CO reduction as well as CO oxidation experiments. To adequately describe and explain the growth of gold on Ru(0001) and to explain the morphologic changes upon oxidation and reduction, an overview on the theory of heterogeneous nucleation and epitaxial growth will be given.

In the second experimental part of this dissertation the growth of thin ruthenium films on a Au(111) single crystal surface was investigated. In a first step the deposition of Ru by PVD on the gold surface was examined, followed by oxidation of the deposited ruthenium by O<sub>2</sub> at higher temperatures (~ 680 K). Compared to its counterpart (Au/Ru(0001)) from the first experimental section, the growth of Ru on the Au(111) surface has been barely investigated under UHV conditions.<sup>[89,90,91]</sup> Therefore the focus on these investigations was to systematically grow and oxidize thin ruthenium films on the Au(111) surface. Based on these experiments the growth of Ru on the Au(111), especially its morphology (before and after oxidation) were characterized and explained by the theory of heterogeneous nucleation and epitaxial growth.

Finally the general applicability of the presented theory of heterogeneous nucleation and epitaxial growth will be evaluated by a brief overview of studied growth behaviors of various systems in literature. From these systems, three examples were chosen to validate the applicability in more detail:

- (1) Metals deposited on TiO<sub>2</sub>(110)
- (2) The growth of RuO<sub>2</sub> on TiO<sub>2</sub>(110)
- (3) The growth of RuO<sub>2</sub>(110) on Ru(0001), i.e. the oxidation of Ru(0001) by O<sub>2</sub> at 680 K.

## 2. Experimental setup and applied methods

### 2.1 The STM chamber setup

Experiments were performed in a home-built ultrahigh vacuum (UHV) chamber system consisting of three separable chamber parts, which are the scanning tunneling microscopy (STM) chamber, the main chamber for preparation and analysis and the loadlock (high pressure chamber). The basis pressure of this three chamber system is about  $2 \cdot 10^{-10}$  mbar. A detailed description of the whole UHV chamber system is given somewhere else.<sup>[92]</sup> Nonetheless, a brief summary of the used chamber setup will be given in the following. The *figures 2.1-1* and *2.1-2* show technical schemes of the UHV chamber system setup. In the STM chamber part (Chamber part (3) in *figure 2.1-1*) variable temperature scanning tunneling microscopy (VT-STM, Omicron) and scanning tunneling spectroscopy (STS) measurements can be done. A vibration damping system is used in the STM to improve the quality of the STM imaging.

In the main chamber (1) analysis by x-ray photoelectron spectroscopy (XPS) can be performed. For physical vapor deposition (PVD), two e-beam evaporators ((9) and (10), *cf. figure 2.1-1*)<sup>3</sup> are attached to the main chamber loaded with gold and ruthenium, respectively. Also attached to the main chamber are a sputter gun (11) for sample cleaning, a quadrupole mass spectrometer ((12) QMS Pfeiffer Vacuum) for residual gas analysis, a dual x-ray anode (14) and hemispherical analyzer ((13) PSP Vacuum Technology) for XPS measurements and a thermal gas cracker (not shown, Oxford Applied Research) that is used to produce atomic oxygen (*cf. figure 2.1-2*). A more detailed description of the evaporators and the thermal gas cracker will be presented in the chapters 2.2 and 2.3. The sample temperature is measured with an infrared (IR) pyrometer, which was calibrated with a K type thermocouple.

The main chamber is separated from the STM chamber and the loadlock (5) via two gate valves ((7) and (8), *cf. figure 2.1-1*). The pumping system of the main chamber consists of a titanium sublimation pump (19), an ion getter pump (16) and a magnetically levitated turbopump (17) (*cf. figure 2.1-2*). Together with the smaller ion getter pump from the STM chamber ((18) in *figure 2.1-2*) the magnetically levitated turbopump and the ion getter pump from the main chamber are able to maintain the UHV during the STM measurements without introducing vibrational noise.

---

<sup>3</sup> e-beam evaporators: EMF 3 e-beam evaporator from FOCUS and e-flux mini e-beam evaporator from tectra.

Linked by a gate valve a gas line with various gases (e.g. Ar, O<sub>2</sub>, H<sub>2</sub>O, CO, borazine) is connected to the main chamber. Each gas type can be dosed very precisely through a leak valve. The gas line is also connected to the loadlock via a gate valve, so experiments in the main chamber and also in the loadlock are possible. The pressure range for experiments in the loadlock ranges from UHV to the mbar region, if all gate valves are closed and the loadlock is used as a batch reactor. The most important function of the loadlock is the possibility to open it to the atmosphere, while maintaining the UHV in the main chamber and the STM chamber. Thereby STM-tips and samples can be exchanged, inserted or removed from the chamber system very easily and without interfering the daily experimental work in the other two chamber parts.

The sample transfer system is highlighted in *figure 2.1-1* (red chamber parts), which consists of a transfer rod (6) (transfer from loadlock to main chamber), two manipulators ((2) and (4)) and a wobble stick for the sample handling in the STM chamber. Sample annealing on the manipulators is done by boron-nitride resistant heaters. With these resistant heaters temperatures up to 1150 K are applied to the single crystal samples. The single crystal samples used in this work are adapted Ru(0001) and Au(111) crystals (MaTecK GmbH) with a hat-like form (*cf. figure C1-1*, appendix C). With a modified sample holder setup these hat-like single crystals could be fixed, thus reducing possible vibrations. Also the direct contact to the BN resistant heater ensured better annealing possibilities. The top sides of hat-like single crystal surfaces have an area of 3 mm x 4 mm, which were analyzed by STM and XPS, measurements. The purity of the Au(111) and the Ru(0001) single crystals is 99.99 %, respectively.

Cleaning of the Ru(0001) single crystal was performed by cycles of cold sputtering ( $p(\text{Ar}) = 1 \cdot 10^{-6}$  mbar, 15 min at room temperature) with subsequent annealing to 900 K in oxygen ( $\sim 1 \cdot 10^{-7}$  mbar O<sub>2</sub>, 30 min). The oxygen treatment is necessary to oxidize carbon impurities that segregate on the sample surface during the annealing.

The cleaning of the Au(111) single crystal surface is similar to the cleaning of the Ru(0001) surface and was also done by cycles of argon sputtering and annealing in oxygen. However if ruthenium was deposited on the Au(111) surface usually longer sputtering times (up to 6 hours) were necessary due to the relatively strong ruthenium-ruthenium binding and the relatively high hardness of bulk ruthenium.<sup>[93]</sup>

Gold (or ruthenium) deposition was carried out by electron beam physical vapor deposition<sup>[94]</sup> of a gold (ruthenium) source (MaTecK GmbH). The purity of the metal sources was > 99.95 %. The amount of the evaporated metal is monitored and controlled by an ion flux controller.

With a certain setting of ion flux and time it is possible to reproducibly prepare metal islands or films on the surface of the deposition target. The total amount the deposited material (gold or ruthenium) was accurately analyzed and determined by STM images and validated by XPS. During deposition, the single crystal temperature was kept at  $\geq 620$  K. Below that threshold temperature the deposited metal starts to form clusters on the surface. This evidently shows that the system did not attain thermodynamic equilibrium during the deposition process. A more general explanation for the growth of metal clusters at lower temperatures is given in chapter 3.3.3, where the epitaxial growth far away from thermodynamic equilibrium will be described.

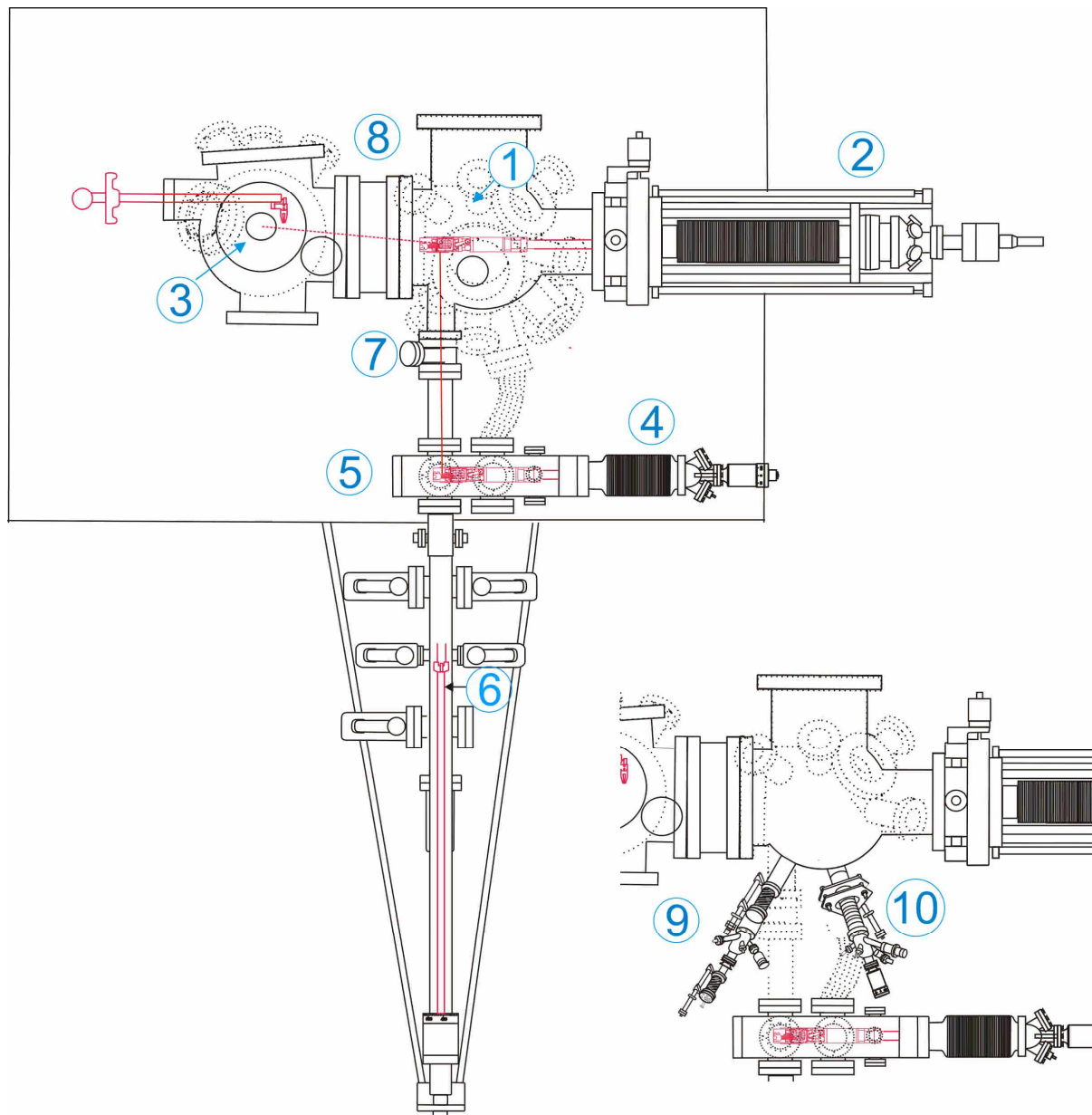


**Figure 2.1-1:** Top view on the schematic STM chamber setup. The larger illustration gives an overview on the sample transporting system (highlighted in red) and the three-chamber setup with their separation by gate valves: (1) Main or analysis chamber, (2) main chamber manipulator, (3) STM chamber including the STM stage, (4) loadlock manipulator, (5) loadlock or high pressure chamber, (6) transfer rod, (7) gate valve between loadlock and main chamber, (8) gate valve between STM and main chamber. The smaller schematic illustration shows the positions of the used evaporators for gold and ruthenium deposition: (9) e-beam evaporator for gold, (10) e-beam evaporator for ruthenium. Figure modified from [92].

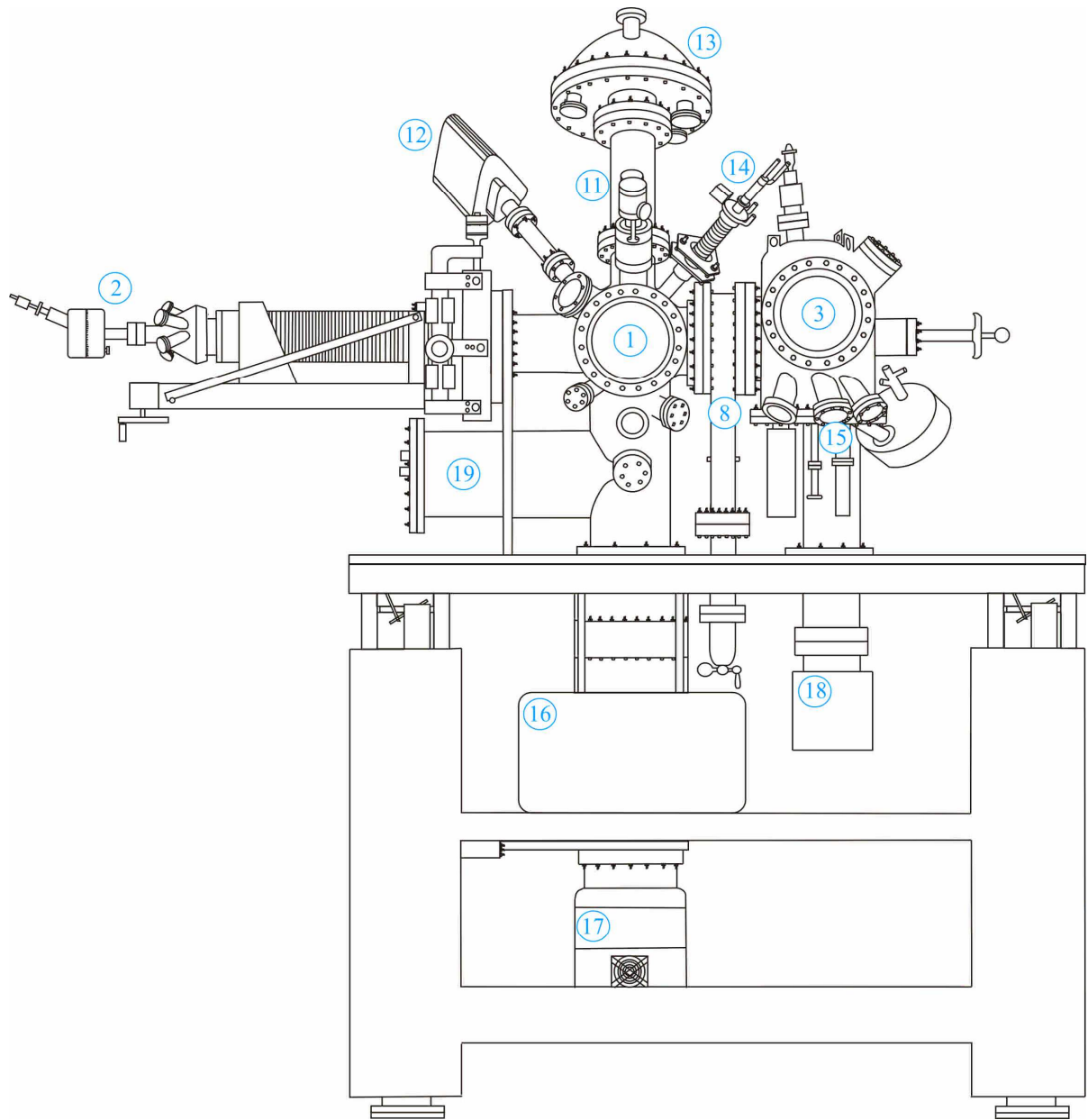


**Figure 2.1-2:** Schematic view on the STM chamber setup, thus showing the arrangement of the used analytics and the pumping system. (1) Main or analysis chamber, (2) main chamber manipulator, (3) STM chamber, (8) gate valve between STM and main chamber, (11) sputter cannon, (12) quadrupole mass spectrometer, (13) XPS analyzer, (14) dual anode x-ray source, (15) flange for CCD camera, (16) ion getter pump, (17) turbomolecular pump, (18) ion getter pump, (19) titanium sublimation pump. Figure modified from [92].

## 2.2 The thermal gas cracker

Dissociation of gas molecules yielding atomic fragments can be achieved by many ways, one of them being thermal excitation.<sup>[95]</sup> The most common and easiest available method for thermal cracking is using a hot tungsten filament as the heat source.<sup>[96,97]</sup> This is however problematic for reactive gases like oxygen or chlorine, which would damage the filament in a matter of seconds. Because of this a different cracker design was needed. The result was the thermal gas cracker TC50 manufactured by Oxford Applied Research.<sup>[96]</sup>

The idea behind this thermal gas cracker is to choose material which on the one hand is able to dissociate the introduced gas but on the other hand is also inert towards the dissociated gases and the damage that might be caused by them, even at higher temperatures. In this TC50 thermal gas cracker the gas is channeled through a thin capillary made of iridium. The gas is leaked into the Ir capillary of the cracker through a standard leak valve which is connected by a CF16 flange to the cracker tubing. The capillary is heated by an electron bombardment mechanism. For this purpose two tungsten filaments coated with thorium oxide are placed at either side of the capillary. By applying high voltage (1000 V) between the filaments and the iridium capillary, the emitted electrons are accelerated towards the capillary. *Figure 2.2-1* gives a schematic illustration of the TC50 thermal cracker setup. To reduce the heat load on the UHV chamber generated by the hot capillary, the entire system is cooled by a copper block heat sink, which in turn is cooled by water. The temperature of the iridium capillary can be regulated by the deployed power ( $\leq 60$  W). Because the acceleration voltage is constant, the power depends solely on the number of impacting electrons and by this relation on the applied heating current of the filament.

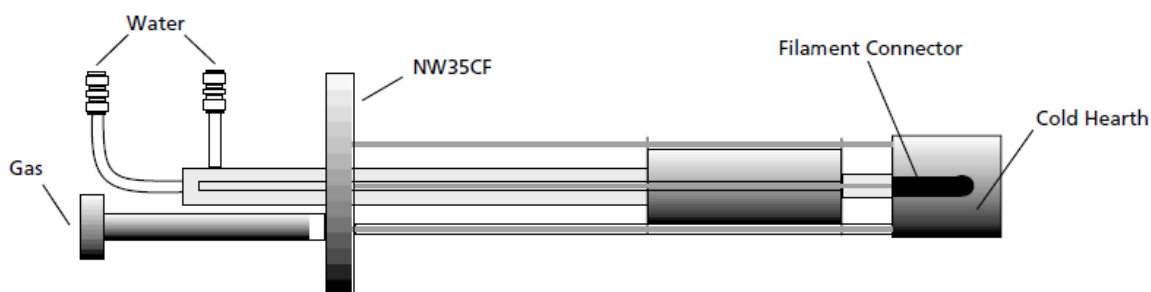


**Figure 2.2-1:** Schematic drawing of the thermal gas cracker setup. Figure taken from [96].

The cracking efficiency (C.E.) depicts how much of the channeled gas is thermally cracked.<sup>[97]</sup> It is determined by the parent molecule loss method using a common Pfeiffer Prisma 200 quadrupole mass spectrometer (QMS).<sup>[97,98]</sup> Because the atomic products of the

cracked gas react with the chamber walls, they are permanently lost from the QMS signal of the parent molecule (i.e. in the case of this thesis only O<sub>2</sub>). The drop in QMS signal after switching on the cracker can therefore be related directly to the C.E. In practice this means that the partial pressure of the parent molecule in the gas chamber was tracked with the QMS Prisma 200 and controlled by the Quadstar software suite. The cracking efficiency then is given as:

$$C.E. = \frac{p_{i,off} - p_{i,on}}{p_{i,off}} = \frac{I_{i,off} - I_{i,on}}{I_{i,off}} \quad (2.2-1)$$

With  $p_{i,off}$  being the partial pressure of O<sub>2</sub> that is leaked into the chamber beforehand and  $p_{i,on}$  being the partial pressure after the gas cracker is switched on.  $I_{i,off}$  and  $I_{i,on}$  are the corresponding ion currents measured by the QMS.

To guarantee a stable exposure of atomic oxygen several precautionary experimental procedure steps were done. First the sample was brought into position in front of the thermal gas cracker. Then the sample was turned away, thus exposing the backside of the manipulator towards the thermal gas cracker and not the sample itself, until a stable oxygen pressure and a stable C.E. was obtained. Only with a stable C.E. and therefore a stable gas beam, containing the atomic oxygen, the sample was exposed to the front of the thermal gas cracker. With this protocol a high reproducibility for all oxidation experiments could be achieved.

The generated atomic species by the TC50 from O<sub>2</sub> are throughout this work referred to as O´.

## 2.3 Electron beam evaporator

Epitaxial film growth can be achieved by various methods: physical vapor deposition (PVD), chemical vapor deposition (CVD), atomic layer deposition (ALD), pulse laser deposition (PLD), molecular beam epitaxy (MBE) and sputtering deposition (SD). For deposition and growth of metal or oxide films, PVD is a widely used method to produce well defined ultra-pure films.<sup>[99,100]</sup>

Standard electron beam evaporators, like the EMF 3 manufactured by FOCUS<sup>4</sup> or the e-flux mini e-beam evaporator from tectra, are used in high or ultrahigh vacuum systems.<sup>[99,100]</sup>

Figure 2.3-1 schematically illustrates the setup of the EMF 3 evaporator.

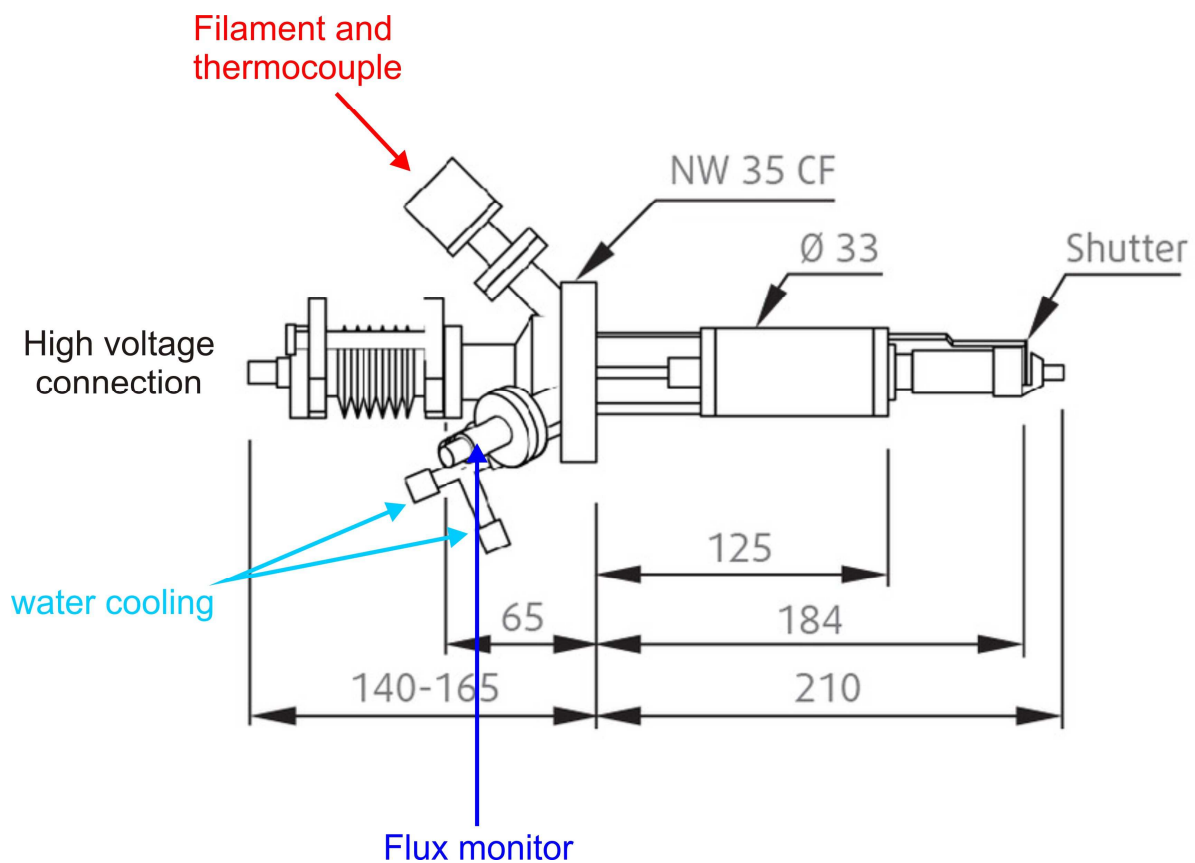


**Figure 2.3-1:** Schematically illustration of the EMF 3 evaporator (FOCUS). Figure modified from [99].

In PVD the material, that is supposed to be deposited, is vaporized into the gas phase. From various possibilities to evaporate the deposition material (like sputtering or annealing in a Knudsen cell) the simplest way for metal evaporation is it's annealing by emitting electrons towards the deposition material (electron bombardment). The deposition materials are usually

<sup>4</sup> Subsidiary company of Oxford Instruments.

mounted as a rod or are placed in a crucible. Applying high voltage between the deposition material and the filament induces the emission of electrons from the nearby tungsten filament towards the deposition target, thus leading to its annealing. When the material is evaporated a small amount of it gets ionized. These ionized atoms are monitored and repelled back into an ion suppressor to determine the flux rate of the deposition material and to avoid damage to the substrate by the ionized atoms.<sup>[99,100]</sup>

For the gold deposition experiments a gold sheet with a purity of 99.95 % (MaTecK GmbH) was mounted in a tungsten crucible of the EMF 3 evaporator. Typical evaporation conditions were an applied high voltage of 880 V and an emission current of 16-19 mA between the filament and the crucible (heating power ~ 14 to 17 W). Ruthenium was evaporated from the e-flux mini e-beam evaporator from mounted ruthenium rods that had a purity of 99.95 % (MaTecK GmbH). Typical evaporation conditions for ruthenium were an applied high voltage of 1.2 kV and an emission current of 35 mA. Compared to gold, a significant higher heating power for ruthenium (~ 41 W) is necessary for its evaporation into the gas phase.

It has to be mentioned that due to different possible setups and positions of the evaporators towards the target sample the total amount of deposited material and the exact deposition rate had to be determined *ex situ*. In this work this was accomplished by statistical analysis of STM pictures of the deposited material in the sub-monolayer region combined and verified with the integrated intensity of the corresponding XPS signals.

## 2.4 Scanning tunneling microscopy (STM)

Scanning tunneling microscopy (STM) is an imaging technique used in surface science. Its possibility to resolve single atoms makes it a powerful tool to investigate various systems and processes at the atomic level, if conducting and semiconducting materials are used as samples. The essential phenomenon behind STM is the quantum mechanical tunneling effect.<sup>[101,102]</sup> This effect stems from the fact that the wave function of a particle does not abruptly fall to zero at a potential barrier with an energy higher than the particle energy. Instead the wave function decays exponentially in it. If it has not decayed to zero when it reaches the other end of the potential barrier it oscillates on the other side with reduced amplitude. This is shown in *figure 2.4-1*. The particle corresponding to the wave function therefore can "tunnel" through the potential barrier despite lacking the energy needed to pass it under classical conditions.

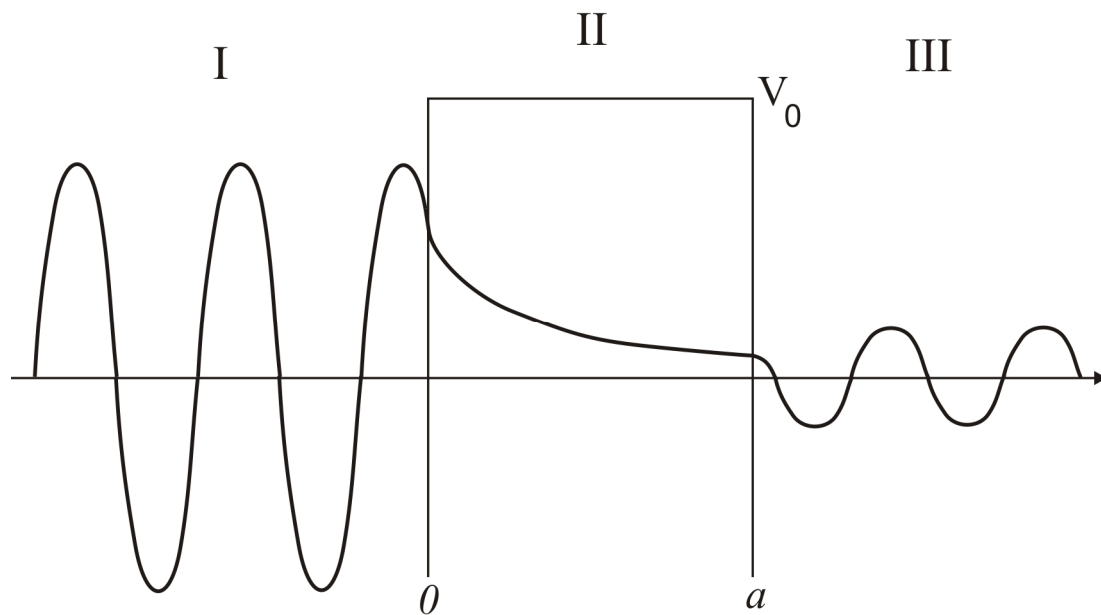


**Figure 2.4-1:** Tunneling of a wavefunction from a potential free zone I to another potential free zone III, through a potential II. Upon reaching the potential, the wavefunction decays exponentially. If the amplitude is sufficient, the wavefunction can start to oscillate again after leaving the potential. Figure modified from [92].

In STM this effect is exploited by placing a metal tip very close (Angstrom scale) to a conducting sample and applying a voltage between sample and tip.<sup>[103,104]</sup> The electrons are then able to tunnel between sample and tip (the potential barrier). Depending on the Fermi level of the conducting surface, the applied voltage determines the direction of the tunneling current, i.e. directed current from tip to surface (positive bias voltage applied to the sample) or

directed current from the surface to the tip (negative bias voltage applied to the sample) (cf. figure 2.4-2). The tunneling current then is defined as a function of the sample to tip distance, the applied voltage and the local density of states (LDOS) of the surface and tip. The height of the potential barrier  $V_0$  is denoted as the work function  $\Phi$ . The work function itself is defined as the energy that is necessary to excite an electron from the Fermi level ( $E_F$ ) to the vacuum level ( $E_V$ ).

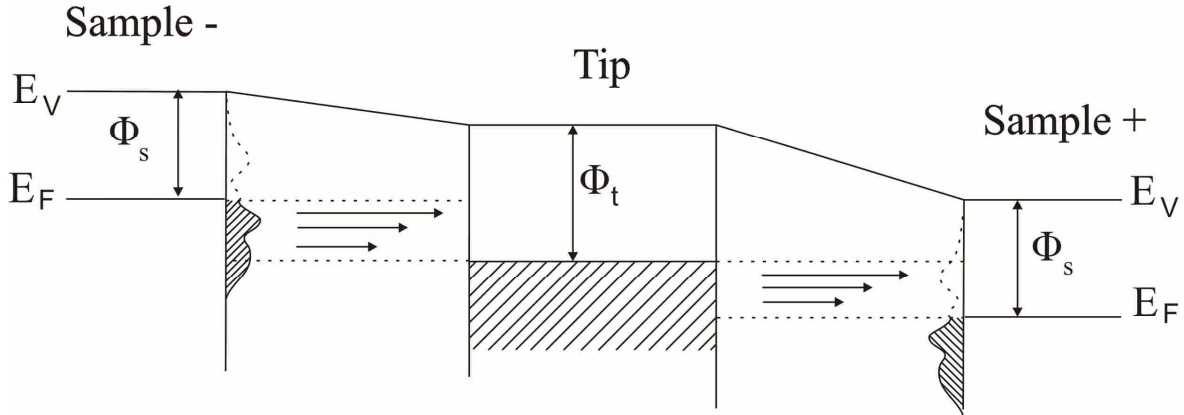


**Figure 2.4-2:** Dependence of the tunneling effect on the electron density of the sample. Figure modified from [105].

Equation (2.4-1) shows the exponential dependency between the tunneling current  $I_t$  and the tip to sample distance  $s$  and the work function  $\Phi$ . Given by this simplified expression the exponential decrease of the tunneling current by simultaneous increase of the tip to sample distance is elucidated. However this equation only shows the topographic dependency of the tunneling current to the tip-sample distance. In STM also the electronic nature is equally important for the tunneling current, which will be further elucidated later.

$$I_t \propto e^{-2ks} \quad \text{with} \quad k = \sqrt{\frac{2m(V_0 - E)}{\hbar^2}} \quad (2.4-1)$$

$m = \text{mass of the tunneling object}$

$$\Phi = V_0 - E$$

The STM can be operated in two modes, keeping constant either the tip to sample distance or the tunneling current. The movement of the tip perpendicular to the surface (in constant current mode) or alternatively the profile of the tunneling current (in constant distance mode) are then directly proportional to the height profile and electronic density of the sample

surface. Therefore scanning the STM tip over the surface yields information of both in the resulting STM image: the morphology and electronic structure of the sample surface.

The movement of the STM tip is controlled by piezoelectric crystals (*cf. figure 2.4-3*). With this instrumentation, atomic resolution can be achieved on single crystalline surfaces. Depending on the material that is investigated, different settings like the applied voltage and the scanning speed have to be chosen wisely. For the widely used tungsten tips in STM, it is necessary to consider different scanning settings for a clean metallic surface and an oxidized single crystal surface containing weakly bound oxygen. *Figure 2.4-3* illustrates the STM imaging process. By moving the tip in  $x$  and  $y$  direction the surface is scanned. From the tip retraction in  $z$  direction, information of the sample topography and the sample LDOS is obtained. Based on the information of the control voltages (in constant current mode) of the piezo tubes an image of the scanned surface is generated, including the height information of the scanned objects.

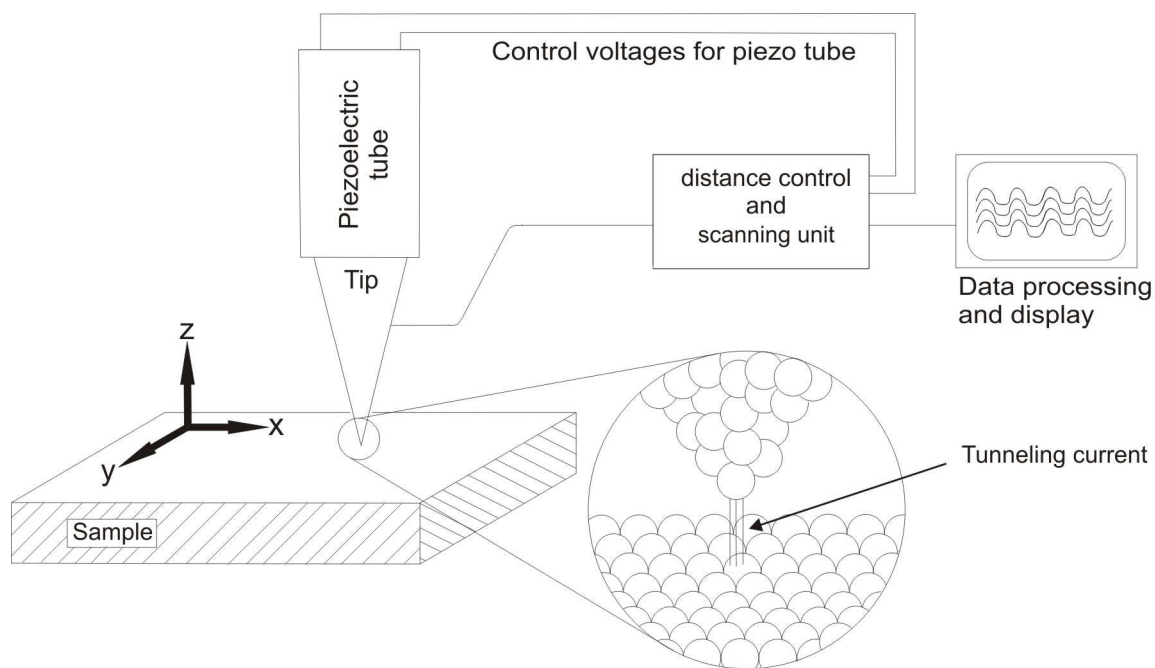


**Figure 2.4-3:** Schematic illustration of the STM imaging process. While the tip scans the surface in  $x$  and  $y$  direction, the movement of the tip in  $z$ -direction gives the height profile of the sample surface. The movement of the tip, i.e. the control voltages of the piezo tubes ( $x,y,z$ ) is transferred into a three-dimensional image of the sample surface. This image combines the information of the surface topography as well as its LDOS. Figure modified from [92].

As the magnified inset suggests, the tunneling current from the tip is mainly induced through only a few atoms. Using standard scanning settings of 1 V (electric potential), 1 nA (tunneling current) and a tip to sample distance of about 1 nm, huge tunneling current densities (up to  $10^5$  A/mm<sup>2</sup>) and field intensities ( $\sim 0.1$  V/Å) are applied. These settings may lead to a local

annealing of the tip, which results in a higher reactivity of the tip material. These effects have to be considered during the measurement, where the tip material may strongly interact with the sample surface. For instance a tungsten tip may interact with an oxygen covered surface, thus reducing the tips stability. One possibility to avoid this problem is to use platinum tips. However their fabrication is more complicated and more expensive than their tungsten counterparts. Therefore tungsten tips are widely used in STM experiments.

A detailed and theoretical description of the tunneling current in the STM was first derived by Tersoff and Hamman.<sup>[106,107]</sup> Here the tunneling current  $I_t$  is directly related to the LDOS of both the sample  $\rho_s$  and the STM tip  $\rho_t$  near the Fermi Level. By placing the metal tip very close to the sample the Fermi levels of such a conducting metallic system are aligned. As a result the electrons tunnel in both directions, giving a net tunnel current of zero. An applied electric potential  $U$  is able to shift the Fermi Levels of sample and tip so that electrons start to tunnel the potential barrier mainly in one direction to travel from occupied states in the sample to empty states in the tip and vice versa, depending on the algebraic sign of  $U$ . This gives rise to a net tunneling current. With this theoretical framework, Tersoff and Hamman derived their now widely used equation:

$$I_t(x, y, s) = e^{-2s\sqrt{\frac{2m\Phi_m}{\hbar^2}}} \cdot \int_0^{eU} \rho_s(x, y, E_F - eU + \varepsilon) \cdot \rho_t(E_F + \varepsilon) d\varepsilon \quad (2.4-2)$$

with  $\Phi_m = \frac{\Phi_s + \Phi_t}{2}$

One should particularly note when looking at equation (2.4-2), that the tunneling current  $I_t$  is related exponentially to both, the distance  $s$  between sample and tip and the work function  $\Phi$ . The convolution of the topographic (first factor: exponential function from eq. (2.4-2)) and the electronic effects (second factor: integral from eq. (2.4-2)) of the sample surface are also clarified.

Because the tunneling current contains information on both, the topographic and electronic nature, the interpretation of STM pictures is not always straightforward. For example: atoms with a low electronic density can be depicted in the STM image as lying lower than atoms of the same geometrical height with higher electronic density. In constant current mode the retraction of the tip from higher lying atoms on the surface is depicted as brighter spots in the STM image, however this would only represents the surfaces topology. But the retraction of the tip also depends on the LDOS of the scanned surface. Above atoms with a higher LDOS the tip has to retract from the surface to keep the tunneling current constant. Contrary, for

atoms with a lower LDOS the tip has to approach to the surface to maintain a constant tunneling current.  $\text{TiO}_2$  is a well known example, where the electronic effects of the sample surface predominate in the resulting STM image.<sup>[108]</sup> The protruding oxygen atoms have a significantly lower LDOS compared to the lower lying Ti atoms. In the STM image the Ti atoms are shown brighter than the oxygen atoms, although it would be other way round if only the topography of the surface would be imaged. This example evidently illustrates that interpretation of STM images can become difficult. Still STM is one of the most powerful methods to identify and visualize different surface species and processes on the atomic scale and is therefore widely-used in surface science.

## 2.5 X-ray photoelectron spectroscopy (XPS)

In surface science photoelectron spectroscopy (PES) is used to investigate the chemical composition (e.g. a pure substance or an alloy) and chemical nature (e.g. oxidation state) of a surface and its adsorbates.<sup>[109-112]</sup> The PES is based on the photoelectric effect described by Einstein in the early 19<sup>th</sup> century.<sup>[113,114]</sup> Herein high energetic, electromagnetic irradiation (typically x-ray irradiation) induces electrons to leave the surface. From the kinetic energies of these emitted photoelectrons it is not only possible to identify the chemical elements that are present in the surface, moreover the chemical nature of these elements, like its oxidation state or the element composition, can be determined, too.<sup>[109-112]</sup> The photoelectron spectroscopy was developed from Kai Siegbahn in the 1960<sup>ies</sup> for which he was honored (in 1981) by the Nobel Prize in physics.<sup>[109]</sup> In the following years the PES adapted in surface science was named x-ray photoelectron spectroscopy because mainly soft x-ray irradiation is used.<sup>[111,114]</sup>

In common laboratories usually x-ray sources with monoenergetic x-rays are used. The specific energy of the photons depends on the material used in the x-ray source. Widely used are the so called dual anode x-ray sources that contain of two different anode materials which are usually aluminium and magnesium<sup>5</sup>. In contrast, at synchrotron radiation facilities the x-ray energy can be changed by monochromators from  $\sim 10$  eV up to far over 1000 eV.<sup>[114]</sup> With a much higher photon flux at lower x-ray energies the XPS measurements at synchrotron facilities are much more surface sensitive.

*Figure 2.5-1A* shows schematically the process of the electron emission of the x-ray source. With incoming photon energy  $h\nu$ , photoelectrons from the core levels of the irradiated materials can be generated. If the x-ray energy is higher than the sum of the binding energy of the atomic orbital  $E_B$  and the work function  $\varphi_S$  of the electron towards the vacuum level ( $E_{vac}$ ) the photoelectron is emitted with a element specific kinetic energy  $E_{kin}$ . The kinetic energy of the detected photoelectron then only depends on the work function of the spectrometer  $\varphi_{Spec}$ . From the conservation of energy the following well known equation for the kinetic energy of the emitted photoelectrons can be derived:

$$E_{kin} = h\nu - E_B - \varphi_{Spec} \quad (2.5-1)$$

---

<sup>5</sup> X-ray energies: Al-K $\alpha$ 1,2 with 1486,6 eV and Mg K $\alpha$ 1,2 with 1253,6 eV

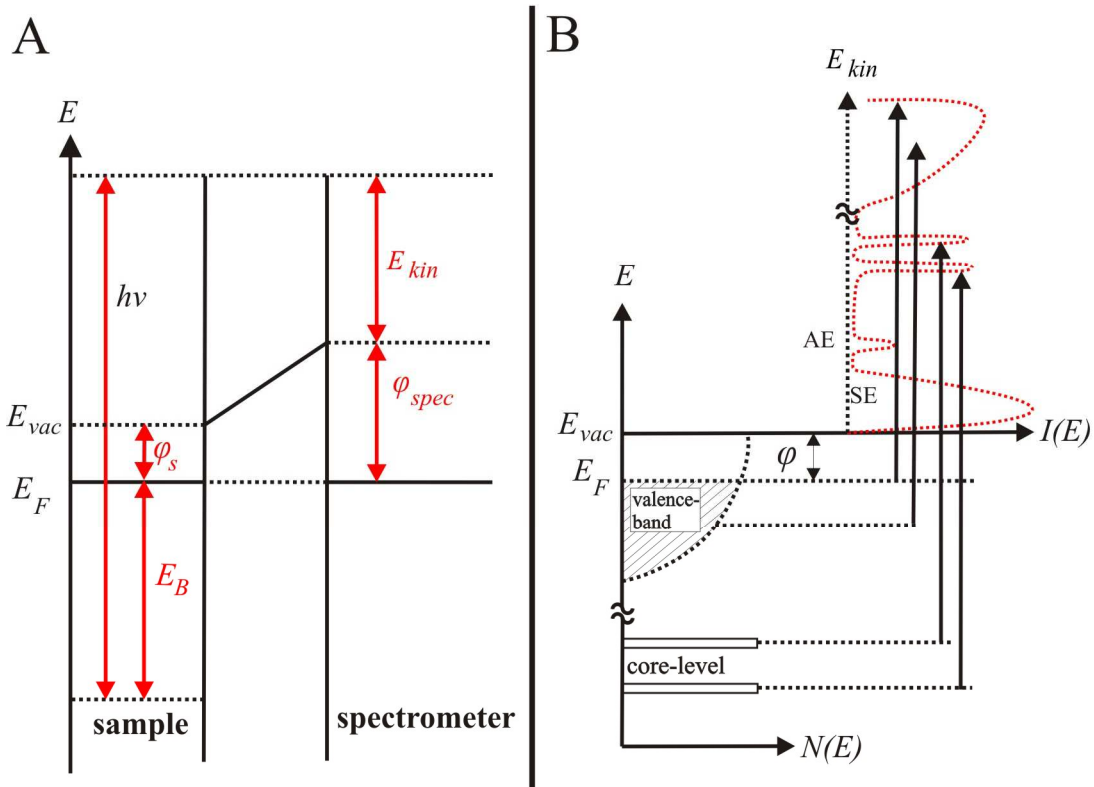


**Figure 2.5-1:** A) Schema of the energetic processes and levels that are important for XPS. B) Development of XPS spectra. AE = Auger electrons, SE = secondary electrons. Figure modified from [110].

For conducting metals (and semiconductors) the Fermi level is usually used as the reference value due to the maximal kinetic energy or the lowest binding energy ( $E_B = 0$ ). The binding energy of the emitted photoelectron correlates to the difference of the energetic ground state ( $E^i(N)$ ) of the atom, consisting of  $N$  electrons, and the excited energetic state of the atom after the emission of the photoelectron ( $E^f(N-1, n, l)$ ). The ground state is called initial state in XPS while the excited state is usually referred as final state. To a first approximation, the so called Koopmans' theorem<sup>[115]</sup>, no relaxation process of the remaining ( $N-1$ ) electrons is assumed to occur during the emission of the photoelectron, thus leaving the ionized atom still in the energetic ground state of the neutral species. With this approximation the binding energy can be assigned to the negative orbital energy  $-\varepsilon(n, l)$  of the emitted photoelectron. The Koopmans' theorem can then be expressed by:

$$E_B^V(n, l) = E^f(N-1, n, l) - E^i(N) = -\varepsilon(n, l) \quad (2.5-2)$$

However this approximation describes only inaccurately the binding energy, due to the so called initial state and final state effects. Due to fast relaxation processes of the remaining electrons (initial state effects) as well as correlation and relativistic effects (final state effects),

the orbital energies of the atoms change immediately after excitation of the photoelectron.<sup>[113]</sup> Therefore the binding energy has to be corrected by these specific terms:

$$E_B^V(n,l) = -\varepsilon(n,l) - \delta\varepsilon_{relax.} - \delta\varepsilon_{rel.} - \delta\varepsilon_{corr.} \quad (2.5-3)$$

A typical example for the initial state effect is the chemical state of an element, which depends on the chemical environment. The energy levels of the element are changed before the photo ionization, e.g. due to the chemical bonding to other elements where the valence electrons are involved. Because the outer (valence) electrons also have electron probability density near the atomic core, they weaken the electrostatic interactions between the protons and the inner (core) electrons. If chemical bonds are formed, this evidently changes the core level energies (orbital energy  $\varepsilon(n,l)$ ) and therefore the measured binding energies by XPS.

Typical examples for final state effects are the plasmon excitation or the electron-hole excitation. When the photoelectron moves out of a metallic surface, it can supply some of its energy to the plasmons. This plasmon excitation is usually visible by small hillocks, which are usually shifted by a few eV ( $\leq 10$  eV) to higher binding energies compared to the metallic XPS signals. The electron-hole excitation is usually visible by the asymmetric shape of XPS signals. In this process the emitted photoelectron loses some of its kinetic energy by exciting another electron to the valence band, thus leaving a hole in the conducting band. Due to the energy loss the asymmetric shape of the metallic XPS signal is visible by a flank at higher binding energies as well as a slight increase of the background signal.

Still, due to the unique orbital energies, it is possible to assign the uniquely kinetic energy (or binding energy) to a specific element. With the possibility to further investigate the oxidation state of the analyzed material, XPS has been proven to be an important method in surface science. The development of a XPS spectrum is schematically illustrated in *figure 2.5-1B*. After x-ray irradiation, photoelectrons are emitted from the surface. The amount of the detected photoelectrons is then plotted against the binding energy leading to a spectrum consisting of peaks at specific binding energies and intensities. From the binding energy of the photoelectrons it is possible to derive the orbital energy by using Koopmans' theorem. From the exact position and the shape of the peaks it is possible to assign the chemical nature of the analyzed element. The intensity of the XPS signals (quantitatively) describes the amount of the specific element type in the sample. Often core level shifts between the same elements are very small, thus leading to an overlapping of XPS signals. To provide an adequate deconvolution such overlapped XPS signals, x-ray sources with a superior surface

sensitivity and resolution like synchrotron facilities may be necessary for quantitative analysis of the XPS data.

Besides the peaks derived from the described photoelectron process, additional peaks are observable in the XPS spectra. These peaks are for instance related to relaxation processes like the Auger effect which are subsequent to the photoelectron emission.<sup>[116]</sup> After the removal of a core electron a hole state is created. Electrons from a higher energetic orbital can fall into the hole state by simultaneous release of energy. This energy can be released by either emission of another photon or by an excitation of a second electron, which is ejected subsequently. This ejected electron is called Auger electron. The kinetic energy of the emitted Auger electrons also gives specific information of the chemical nature of the atom due to element specific electron transfer during the Auger process.

The surface sensitivity of XPS can be illustrated by the universal curve (*cf. figure 2.5-2*). While the x-rays can enter up to several micrometers into the material the escape depth of the emitted electrons depends on the mean free path through the material. With a kinetic energy of 100 – 1000 eV the mean free pathway of the emitted photoelectrons is approximately 3 to 8 atomic layers of the material. Therefore emitted electrons from the bulk cannot leave the material. Only photoelectrons from the topmost atomic layers can leave the material, resulting in high surface sensitivity.

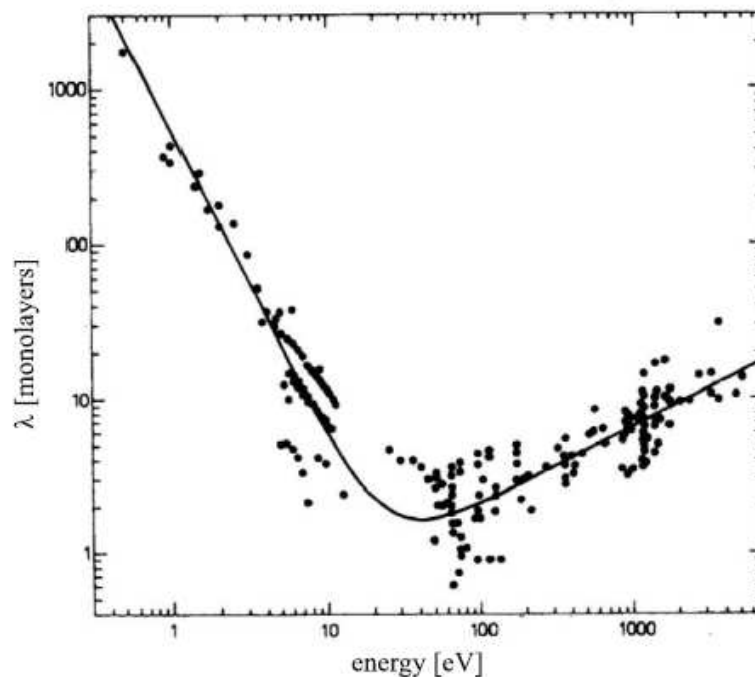


**Figure 2.5-2:** The so called “universal curve” depicts the energy dependence of the mean free path (given in monolayers) of electrons in solids to show the surface sensitivity of a used method. Figure taken from [117].

### 3. Epitaxial growth and nucleation theory

The deposition of metals and their growth on a substrate is usually a complex process. The description and explanation of the formed morphologies is not straightforward and much information about the system has to be gathered to adequately describe the observed growth behavior and structures. For this, the general theory of nucleation and growth is well known in literature: Variety of specialized books<sup>[118-124]</sup> and review papers<sup>[125-135]</sup> have already been published to present an overview of mechanisms in the theory of homogeneous and heterogeneous nucleation as well as in the field of epitaxial growth. Based on these general descriptions more specialized growth models have been derived to explain the observed growth behaviors.<sup>[128,136,137]</sup>

This chapter will be subdivided into a general introduction of nucleation theory, starting with the homogeneous nucleation and the heterogeneous nucleation. Afterwards an introduction into the theory of epitaxial growth will be given. The author of this dissertation used the knowledge of the specialized books and the review papers to briefly summarize these general concepts.<sup>[118-135]</sup>

### 3.1 Homogeneous nucleation

Nucleation describes the phase transition of a material or element by the formation of small (hemi-)spheres, e.g. the formation of water droplets in a moisture atmosphere. The term nucleation is also widely used by the structural arrangement of smaller elements or molecules into larger particles or clusters. Generally nucleation is divided into homogeneous nucleation and heterogeneous nucleation. The homogeneous nucleation describes the transition without the influence of a surface. A common example is the formation of water droplets in gas phase from H<sub>2</sub>O molecules. In heterogeneous nucleation a surface or interface is always involved in the nucleation process.

In the following the theory of homogeneous nucleation will be illustrated by the simple example of spontaneous formation of liquid droplets in a gas phase.<sup>[118-124]</sup>

Starting from a phase transition between gas and liquid the Gibbs free energy is given by:

$$\Delta G = -nRT \cdot \ln\left(\frac{p}{p_{eq}}\right) \quad (3.1-1)$$

*p* : vapor pressure

*p<sub>eq</sub>* : equilibrium vapor pressure

*T* : Temperature

*R* : universal gas constant

*n* : amount of substance

The quotient  $p/p_{eq}$  determines if the formed droplet is re-evaporates or grows by accumulating more molecules or atoms (depending on the material) from the gas phase:

$\Leftrightarrow p > p_{eq}$     accumulation from gas phase favored

$\Leftrightarrow p < p_{eq}$     evaporation favored

Considering the formation and stability of small spherical liquid droplets the surface free energy plays an important role for formation of these droplets. The Gibbs free energy changes to:

$$\Delta G_{total} = -nRT \cdot \ln\left(\frac{P}{P_{eq}}\right) + 4\pi r^2 \cdot \sigma \quad (3.1-2)$$

$r$  : particle radius

$\sigma$  : surface tension or surface energy

The total free energy decreases with the formation of bulk (first summand) on the one hand and it increases with the formation of a surface (second summand) on the other hand. If the formed droplets are spherical, their volume can be described by:

$$V = \frac{4}{3}\pi \cdot r^3 \quad (3.1-3)$$

By introducing the molar volume ( $V_m$ ), equation (3.1-3) can be expressed by the amount of substance:

$$n = \frac{4}{3} \cdot \frac{\pi}{V_m} \cdot r^3 \quad (3.1-4)$$

Therefore equation (3.1-2) changes to:

$$\Delta G_{total} = -\frac{4}{3} \cdot \frac{RT}{V_m} \cdot \pi \cdot r^3 \cdot \ln\left(\frac{P}{P_{eq}}\right) + 4\pi r^2 \cdot \sigma \quad (3.1-5)$$

Equation (3.1-5) clearly demonstrates that the formed droplets are not stable for any size: For a small radius the surface free energy increases faster than the free energy term for bulk formation. Only by exceeding a certain radius the formed droplets will become stable. This radius is called the *critical radius* of a droplet. *Figure 3.1-1* illustrates the total free energy plotted against the droplet radius.

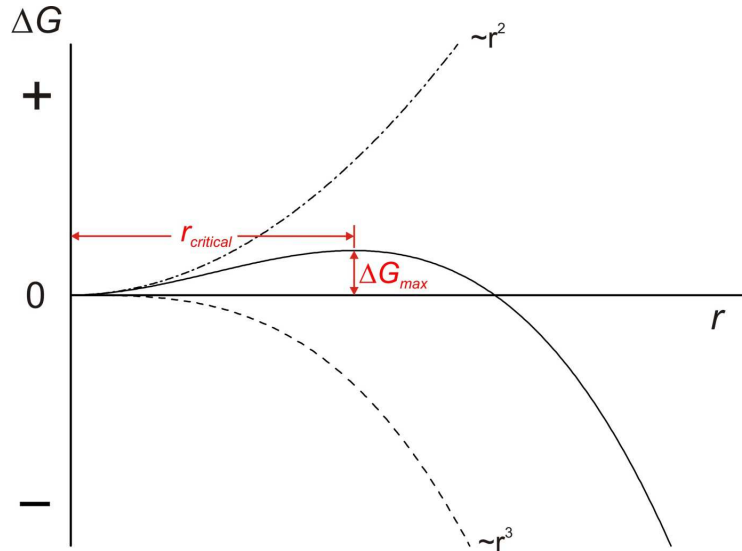


**Figure 3.1-1:** Total free-energy change,  $\Delta G_{total}$ , of a particle as a function of its radius  $r$  and the change of its surface and volume free energy as a function of  $r$ .

As can be seen from figure 3.1-1 the total free energy of the droplet increases to a critical radius  $r_{critical}$  where the total free energy reaches its maximum ( $\Delta G_{max}$ ). If the formed droplets attain the critical size (or critical radius) they become stable and can grow further. If the formed droplets do not overcome the critical size they are not stable and evaporate again. The critical radius of a droplet can be calculated by differentiation of  $\Delta G_{total}$  (equation (3.1-5)) with respect to the radius:

$$\frac{\partial(\Delta G_{total})}{\partial r} = -4 \cdot \frac{RT}{V_m} \cdot \pi \cdot r^2 \cdot \ln\left(\frac{p}{p_{eq}}\right) + 8 \cdot \pi \cdot r \cdot \sigma = 0 \quad (3.1-6)$$

When the total free energy reaches its maximum ( $\partial(\Delta G_{total})/\partial r = 0$ )  $r$  becomes the *critical radius*. Rewriting equation (3.1-6) leads to the description for the critical radius:

$$r_{critical} = \frac{2 \cdot \sigma \cdot V_m}{RT \cdot \ln\left(\frac{p}{p_{eq}}\right)} \quad (3.1-7)$$

Inserting equation (3.1-7) in equation (3.1-5)  $\Delta G_{max}$  is given by:

$$\Delta G_{max} = \frac{4}{3} \pi \cdot \sigma \cdot r_{critical}^2 \quad (3.1-8)$$

By including the Clausius-Clapeyron relation in equation (3.1-7) the temperature dependency of the critical radius can be shown:

$$\begin{aligned}
 r_{critical} &= \frac{2 \cdot \sigma \cdot V_m}{RT \cdot \ln\left(\frac{p}{p_{eq}}\right)} = \frac{2 \cdot \sigma \cdot V_m}{RT \cdot \frac{\Delta H_m}{R} \cdot \left(\frac{1}{T_{eq}} - \frac{1}{T}\right)} = \frac{2 \cdot \sigma \cdot V_m \cdot T_{eq}}{T_{eq} \cdot T \cdot \Delta H_m \cdot \left(\frac{1}{T_{eq}} - \frac{1}{T}\right)} \\
 &= \frac{2 \cdot \sigma \cdot V_m \cdot T_{eq}}{\Delta H_m \cdot (T - T_{eq})} = -\frac{2 \cdot \sigma \cdot V_m \cdot T_{eq}}{\Delta H_m \cdot (T_{eq} - T)} \quad (3.1-9)
 \end{aligned}$$

Therefore the expression for the total free energy changes to:

$$\Delta G_{max} = \frac{16\pi \cdot \sigma^3 \cdot T_{eq}^2}{3 \cdot (\Delta H_m)^2} \cdot \left( \frac{1}{(T_{eq} - T)^2} \right) \quad (3.1-10)$$

The temperature dependent descriptions of the total free energy (3.1-10) and the critical radius (3.1-9) are used to explain a fundamental behavior in nucleation (assuming that  $\sigma$  and  $\Delta H_m$  are approximately temperature independent):

**For small values of  $T_{eq}-T$ , the critical radius of the nucleus increases as well as its maximum total free energy.**

## 3.2 Heterogeneous nucleation

In the following the heterogeneous nucleation will be elucidated by the formation of a liquid droplet on a solid surface by condensation from the gas phase.<sup>[118-124]</sup> This general model is valid for various nucleation processes. *Figure 3.2-1* shows a schematic illustration of a liquid droplet on a solid surface. The involved interfacial tensions that determine the nucleation process are indicated.

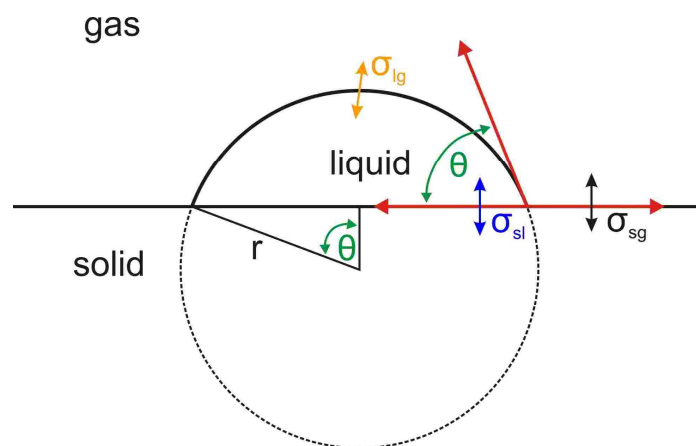


**Figure 3.2-1:** Definition of the contact angle  $\theta$  at the solid-liquid interface: With increasing contact angle the surface area between the liquid and the gas phase increases as well. Therefore the size of the formed droplet on the solid surface is related to the contact angle at the solid-liquid interface. Related to that are the interfacial tensions between the different interfaces:  $\sigma_{sg}$  (at the solid-gas interface),  $\sigma_{lg}$  (at the liquid-gas interface),  $\sigma_{sl}$  (at the solid-liquid interface).

$\sigma_{sg}$  : interfacial tension between solid - gas

$\sigma_{lg}$  : interfacial tension between liquid - gas

$\sigma_{sl}$  : interfacial tension between solid - liquid

The relationship of the contact angle of the condensing liquid droplet with the interfacial tensions is given by the well known Young's equation<sup>6</sup>:

$$\sigma_{sg} = \sigma_{sl} + \sigma_{lg} \cdot \cos(\theta) \quad (3.2-1)$$

Similar to the critical radius and Gibbs free energy in homogeneous nucleation it is possible to derive the analogous equations in heterogeneous nucleation. A detailed description of the derivation for the critical nucleus and the Gibbs free energy of a stable liquid droplet on a

<sup>6</sup> Also known as Young's relation.

solid surface are given in the appendix A. The critical radius and the Gibbs free energy for the heterogeneous nucleation process are:

$$r_{critical,het} = \frac{2 \cdot \sigma_{lg} \cdot V_{m,sc}}{RT \cdot \ln\left(\frac{p}{p_{eq}}\right)} = -\frac{2 \cdot \sigma_{lg} \cdot V_{m,sc} \cdot T_{eq}}{\Delta H_m \cdot (T_{eq} - T)} \quad (3.2-2)$$

$$\Delta G_{max,het} = \frac{16\pi \cdot \sigma_{lg}^3 \cdot T_{eq}^2}{3 \cdot (\Delta H_m)^2} \cdot \left(\frac{1}{(T_{eq} - T)^2}\right) \cdot S(\theta) \quad (3.2-3)$$

with

$$S(\theta) = \frac{(2 + \cos(\theta)) \cdot (1 - \cos(\theta))^2}{4} = \frac{2 - 3 \cdot \cos(\theta) + (\cos(\theta))^3}{4} \quad (3.2-4)$$

$S(\theta)$  is called as the catalytic factor that describes the catalytic potential of the substrate with respect to the nucleation process. Its values range between 0 and 1. Therefore the simplified relation between homogeneous nucleation and heterogeneous nucleation is given by (cf. derivation in appendix A):

$$\Delta G_{max,het} = \Delta G_{max,hom} \cdot S(\theta) \quad (3.2-5)$$

With a contact angle of  $180^\circ$  the catalytic factor becomes 1 and the nucleation process can be described by homogeneous nucleation. From equation (3.2-5) it becomes evident that  $\Delta G_{max,het} \leq \Delta G_{max,hom}$  and therefore nucleation on a surface is always more favored than the corresponding homogeneous nucleation process.

The connection between the catalytic factor, the contact angle and the corresponding degree of wetting is illustrated in *figure 3.2-2*.

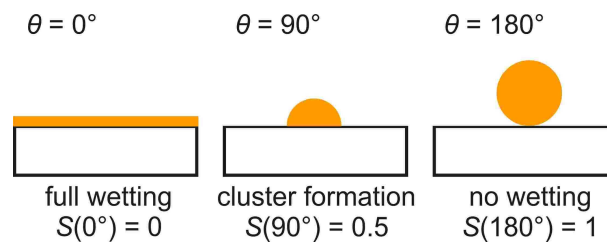


**Figure 3.2-2:** Schematic illustration of the degree of wetting in dependence of the contact angle from a liquid on a solid surface.

### 3.3 Epitaxial growth

#### 3.3.1 Ideal growth near thermodynamic equilibrium

Based on Young's equation the three widely known ideal types of growth for thin films can be described: Layer by layer or "Frank-van-der-Merwe" growth, three-dimensional island or "Volmer-Weber" growth and layer plus island or "Stranski-Krastanov" growth.<sup>[118-135]</sup> It should be noted that these ideal growth modes only describe the growth near the thermodynamic equilibrium. At lower temperatures kinetic effects might have significant influence on the growth behavior, thus changing the growth behavior considerably (cf. chapter 3.3.3).

The three ideal growth modes near thermodynamic equilibrium are:

1. The Frank-van-der-Merwe (FvdM) growth describes a two-dimensional layer by layer growth. Under ideal conditions a completely wetting layer of the growing film covers the substrate before the growth of the second layer starts.
2. The Volmer-Weber (VW) growth describes the three-dimensional growth of islands on the substrate which in the following coalesce to form a (rough) film.
3. The Stranski-Krastanov (SK) growth describes the growth of few wetting layers on the substrate which changes to a three-dimensional growth of islands after a critical film thickness.

A schematic illustration of these three growth mechanisms is given in *figure 3.3.1-1*.

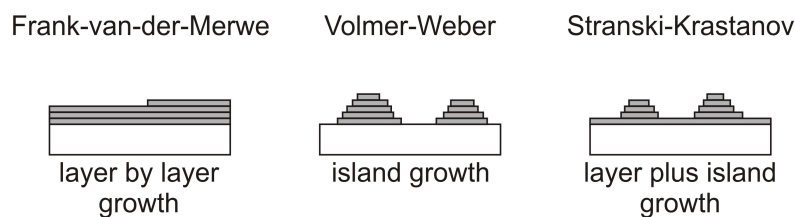


**Figure 3.3.1-1:** Schematic illustration of the three main film growth modes near thermodynamic equilibrium. Figure modified from [122].

Young's equation, which describes the energy relation of the interfacial energies in heterogeneous nucleation, is also used to describe the film growth process. Therefore equation (3.2-1), which displays the nucleation of a liquid droplet on a solid surface,

$$\sigma_{sg} = \sigma_{sl} + \sigma_{lg} \cdot \cos(\theta) \Leftrightarrow \cos(\theta) = \frac{\sigma_{sg} - \sigma_{sl}}{\sigma_{lg}} \quad (3.2-1)$$

is adapted to the formation of a solid adsorbate growing epitaxially on the substrate surface:

$$\sigma_{gS} = \sigma_{AS} + \sigma_{gA} \cdot \cos(\theta) \Leftrightarrow \cos(\theta) = \frac{\sigma_{gS} - \sigma_{AS}}{\sigma_{gA}} \quad (3.3.1-1)$$

$\sigma_{gS}$  : interfacial tension gas - substrate

$\sigma_{gA}$  : interfacial tension gas - adsorbate

$\sigma_{AS}$  : interfacial tension adsorbate - substrate

For a solid material growing on a solid substrate, the interfacial tension between the solid phases and the gas phase ( $\sigma_{gA}$  and  $\sigma_{gS}$ ) corresponds to the surface free energies of the adsorbate ( $\sigma_A$ ) and substrate ( $\sigma_S$ ), respectively. The interfacial tension between both solids ( $\sigma_{AS}$ ) is expressed by the interfacial energy ( $\sigma_I$ ).

In the following the three ideal growth mechanisms will be described and explained by Young's equation. If the interfacial energy can be neglected ( $\sigma_I$  small compared to  $\sigma_A$  and  $\sigma_S$ ), the growth is mainly determined by the surface free energies of the deposited material and the substrate. This is the case for the Frank-van-der-Merwe and the Volmer-Weber growth modes, which qualitatively describe the growth of a system where the surface free energies are considered to be more important than the interface energy on the overall resulting morphology. In the case of the Stranski-Krastanov growth, the transition of a two-dimensional growth of films to the formation of three-dimensional islands, the interfacial energy becomes important and cannot be neglected to explain this ideal growth mechanism<sup>7</sup>.

*Frank-van-der-Merwe growth:  $\theta \approx 0$*

The FvdM growth describes the two-dimensional layer-by-layer growth of the deposited material. With a contact angle of  $0^\circ$  the deposited material is wetting the substrate surface, i.e.  $\cos(\theta)$  must be small. Therefore Young's equation must fulfill the following relation:

$$\sigma_S \geq \sigma_I + \sigma_A \quad (3.3.1-2)$$

The FvdM growth usually occurs on surfaces if there is no lattice misfit between the deposited material and the substrate, e.g. for homoepitaxial growth where  $\sigma_I = 0$ . Therefore the adsorbate with the lower surface free energy is going to completely cover the substrate

---

<sup>7</sup> In principle the strain energy is also important to adequately describe the SK-growth. However in this first approach this growth mode is only explained by the energy relations from Young's equation, which already can be used as a guideline to explain the SK growth behavior.

with the higher surface free energy in order to decrease the total Gibbs free energy of the system.

*Volmer-Weber:*  $\theta > 0$

The VM growth describes the three-dimensional growth of the deposited material. At large contact angles nucleation processes or three-dimensional island growths occur on the surface, i.e.  $\cos(\theta)$  is assumed to be large. Therefore Young's equation must fulfill the following relation:

$$\sigma_s < \sigma_l + \sigma_a \quad (3.3.1-3)$$

During the initial growth the surface free energy of the adsorbate is higher than the surface free energy of the substrate. The deposited material favors internal binding over binding to the substrate, resulting in a three-dimensional island growth.

*Stranski-Krastanov:*

The SK growth is way more complex than the FvdM and the VW growth. Additional explanations are necessary so that the SK growth can be described by Young's equation. The terms stress, strain and lattice misfit will be used for the explanation of the SK growth. A thorough explanation of these quantities and how these contribute to the interface energy is given in the forthcoming chapter 3.3.2 and in Appendix B.

First of all the SK growth mode consists of two different growth phases: the initial growth of several layers wetting the substrate surface, which is followed by the three-dimensional growth of islands on top of these layers. To describe both of these growth phases individually, the modified Young's equations (3.3.1-2) and (3.3.1-3) can be used. However to describe the transition from the two-dimensional layer-by-layer growth to the three-dimensional formation of islands, the interfacial energy now plays a decisive role and has to be included into the explanations.

In the beginning of the SK growth wetting layers are formed until a critical thickness ( $d_c$ ) is reached. For the first stage of growth the adsorbate grows pseudomorphically due to a relatively small lattice misfit and small interfacial energy. The growing adsorbate layer is either under compressive or tensile strain, depending on the lattice misfit<sup>8</sup>. For very small

---

<sup>8</sup> E.g.: If the lattice parameters of the adsorbate crystal structure are larger than the lattice parameters of the substrate, the adsorbate film will be compressed.

lattice misfits the resulting strain in the pseudomorph layer is **at first** small, too. As a result the pseudomorphic layer-by-layer growth is then mainly determined by the surface free energies and Young's relation (3.3.1-2) is valid. With increasing film thickness, the induced compressive or tensile strain in the growing film increases, too. This strain then becomes a relevant term of the interface energy which increases up to the critical film thickness  $d_c$ . At the critical film thickness the strain in the film is reduced by either introducing crystallographic defects like point dislocations or by changing the growth towards a three-dimensional island growth. This means that after the  $n^{\text{th}}$  adsorbate layer the new adsorbed atoms more likely bind on top of newly formed two dimensional islands instead of attaching at its island side. Therefore a three dimensional growth of these islands is facilitated instead of their two dimensional spreading over the  $n^{\text{th}}$  adsorbate layer. Evidently the occurring strain in the adsorbate film significantly influences the growth behavior. To give further insight into the strain of a growing film and the thickness dependent formation of dislocations a brief overview on the misfit dislocation theory will be presented in the following and in Appendix B (cf. page 194ff).

Figure 3.3.1-2 shows different stages in the SK growth and the corresponding expressions of Young's equation.

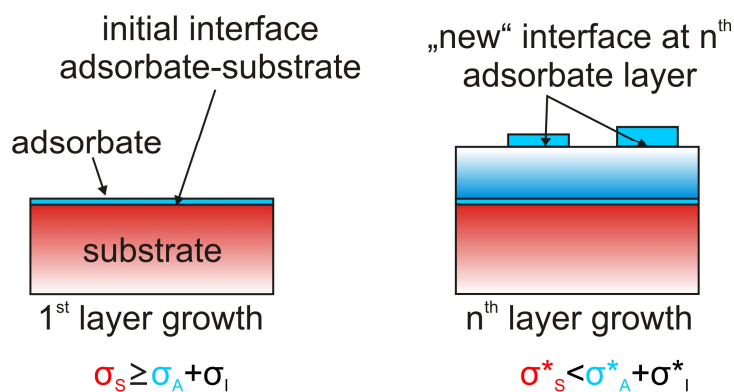


**Figure 3.3.1-2:** Schematic illustration of the Stranski-Krastanov growth mechanism with the corresponding interfacial energy relationship. Initially the sum of the surface free energies of the growing material ( $\sigma_A$ ) and the interface energy ( $\sigma_I$ ) are smaller than the surface free energy of the substrate ( $\sigma_S$ ) and a two dimensional growth occurs. After a thickness of  $n$  layers, the growth behavior changes from two dimensional layer-by-layer growth to the three dimensional growth of islands. With increasing thickness of the adsorbate film, the occurring strain increases, too. As a result the interface energy as well as the occurring strain energy increase, which significantly changes the energy relation given in Young's equation. After the  $n^{\text{th}}$  layer the sum of  $\sigma_A^*$  and  $\sigma_I^*$  are smaller than  $\sigma_S^*$ , with  $\sigma_A^*$  being the surface free energy of the adsorbed species on the  $n^{\text{th}}$  layer,  $\sigma_S^*$  the surface free energy of the substrate and the already grown  $n$  layers, and  $\sigma_I^*$  being the interface energy between the  $n^{\text{th}}$  layer and the now growing islands.

With Young's equation it is now possible to describe the different stages of the SK growth. In the beginning a pseudomorph two dimensional growth occurs on the surface because the sum of the surface free energy of the adsorbate ( $\sigma_A$ ) and the interface energy ( $\sigma_I$ ) is lower than the surface free energy of the substrate ( $\sigma_S$ ). With increasing thickness of the grown film, the values of  $\sigma_A$ ,  $\sigma_S$ , and  $\sigma_I$  are permanently changing. Therefore new energetic values for the substrate-gas interface, the adsorbate-gas interface and the substrate-adsorbate interface have to be considered, which makes the explanation of the SK growth solely based on surface free energies values of the corresponding bulk materials of A and S nonsensical.

After a thickness of  $n$  adsorbate layers the transition from two dimensional growth to three dimensional growth occurs. This island formation can in principle be described by an adapted Young's equation, where the sum of the surface free energy of the adsorbed species on the  $n^{\text{th}}$  layer ( $\sigma_A^*$ ) and the interface energy between the  $n^{\text{th}}$  layer and the growing islands ( $\sigma_I^*$ ) are considered to be smaller than the surface free energy of the substrate and the already grown  $n$  layers ( $\sigma_S^*$ ). These values are very elusive thus depicting the complexity of the SK growth.

### 3.3.2 Interface energy and strain energy

As described in the previous chapter an occurring strain can have a big influence on the growth mechanism due to its contribution to the interface energy. Generally, the interface energy represents the various interactions at the interface between two materials. If the growth shall be described qualitatively on the basis of Young's equation (3.2-1), it is mandatory to further describe the interface energy and its respective contributions. Therefore the different terms (or contributions) of the interface energy will be described in the following:

In the mid 60s crystal interfaces were investigated.<sup>[138-142]</sup> In a first approach van der Merwe described the interface energy for different interfaces depending on the properties of the two crystals at the interface. It could be shown that the interface energy increases monotonically with increasing misfit between the crystal lattices.<sup>[140]</sup> Also the binding strength between both crystals and their relative hardness or rigidity have direct influence on the interface energy, which is displayed in the increase of the interface energy with increasing misfit: soft films with weak bonding towards the substrate show a larger increase in interface energy than hard/rigid films that are strongly bound to the substrate.<sup>[140]</sup> Finally, the influence of film thickness on the interface energy has been investigated. With a defined misfit between both crystal lattices, the interface energy increases with increasing adsorbate film thickness.<sup>[140]</sup> From these conclusions it is evident that the interface energy depends on the following properties: misfit or strain, relative hardness, bond strength to the substrate and the thickness of the films. Therefore it cannot be concluded that any single one of these quantities solely explains the contribution of the interface energy to the growth behavior. For instance: A thin and soft film (low rigidity/hardness) that strongly binds to the substrate can have a low interface energy, even if strain occurs due to the misfit between both crystal lattices.

A few years later W.A. Jesser and D. Kuhlmann described the interface energy in a general equation.<sup>[138]</sup> As a model two finite semi-crystals are brought into contact, thus forming a two-dimensional interface (with directions x and y). The interface energy can now be described by the surface free energies of these two crystals and the binding energy between them:

$$E_I = E_1 + E_2 - E_B \quad (3.3.2-1)$$

$E_1$  : surface free energy of crystal 1

$E_2$  : surface free energy of crystal 2

$E_B$  : binding energy between both crystals

In this definition of the interface energy it is assumed (at first) that the lattice parameters do not change during the binding of the crystals, thus leading to the formation of dislocations at the interface due to the different lattice parameters. The binding energy can be specified by the following equation:

$$E_B = E_b - ({}_x E_d + {}_y E_d) \quad (3.3.2-2)$$

$E_b$  : binding energy, if no misfit would exist

${}_x E_d$  : energy of interfacial dislocation in x direction

${}_y E_d$  : energy of interfacial dislocation in y direction

If the equation (3.3.2-1) is included into equation (3.3.2-2) the interface energy changes to:

$$E_I = E_1 + E_2 - E_b + {}_x E_d + {}_y E_d \quad (3.3.2-3)$$

This general description of the interface energy summarizes the previously summarized parameters that contribute to the interface energy. The energy term  $E_b$  displays binding strength between both crystals. The energy terms  ${}_x E_d$  and  ${}_y E_d$  describe the formation of dislocations at the interface. To describe the pseudomorph growth of the adsorbate (crystal 1) on the substrate (crystal 2), Jesser et al. introduce the strain energy that is related to the deformation of the crystal lattices. The total strain energy at the interface is defined by the sum of the strain energy of both crystal lattices:

$$E_S = E_{S,1} + E_{S,2} \quad (3.3.2-4)$$

$E_{S,1}$  : strain energy of crystal 1

$E_{S,2}$  : strain energy of crystal 2

The strain energy of each crystal depends on its deformation parameters and deformation properties, i.e. the interfacial shear modulus and the elastic strains in plane (x and y direction). If it is assumed that the semicrystal of the substrate is significantly thicker than the adsorbate crystal, the elastic strain of the substrate can be neglected and it is assumed that only the adsorbate lattice will be deformed. Therefore the total strain energy is only determined by the strain energy of the adsorbate crystal ( $E_{S,1}$ ).

The total energy is defined as the sum of the interface energy and the strain energy:

$$E = E_I + E_S = E_1 + E_2 - E_b + xE_d + yE_d + E_{S,1} \quad (3.3.2-5)$$

For this definition of the total energy, the interplay between the dislocation energy and the strain energy has to be further clarified. Starting from two unstrained semicrystals, the increasing strain is related to the deformation of the adsorbate crystal to adapt the crystal lattice of the substrate. As a result the amount of formed dislocations at the interface is reduced. This evidently shows that the strain energy and the interface energy do not have to promote the growth behavior of the adsorbate in a similar way. While a low interface energy might induce a two-dimensional growth of the adsorbate layers, a strong strain energy can prevent the two-dimensional spreading and instead leading to a three-dimensional growth of islands.

To further explain the strain energy in the film growth (especially the SK growth) the equilibrium theory of Matthews and Blakeslee will be presented in the following.<sup>[119,133]</sup> A detailed derivation of the following equations is presented in Appendix B. It has to be emphasized that in this theory the epitaxial growth is described for pseudomorph growing layers. This means that at the beginning no dislocations are formed at the interface and the growing film is under stress and therefore strained. With increasing thickness of the growing film the strain energy will accumulate, too, until dislocations are formed that reduce the strain in the film.

In brief summary: the total strain energy ( $E_{total}$ ) is induced by the lattice misfit between the growing material (adsorbate) and the substrate:

$$E_{total} \sim \varepsilon \sim \underline{f} \quad (3.3.2-6)$$

$\varepsilon$  : strain in the film

$\underline{f}$  : lattice misfit

The lattice misfit can be expressed by the lattice parameters of the on growing film ( $a_0(A)$ ) and the underlying substrate ( $a_0(S)$ ):

$$\underline{f} = \frac{a_0(S) - a_0(A)}{a_0(A)} \quad (3.3.2-7)$$

This simplification of the total strain energy is valid, if the deformation parameters of the adsorbate film and the substrate are assumed to be equal, meaning both materials have the

same deformation properties. By this assumption, the total strain energy only depends on the strain in the film or the lattice misfit.

If a critical thickness ( $d_{c,dist}$ ) is reached, dislocations are formed to release the strain in the film. The relation of the critical thickness of the growing film and the lattice misfit can be described:

$$d_{c,dist} \sim \frac{1}{\underline{f}} \quad (3.3.2-8)$$

This inverse proportionality shows that with high strain or lattice misfit values, the critical thickness of the growing film is small. By introducing the strain energy it can be explained why pseudomorph growing films form dislocations at a certain thickness, or why three-dimensional islands on top of a wetting film are formed. In both cases defects are formed that might either be displayed in the form of point dislocations (e.g. edge or screw dislocation) or by introducing steps. At these steps, the attachment of new atoms is inhibited due to the axial strain in the film. Instead the atoms attach on top of this step, thus leading to a three-dimensional growth: the island formation.

By equation (3.3.2-3), the general components of the interface energy are presented. Further distribution of each of these individual energies is possible and sometimes necessary to explain rather complex growth mechanisms in more detail. In surface science the terms and definitions of adsorption energy, sticking coefficient and coverage become important for the adsorption of atoms and molecules on a substrate surface, which in turn may have a big influence on the growth behavior. For example: it has been shown, that the adsorption energy of CO on RuO<sub>2</sub>(110) depends on the coverage of already bound CO.<sup>[143,144]</sup>

Similarly the adsorption energy of a single metal atom on the bare substrate surface is different to the adsorption energy on several layers of the already grown material. A recent example would be the growth of RuO<sub>2</sub> on the TiO<sub>2</sub>(110) surface: At first the deposited RuO<sub>2</sub> grows as small, three to four layered, square shaped islands on the TiO<sub>2</sub>(110) surface. After a whole covering film of merged RuO<sub>2</sub> islands is formed, the continuing growth changes to a two-dimensional step-flow mechanism.<sup>[145]</sup>

Generally, if the growth has already progressed and larger or thicker structures have been formed, the lattice energy of these structures might also become important for the further growth behavior. Accompanied by this are also changes of the surface free energy contribution to the overall growth on the surface. For flat growing islands on a surface with a

certain crystallographic orientation, the surface free energy of this orientation has to be considered in the growth behavior. But with increasing thickness of this island, the side surfaces of these islands increase as well. These new formed surfaces also have a crystallographic orientation and the surface free energy of these island sides also start to contribute in the total surface free energy of the growing material.

These considerations evidently show that the explanation of an observed growth behavior can become very complicated. As Bauer already declared: The interplay between the surface free energies, the interface energy and the strain energy can be used as a first guideline to explain epitaxial growth.<sup>[134]</sup>

The last issue within this section is to determine for which lattice misfit values the adsorbate film grows pseudomorph on the substrate. Van der Merwe derived an equation with which it is possible to calculate critical lattice misfit values, depending on the film thickness.<sup>[140]</sup> If the lattice misfit between two crystals is lower than this critical lattice misfit value at a certain thickness, the newly formed layer will grow pseudomorph. The critical misfit strongly depends on the relative hardness and the strength of bonding between the growing layer and the underlying crystal lattice. As a general guideline the results can be summarized as the following:

- With increasing film thickness, the critical misfit values for pseudomorph growth decrease.<sup>[140]</sup> This observed trend is similar to the theory of misfit dislocation formation from the Matthews-Blakeslee equilibrium theory.<sup>[133]</sup>
- A soft adsorbate film material with strong bonding towards the substrate is generally favorable for large critical misfit values ( $\underline{f} \approx 13\%$ )<sup>[140]</sup>. Vice versa, a rigid adsorbate material with weak bonding towards the substrate surface leads to very small critical misfit values ( $\underline{f} \approx 0.1\%$ )<sup>[140]</sup>. Besides these rather extreme cases, van der Merwe also calculated the critical misfit value for a moderately hard monolayer film that binds strongly to the substrate. The resulting value of approximately 9 % is widely used in literature as a guideline to estimate if pseudomorph growth is possible.<sup>[118,119]</sup>

In summary, the growth at (thermodynamic) equilibrium can be explained by the interface energy and the surface free energies of the involved species (Young's equation) in a first approach. Including the strain energy of the growing stressed film into the considerations, manifold observed growths in literature can be described by the interplay of these energies. Based on this knowledge, the growth behavior and the resulting morphologies can be manipulated by changing one of these energies.

### 3.3.3 Growth far away from thermodynamic equilibrium

At thermodynamic equilibrium the growth of the deposited material on the substrate can be described by the interface energy, the surface free energies and the strain energy. In the experiment, temperature and deposition rate have to be chosen wisely.<sup>[118-135]</sup> Both are essential for growth factors like the adsorption and surface diffusion of adsorbed atoms as well as the stability of critical nuclei that might act as starting points for the formation of islands or a wetting film. By regulating temperature and deposition rate different growth modes can be adjusted. For instance: Consider a system, where the deposited atoms are forming wetting layers in a FvdM-like growth for a certain temperature and deposition rate. If the temperature is kept constant, but the deposition rate is significantly increased a rough film of merged islands will be formed instead of a smooth and flat film. This is generally explainable by the mean free pathway of the adsorbed atoms and the stability of critical nuclei on the surface. Venable et al. have shown, that the formation of critical nuclei on the surface does not only depend on the applied temperature, also other parameters like the deposition rate strongly influence the stability of a formed cluster.<sup>[146]</sup> So if the deposition rate is higher than the mean free pathway of the adsorbed atoms on the surface decrease, which facilitates the formation of critical nuclei. Therefore the formation of many islands on the surface is observed. This evidently shows the influence of kinetic parameters on the growth behavior. Working far away from thermodynamic equilibrium has major impact on the formed morphologies, as will be examined in the following.

General description of the growth modes far away from thermodynamic equilibrium can become very complex, especially for the heteroepitaxial growth. Therefore the ideal FvdM homoepitaxial growth mode was chosen as a model system to describe the growth at lower temperatures because the interface energy and relating effects like strain, which would further complicate the growth mechanism, can be neglected. Therefore the changes in the growth at lower temperatures can be explained by the increasing influence of the kinetic processes on the surface. *Figure 3.3.3-1* schematically summarizes the relevant kinetic processes on the surface during growth.

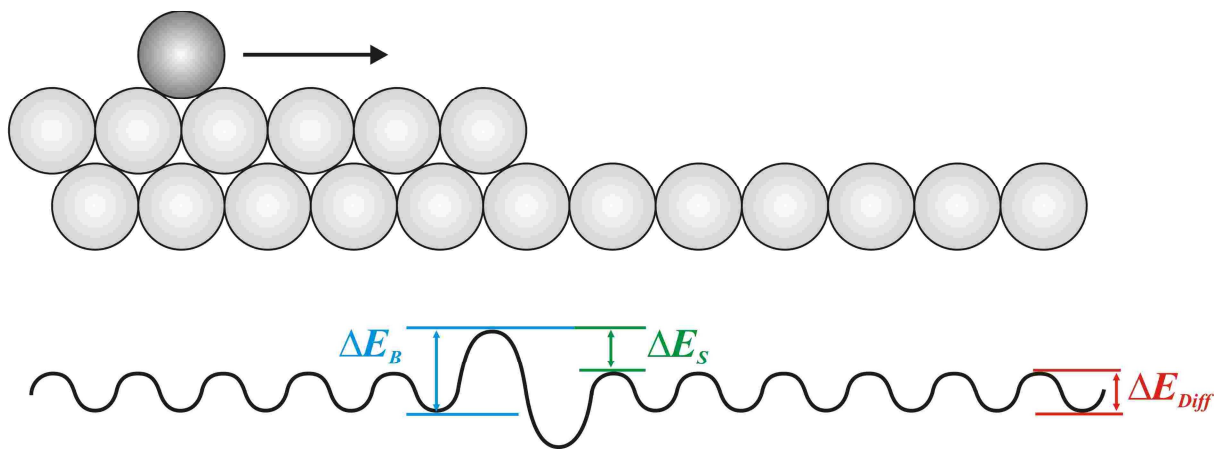
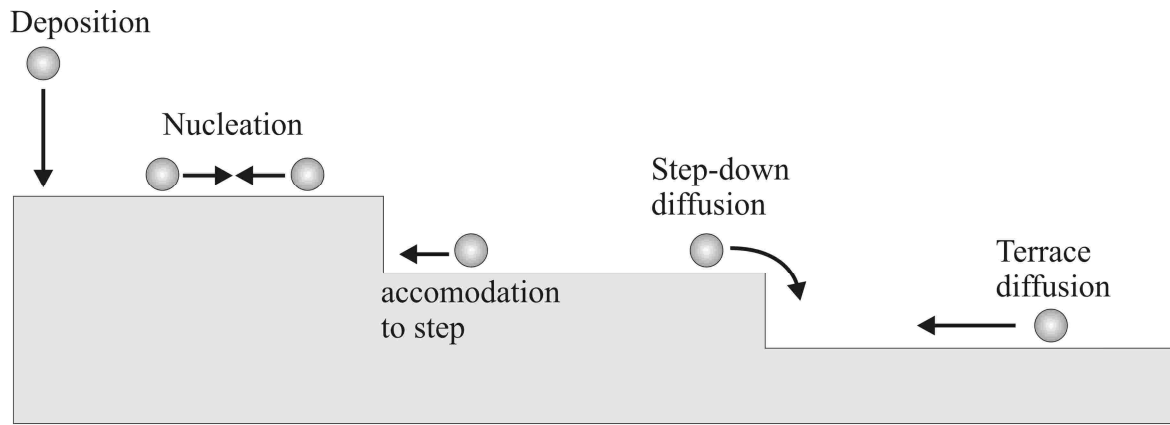


**Figure 3.3.3-1:** Top: surface processes involved in film growth. Bottom: Potential energy hyper surface of surface diffusion across a step with the corresponding diffusion barriers. The involved diffusion barriers for this step-down diffusion process are: The Ehrlich-Schwoebel barrier ( $\Delta E_S$ ), the terrace diffusion barrier ( $\Delta E_{Diff}$ ) and the barrier for the diffusion across the step ( $\Delta E_B$ ), respectively. Figure modified from [122].

The surface diffusion of adsorbate atoms is controlled by kinetics. By describing the diffusion process, the kinetic influence on the growth mechanism at lower temperatures can be explained. The temperature dependent diffusion can be described by an Arrhenius-like expression of the diffusion coefficient ( $D$ ), which includes the activation energy ( $\Delta E_i$ ) of the respective diffusion barriers on the surface:

$$D = D_0 \exp\left(-\frac{\Delta E_i}{k_B T}\right) \quad (3.3.3-1)$$

with

$$D_0 = \frac{1}{2 \cdot b} \cdot v_0 \cdot d^2$$

$b$  : dimensionality of motion :  $b = 1$  for 1D,  $b = 2$  for 2D

$v_0$  : vibrational frequency of jumps

$d^2$  : mean – square jump length

Besides the diffusion over the single crystal terraces ( $\Delta E_{Diff}$ , cf. figure 3.3.3-1) the diffusion along and across the steps are important for the growth at lower temperatures. The bottom part of figure 3.3.3-1 schematically shows the potential energy hyper surface for diffusion across the step. As can be seen the diffusion over steps ( $\Delta E_B$ ) has a higher energy barrier than the diffusion across the terrace ( $\Delta E_{Diff}$ ). This additional barrier is called the Ehrlich-Schwoebel barrier ( $\Delta E_S$ ).<sup>[147-152]</sup> Besides the activated diffusion across a step from a higher terrace onto a lower terrace also the stronger binding of adsorbate atoms along the steps becomes apparent. This stronger binding can be explained by a higher coordination of the atoms. While on terraces the adsorbate atoms can only be coordinated from below - this is significantly different at the steps. Additional coordination from the side occurs, which further stabilizes the binding towards the surface. Furthermore the diffusion from a lower terrace onto a higher terrace is very unlikely due to the very high energy barrier and worse coordination towards the surface afterwards. By introducing these diffusion barriers at the steps of a surface the temperature dependent growth can be explained. At higher temperatures (near thermodynamic equilibrium) the diffusion across steps is not inhibited because the Ehrlich-Schwoebel barrier can be overcome. By decreasing the temperature the Ehrlich-Schwoebel barrier becomes too high, resulting in diffusion exclusively on the terrace itself. This would lead to a three-dimensional growth at lower temperatures although the deposited material can grow homoepitaxially. Figure 3.3.3-2 shows the changes in the homoepitaxial FvdM-growth if the temperature is decreased during the deposition process:

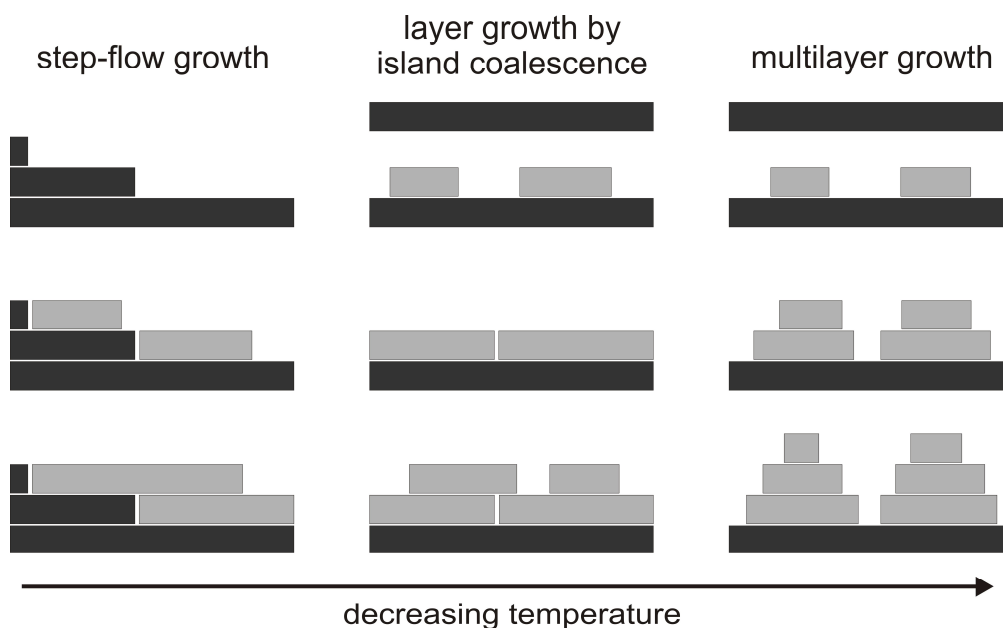


**Figure 3.3.3-2:** Schematic illustration of the non-equilibrium growth modes for homoepitaxy. Ordered by decreasing temperature: *step-flow growth*; *layer growth by island coalescence*; *multilayer growth*. Figure modified from [122].

The non-equilibrium growth at lower temperatures can be divided into the following three mechanisms: the *step-flow growth*, the *layer growth by island coalescence* and the *multilayer growth*.

At higher temperatures, near thermodynamic equilibrium, the deposited atoms are so mobile at the surface that they diffuse to and stay at the steps where a higher coordination is possible. Nucleation on the terrace between several adsorbate atoms is inhibited due to the high temperature. As concluded from nucleation theory at higher temperatures the critical radius for a nucleus on a terrace is also larger. With a bigger critical nucleus and the high mobility of the adsorbate atoms a nucleation and growth mode is inhibited and the two-dimensional growth starts exclusively at the steps from which they spread over the surface.

With decreasing temperature the mobility of the deposited atoms and the critical radius of the nuclei on the terraces also decrease. If the temperature is high enough to still permit diffusion across steps but low enough to produce critical nuclei on a terrace, a two-dimensional layer growth by island coalescence occurs on the surface. The amount of the formed critical nuclei strongly depends on the deposition rate. At higher deposition rates more nucleation processes occur which leads to a higher number of two-dimensional islands on the surface.

If the temperature is so low that the diffusion over steps is inhibited, the two-dimensional *layer growth by island coalescence* changes to the three-dimensional *multilayer growth*. Due to the Ehrlich-Schwoebel barrier the adsorbate atoms cannot diffuse between different terraces leading to a three-dimensional growth of islands because the newly adsorbed atoms

are stuck on their terraces. Depending on the deposition rate fewer but larger three-dimensional islands (at low deposition rates) or many smaller islands (at higher deposition rates) are formed. If the surface-to-volume ratio of very small islands becomes too high clusters instead of islands are usually formed during the deposition and growth.

## 4. Oxidation of Au(111) by atomic oxygen

The oxidation of gold single crystal surfaces has been investigated by a large variety of atomic oxygen sources, i.e. exposure of ozone, thermal dissociation of  $O_2$  using hot filaments,  $O^+$  sputtering, radiofrequency-generated plasma source, coadsorption of  $NO_2$  and  $H_2O$  and electron bombardment of  $NO_2$ .<sup>[16,32,36,58,59,64,66,70,71-77]</sup> Depending on the source of atomic oxygen the oxidation behavior of the gold surface can change significantly, thus leading to different oxidized gold species and different morphologies.<sup>[16,55]</sup>

In this work the atomic oxygen was produced by a thermal gas cracker (TC 50, Oxford Applied Research), i.e. the molecular oxygen is channeled through a heated iridium tube in order to get cracked. To validate the oxidative potential of this thermally cracked oxygen, oxidation and reduction experiments of the Au(111) single crystal surface were conducted at room temperature, investigated by STM and XPS and compared to the literature. *Figure 4-1* shows a series of STM pictures of the oxidized Au(111) surface after exposure of 40 L thermally cracked oxygen at room temperature.

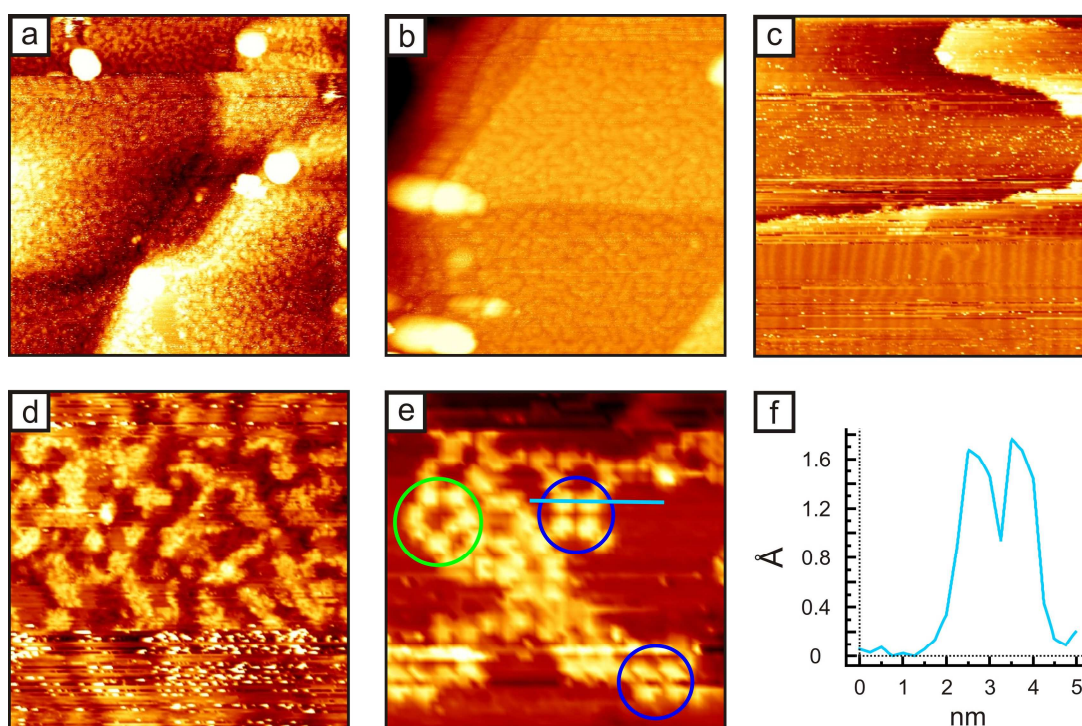


**Figure 4-1:** STM pictures of an oxidized Au(111) surface after exposure of 40 L atomic oxygen. The bigger clusters in picture a) and b) are related to agglomerations of carbon impurities on the surface. a) 200 nm x 200 nm, b) 150 nm x 150 nm, c) 100 nm x 100 nm, d) 40 nm x 40 nm, e) 13 nm x 13 nm. The morphology of the rough oxidized gold structures on the Au(111) surface are shown (a,b,d) as well as an illustration on the nanoscale (e). Besides the formed oxide also areas are visible with a lifted Au(111) reconstruction, which is identified on the basis of the linear arrangement of the herringbones (f). Tunneling conditions:  $U = 0.7 - 1.0$  V,  $I = 0.1 - 1.0$  nA.

The huge clusters depicted in the STM pictures *figure 4-1a* and *4-1b* are related to agglomerations of carbon impurities on the Au(111) surface that could not be removed by the standard single crystal surface cleaning process (see chapter 2.1, page 12).<sup>9</sup> XPS measurements confirmed that carbon impurities on the Au(111) surface existed (C 1s peak area not presented here).

During oxidation by 40 L atomic oxygen, the herringbone structure of Au(111) is lifted and roughening of the gold surface starts (*cf. figure 4-1a-c*). A two-dimensional structure of connected oxidized gold islands is depicted in *figure 4-1a* and *4-1b*. Magnification of these roughened overlayer structures reveal that these connected islands consist of agglomerated small particles (*cf. figure 4-1d* and *4-1e*). These agglomerations seem to be randomly (green circle *figure 4-1e*), but also particles that are quadratically arranged can be identified (blue circle *figure 4-1e*). The nearest distance between two of these particles is always approximately 1 nm. To investigate the roughness of the oxidized surface, line scan analysis was done (*cf. figure 4-1f*). With a height difference ranging from approximately 1 Å to 2 Å the roughening is mainly restricted to the first two layers of the Au(111) surface. The morphology and the height of this oxidized gold surface fits well to STM measurements from Friend et al. and calculations of Au-Au distances in gold oxides by Stampfl et al., respectively.<sup>[36,66,82]</sup> Besides the roughening of the surface, in some areas straightened soliton lines of the herringbone structures are visible (*cf. figure 4-1c*).<sup>10</sup> These straightened lines indicate a lifted herringbone structure, which is related to the formation of chemisorbed oxygen phase on Au(111) that is known to coexist with the surface oxide in a wide range of oxidation conditions.<sup>[57,66,153]</sup> Only at higher temperatures and significant higher exposures of atomic oxygen nearly the whole Au(111) surface should be oxidized so that a completely wetting surface oxide is formed.<sup>[57]</sup>

XPS was used to further investigate the oxidation state of the surface. *Figure 4-2* shows the XPS spectra of the Au 4f and O 1s peak regions. During oxidation the metallic Au 4f signals (84.0 eV and 87.7 eV) decrease while two new Au 4f signals appear, each shifted by 1.8 eV to higher binding energies. These oxidized gold species (“Au oxide” 4f<sub>7/2</sub> 85.8 eV, “Au oxide” 4f<sub>5/2</sub> 89.5 eV) are assigned to Au<sup>3+</sup> and the formation of Au<sub>2</sub>O<sub>3</sub>.<sup>[58,59,74]</sup> Therefore this gold oxide probably consists of agglomerated Au<sub>2</sub>O<sub>3</sub> particles. *Chemisorbed O on Au(111) in the Au 4f peak region could not be identified by XPS due to resolution limitation. However, for the O 1s signal a differentiation between the chemisorbed O on Au and Au<sub>2</sub>O<sub>3</sub> is more reliable due to a more evident chemical shifting between both species.* From the O 1s spectra (*cf.*

---

<sup>9</sup> To remove these impurities mechanical polishing of the single crystal was necessary.

<sup>10</sup> Also known as „striped soliton wall“ structure.

figure 4-2, right) an oxygen peak for a clean Au(111) surface is observable with its maximum at 531.7 eV. This species is assigned to subsurface oxygen, which is a result of the cleaning process of the single crystal surface.<sup>[75,76]</sup> After oxidation the maximum of the O 1s signal shifts to a binding energy of 530.2 eV that is also assigned to the formation of Au<sup>3+</sup> species, i.e. Au<sub>2</sub>O<sub>3</sub>.

By dosing 100 L CO at room temperature a partial reduction of the surface occurred as can be seen from the XPS spectra for the Au 4f and O 1s signal regions. For the Au 4f region the signals for the metallic Au species (84.0 eV and 87.7 eV) increase while simultaneously the gold(III)oxide (85.8 eV, 89.5 eV) signals nearly vanish. In the O 1s peak region the oxygen signal shifts back to a higher binding energy (to 531.2 eV), which confirms the reduction of the surface. However the oxygen signal does not restore its initial shape, thus indicating that still some oxide species is left on the surface and the amount of CO was insufficient for a complete reduction.

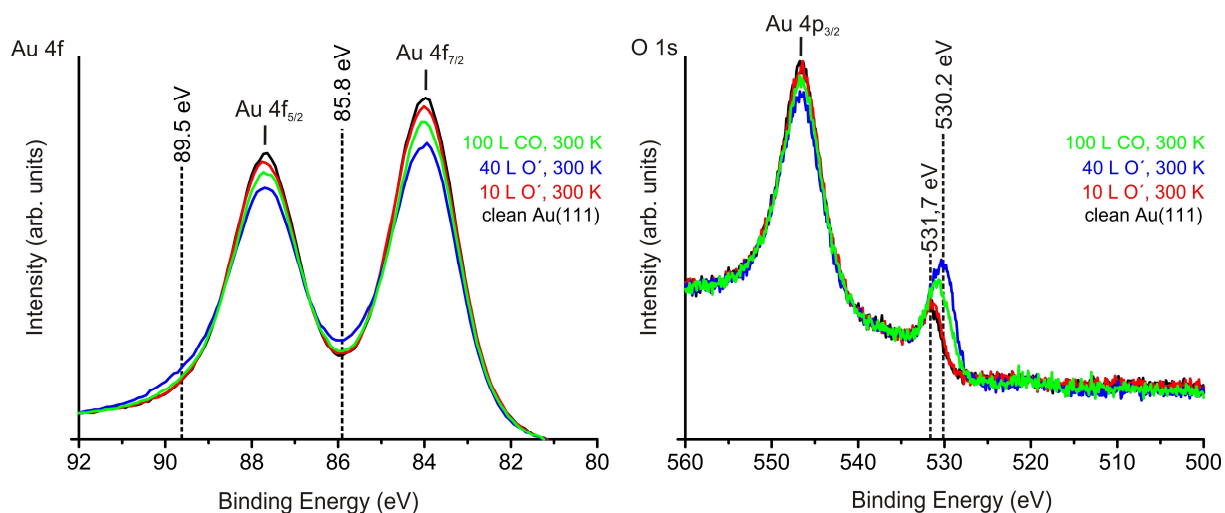


**Figure 4-2:** XPS spectra of the Au 4f and O 1s peak signal regions for Au(111) oxidation and reduction experiments done at room temperature.

With these STM and XPS measurements of the oxidation of Au(111) by using thermally cracked oxygen (from the TC 50 thermal gas cracker) at room temperature the similarities to the oxidation experiments of single crystal surfaces in literature are demonstrated. Both, the morphologic changes observed by STM and the chemical shifts of the Au 4f and the O 1s signals are consistent with oxidation of Au(111) surfaces described in literature.<sup>[36,59,64,66,71,74]</sup>

Tables 4-1 and 4-2 provide a brief overview of the chemical shifts of the Au 4f and O 1s signals for oxidized Au(111) surfaces and Au nanoparticles (NP) and polycrystalline films, respectively.

**Table 4-1:** Binding energies of Au 4f and O 1s XPS signals for the oxidation auf Au(111) using different sources of atomic oxygen.

| System  | Binding energies in eV      | Assignment                     | Reference |
|---|-----------------------------|--------------------------------|-----------|
| <i>Oxygen plasma on Au(111)</i>                                 | Au 4f <sub>7/2</sub> : 84.0 | Bulk gold                      | 58,74     |
|   | Au 4f <sub>7/2</sub> : 85.8 | Au <sub>2</sub> O <sub>3</sub> | 58,74     |
| <i>Ozone on Au(111)</i>   | O 1s: 530.1                 | Au <sub>2</sub> O <sub>3</sub> | 71        |
|   | O 1s: 529.3                 | O-chem                         | 71        |
| <i>Ozone on Au(111)</i><br>400 K<br>200 K                       | O 1s: 529.4                 | Surface oxide                  | 66        |
|   | O 1s: 529.1                 | O-chem                         | 66        |
|   | O 1s: 530.1                 | Bulk Au oxide                  | 66        |
| <i>Thermally cracked O<sub>2</sub> on Au(111) in UHV</i>        | Au 4f <sub>7/2</sub> : 84.0 | Metallic Au                    | 59        |
|   | Au 4f <sub>7/2</sub> : 85.9 | Au <sub>2</sub> O <sub>3</sub> | 59        |
|   | O 1s: 530.2                 | Au <sub>2</sub> O <sub>3</sub> | 59        |
| <i>Reactive sputtering of 0.1 mbar O<sub>2</sub> on Au(111)</i> | Au 4f <sub>7/2</sub> : 84.0 | Metallic Au                    | 59        |
|   | Au 4f <sub>7/2</sub> : 86.1 | Au <sub>2</sub> O <sub>3</sub> | 59        |
|   | Au 4f <sub>7/2</sub> : 85.5 | Au <sub>2</sub> O              | 59        |
|   | O 1s: 530.0                 | Au <sub>2</sub> O <sub>3</sub> | 59        |
|   | O 1s: 532.5                 | Adsorbed OH                    | 59        |

**Table 4-2:** Binding energies of Au 4f and O 1s XPS signals for the oxidation auf gold NP and bulk like gold surfaces using various sources of atomic oxygen.

| System   | Binding energies in eV      | Assignment  | Reference |
|--|-----------------------------|---|-----------|
| <i>x-ray irradiation of O<sub>2</sub> on Au foil and NP</i>          | Au 4f <sub>7/2</sub> : 84.0 | Au foil   | 64        |
|  | Au 4f <sub>7/2</sub> : 85.3 | Gold oxide  | 64        |
|  | Au 4f <sub>7/2</sub> : 84.2 | Au NP   | 64        |
|  | Au 4f <sub>7/2</sub> : 85.5 | Gold oxide  | 64        |
| <i>Thermally cracked O<sub>2</sub> on Au film on SiO<sub>2</sub></i> | O 1s: 529-530               | Au <sub>2</sub> O <sub>3</sub>                                      | 75        |
|  | O 1s: 533                   | Subsurface oxygen   | 75        |
| <i>Thermally cracked O<sub>2</sub> on Au NP</i>                      | O 1s: 530                   | Au <sub>2</sub> O <sub>3</sub>                                      | 76        |
|  | O 1s: 532-533               | Subsurface oxygen   | 76        |
| <i>Au NP on TiO<sub>2</sub></i>                                      | Au 4f <sub>7/2</sub> : 83.9 | Metallic Au   | 70        |
|  | Au 4f <sub>7/2</sub> : 85.2 | Metallic Au <sup>1</sup>  | 70        |
| 1.0 mbar O <sub>2</sub> +<br>x-ray, 1h<br>transferred to<br>UHV      | Au 4f <sub>7/2</sub> : 84.4 | Metallic Au   | 70        |
|  | Au 4f <sub>7/2</sub> : 86.5 | O-chem + Au oxide   | 70        |
|  | Au 4f <sub>7/2</sub> : 84.2 | Metallic Au   | 70        |
|  | Au 4f <sub>7/2</sub> : 85.8 | Non stoichiometric Au oxide   | 70        |
| <i>Oxygen plasma on Au NP on TiO<sub>2</sub></i>                     | Au 4f <sub>7/2</sub> : 84.6 | Metallic Au   | 32        |
|  | Au 4f <sub>7/2</sub> : 86.9 | Au <sup>3+</sup> in Au <sub>2</sub> O <sub>3</sub>                  | 32        |
| <i>Oxygen Plasma on Au films</i>                                     | Au 4f <sub>7/2</sub> : 84.1 | Metallic Au   | 73        |
|  | Au 4f <sub>7/2</sub> : 85.5 | Au <sub>2</sub> O <sub>3</sub>                                      | 73        |
|  | O 1s: 530.4                 | Au <sub>2</sub> O <sub>3</sub>                                      | 73        |
|  | O 1s: 531.8                 | Adsorbed OH   | 73        |
| <i>Electrochemically oxydized Au</i>                                 | Au 4f <sub>7/2</sub> : 84.0 | Metallic Au   | 77        |
|  | Au 4f <sub>7/2</sub> : 85.7 | Au <sup>3+</sup>  | 77        |
|  | O 1s: 529.3-532.5           | Mixed oxide: Au <sub>2</sub> O <sub>3</sub> and Au(OH) <sub>3</sub> | 77        |

**Table 4-2:** *continued from previous page*

| System                                 | Binding energies in eV      | Assignment                                  | Reference |
|--|-----------------------------|---|-----------|
| <i>Au film growth in O<sub>2</sub></i> | Au 4f <sub>7/2</sub> : 84.1 | Metallic Au                                 | 72        |
|  | Au 4f <sub>7/2</sub> : 85.9 | Au <sub>2</sub> O <sub>3</sub>              | 72        |
|  | O 1s: 529.8                 | Au <sub>2</sub> O <sub>3</sub> <sup>2</sup> | 72        |
|  | O 1s: 530.7                 | Au <sub>2</sub> O <sub>3</sub> <sup>2</sup> | 72        |
|  | O 1s: 531.9                 | O reacted with impurities                   | 72        |
|  | O 1s: 532.7                 | Adsorbed OH or H <sub>2</sub> O             | 72        |

<sup>1</sup>assigned to very small Au clusters or Au atoms from the periphery of larger clusters

<sup>2</sup>addition of both deconvoluted peak areas leads to a total ratio of 2/3 for Au/O

## 5. Deposition of Au on Ru(0001)

Based on the research in the field of gold catalysis two interesting systems have been developed and investigated in the last ten years, which show exceptional high conversion of CO at low temperatures. These two systems are: gold bilayers deposited on reducible metal oxide surfaces and gold surfaces that have been oxidized using atomic oxygen.<sup>[20-22,40,66]</sup> For the latter of these systems it has to be emphasized that the oxidation increases the conversion of CO at room temperature as well as the O<sub>2</sub> splitting.<sup>[40,51,66]</sup> However in each case it has to be discriminated if the oxidized gold surfaces exhibit a catalytic activity or if only a transient activity in form of CO oxidation via gold oxide reduction is observed.

To further elucidate the unique properties of the gold bilayer system, flat gold islands and films were prepared and subsequently oxidized by atomic oxygen at room temperature. The main focus within this work was to identify the possible morphologic changes that occur during the oxidation process. Especially by taking into account that the morphology and the accessibility of undercoordinated gold atoms are assumed to be crucial for the catalytic activity.<sup>[20,21,26,28,29,33,34,36,44,50,52-54]</sup> The information that are obtained from the oxidized thin gold films might be useful to understand possible dynamic changes of a gold catalyst during the catalytic process. An explanation for the morphologic changes of the oxidized gold films is given, based on the theories of epitaxial film growth and heterogeneous nucleation described in chapter 3.

Gold deposited on Ru(0001) single crystal surfaces was chosen as the model system because the heteroepitaxial growth of gold on ruthenium is well described and understood.<sup>[154-167]</sup> For the sub-monolayer deposition of gold, the growth on oxygen free Ru(0001) surfaces as well as the growth on oxygen precovered Ru(0001) is well described.<sup>[154-158,162,163]</sup> Determined by the surface free energies of gold and ruthenium as well as the adsorption energies for gold on ruthenium, the growth behavior changes by preadsorption of oxygen on the ruthenium surface. Generally oxygen binds strongly to the Ru(0001) single crystal surface but only poorly to the very noble metallic gold. Hwang et al. stated that the adsorption energy for gold on bare Ru(0001) is larger than the adsorption energy for gold on gold.<sup>[157]</sup> Introduction of a covering oxygen layer on the ruthenium surface changes this situation dramatically: The adsorption energy of gold on the oxygen covered ruthenium surface is now smaller than the adsorption energy of gold on gold.<sup>[157]</sup>

In the case of oxygen free Ru(0001) surfaces the deposition of gold at temperatures above 650 K leads to a two-dimensional film, which is covering the ruthenium surface alongside the

formation of herringbone patterns after only 1 ML of gold.<sup>[157,159,166]</sup> After the second gold layer is formed, the gold islands start to grow on top of the gold layer, which evidently shows a Stranski-Krastanov-like growth mechanism for gold on oxygen free Ru(0001).<sup>[154,157,163]</sup>

The growth changes significantly if oxygen is preadsorbed at the ruthenium surface before the gold deposition process. When the Ru(0001) surface is exposed towards molecular oxygen a (2x2)-O<sup>[168-170]</sup> or a (2x1)-O<sup>[171-173]</sup> overlayer is formed depending on the oxygen coverage. At higher temperatures and higher oxygen exposures two additional oxygen overlayer phases can be stabilized, namely the (2x2)-3O<sup>[174-176]</sup> and the (1x1)-O<sup>[177]</sup>. An overview of the different oxygen overlayer structures is given in literature and briefly summarized in *figure 5-1*.<sup>[8]</sup>

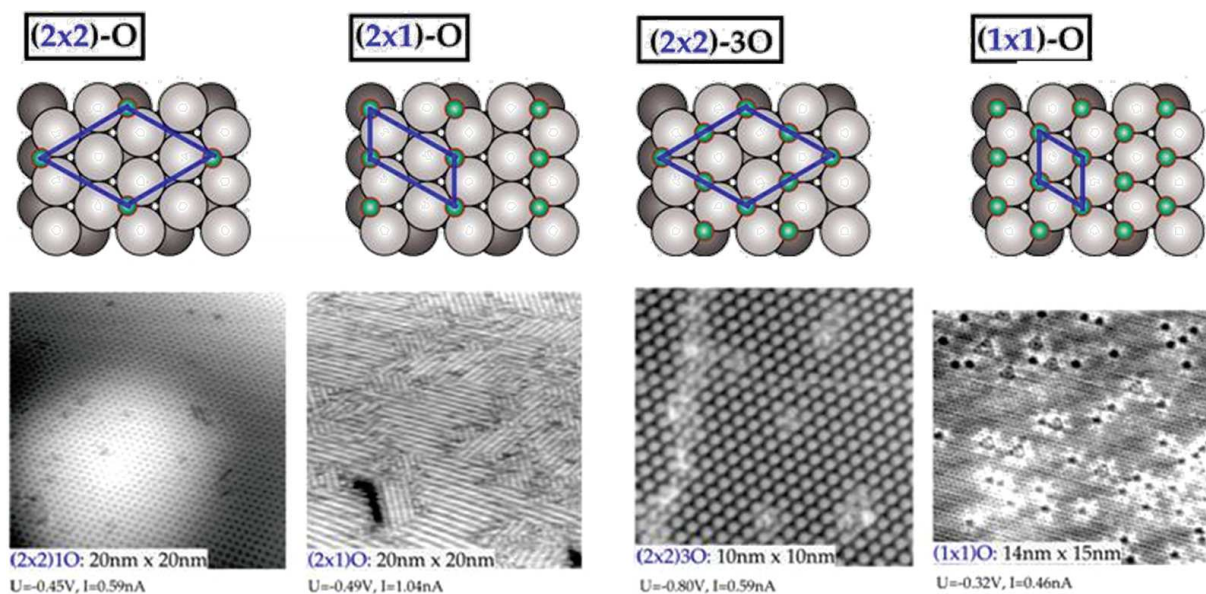


**Figure 5-1:** Chemisorbed oxygen (green balls) surface structures on Ru(0001) including the surface unit cell in blue and corresponding STM images. From left to right the (2x2)-O (at 0.25 ML O coverage), (2x1)-O (at 0.5 ML O coverage), (2x2)-3O (at 0.75 ML O coverage) and the (1x1)-O (at 1.0 ML O coverage) overlayer structures are presented. Figure taken from [8].

With the formation of oxygen overlayer structures the surface free energy of the ruthenium surface decreases below the surface free energy of gold ( $\sigma < 1.6 \text{ J/m}^2$ ).<sup>[163]</sup> As a consequence the deposited gold ( $\sigma = 1.6 \text{ J/m}^2$ ) tends to form Au-Au bonds rather than Au-O/Ru bonds and three-dimensional gold island growth is observed.<sup>[154,157,163]</sup> At the initial stage of the gold island growth on oxygen precovered Ru(0001), the adsorbing gold atoms bind towards oxygen-free ruthenium atoms by pushing the oxygen away. As a result the oxygen overlayer is compressed, which was first proposed by Hrbek et al. and later confirmed by STM from Behm et al.<sup>[156,163]</sup> After formation of the (1x1)-O the gold is not able to compress the oxygen overlayer furthermore.

With ongoing deposition the gold islands spread over the surface in a typical VW-like growth behavior until they merge together. The chemisorbed oxygen overlayer gets buried at the gold and ruthenium interface, which has been shown for the growth of gold on Ru(10-10). A combination of TDS, LEED and Auger spectroscopy experiments revealed that oxygen is again exposed if the covering gold films were removed by annealing.<sup>[160,161]</sup> In summary, the growth of gold on oxygen precovered Ru(0001) is a typical example for a Volmer-Weber growth.

## 5.1 Gold deposited on ruthenium surfaces – General Considerations

To appropriately describe the heteroepitaxial growth of gold on bare and oxygen precovered Ru(0001), the lattice misfit between both materials and the resulting strain have to be included in the interpretation of the different growth behaviors.

Given from equation (3.3.2-7) the lattice misfit  $\underline{f}$  is calculated by the lattice parameters of the hexagonal Ru(0001) and the corresponding gold surface structures with similar symmetry, i.e. fcc Au(111). Taken from literature the lattice parameter of Ru(0001) (2.706 Å) is larger than the lattice parameters of the Au(111) (2.884 Å) surface.<sup>[8,178-181]</sup> Therefore the lattice misfit between Au(111) and Ru(0001) is calculated:

$$\underline{f} = \frac{a_0(\text{Ru}) - a_0(\text{Au})}{a_0(\text{Au})} = \frac{2.706 - 2.884}{2.884} \approx -0.062$$

Due to the lattice misfit of about – 6.2 % the gold film is exposed to an in-plane compressive strain when growing on the Ru(0001) surface. To describe the growth of gold films on the ruthenium surface the theoretical model for heterogeneous nucleation and epitaxial film growth from chapter 3 is transferred to the Au on Ru system. Starting from the theory of heterogeneous nucleation, *figure 3.2-1* (from chapter 3.2) changes to:

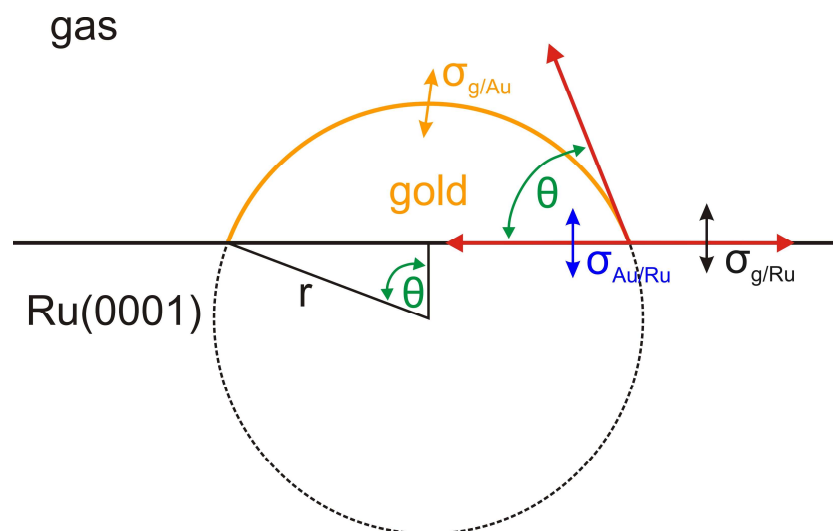


**Figure 5.1-1:** Adapted model for heterogeneous nucleation of gold on the ruthenium surface. Definition of the contact angle  $\theta$  at the gold ruthenium interface, the related surface free energies and the interface energy to derive Young's equation.

$\sigma_{g/Ru}$  = interfacial tension gas – Ru surface  $\cong$  surface energy Ru

$\sigma_{g/Au}$  = interfacial tension gas – Au surface  $\cong$  surface energy Au

$\sigma_{Au/Ru}$  = interfacial tension Au – Ru

If the surface tension of gold and ruthenium are expressed by their surface free energy, respectively, the angle dependent Young's equation can be written as:

$$\cos(\theta) = \frac{\sigma_{Ru} - \sigma_{Au/Ru}}{\sigma_{Au}} \quad (5.1-1)$$

As described in chapter 3.2: if the wetting angle  $\theta$  increases the growing film shows a smaller degree of wetting, i.e.  $\theta = 0^\circ$  leads to full wetting and  $\theta = 180^\circ$  in complete dewetting. As a consequence, if the quotient in equation (5.1-1) (involving the surface free energies and the interface energy) increases a higher degree of wetting is assumed to occur.

In case of gold deposition on oxygen free Ru(0001) a two-dimensional growth for the first layers of gold is expected. To fulfill the adapted Young's equation (5.1-1), the wetting angle has to be very small. As a result the sum of the surface free energy of ruthenium and the interface energy has to be larger than the surface free energy of gold. It is assumed that the surface free energies dominate the growth behavior near thermodynamic equilibrium, due to the large difference between the surface free energies of ruthenium (Ru(0001): 3.1 J/m<sup>2</sup>) and gold (Au(111): 1.5 J/m<sup>2</sup>).<sup>[163,182-184]</sup> The interface energy between ruthenium and gold is assumed to be smaller than 1.5 J/m<sup>2</sup>, otherwise Young's equation would not fulfill the condition for two-dimensional growth. Based on the description of the interface energy from van der Merve<sup>[139,140]</sup> and Jesser et al.<sup>[138]</sup> the following properties have to be considered: bond strength between ruthenium and gold, rigidity/hardness of the gold adlayer, lattice misfit and strain. The binding strength between gold and ruthenium is assumed to be rather strong. This statement is confirmed by TDS data from Hribek et al. who measured desorption temperatures for gold multilayers on Ru(0001) to be higher than 1200 K<sup>[165]</sup>, which is to similar desorption temperatures for chemisorbed oxygen phases on Ru(0001)<sup>11</sup>.<sup>[185]</sup> Moreover the desorption temperature of one monolayer of gold on ruthenium (1300 K) is higher than the gold multilayer desorption temperature (1200 K), thus evidently showing that gold strongly binds to ruthenium.<sup>[165,186]</sup> Also gold has a low melting point and is a rather ductile metal, which makes a compression of the gold lattice for a better adoption of the ruthenium lattice

---

<sup>11</sup> The desorption temperature of the different chemisorbed oxygen phases from Ru(0001) is  $\geq 1100$  K.

parameters likely. With the relatively small lattice misfit of 6.2 % also the in plane stress is assumed to be moderately. Altogether it can be assumed that the interface energy is small, thus facilitating wetting of gold on Ru(0001).

The energy relation from Young's equation changes significantly if oxygen is preadsorbed on the Ru(0001) surface. The growth changes from a two-dimensional wetting of gold on bare Ru(0001) to the formation of single gold islands that grow three-dimensional upon gold deposition. Similarly to the gold island growth the oxygen overlayer gets compressed, so the deposited gold islands can bind directly to the ruthenium surface without oxygen atoms at the interface. Generally, with increasing coverage of oxygen on Ru(0001) the surface energy of ruthenium decreases.<sup>[163,187]</sup>

By simply comparing the degree of wetting for gold deposited on bare and oxygen precovered Ru(0001) the following relation can be derived, based on the theory of heterogeneous nucleation and epitaxial growth (*cf. figure 3.2-2, page 33*):

$$\cos(\theta, Au / Ru) > \cos(\theta, Au / O / Ru)$$

$$\frac{\sigma_{Ru} - \sigma_{Au/Ru}}{\sigma_{Au}} > \frac{\sigma_{O/Ru} - \sigma_{Au/O/Ru}}{\sigma_{Au}}$$

$$\sigma_{Ru} - \sigma_{Au/Ru} > \sigma_{O/Ru} - \sigma_{Au/O/Ru} \quad (5.1-2)$$

This relation evidently illustrates that the sum of surface free energy and interface energy for the Au/Ru system is higher than for the Au/O/Ru system, if the surface free energy of gold is assumed to be equal for both growth behaviors. This can be explained by both, the decreasing surface free energy of Ru with preadsorbed oxygen, and increased interface energy due to buried oxygen beneath the gold islands. This buried oxygen weakens the the Ru-Au binding and the strain of the Au film increases because direct binding is not always likely due to the oxygen atoms at the interface. But if it is assumed that all oxygen atoms are pushed away to form a compressed oxygen overlayer and the interface between the gold islands the ruthenium is therefore oxygen free, equation (5.1-2) can be simplified to:

$$\sigma_{Ru} - \sigma_{Au/Ru} > \sigma_{O/Ru} - \sigma_{Au/Ru}$$

$$\sigma_{Ru} > \sigma_{O/Ru} \quad (5.1-3)$$

This result evidently displays the relation of the surface free energies given from literature.<sup>[163,187]</sup> In summary, the growth of gold on oxygen free and oxygen precovered Ru(0001) can be described by Young's equation.

### 5.1.1 Gold deposited on oxygen precovered Ru(0001)

To investigate the growth of gold on oxygen precovered Ru(0001), 0.5 ML gold were deposited on ruthenium with a (2x1)-O and (1x1)-O overlayer. The intention of this experiment was to investigate the morphology of the growing gold islands, if the precovered oxygen layer cannot be compressed further.

During the deposition process of gold, higher temperatures ( $> 650$  K) and low deposition rates (0.05 ML/min) for gold were used so that the mobility of the deposited gold atoms is high and kinetic limitations are negligible, i.e. the system is at thermodynamic equilibrium. As a result the growth can be well described by the energy contributions (i.e. Young's equation) according to Bauer.<sup>[134]</sup>

Figure 5.1.1-1 shows STM pictures of the formed gold islands on the Ru(0001) surface depending on the oxygen precoverage.

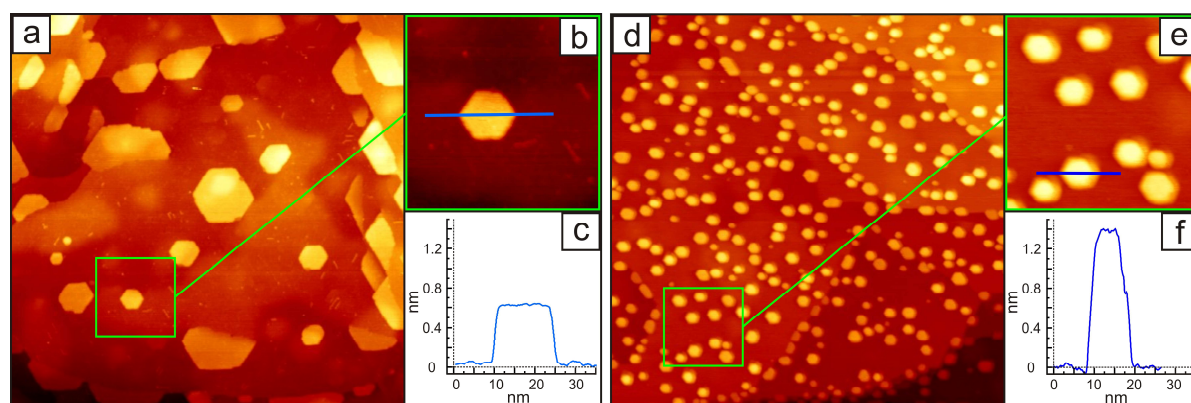


**Figure 5.1.1-1:** STM images of gold deposition (0.5 ML) on Ru(0001)-(1x1)-O and Ru(0001)-(2x1)-O. STM pictures (a) and (d) are in the range of 250 nm x 250 nm. The magnifications (b) and (e) are in the range of 50 nm x 50 nm. Tunneling conditions:  $U = 1.2$  V,  $I = 1.0$  nA.

If the ruthenium surface is precovered with an (2x1)-O overlayer, hexagonally shaped gold islands are formed and predominately located along the ruthenium steps due to a better coordination towards the surface (cf. figure 5.1.1-1a). At steps the nucleation of single gold atoms is facilitated because the size of a stable critical nucleus of gold, from which the gold island growth starts, is smaller. Vice versa, the size of stable critical gold nuclei on the ruthenium terraces are significantly larger at 670 K, thus leading to less formed islands on the terraces. Simultaneous to the gold island formation, the oxygen overlayer is compressed. These results fit well to the observations in literature.<sup>[156,157]</sup> The three-dimensional Volmer-Weber like growth of gold, in the presence of oxygen on the ruthenium surface, is depicted by the line scan analysis of a hexagonal gold island which has a height of  $6.5 \text{ \AA}$  (cf. figure 5.1.1-

*1b,c*). The hexagonal shape of the gold islands is induced by the underlying hcp(0001) orientation of ruthenium. Therefore the grown gold islands are assumed to grow in fcc(111) orientation.

However if the oxygen coverage is increased to an (1x1)-O overlayer the gold island growth changes as can be seen in *figure 5.1.1-1d,e*. Due to the high oxygen coverage no further compression of the overlayer is possible. Therefore the deposited gold atoms have to bind towards the O/Ru surface, thereby burying oxygen atoms at the interface. The gold islands are now randomly distributed over the whole ruthenium surface with a significantly higher concentration of islands if compared with the (2x1)O case (comparison of *figure 5.1.1-1a* and *5.1.1-1d*). As described previously, the adsorbed oxygen decreases the surface free energy of ruthenium to an extent that the surface free energy of gold now exceeds the sum of the surface free energy of O/Ru(0001) and the interface energy. This energy relation and a Au-Au binding stronger than to the Au-O/Ru binding induces the three-dimensional growth of gold. The strong influence of precovered oxygen on the three-dimensionality of the gold islands becomes evident by comparing the heights of the formed hexagonal islands on the (2x1)-O and the (1x1)-O precovered Ru(0001) surface, i.e. 6.5 Å and 13.1 Å respectively (cf. line scans *figure 5.1.1-1c* and *5.1.1-1f*). Therefore the thickness of the gold islands increased while their lateral size decreased significantly, if the oxygen precoverage is increased. Also the nucleation sites for the gold atoms and the starting points for the gold islands are strongly affected by the oxygen overlayer. Induced by the weak Au-O/Ru binding, the former energy gain by nucleation at the steps decreases so significantly, that nucleation on the terraces became energetically favorable, too (cf. *figure 5.1.1-1d,e*).

Derived from statistical analysis, the height distributions of the gold islands formed on (2x1)-O and (1x1)-O precovered ruthenium surfaces are depicted in *figure 5.1.1-2a* and *figure 5.1.1-2c*, respectively. Statistical analysis of the gold islands (0.5 ML) formed at 670 K on a (2x1)-O precovered surface show two distributions. Most of the gold islands are three layers thick (distribution around 6.5 Å) but also two layered gold islands are formed (smaller distribution at 4.4 Å). As comparison, gold deposition (0.5 ML) on the (1x1)-O precovered surface induced the formation of thicker islands with a thickness of 4 to 8 layers and the majority having an average thickness of approximately 6 to 7 layers (13.2 Å to 15.4 Å). Increasing the oxygen coverage from 50 % ((2x1)-O) to 100 % ((1x1)-O) results in formed gold islands that are approximately double as thick.

Another possibility to control the island thickness is the applied sample temperature during the deposition process. At higher temperatures the gold-ruthenium system is even more forced towards the thermodynamic equilibrium and thicker gold islands are formed.

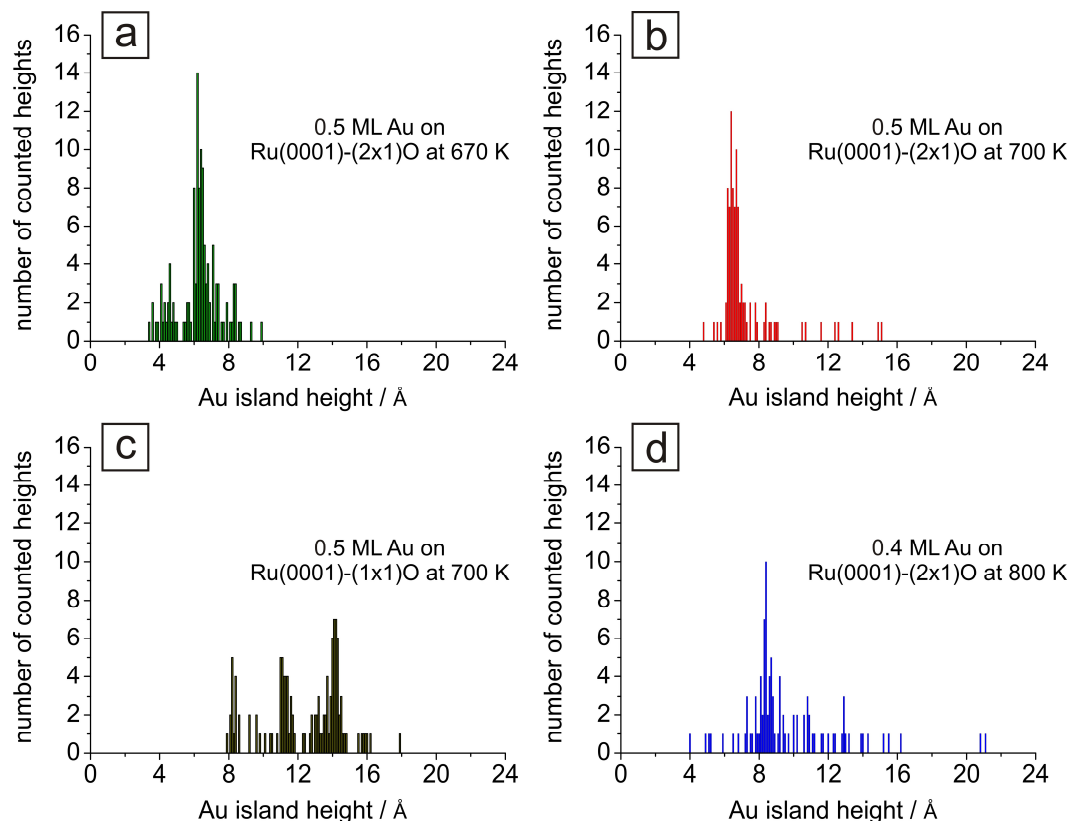


**Figure 5.1.1-2:** Statistical examination of the gold island thickness depending on the oxygen precoverage and the Ru(0001) temperature during the deposition process. (a) 0.5 ML Au deposited on a (2x1)O precovered surface at 670 K leads to the formation of two or three layered gold islands. By increasing the temperature to 700 K (b) the deposition of 0.5 ML Au now exclusively forms three layered Au islands. By increasing the temperature during deposition to 800 K the formation of four layered gold islands is induced (d). The island thickness can also be regulated by the oxygen precoverage, which is presented in (c). Deposition of Au on a (1x1)O precovered Ru(0001) surface significantly increases the resulting Au island thickness.

From line scan analysis a statistical evaluation of the island heights for gold islands prepared at 700 K (cf. figure 5.1.1-2b) and 800 K (cf. figure 5.1.1-2d) on a Ru(0001)-(2x1)O surface are obtained, respectively. While at 700 K mainly three layered gold islands are formed, at 800 K the gold islands are usually at least four layers thick. It is noteworthy that increasing the temperature from 670 K to 700 K results in the complete disappearance of the two layered island, i.e. only three layered islands are formed.

To further comprehend on this temperature dependent thickness of the growing gold islands, further considerations are necessary. Gold deposition experiments, performed at room temperature, showed the formation of many small gold nanoparticles, which were covering

the whole Ru(0001) surface (data not shown). This indicates a strong inhibition for surface diffusion of the deposited gold atoms at room temperature. This growth behavior and the resulting morphology of the deposited gold can be assigned to a growth mechanism far away from thermodynamic equilibrium (e.g. the multilayer growth<sup>12</sup>). A threshold temperature of at least 650 K has to be exceeded to enable the diffusion of the gold atoms on the ruthenium surface during the deposition process.

Finally, XPS measurements of 0.5 ML Au deposited on a (2x1)O precovered Ru(0001) surface at 700 K for the Au 4f and O 1s signal area are presented, before and after the gold deposition (*cf. figure 5.1.1-3*).

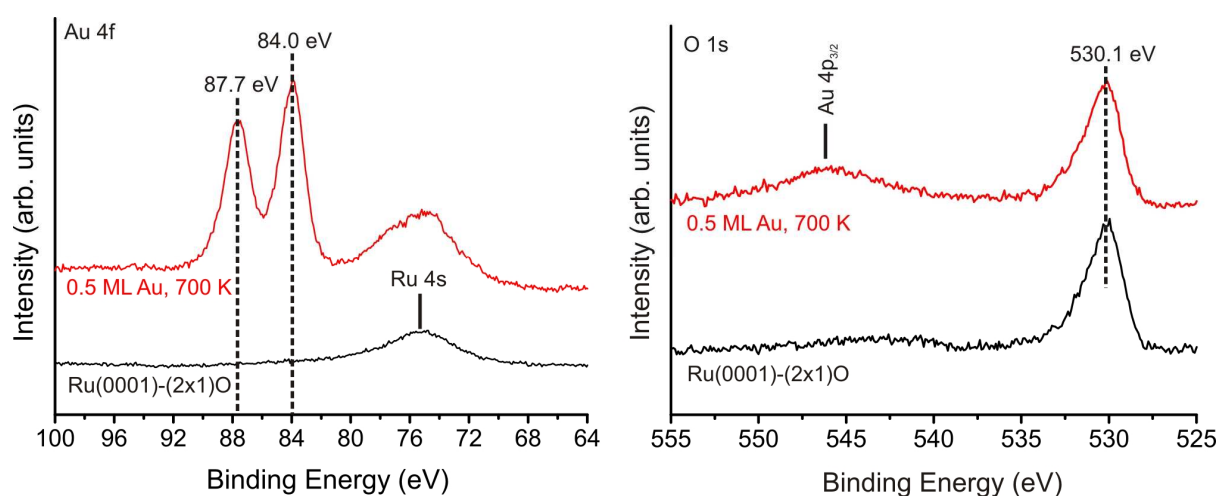


**Figure 5.1.1-3:** Au 4f and O 1s XPS data for 0.5 ML gold deposited on an oxygen precovered Ru(0001) surface at 700 K. The Au 4f signals evidently display the metallic character of the hexagonal gold islands. The constant O 1s signal confirms the interpretation of a compressed oxygen overlayer. It is therefore assumed that no oxygen gets buried beneath the gold islands.

The Au 4f binding energies of 84.0 eV and 87.7 eV evidently show the metallic character of the formed hexagonal gold islands. The corresponding O 1s spectra show no change of the oxygen signal after deposition of gold on the surface. Neither does the binding energy of the O 1s signal change nor is the signal attenuating. The constant O 1s signal intensity indicates that no oxygen is buried beneath the gold at the gold-ruthenium interface. With a constant amount of oxygen exposed on the surface, the conclusion of a compressed oxygen overlayer is evident consistent with literature.<sup>[156,163]</sup>

In summary, the influence of the oxygen precoverage and the applied temperature on the growth of gold on Ru(0001) have been presented. Changing the conditions for the growth of gold on Ru(0001) by changing the oxygen overlayer density (i.e. changing the surface free energy of ruthenium) is more important for the resulting morphologies of the ruthenium

<sup>12</sup> cf. Chapter 3.3.3, page 44ff.

islands than overcoming kinetic limitations by increasing the temperature. Based on the presented experimental data, it is possible to control the thickness of the growing gold islands, which will be crucial for the upcoming oxidation experiments.

### 5.1.2 Gold deposited on oxygen free Ru(0001)

To prepare wetting films of gold on Ru(0001), deposition and growth was carried out on an oxygen free surface. For the preparation of an oxygen free ruthenium surface, an additional annealing step in vacuum to 1000 K for 30 minutes was added to the typical cleaning process described in chapter 2.1 (see page 12). This annealing step should induce desorption of the oxygen overlayer that is usually formed during the cleaning process.

For all preparations of wetting gold films the Ru(0001) surface was kept at 700 K and higher deposition rates<sup>13</sup> of 0.1 ML/min were employed. The total amount of deposited gold was determined by the evaporation rate *in situ* and afterwards verified by the XPS signal intensity.

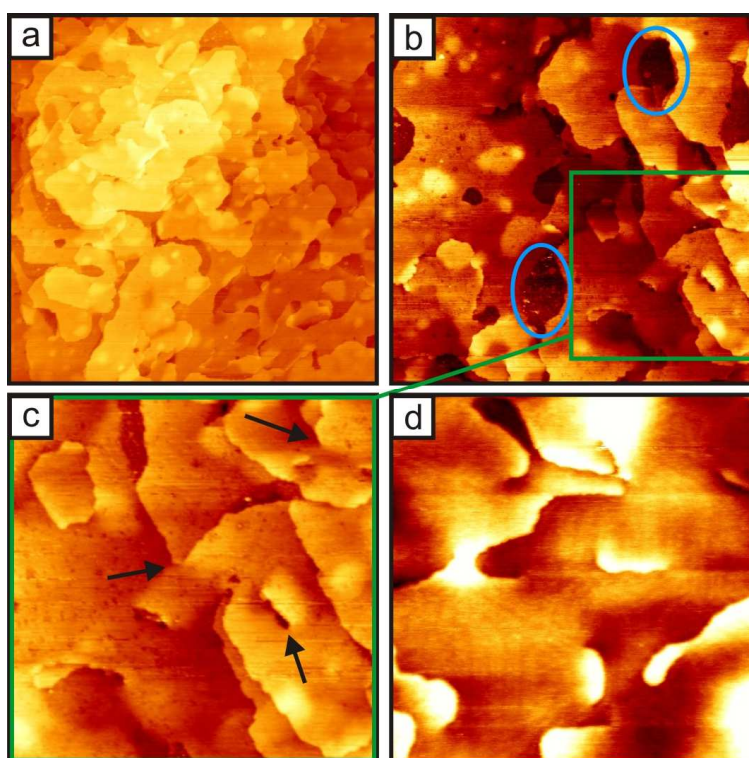


**Figure 5.1.2-1:** (a) 500 nm x 500 nm area of the 2 ML gold film covering the oxygen free Ru(0001) surface. (b) The 300 nm x 300 nm area illustrates the formation of wholes in the gold film (blue circles) induced by residual oxygen from the former cleaning process of the single crystal surface; (c) The 150 nm x 150 nm magnification evidently shows the formation of point dislocations within the gold film (black arrows). (b) and (c) both evidently show the influence of the residual oxygen on the Au film morphology. Compared to literature the resulting gold film is less smooth and does not show the herringbone structure of thin gold films on Ru(0001).<sup>[157,159]</sup> Due to the relatively high roughness, the typical Stranski-Krastanov growth for gold on bare Ru(0001) is not clearly visible by STM. (d) This 150 nm x 150 nm area from the top of a 50 nm thick gold mountain or “mesa” evidently illustrates the (111) crystallographic orientation of gold. Tunneling conditions:  $U = 0.7 - 1.0$  V,  $I = 0.1 - 1.0$  nA.

<sup>13</sup> Compared to the deposition rate used to form the islands on oxygen precovered Ru(0001), i.e. 0.05 ML/min.

*Figure 5.1.2-1* shows STM images of a wetting 2 ML thick gold film deposited on nearly oxygen free Ru(0001). Although the lattice misfit between gold and ruthenium is relatively small ( $\sim 6.2\%$ ) the gold film is not very smooth. Instead many steps and defects are visible as well as the formation of flat islands on already grown gold layers (*cf. figure 5.1.2-1a,b*). This is consistent with the observed Stranksi-Krastanov growth mechanism for Au on Ru(0001) in literature.<sup>[154,157,163]</sup> However many point dislocations (screw dislocations, see black arrows) are formed while the typical island formation of the SK growth is less pronounced (*cf. figure 5.1.2-1c*).

The depicted STM image from *figure 5.1.2-1b* reveals several areas where the gold is not covering the ruthenium substrate (highlighted by blue ellipses). The corresponding XPS O 1s spectra illustrate that some oxygen from the cleaning process was still present on the surface (*cf. figure 5.1.2-2*, black curve). A small and broad O 1s peak at  $\sim 530.1$  eV is observable that is assigned to the oxygen residues adsorbed on ruthenium.<sup>[8]</sup> However the O 1s spectrum after deposition of 2 ML Au (XPS) evidently shows that the oxygen signal is reduced (*cf. figure 5.1.2-2*, red curve). This is an indication of buried oxygen beneath the gold film. With an applied temperature of 700 K during the Au deposition process, desorption of O<sub>2</sub> from the Ru(0001) surface can be excluded. Due to the higher deposition rate of gold and the significantly lower amount of residual oxygen, the oxygen atoms are rather overgrown by the gold film than being compressed to a dense overlayer to whom the gold less tends to bind. These incorporated oxygen atoms at the interface are assumed to increase the strain of the wetting gold film, which is released by the formation of dislocations (*cf. figure 5.1.2-1c*, black arrows). In some areas the residual oxygen is partially compressed to a dense oxygen overlayer on Ru(0001) to which the deposited gold is reluctant to bind at 700 K. As a consequence the observable holes in the gold film are formed (blue ellipses *figure 5.1.2-1b*).

It should be mentioned that the deposition of more than 4 ML gold leads to the formation of very thick gold islands or “mesas” with a thickness of at least 100 layers (thickness  $> 20$  nm, lateral size up to 500 nm) at the step bunching areas of the ruthenium surface. Similar mountain formation has been observed in literature for the growth of Cu and Ag on Ru(0001).<sup>[188]</sup> STM pictures of these thick gold mountains reveal a herringbone structure on top of the mountain surface (*cf. figure 5.1.2-1d*), thus confirming the fcc(111) orientation of gold growing on the Ru(0001) surface.

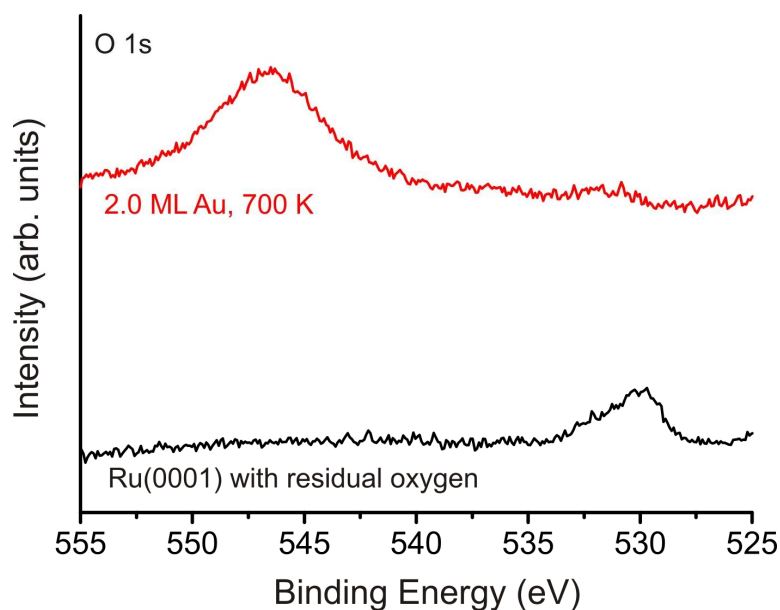


**Figure 5.1.2-2:** XP spectra of a 2 ML gold film formed on a nearly oxygen free Ru(0001) surface. The O 1s spectrum of the clean Ru(0001) surface (black curve) shows a small O 1s peak of residual oxygen, which was not removed by the final cleaning step, i.e. annealing in vacuum. After deposition of Au on the surface (red curve), the O 1s signal nearly vanished, thus indicating that the oxygen is now mainly buried beneath the Au film.

Overall, gold deposited on the oxygen free Ru(0001) surface at 700 K leads to the formation of wetting gold films that is in good agreement to the literature.<sup>[154,157,163]</sup> However the morphologies of these films are slightly different to reference data from Hwang et al.<sup>[157,159]</sup> These differences in morphology may be explained by the influence of the residual oxygen on the Ru(0001) surface.

Lambert et al have shown, that gold is able to overgrow an oxygen overlayer on the Ru(10-10) surface.<sup>[161]</sup> The vanishing O 1s (530.1 eV) signal as well as the high amount of dislocations within the gold film strongly indicate the presence of buried oxygen at the interface. It is assumed that these buried oxygen atoms induce an additional strain on the gold film. This additional strain explains the higher number of defects and point dislocations within the wetting gold film.

However, these mentioned differences are negligible compared to the morphologic similarities for the growth of Au on oxygen free Ru(0001) in the literature, i.e. the two-dimensional wetting behavior of gold with absence of adsorbed oxygen. This is also consistent with the general thermodynamic considerations for the gold-ruthenium system by Young's equation (eq. (5.1-1), page 59).

### 5.1.3 Gold deposited on RuO<sub>2</sub>(110)

Wu and Hrbek studied the deposition of gold on the oxidized Ru(0001) surface by thermal desorption spectroscopy.<sup>[165]</sup> For this heterostructure a higher activity towards CO oxidation has been observed, compared to the pure RuO<sub>2</sub>(110) surface. As a result a synergistic effect between Au and RuO<sub>2</sub> has been suggested. Structural details of this system have not been reported in the literature, but will be presented here.

A completely covering and flat film of RuO<sub>2</sub>(110) on Ru(0001) was prepared by oxidizing the single crystal surface with molecular oxygen. This oxidation was conducted at 720 K and oxygen pressures of  $1 \cdot 10^{-4}$  mbar to form a wetting oxide film (*cf. figure 5.1.3-1a* and *5.1.3-1b*), which partially consists of relatively broad RuO<sub>2</sub>(110) terraces.<sup>[189,190]</sup>

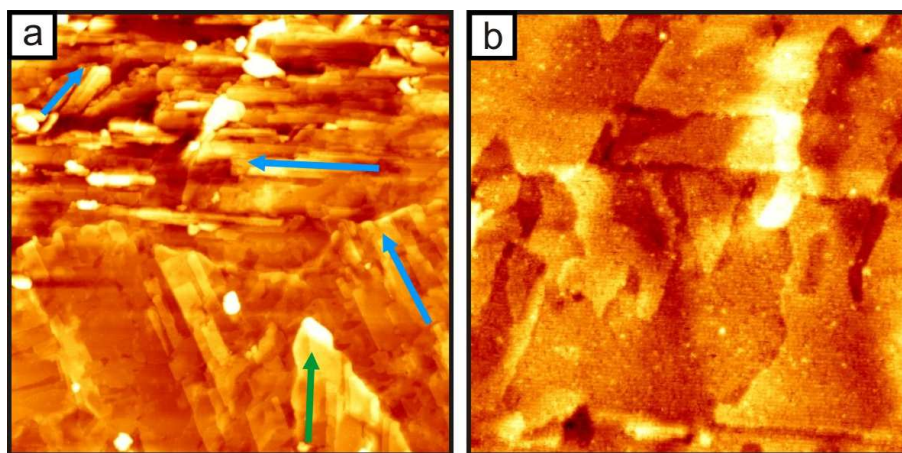


**Figure 5.1.3-1:** (a) 500 nm x 500 nm, (b) 100 nm x 100 nm : STM pictures of RuO<sub>2</sub>(110) prepared by oxidation of Ru(0001) at 720 K by dosing  $1 \cdot 10^{-4}$  mbar O<sub>2</sub>. The rotational domains of RuO<sub>2</sub>(110), that are tilted by 120° to each other, are highlighted by the blue arrows in (a). Also a slightly rotated domain of RuO<sub>2</sub> is visible in the STM picture (green arrow in (a)). These rotated oxide domains have been reported in recent studies and are a result of the relatively high temperature during oxidation.<sup>[191]</sup> Besides the relatively rough areas of RuO<sub>2</sub>, also large and relatively flat terraces of RuO<sub>2</sub>(110) are formed as indicated in (b). Tunneling conditions:  $U = 0.9 - 1.2$  V,  $I = 1.0$  nA.

Depending on the oxidation conditions, the roughness of the oxide film can be varied. At lower temperatures (e.g. 650 K) the oxide film is usually rougher and the oxide terrace width is smaller.<sup>[189,190]</sup> A STM image of the resulting RuO<sub>2</sub>(110) film (*cf. figure 5.1.3-1a*) displays the overall morphology of the formed oxide. Indicated by the blue arrows are the three rotational domains of RuO<sub>2</sub>(110) that are formed due to the difference in symmetry between the Ru(0001) substrate ( $C_3$ ) and the growing oxide ( $C_2$ ). Additionally formed to those three rotational domains is a newly growing RuO<sub>2</sub>(110) domain (green arrow), which is slightly rotated. Such additional, slightly rotated domains have recently been reported and are a result

of higher temperatures ( $> 680$  K) during the Ru(0001) oxidation process.<sup>[191]</sup> The larger scan area of *figure 5.1.3-1a* also shows that the surface consists of regions with a high roughness (upper half) as well as flat regions with wide and atomically flat RuO<sub>2</sub>(110) terraces (lower half). A magnification of these flat RuO<sub>2</sub> regions is provided in *figure 5.1.3-1b*.

Subsequently 0.5 ML gold were deposited on this RuO<sub>2</sub>(110)/Ru(0001) surface at 700 K, which is visualized by a series of STM images (*cf. figure 5.1.3-2*).

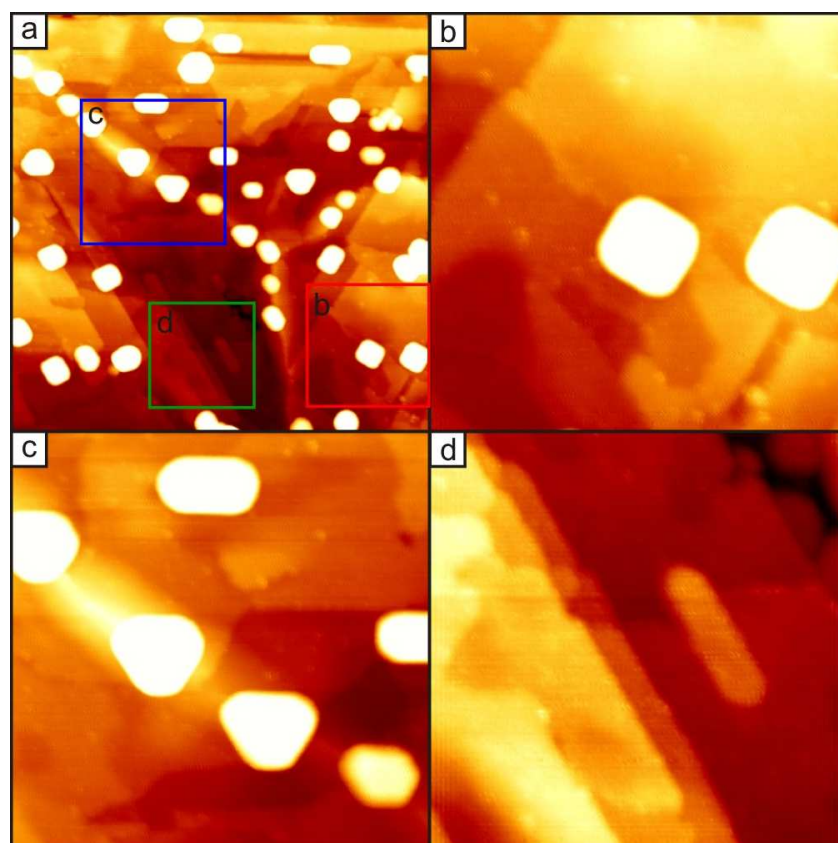


**Figure 5.1.3-2:** STM images of 0.5 ML Au deposited at 700 K on the previously prepared RuO<sub>2</sub>(110) wetting film: (a) Three different kinds of gold islands on RuO<sub>2</sub>(110) are discernible, i.e. flat and slender islands (green, d), cuboid-like islands (red, b), and hexagonal islands (blue, c). (b) The cuboid islands are located on the flat RuO<sub>2</sub>(110) regions. (c) The hexagonal gold islands are preferentially located at the intersections of differently rotated domains of RuO<sub>2</sub>(110). (d) From the three different island types the flat and slender islands are found to be the minority on RuO<sub>2</sub>(110). For these islands no preferential location could be determined and their chemical nature is unclear. The STM image areas are: (a) 200 nm × 200 nm, (b) 60 nm × 60 nm, (c) 70 nm × 70 nm, (d) 50 nm × 50 nm. Tunneling conditions:  $U = 0.7 - 1.0$  V,  $I = 1.0$  nA.

By STM the three-dimensional growth of gold islands on the RuO<sub>2</sub>(110) is evident (*cf. figure 5.1.3-2a*). Three different types of gold islands are discernable on the surface: hexagonal islands (*cf. figure 5.1.3-2c*), cuboid islands (*cf. figure 5.1.3-2b*) as well as slender thin islands (*cf. figure 5.1.3-2d*). While the hexagonal and cuboid islands are assigned to gold, the chemical nature of the thin and slender islands is unclear. Although their morphology is

similar to thin gold islands formed on  $\text{TiO}_2(110)$ <sup>[20,21]</sup>, these islands might also be assigned to small  $\text{RuO}_2(110)$  flakes. The shape of the hexagonal and cuboid gold islands indicates different crystallographic orientations of the growing gold on the  $\text{RuO}_2$ . The cuboid gold islands are assigned to gold with (100). These islands are located on flat terraces of  $\text{RuO}_2(110)$  (*cf. figure 5.1.3-2b*). The hexagonal islands are predominantly found at the intersection areas of differently rotated  $\text{RuO}_2(110)$  domains (*cf. figure 5.1.3-2c*). From their truncated triangular shape the fcc (111) orientation is inferred.

Depending on the orientation of the gold island its thickness differs markedly. A statistical analysis of the island heights is illustrated in *figure 5.1.3-3*.

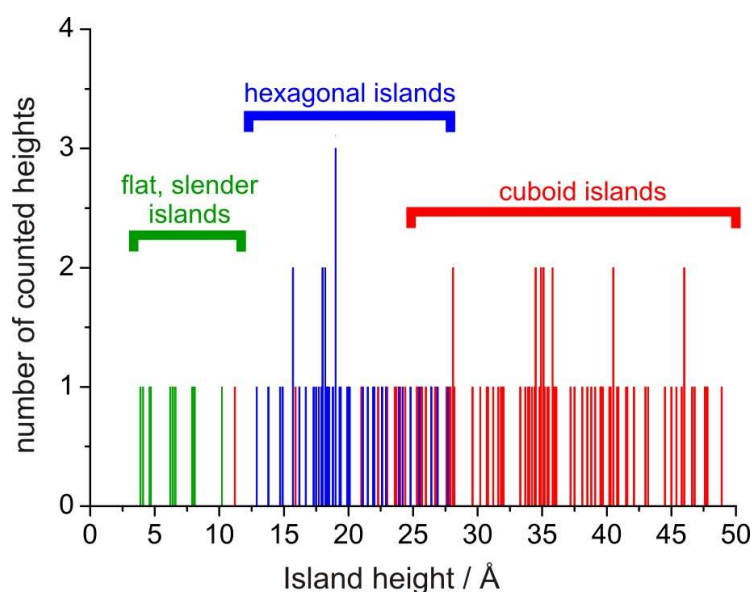


**Figure 5.1.3-3:** Statistical examination of the island thickness of the differently shaped islands that are observable by STM after deposition of 0.5 ML gold on a flat  $\text{RuO}_2(110)$  surface. The thickness of the hexagonal islands ranges between 7 to 12 layers of gold, while the much thicker cuboid islands reach heights up to nominal 22 layers of gold.

The hexagonal gold islands are generally thinner than the cuboid gold islands. The height distribution for each island type is very broad. The thickness of the hexagonal islands ranges from approximately 7 to 12 layers. The cuboid islands are about as double as thick as the hexagonal islands and they reach heights up to 22 layers of gold. Therefore the gold islands formed on  $\text{RuO}_2$  are significantly thicker than gold islands formed on oxygen precovered  $\text{Ru}(0001)$  (4 to 8 layers on the (1x1)O phase, *cf. figure 5.1.1-2c*).

The thickness of the gold islands grown on  $\text{RuO}_2(110)$  strongly depends on the complex relation between the interface energy, the surface free energy of each respective crystallographic orientation of gold and on the occurring strain energy, which is assumed to

be very large if the gold grows epitaxial on the  $\text{RuO}_2(110)$  surface. To give a first impression how the gold may bind to the  $\text{RuO}_2$  surface, a schematic illustration is given in *figure 5.1.3-4*.

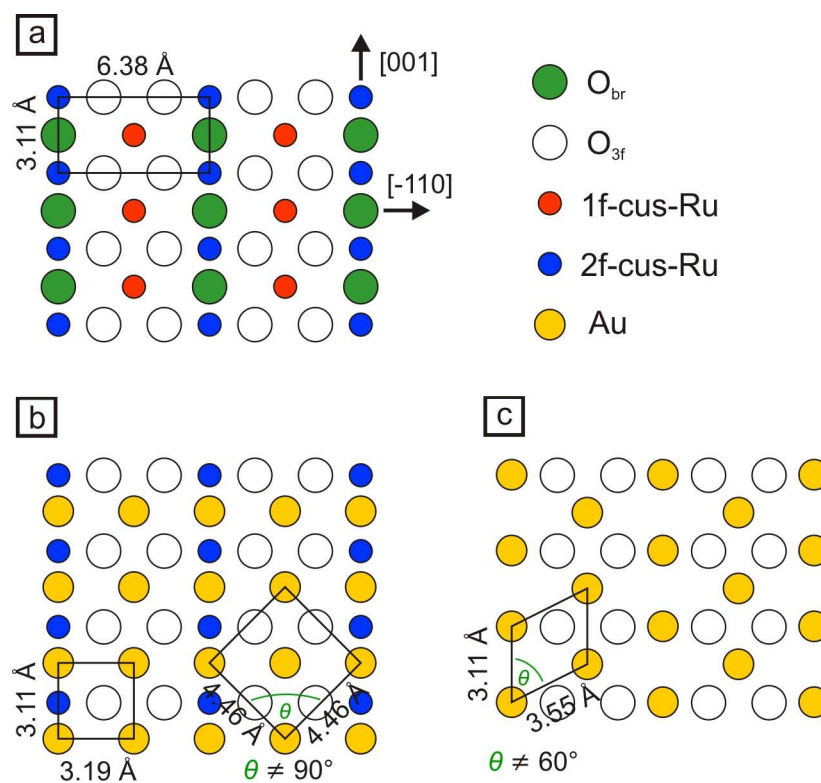


**Figure 5.1.3-4:** Schematic illustration of the top view on the stoichiometric  $\text{RuO}_2(110)$  surface (a). By removal of the bridging oxygen atoms, two different binding structures of a single layer gold atoms on this mildly reduced  $\text{RuO}_2(110)$  surface are shown. (b) Gold layer with a square unit cell, which is similar to a strained single layer of  $\text{Au}(100)$  that exclusively binds to ruthenium atoms. (c) Gold layer with a hexagonal unit cell, which is similar to a single layer of  $\text{Au}(111)$  but with much larger strain within the layer. For comparison, the nearest neighbor distance between Au atoms in  $\text{Au}(111)$  and  $\text{Au}(100)$  are  $2.885 \text{ \AA}$ , respectively. Therefore the  $(100)$  Au overlayer is more favorable, if gold grows pseudomorph on the mildly reduced  $\text{RuO}_2(110)$  surface.

Illustrated in *figure 5.1.3-4a* is the top view on the stoichiometric  $\text{RuO}_2(110)$  surface. Due to the weak gold-oxygen binding, it is reasonable that the adsorbed gold atoms would preferentially bind to the ruthenium atoms i.e. on-top to the 1f-cus ruthenium atoms and in bridge position between two 2f-cus ruthenium atoms by replacing the bridged oxygen atoms. *Figure 5.1.3-4b* illustrates this situation where gold binds to this so called mildly reduced  $\text{RuO}_2(110)$  surface.<sup>[192]</sup> This first overlayer of gold is very similar to  $\text{Au}(100)$ . By considering the nearest neighbor distance for  $\text{Au}(100)$  ( $2.885 \text{ \AA} \times 2.885 \text{ \AA}$ ) a linear tensile strain of 7.8 % results in the  $[001]$ <sup>14</sup> direction and a linear tensile strain of 10.6 % occurs in the  $[-110]$  direction, if the first gold layer grows pseudomorph on the mildly reduced  $\text{RuO}_2(110)$  surface. In principle it is also possible to envision a gold overlayer, where all gold atoms bind

<sup>14</sup> The directions are given with respect to the  $\text{RuO}_2(110)$  (cf. *figure 5.1.3-4a*).

from the on-top position to the 1f-cus and the 2f-cus ruthenium atoms, respectively (cf. *figure 5.1.3-4c*). By this arrangement a strained hexagonal gold overlayer becomes visible. But comparing this overlayer to a unstrained Au(111) layer (with nearest neighbor distance of  $2.885 \text{ \AA} \times 2.885 \text{ \AA}$ ), nominally linear tensile strain of 7.8 % and 23.1 % are introduced, with additional shear strain because of  $\theta \neq 60^\circ$  (cf. *figure 5.1.3-4c*). These two illustrations of gold binding to the mildly reduced RuO<sub>2</sub>(110) surface indicate why the crystallographic orientation of Au(100) is more favored on the flat terraces. Purely considering the surface free energy of Au(100) and Au(111) (Au(111):  $1.3 \text{ J/m}^2$ , Au(100):  $1.6 \text{ J/m}^2$ )<sup>[182,184]</sup>, the formation of Au(111) would be favored. But taking the two illustrated structures of *figure 5.1.3-4* into account and estimating the interface energy and the strain energy of these structures, the growth of (100) oriented gold islands is more preferred than the growth of (111) oriented gold islands. With a significantly smaller in-plane strain and in-plane lattice misfit, the interface energy and the strain energy of Au(100) islands is assumed to be much smaller than the interface energy and the strain energy of Au(111) islands on the flat RuO<sub>2</sub>(110) terraces, thus explaining the observed growth of gold in (100) direction. At the intersection of different RuO<sub>2</sub>(110) domains, the formation of Au(111) islands is favored (cf. 5.1.3-2c). This indicates a strong influence of the symmetry of the RuO<sub>2</sub>(110) at these intersections. Obviously at these intersections the complex energy relation of interface energy, surface free energy and strain energy changes in favor of (111) oriented gold islands. But without any further information about the binding between the gold islands and the underlying RuO<sub>2</sub>(110) on the atomic scale, it is not possible to derive which of the energy contributions mostly determines the resulting crystallographic orientation of the gold island.

In conclusion: the three-dimensional growth of gold islands on RuO<sub>2</sub>(110) is reasonable. At first, the surface free energy of gold is significantly higher than the one of RuO<sub>2</sub> ( $\sigma_{\text{Au}}: >1.3 \text{ J/m}^2$ ;  $\sigma_{\text{RuO}_2}: 0.7 \text{ J/m}^2$ )<sup>[182,184,193]</sup> which facilitates the three-dimensional growth. Secondly, the lattice mismatch between gold and the RuO<sub>2</sub>(110) surface is assumed to be high. This induces a strain at the interface that leads to higher interface and strain energies. As a result the deposited gold is even more pronounced to grow three-dimensional on the RuO<sub>2</sub>(110) surface. Evidently, the symmetry of the RuO<sub>2</sub>(110) substrate favors the formation of gold islands with a similar symmetry, i.e. Au islands with (111) orientation are formed on the intersections of different RuO<sub>2</sub> domains while (100) oriented Au islands are formed on the flat RuO<sub>2</sub> terraces. Therefore, the energy relation of interface energy, strain energy and surface free energy is assumed to determine the crystallographic orientation of gold on the RuO<sub>2</sub>(110) surface.

## 5.2 Redox chemistry of thin gold islands

### 5.2.1 Oxidation at room temperature by atomic oxygen

Supported thin gold layers (Au bilayer system) on  $\text{TiO}_2(110)$  have shown an extraordinary high catalytic activity towards CO oxidation at room temperature.<sup>[20,21]</sup> However, it was mentioned by the authors that under realistic catalytic reaction conditions, these flat gold bilayers may restructure, exposing the substrate to the reactants.<sup>[21]</sup> In the forthcoming chapter this particular issue will be elucidated by investigating the oxidation of thin gold islands and the undergoing morphologic changes. As presented in the previous chapter, the thickness and the morphology of thin gold islands and films can be controlled properly by the applied temperature during the gold deposition and the oxygen precoverage on the Ru(0001) single crystal substrate.

The thin gold islands were formed on a (2x1)O precovered Ru(0001) surface by deposition of 0.5 ML Au at 670 K. As described in the previous chapter 5.1.1 (page 62ff) two and three layered hexagonal gold islands are formed (*cf. figure 5.1.1-2a*). The subsequent oxidation was carried out by dosing 40 L atomic oxygen towards these thin gold islands at room temperature. *Figure 5.2.1-1* summarizes the oxidation experiments of the thin gold islands.

The first STM image (*cf. figure 5.2.1-1a*) and the corresponding line scan (*cf. figure 5.2.1-1c*) show the morphology of thin gold islands on the Ru(0001)-(2x1)O surface. *Figure 5.2.1-1b* shows the surface after the oxidation by 40 L atomic oxygen. During oxidation the morphology of the gold islands changes significantly. The former flat islands are fragmented into gold nanoparticles. They are located at the positions of the former gold islands, thus reflecting the former shape of the hexagonal gold islands. From line scan analysis the height of the nanoparticles was determined to be 18.2 Å (*cf. figure 5.2.1-1d*). This height distribution illustrates that the oxidized gold nanoparticles are thicker (~ 17.4 Å) than the relative flat former gold islands (~ 6.2 Å) (*cf. figure 5.2.1-1c*). With a lateral size ranging from ~ 5 nm for the smallest nanoparticles to ~ 9 nm for the largest, the fragmented gold islands are more like flat droplets instead of spherical particles. Also the variation in lateral size reveals that the fragmentation process does not occur uniformly over the gold island surface. This indicates random positions where the fragmentation process of the gold islands starts.

XPS measurements were performed to elucidate the change of the chemical nature of the gold due to its oxidation (*cf. figure 5.2.1-1e*). The Au 4f XP spectra of the gold islands on

Ru(0001)-(2x1)O (cf. figure 5.2.1-1e, red curve a) reveals signals at 84.0 eV and 87.7 eV, which are assigned to the metallic Au 4f<sub>7/2</sub> and Au 4f<sub>5/2</sub> species.

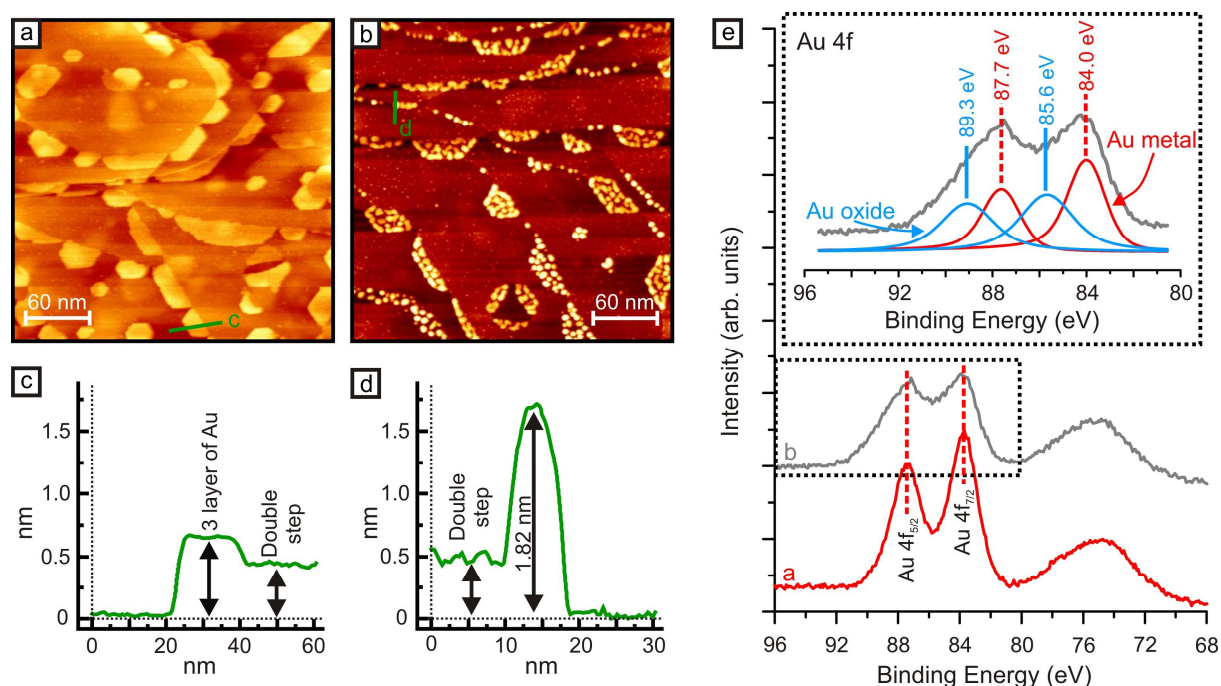


**Figure 5.2.1-1:** Overview of the morphologic changes due to oxidation of thin gold islands. The STM images illustrate a section of 300 nm x 300 nm. (a) Deposition of 0.5 ML Au at 670 K on a (2x1)O precovered Ru(0001) surface; (b) Oxidation of the thin gold islands by 40 L atomic oxygen at 300 K; (c) Line scan analysis of a thin gold islands; (d) Line scan analysis of an oxidized gold nanoparticle; (e) Corresponding Au 4f spectra of prepared Au islands (a, red) and oxidized Au islands (b, gray) including a peak deconvolution of the Au 4f signal area into the metallic Au (red) and the Au oxide (light blue) signals to elucidate the oxidation of gold. Tunneling conditions:  $U = 1.1 - 1.2$  V,  $I = 1.0$  nA.

After oxidation of the Au islands these signals decreased while new peak shoulders are evolving shifted to higher binding energies (cf. figure 5.2.1-1e, grey curve b). The peak deconvolution of the Au 4f signals gives further insight into the chemical nature of the formed nanoparticles (cf. figure 5.2.1-1e, inset). Besides the metallic Au 4f signals (deconvoluted red peaks) two new Au 4f signals are found, each shifted by 1.6 eV to higher binding energies. By comparison to the chemical shifts for the oxidized Au(111) single crystal surfaces presented in chapter 4 (cf. tables 4-1 and 4-2), this additional doublet is assigned to gold oxide, most probably Au<sub>2</sub>O<sub>3</sub>.<sup>[58,64,70,73,74,77]</sup> Additionally, an inhomogeneous broadening of the deconvoluted Au 4f signals is visible (cf. figure 5.2.1-1e, inset). The width of the Au 4f oxide signals is broader than the width of the corresponding metallic Au 4f signals. This broadening of the Au 4f peak is induced by several effects: At first, the fragmentation of the gold island leads to size-dependent final state effects of Au 4f features for the small oxidized gold nanoparticles, thus broadening the peaks. This shift of the Au 4f signals has been reported in

the literature for gold nanoparticles smaller than 5 nm.<sup>[76,194,195]</sup> Secondly, this broadening may be explained by different gold-oxygen species, which are formed during the oxidation and fragmentation process. Besides the formed Au(III)oxide species also the metallic gold atoms that are directly bound to the oxide as well as gold atoms with chemisorbed oxygen contribute to the Au 4f signals that are shifted to higher binding energies. This interpretation is similar to the one given by Gottfried et al., who also observed an inhomogeneous broadening of the Au 4f signals upon the oxidation of small gold nanoparticles.<sup>[70]</sup>

To further elucidate the oxidation of the gold islands, the corresponding O 1s signals are presented in *figure 5.2.1-2*.

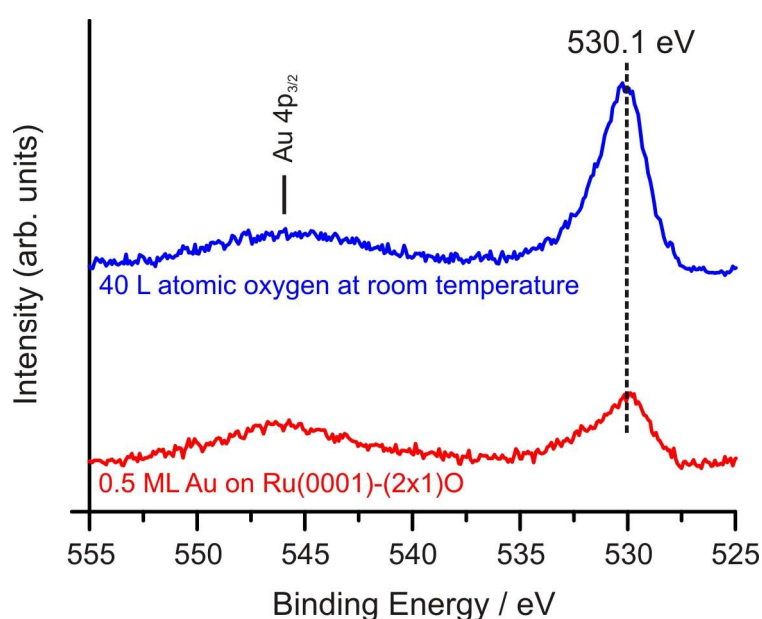


**Figure 5.2.1-2:** O 1s XPS signal area before (red curve) and after (blue curve) the oxidation of the hexagonal gold islands by 40 L atomic oxygen at room temperature. With no visible chemical shift of the O 1s signal, the strong increase is assigned to the formation of gold(III)oxide and a (1x1)O overlayer on Ru(0001).

From literature it is known that the gold island formation on a (2x1)O precovered Ru(0001) surface leads to the compression of the adsorbed oxygen to a denser (e.g. (2x2)3O) overlayer.<sup>[156]</sup> Therefore the O 1s peak that is observable at 530.1 eV (*cf. figure 5.2.1-2*, red curve) is assigned to such a compressed oxygen overlayer on Ru(0001).<sup>[196]</sup> After oxidation no shift is observable for the O 1s signal, but the oxygen signal intensity at 530.1 eV increased significantly (*cf. figure 5.2.1-2*, blue curve). This additional O 1s signal at 530.1 eV can be assigned to the formation of gold oxide (most likely Au<sub>2</sub>O<sub>3</sub>).<sup>[59,66,71,73,75,76]</sup> It should be mentioned, however, that the increase of the oxygen signal at 530.1 eV can also be assigned to the formation of a denser oxygen overlayer structure.<sup>[8,196]</sup> Herd et al. observed the formation of a (1x1)O overlayer on the Ru(0001) surface after exposure of 10 L atomic

oxygen at room temperature.<sup>[197]</sup> With the elucidated formation of oxidized Au species on the basis of the Au 4f signals, the increase of the O 1s signal is assigned to both: The formation of a more dense oxygen overlayer and the oxidation of the gold islands to Au oxide/Au nanoparticles.

On the basis of the STM images and the XPS data, a core-shell structure for the fragmented Au particles is proposed. In particular, the peak deconvolution of the Au 4f signals does not only provide the information for the presence of Au<sub>2</sub>O<sub>3</sub> (*cf. figure 5.2.1-1* inset, deconvoluted light blue peaks) but also shows that metallic gold is still present (*cf. figure 5.2.1-1* inset, deconvoluted red peaks). Since gold oxide has a lower surface free energy than metallic gold,<sup>[82]</sup> the oxidized gold species tend to cover the metallic gold. The occurrence of the metallic gold and the oxidized gold in the formed nanoparticles indicates a core-shell structure, with the Au oxide shell covering the metallic Au core. Such a core-shell nanoparticle structure is consistent with current interpretations in the literature.<sup>[32,74]</sup> However, without thickness-dependent high-resolution XPS measurements the composition and structure of the formed nanoparticles from this fragmentation process remain elusive.

## 5.2.2 Au oxide/Au nanoparticle reduction and Au island reformation

To gain insight into the chemical properties of the oxidized gold nanoparticles, reduction experiments at higher temperatures were carried out to restore the structure of flat gold islands on the ruthenium surface. Similar experiments were done on the Ru(10-10) single crystal surface.<sup>[160,161]</sup>

The restoration of metallic gold islands can be achieved by either reducing the Au oxide nanoparticles in CO at higher temperatures, or by simple annealing to higher temperatures due to metastability of oxidized gold structures in UHV. By TDS, the decomposition of Au oxide and the desorption of chemisorbed oxygen from metallic Au has been observed by annealing to 390-473 K<sup>[62,63,68,69,198]</sup> or to 520-590 K<sup>[51,55,56,65,68,69,71]</sup>, respectively. The restoration of metallic gold islands was performed by two experiments: At first the Au oxide/Au nanoparticles were reduced by 100 L CO ( $p(\text{CO}) = 1 \cdot 10^{-6}$  mbar, 14 min) at 670 K. In the second reduction experiment the nanoparticles were annealed to 670 K in vacuum for the same time period as in the chemical reduction experiment, i.e. for 14 minutes. By this procedure the influence of CO at higher temperatures on the gold island restoration is elucidated. *Figure 5.2.2-1* summarizes the chemical and the thermal reduction of the fragmented Au nanoparticles.

By STM the reformation of hexagonal islands due to reduction becomes evident. In case of the chemical reduction process (100 L CO, 670 K) large hexagonal islands were formed (*cf. figure 5.2.2-1b*). From line scan analysis a thickness of about 3 ML for these gold islands has been determined (*cf. figure 5.2.2-1d*). Therefore the former island thickness could be restored by reduction in CO. These gold islands are mainly located at the steps of the ruthenium surface, but STM also reveals that not all gold islands have the same lateral size as the as-prepared 3 layered gold islands on oxygen precovered Ru(0001). Evidently the mobility of the gold atoms was not sufficient to facilitate the merging of all smaller gold islands during the chemical reduction process.

If the fragmented gold nanoparticles are thermally reduced the resulting gold island morphology is different. A higher concentration of laterally smaller gold islands are formed on the Ru(0001) surface, which are located near the ruthenium steps (*cf. figure 5.2.2-1c*). Line scan analysis revealed that the height of these laterally smaller islands is about 6 layers of gold (*cf. figure 5.2.2-1e*). Therefore these islands are as double as thick as hexagonal gold islands that are formed during the chemical reduction process at similar temperature. XPS confirms the reduction of the oxidized Au particles. The metallic Au 4f signals at 84.0 eV and

87.7 eV increase while the Au oxide features at 85.6 eV and 89.3 eV decrease (*cf. figure 5.2.2-1f*).

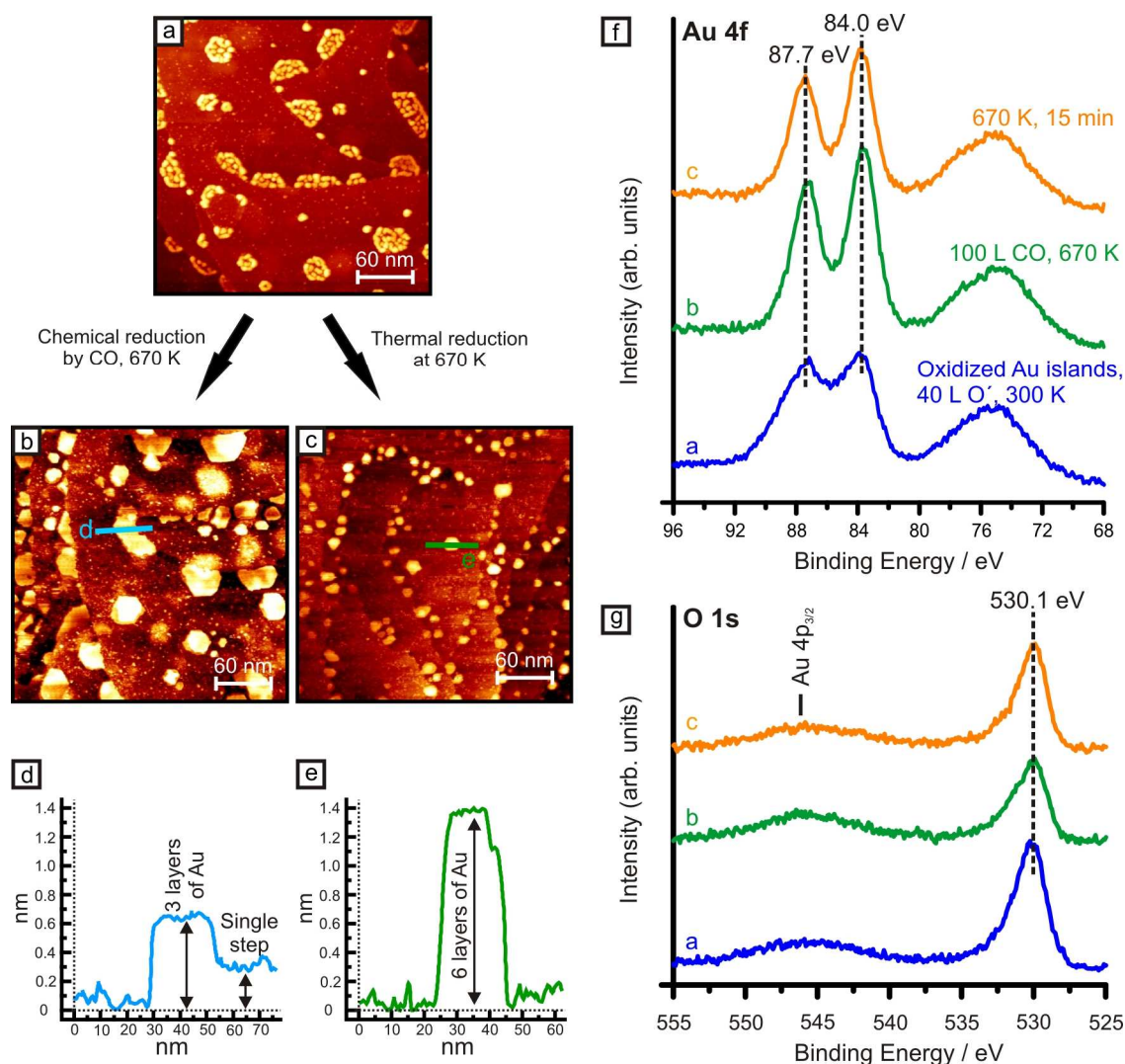


**Figure 5.2.2-1:** Chemical and thermal reduction of oxidized 3 ML thick Au islands on Ru(0001)-(2x1)O: (a) STM image (300 nm x 300 nm) of the oxidized islands. (b) Chemical reduction of Au oxide/Au nanoparticles by exposing 100 L of CO at 670 K (STM image area: 300 nm x 300 nm). (c) Thermal reduction by annealing to 670 K in a vacuum for 14 min (STM image area: 300 nm x 300 nm). Both, the line scan analysis (d, e) and XPS data of the Au 4f signals (f) and the O 1s signals (g) evidently show the reduction of the nanoparticles as well as the gold island reformation and their lateral expansion on the surface depending on the oxygen overlayer. Tunneling conditions:  $U = 1.1$  V,  $I = 1.0$  nA.

Also the O 1s signal at 530.1 eV decreases (*cf. figure 5.2.2-1g*). This confirms the reduction of the fragmented Au oxide nanoparticles and the loss of oxygen from the surface.

By the Au 4f and the O 1s spectra, the resulting lateral size and thickness of the formed hexagonal islands, depending on the reduction procedure, can be confirmed, too. The Au 4f signal intensity of the formed gold islands after chemical reduction is higher than the Au 4f signal intensity of the thicker gold islands that are formed after thermal reduction (*cf. figure*

5.2.2-1f). Also the O 1s signal is lower for the chemically reduced surface than the O 1s signal after thermal reduction (cf. figure 5.2.2-1g). With a desorption temperature of  $> 1200$  K for Au from the Ru(0001) surface<sup>[165,186]</sup>, it is excluded that Au desorbed from the surface during both reduction experiments. Instead the lower Au 4f signals for the thermally reduced surface are explained by the thickness of the resulting Au islands (cf. figure 5.2.2-1f, orange curve c). After chemical reduction, the formed Au islands are as thick as freshly prepared Au islands on the (2x1)O precovered Ru(0001) surface. The Au 4f signal intensities for these two surfaces are equal, i.e. the same amount of gold is detected by XPS.

The difference in gold islands thickness after reduction can be explained by the oxygen overlayer on Ru(0001) surrounding the Au oxide/Au nanoparticles. By comparing the O 1s signals, the influence of CO on the removal of oxygen from the surface during the reduction process becomes evident. The reduction of the surface with 100 L CO at 670 K does not only lead to the reduction of the nanoparticles. It is assumed that the oxygen overlayer is reduced at these conditions (cf. figure 5.2.2-1g, green curve b), thus giving the reduced gold atoms more space to rewet the ruthenium surface with no oxygen bound at the interface. The adsorbed CO also increases the mobility of the gold atoms on the surface during the reduction process, thus further facilitating the rewetting behavior on the ruthenium surface.<sup>[199]</sup>

However this does not happen by the thermal reduction at 670 K because the temperature is too low to desorb oxygen from the Ru(0001) surface.<sup>15</sup> Therefore the oxygen stays in the compressed (1x1)O or (2x2)3O overlayer structures, thus giving the gold atoms less space to rewet the surface, which leads to more three-dimensional gold islands on the surface.

The effect of the oxygen overlayer on the rewetting behavior of the reduced Au nanoparticles becomes even more evident by comparing the islands morphology (i.e. the island thickness and its lateral expansion after the reduction) to the as-prepared Au islands on the (2x1)O and (1x1)O precovered Ru(0001) surface (cf. chapter 5.1.1), respectively. The height and the lateral expansion of the Au islands after thermal reduction is similar to gold islands prepared on the Ru(0001)-(1x1)O surface. This also indicates a dense (1x1)O overlayer on the ruthenium surface after the thermal reduction. In the case of the chemical reduction, the morphology of the formed Au islands is similar to the morphology of as-prepared Au islands on the Ru(0001)-(2x1)O surface. This comparison also supports a reduction of the oxygen overlayer by CO during the chemical reduction process.

---

<sup>15</sup> Desorption of chemisorbed oxygen from the Ru(0001) starts above 1100 K.[185]

### 5.3 Thickness dependent oxidation of gold islands

Upon oxidation at room temperature, the former flat thin gold islands are fragmented into Au oxide/Au nanoparticles. Depending on the gold island thickness, the size of the formed particles as well as the degree of the fragmentation changes significantly, which is summarized in the following series of STM pictures (*cf. figure 5.3-1*). To study this thickness depending oxidation, very thin gold islands with a thickness of 2 and 3 layers as well as thicker gold islands with a thickness of  $\geq 4$  layers were prepared. These gold islands were all oxidized using the same conditions, i.e. 40 L atomic oxygen at room temperature. As previously described, the thickness of gold islands can be controlled by the applied temperature and the precoverage of the chemisorbed oxygen layer.

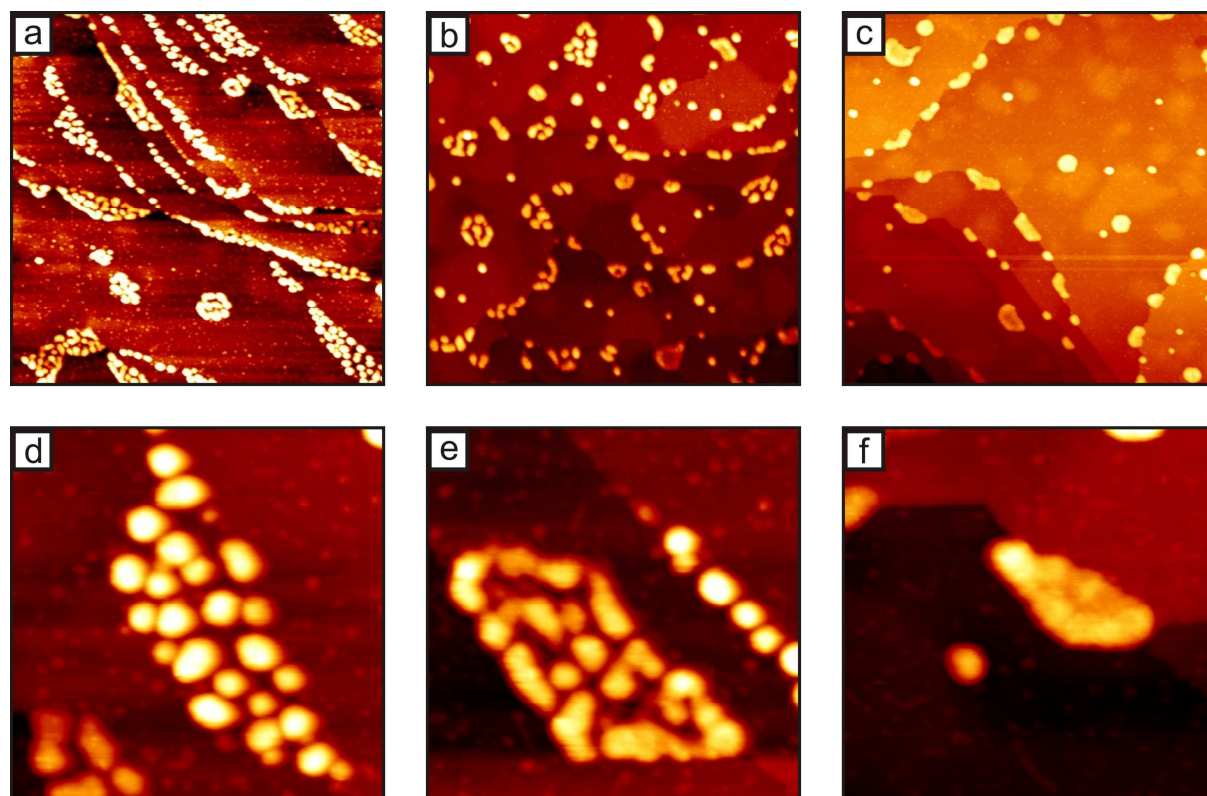


**Figure 5.3-1:** Gold islands were formed on a  $(2 \times 1)\text{O-Ru}(0001)$  surface at different temperatures to regulate their thickness. The STM images (a), (b), (c) illustrate a section of  $300 \text{ nm} \times 300 \text{ nm}$ . The magnifications (d), (e), (f) are in the range of  $60 \text{ nm} \times 60 \text{ nm}$ . (a) Two layered gold islands after exposure of 40 L atomic oxygen at room temperature, (b) three layered gold islands after exposure of 40 L atomic oxygen at room temperature, (c) four or five layered gold islands after exposure of 40 L atomic oxygen at room temperature. (d),(e),(f) Magnification of a former two, three or four layered gold island that is oxidized by 40 L  $\text{O}'$ , respectively. Tunneling conditions:  $U = 1.1 - 1.2 \text{ V}$ ,  $I = 1.0 \text{ nA}$ .

From this series of STM images, the following conclusion is drawn:

**With increasing thickness of the former gold island the number of fragmented gold oxide nanoparticles decreases while their lateral size increases.**

The STM images show the thickness depending oxidation behavior of the gold islands (*cf. figure 5.3-1a-c*). The corresponding magnifications of the respective oxidized surfaces elucidate these thickness dependent morphologic changes (*cf. figure 5.3-1d-f*). After dosage of 40 L atomic oxygen to two layered gold islands (*cf. figure 5.3-1d*) nanoparticles are formed that are completely separated from each other. The oxidation of three layered gold islands (*cf. figure 5.3-1e*) leads to particles that are still connected to each other. For even thicker gold islands ( $\geq$  four layers) the exposure of 40 L atomic oxygen is insufficient to either form a single gold particle, or to fragment the gold island into a network of connected nanoparticles (*cf. figure 5.3-1f*).

Although the resulting morphology is different, it should be noted that further oxidation of the three or four layered islands also leads to separated nanoparticles but with larger size. Therefore not only the size and the amount of the formed nanoparticles depend on the former island thickness, the rate of the Au oxide/Au nanoparticles formation is also thickness dependent.

The corresponding Au 4f XPS data indicate that these bigger particles also consist of Au oxide and metallic Au (not shown due to its similarity to the previously shown spectra in *figure 5.2.1-1f*)<sup>16</sup>. In principle, with high resolution XPS measurements of the oxidized Au nanoparticles it would be possible to determine the amount of the formed Au oxide, depending on the Au nanoparticle size. Also further deconvolution of the Au 4f signals would be desirable to determine the influence of the final state effects on the one hand and to distinguish between the different gold-oxygen species in the fragmented Au nanoparticles on the other hand. However this quantitative evaluation of the amount of formed Au oxide was beyond the scope of this work.

In the following a more detailed description of the oxidation of three layered and four layered gold islands will be presented. Especially the morphologic changes during the oxidation process will be elucidated by stepwise increasing the amount of atomic oxygen at room temperature.

---

<sup>16</sup> The XPS data is not shown, because the Au 4f spectra look similar to the previously presented data from figure 5.2.1-1e.

### 5.3.1 Incremental oxidation of three layered gold islands

Successive exposures of atomic oxygen (5 L, 10 L, 20 L, 40 L, 80 L, 150 L, and 250 L) were introduced to three layered gold islands at room temperature. With *ex-situ* STM measurements a deeper understanding of the processes at the atomic level during the oxidation were gained (*cf. figure 5.3.1-1*).

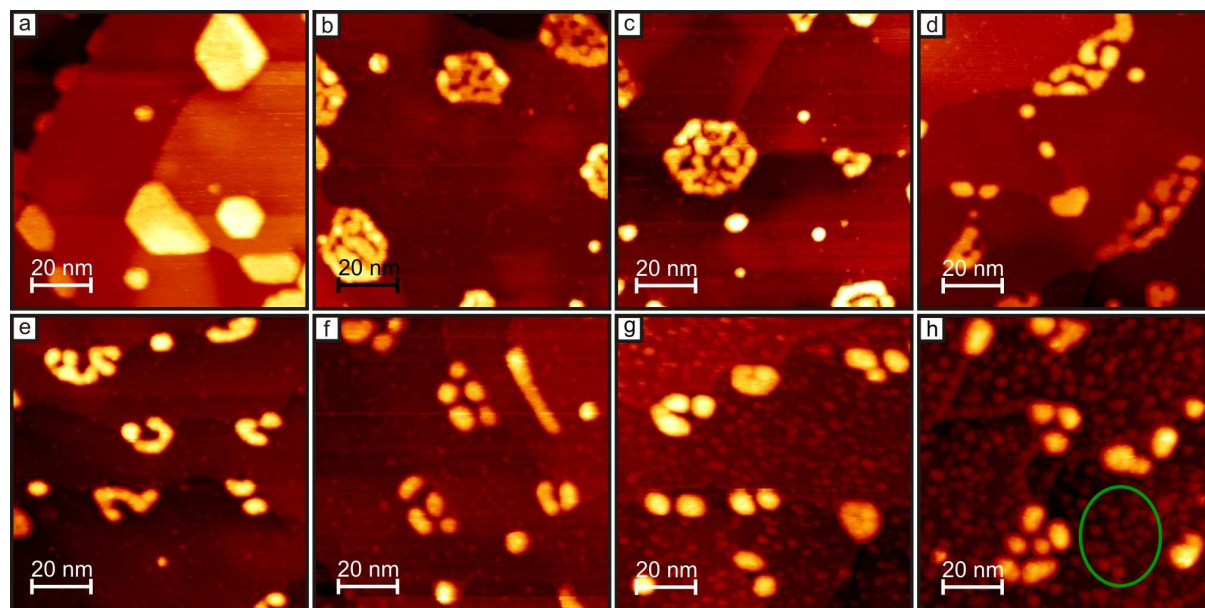


**Figure 5.3.1-1:** All STM images illustrate a surface area of 100 nm x 100 nm. (a) 0.5 ML Au deposited at 700 K on the (2x1)O precovered Ru(0001) surface. (b) 5, (c) 10, (d) 20, (e) 40, (f) 80, (g) 150, and (h) 250 langmuirs of O' dosed to the three layered gold islands, respectively. Until 80 L of O' only oxidation and fragmentation of the gold islands is visible (b–f). At higher dosages of atomic oxygen (g, h) the morphology of the fragmented Au nanoparticles does not change furthermore. Instead the oxidation of the Ru(0001) substrate is more pronounced (highlighted in h). Tunneling conditions:  $U = 1.1 - 1.2$  V,  $I = 0.7 - 1.0$  nA.

Compared to the oxidation of a two layered gold island (*cf. figure 5.3-1a,d*, page 82), this series of STM images evidences that higher exposures of atomic oxygen are necessary to form separated Au oxide/Au nanoparticles from a former three layered gold island. Between total exposures of 40 to 80 L O' the fragmentation of most of the three layered gold islands into separated nanoparticles is complete (*cf. figure 5.3.1-1e* and *5.3.1-1f*). A closer inspection of the STM images reveals the simultaneous oxidation of the gold islands from on-top and at their sides: The oxidation at the side is visible by the continuous loss of the hexagonal shape of the gold islands (*cf. figure 5.3.1-1d,e*), while the oxidation from the top is visible by the formation of cracks and holes in the gold island (*cf. figure 5.3.1-1b-d*). These cracks are enlarged at higher dosages of atomic oxygen leading first to a network of connected nanoparticles (*cf. figure 5.3.1-1d,e*), followed by the complete separation of the nanoparticles

(*cf. figure 5.3.1-1f*). Between an exposure of 100 L and 250 L atomic oxygen (*cf. figure 5.3.1-1g* and *5.3.1-1h*, respectively), the size of the separated nanoparticles does not change furthermore. This leads to the suggestion that the oxidation of gold is saturated. By assuming a core shell structure for the oxidized gold nanoparticles, the formation of the covering  $\text{Au}_2\text{O}_3$  shell inhibits further oxidation of the gold core due to the lack of exposed metallic gold atoms to the atomic oxygen. At dosages of 80 L atomic oxygen the oxidation of the ruthenium surface becomes noticeable by the formation of small ruthenium oxide nanoparticles on the terraces (*cf. figure 5.3.1-1f*). At higher dosages of atomic oxygen (150 L to 250 L) the oxidation of the Ru(0001) terraces is now favored (*cf. figure 5.3.1-1g,h*). For comparison: to form similar concentrations of these small  $\text{RuO}_x$  clusters on the bare Ru(0001) surface, significant lower amount of atomic oxygen are needed, i.e. 10 L  $\text{O}^\cdot$  to 20 L  $\text{O}^\cdot$ .<sup>[197,200]</sup> This observation confirms the interpretation that most of the dosed atomic oxygen first oxidizes the gold islands ( $< 80 \text{ L O}^\cdot$ ). The oxidation of the Ru(0001) surface starts after most of the covering gold oxide shell is already formed, thus leaving decreasingly amounts of metallic gold atoms left on the surface for the oxidation. Therefore the oxidation of the gold islands and the fragmentation into nanoparticles depends on the availability of metallic gold atoms, which itself strongly depends on the degree of fragmentation and the size of the formed oxidized gold nanoparticles.

### 5.3.2 Incremental oxidation of four layered gold islands

To further elucidate the thickness dependent oxidation, thicker gold islands ( $\geq 4$  layers) were exposed to successive amounts of atomic oxygen (5 L, 10 L, 20 L, 40 L, 80 L, 150 L, and 250 L) at room temperature. STM measurements were performed to monitor the morphologic changes of four layered gold islands due to their oxidation (*cf. figure 5.3.2-1*).

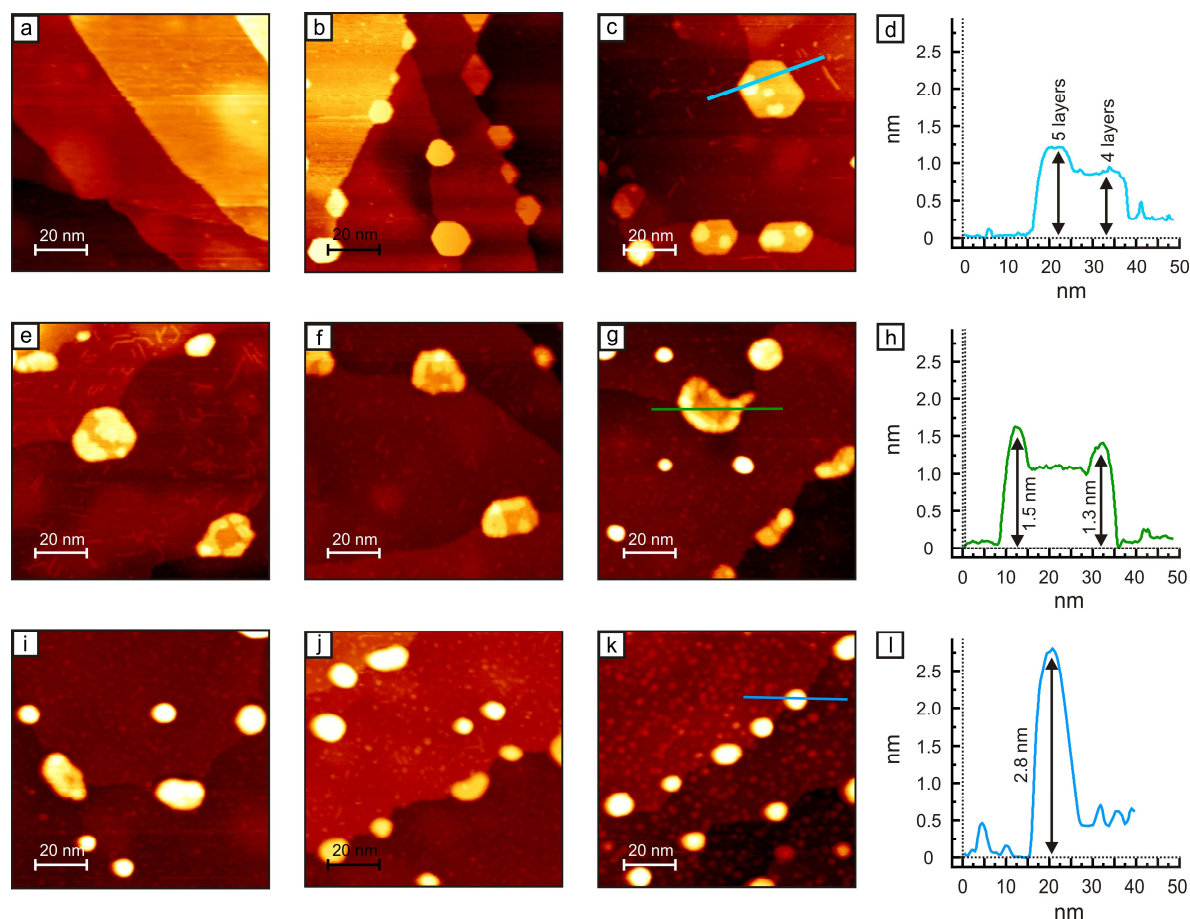


**Figure 5.3.2-1:** A series of STM images (100 nm x 100 nm) displays the oxidation of four layered gold islands at room temperature by increasing amounts of atomic oxygen: (a) clean Ru(0001)-(2x1)O surface; (b) 0.4 ML of Au deposited at 800 K; (c) 5 L, (e) 10 L, (f) 20 L, (g) 40 L, (i) 80 L, (j) 150 L, and (k) 250 L of atomic oxygen. During oxidation no fragmentation into several nanoparticles was observed, instead the transformation of single gold islands into one bigger nanoparticle occurred at higher dosages of atomic oxygen (j, k, l) simultaneous to the oxidation of the Ru(0001) substrate. From the line scans (d, h) the shoveling of Au atoms to the rim of the islands during the oxidation becomes evident. Tunneling conditions:  $U = 1.1 - 1.2$  V,  $I = 0.8 - 1.0$  nA.

From this series of STM images the differences between the oxidation of thinner gold islands (*cf. three layered gold islands, figure 5.3.1-1*) and these thicker gold islands (*cf. figure 5.3.2-1*) becomes evident. To form separated gold oxide nanoparticles, approximately 80 to 150 L O<sup>•</sup> of atomic oxygen is needed (*cf. figure 5.3.2-1i and 5.3.2-1j*). Therefore more atomic

oxygen is necessary to form separated nanoparticles, compared to the oxidation of three layered gold islands.

The oxidation process of the four layered gold islands is different from the oxidation of the three layered gold islands: Neither the formation of deep cracks and holes nor a fragmentation of the island into many nanoparticles is observable (*cf. figure 5.3.2-1e-g*). Instead the four layered gold islands already lost their hexagonal shape after exposure of 40 L atomic oxygen (*cf. figure 5.3.2-1e-g*). STM images and corresponding line scans illustrate that most of the oxidized gold is shoveled to the top of the Au island (*cf. figure 5.3.2-1c,d,e*). With ongoing oxidation (20 L to 40 L O<sup>•</sup>), the shoveled gold atoms agglomerate at the rim of the island, thus leading to the shape of a volcano-like island structures (*cf. figure 5.3.2-1g and 5.3.2-1h*). At even higher exposures of atomic oxygen (80 – 150 L O<sup>•</sup>) very few but big gold nanoparticles are formed (*cf. figure 5.3.2-1i*). The four layered islands are directly transformed into single big nanoparticles, because no fragmentation of the gold island occurs. Again the oxidation of the ruthenium surface starts at higher exposures of atomic oxygen ( $\geq 150$  L O<sup>•</sup>) (*cf. figure 5.3.2-1i-k*), after most of the gold islands are already oxidized and transformed into nanoparticles.

### 5.3.3 Statistic evaluation of the gold nanoparticle height

By line scan analysis in the STM images, the heights of the fragmented three and four layered gold islands are obtained and presented in the following histograms (*cf. figure 5.3.3-1*).

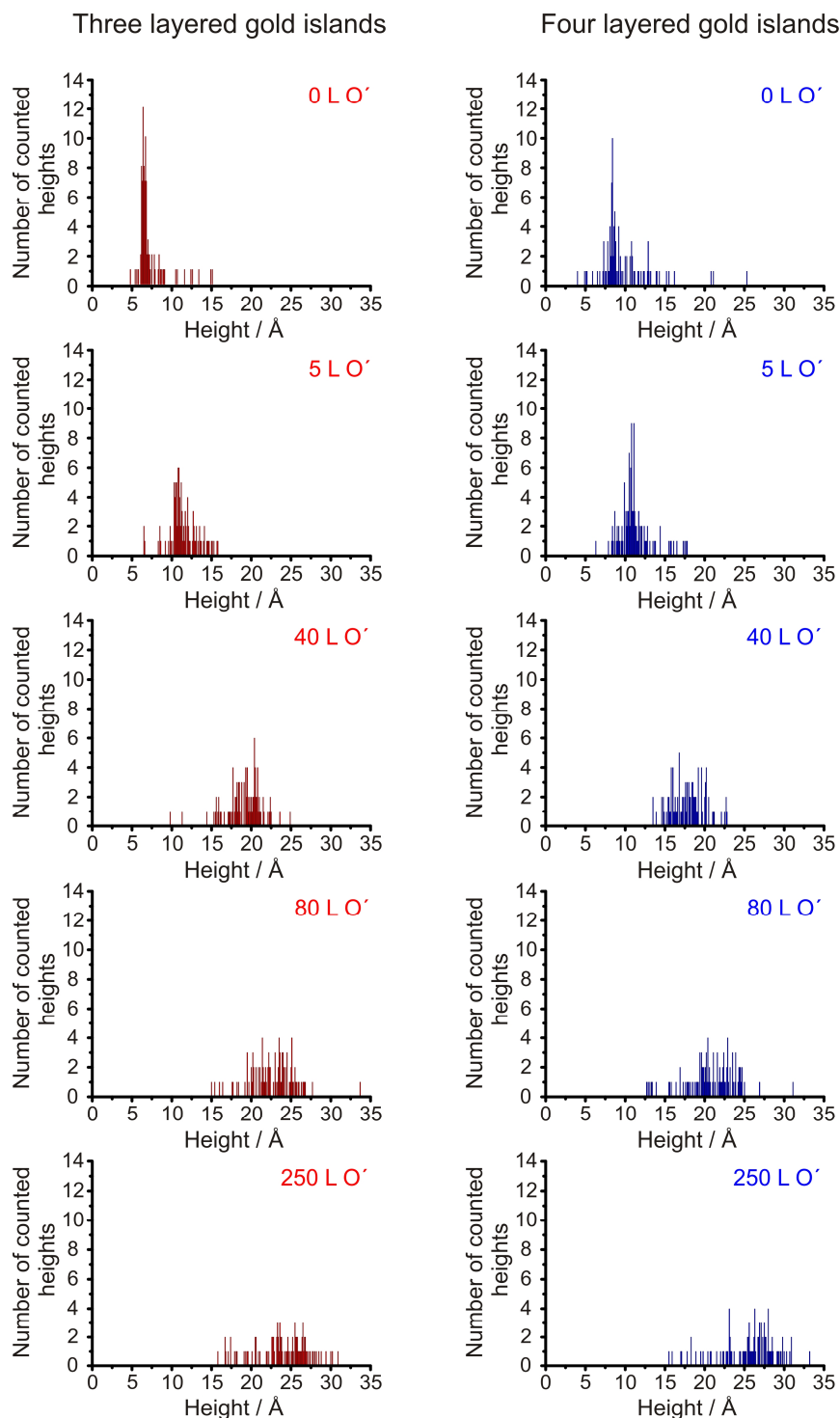


**Figure 5.3.3-1:** Statistics of the gold nanoparticle thickness evolution with increasing exposures of atomic oxygen. Starting from three layered gold islands (red distributions, left) or four layered gold islands (blue distributions, right), the height of the formed gold nanoparticles increases steadily with increasing dosages of atomic oxygen. In both cases, saturation at around 2.6 nm is obtained after exposure of 250 L atomic oxygen.

Starting from a very narrow height distribution for the three ( $\sim 6.3 \text{ \AA}$ ) and the four layered gold islands ( $\sim 8.4 \text{ \AA}$ ), the thickness of the resulting separated gold nanoparticles is significantly higher. Although the thickness of the gold islands was different, the height of the formed nanoparticles is similar. After a total exposure of 250 L atomic oxygen, the thickness of the formed gold particles saturates around  $25 \text{ \AA}$  with a relative broad height distribution of  $\pm 5 \text{ \AA}$ . It should be mentioned that, although the nanoparticle height is similar for an oxidized three layered or four layered gold islands, the amount of formed nanoparticles and their lateral size differ significantly. A three layered gold island is fragmented into more gold nanoparticles that are smaller than the nanoparticle formed by oxidation of a four layered gold island. They are either fragmented into very few bigger nanoparticles or completely transformed into one single big nanoparticle. As a result, the oxidation of the three layered gold islands leads to a higher surface to volume ratio of gold on the surface than the oxidation of four layered gold islands.

### 5.3.4 Oxidation of thick Au islands grown on RuO<sub>2</sub>(110)

While thinner gold islands are fragmented into nanoparticles upon exposure of atomic oxygen, thicker gold islands (> 5 layers) are either transformed into only a single oxidized gold nanoparticle or seem to stay mainly unaffected. A good example is the oxidation of the hexagonal or the cuboid islands deposited on RuO<sub>2</sub>, which are 7-12 or 11-22 layers thick, respectively (*cf. figure 5.3.4-1*). For oxidation of these thick islands, 40 L of atomic oxygen were dosed at room temperature.

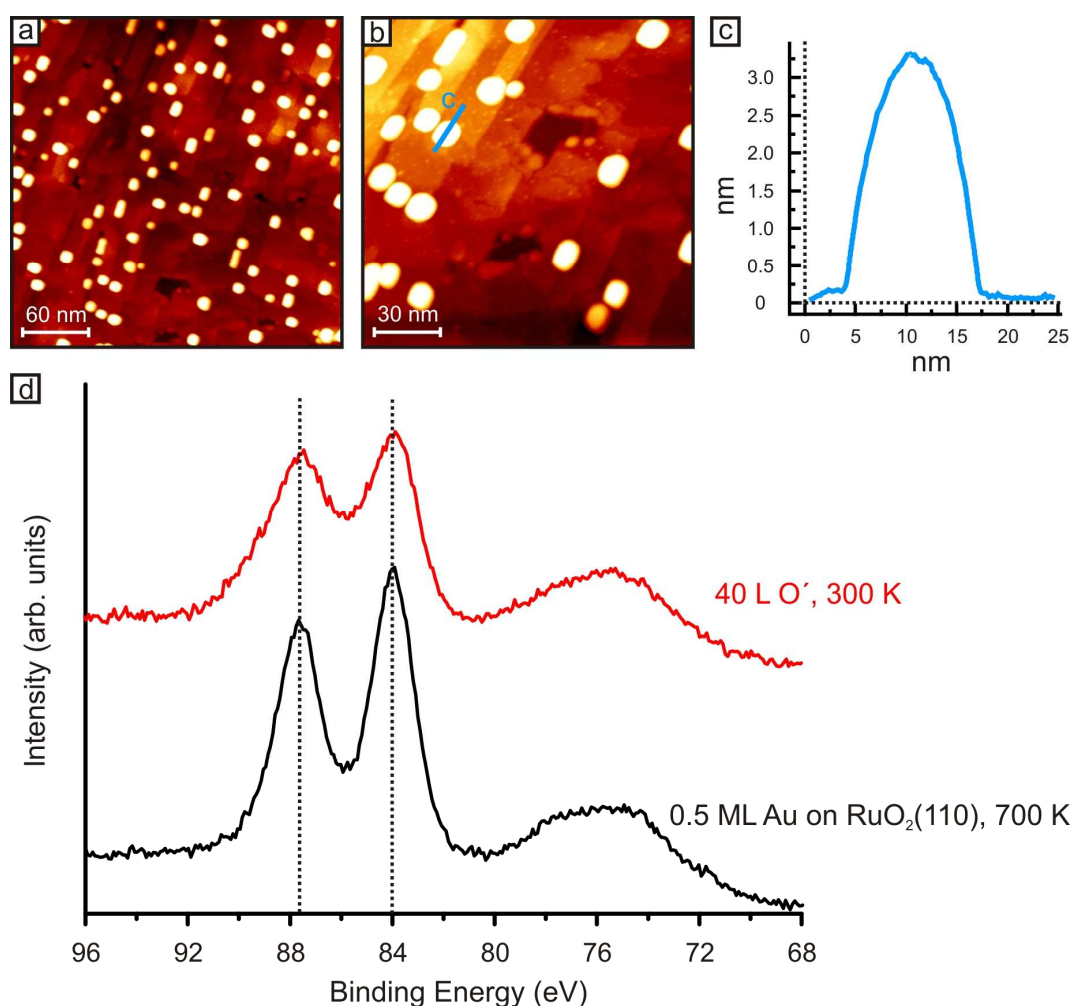


**Figure 5.3.4-1:** Oxidation of 0.5 ML gold deposited on RuO<sub>2</sub>(110) by dosing 40 L O' at room temperature. STM image area range: (a) 300 nm x 300 nm, (b) 150 nm x 150 nm. The former hexagonal islands are now round-shaped, while the cuboid islands are still recognizable. Only their corners are slightly rounded. (c) The line scan illustrates the shape of the oxidized gold island. (d) XPS data of the Au 4f signal area shows the partial oxidation of the gold islands, i.e. gold oxide signals evolving at higher binding energies while the Au 4f signals for metallic gold decreases. Tunneling conditions:  $U = 1.1$  V,  $I = 1.0$  nA.

The STM images show round-shaped islands that are equally distributed over the RuO<sub>2</sub>(110) surface after the exposure of 40 L atomic oxygen (*cf. figure 5.3.4-1a,b*). No fragmentation of

any of these thicker islands is observed on the surface. While the former hexagonal islands lost their former shape, the cuboid islands can still be recognized by their overall shape. Only a slight chamfer of the cuboid island corners is visible (*cf. figure 5.3.4-1b*). From STM, no reaction of the underlying RuO<sub>2</sub>(110) film with the exposed atomic oxygen has been observed. The partial oxidation the hexagonal and cuboid gold islands is confirmed by XPS (*cf. figure 5.3.4-1c*). The Au 4f signals for oxidized gold (e.g. Au<sub>2</sub>O<sub>3</sub>) located at higher binding energies are visible as well as the decrease of the metallic gold signal intensity at 84.0 eV and 87.7 eV, respectively.

Evidently the oxidation of the hexagonal gold islands occurs mainly at the corners of the islands and therefore at the island sides. From the fast formation of roundly shaped islands, it is assumed that the oxidized mobile gold atoms are not exclusively shoveled to the top of the islands. With island heights up to 5 nm, the island sides are considered as larger facets of gold, i.e. a different crystallographic orientation of gold. With increasing height of the gold islands, it is possible that the mobile gold atoms also start to agglomerate at the island sides, thus facilitating the rounding of the gold islands. A line scan of an oxidized gold island shows droplet like form, which confirms the shoveling of gold atoms to the top of the former metallic gold island. However the height of approximately 3.5 nm reveals only a rather small increase of height due to the agglomeration of gold atoms on-top of the island. For comparison: the four layered gold island thickness increased from 8.4 Å to about 17 Å after exposure of 40 L atomic oxygen, thus evidently showing the shoveling of gold atoms to the top of the gold island. In case of the already very thick gold islands (*cf. figure 5.1.3-3*, page 72) on RuO<sub>2</sub>, this increase in height is significantly lower than one would expect if all the oxidized gold atoms are transported to the top side of the gold island, too. Therefore it is assumed that either these thicker gold islands on RuO<sub>2</sub>(110) are significantly less oxidized by the 40 L O<sub>2</sub>, or the oxidized atoms do not exclusively agglomerate on the top of the island. An agglomeration of the oxidized and mobile gold atoms at the island sides may also be possible.

## 5.4 Oxidation of gold films

### 5.4.1 Oxidation of thin gold films by atomic oxygen

After the investigation of the thickness dependent oxidation of thin gold islands grown on the Ru(0001) surface, one major question is still not elucidated: Is the ruthenium substrate involved in the gold oxidation and island fragmentation process? To deal with this particular question, thin and wetting films of gold were prepared on the oxygen free Ru(0001) surface. By covering the complete Ru(0001) surface, the exposure of atomic oxygen at room temperature can solely oxidize the gold film, i.e. the direct influence of the Ru(0001) substrate on the oxidation and fragmentation process is excluded. However, the influence of the underlying ruthenium substrate on the chemical properties and the electronic structure of the thin gold films (or islands) remain elusive.

The oxidation of the thin gold films was carried out at room temperature by the exposure of atomic oxygen, which has been produced from a thermal gas cracker. *Figure 5.4.1-1* shows Au 4f spectra and STM images of the oxidation of a 2 ML gold film<sup>17</sup> by 40 L O<sup>•</sup>.

As described previously, the deposition of gold on oxygen free Ru(0001) at 700 K leads to the formation of wetting films of gold on the ruthenium surface. However these covering films exhibit several holes, thus exposing still some of the underlying Ru(0001) surface (*cf. figure 5.4.1-1c*). This is explained by residual oxygen, which could not be removed during the cleaning process of the Ru(0001) single crystal surface. Although the gold film is not completely covering, the two-dimensional growth of gold on this oxygen free Ru(0001) surface is evident. By the holes in the gold film, the final height of the grown gold layer could be confirmed by STM line scan analysis. The morphology of the covering 2 ML thick gold film changes to separate gold nanoparticles (*cf. figure 5.4.1-1d*) after the exposure of 40 L O<sup>•</sup>. The oxidation of the gold film is monitored by XPS (*cf. figure 5.4.1-1a*). By STM the former holes in the gold film are still recognizable after the oxidation and the fragmentation process.

---

<sup>17</sup> The preparation of gold films and its morphology on ruthenium has previously been described in chapter 5.1.2 (cf. page 67ff).

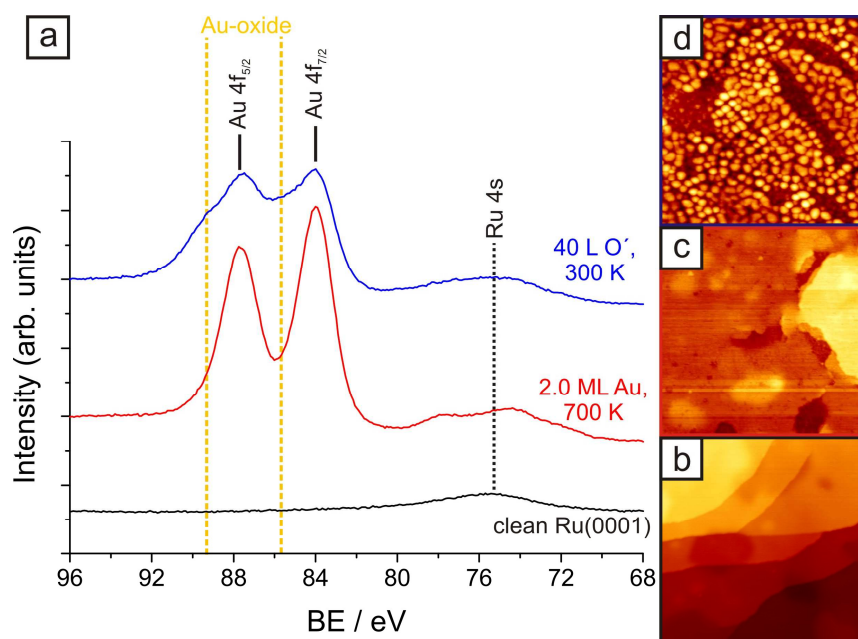


**Figure 5.4.1-1:** XPS data of the Au 4f region (a) and the series of STM images ((b),(c),(d): 150 nm x 150 nm) evidently show the oxidation of the 2 ML thin gold film by the dosed atomic oxygen at room temperature. Similar to the oxidation of thin gold islands, the exposure of atomic oxygen, the morphology of the covering gold film changes to separated oxidized gold nanoparticles. (b) The clean and oxygen free Ru(0001) surface; (c) Covering 2 ML thin gold film formed at 700 K; (d) Oxidation of the gold film by exposure of 40 L O' at room temperature. Tunneling conditions:  $U = 0.7 - 1.0$  V,  $I = 0.1 - 1.0$  nA.

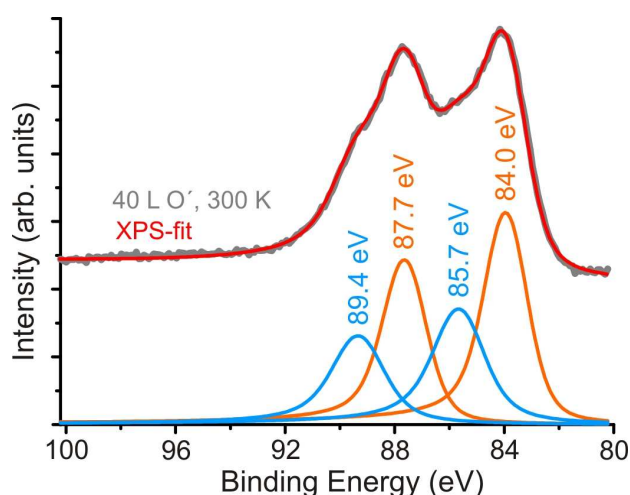


**Figure 5.4.1-2:** Peak deconvolution of the Au 4f region to display the formation of gold oxide due to the fragmentation process of a 2 ML gold film that was exposed to 40 L O' at room temperature. The red XPS-fit nicely matches to the XPS data of the Au 4f region. The Au 4f signals shifted by 1.7 eV to higher binding energies are assigned to gold oxide species (e.g. Au<sub>2</sub>O<sub>3</sub>). Therefore the formed nanoparticles evidently consist of metallic gold as well as oxidized gold.

The peak deconvolution of the Au 4f signals evidently illustrates the oxidation of the gold film (cf. figure 5.4.1-2). Shifted by ~ 1.7 eV to higher binding energies, the evolving Au 4f

signals (*cf. figure 5.4.1-2*, light blue signals) are assigned to oxidized gold ( $\text{Au}_2\text{O}_3$ ). Simultaneously the Au 4f signals for metallic gold are decreasing (*cf. figure 5.4.1-1a*).

The deconvoluted Au 4f XPS signals indicate that these nanoparticles have a similar structure and morphology as the previously described gold nanoparticles that are formed by the oxidation of thin gold islands. Also the fragmentation process and the morphology of the formed separated gold nanoparticles are similar to the nanoparticles formed by oxidation of equally thin (2 ML) gold islands. Due to these similarities the fragmentation process is thought to be independent on the lateral size of the gold island or the amount of the exposed Ru(0001) surface.

Thermal reduction of the gold nanoparticles was performed by annealing the fragmented gold film to 700 K for 15 min (*cf. figure 5.4.1-3*). XPS measurements (not shown) reveal the increase of the metallic gold signals, while the signals for gold oxide (Au 4f<sub>7/2</sub> at 85.7 eV and 89.4 eV) disappear. STM images show that no complete wetting gold film on ruthenium is formed during this thermal reduction. Instead many hexagonal gold islands are distributed over the surface (*cf. figure 5.4.1-3*). This island formation is assumed to be induced by a formed oxygen overlayer on the Ru(0001) surface. During oxidation most of the ruthenium substrate stays covered by gold, even after the Au oxide/Au nanoparticle formation (*cf. figure 5.4.1-1d*). So where does the oxygen for the overlayer on Ru(0001) come from?

During this thermal reduction at 700 K, the gold atoms are mobile on the ruthenium surface. By annealing the fragmented nanoparticles to 700 K the gold oxide decomposes, thus releasing the oxygen. The oxygen atoms can either diffuse and bind to the ruthenium substrate or recombine and desorb as molecular oxygen from the gold. Cuenya et al. suggested an oxygen spillover mechanism from oxidized gold nanoparticles to the underlying, partially reduced  $\text{TiO}_2$  substrate surface as a possible decomposition pathway.<sup>[32]</sup> With the strong oxygen-ruthenium binding as a driving force, the thermal reduction of the gold oxide nanoparticles on Ru(0001) is assumed to proceed by a similar oxygen spillover process. TDS experiments of different oxidized gold surfaces further support this suggestion: As already presented in table 1.2-1 the decomposition of gold oxides occurs at lower temperatures than desorption of chemisorbed oxygen from gold (*cf. chapter 1.2*).<sup>[68,69]</sup> Even if some oxygen immediately desorbs during the decomposition process, it is assumed that most of the oxygen atoms diffuse to the ruthenium surface where they form a strongly bound chemisorbed oxygen species. As previously described, the metallic gold does not tend to bind to the oxygen covered Ru(0001) surface. Therefore the increasing amounts of chemisorbed oxygen on Ru(0001) leave less space for the metallic gold to rewet the surface. As a consequence

thick hexagonal gold islands (6 to 9 layers) are formed besides a compressed oxygen overlayer on Ru(0001).

The applied temperature of 700 K during this thermal reduction process excludes the desorption of gold from the Ru(0001) surface, which occur at temperatures above 1200 K.<sup>[165,186]</sup> Therefore the former 2 ML gold film has been completely rearranged to these thick hexagonal gold islands by this reduction procedure. To reform a wetting gold film on ruthenium it is necessary to remove the oxygen overlayer. This could be achieved by reduction at higher temperatures in a reductive atmosphere (i.e. CO or H<sub>2</sub>).

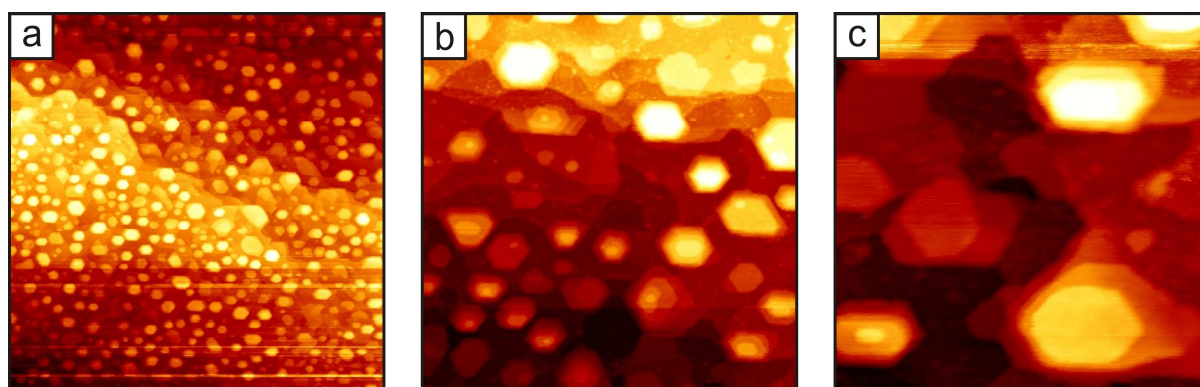


**Figure 5.4.1-3:** The STM images ((a) 300 nm x 300 nm, (b) 140 nm x 140 nm, (c) 60 nm x 60 nm) show the thermal reduction of the oxidized gold nanoparticles, which was accomplished by annealing the surface to 700 K in vacuum for 15 min. The gold is reduced and rearranged into broad and thick Au islands (6 to 9 ML). Thick thickness of the gold islands is significantly higher than the thickness of the former gold film (2 ML). Because the annealing temperature of 700 K is much lower than the desorption temperature of gold from ruthenium it is assumed that the gold from the nanoparticles is completely transformed to the hexagonal islands. An oxygen spillover process from the decomposing gold oxide to the ruthenium surface is suggested, which form an oxygen overlayer on the Ru(0001) surface to whom the metallic gold less tends to bind. Instead of rewetting the ruthenium surface and forming a thin gold film, the gold coalescences to three-dimensional hexagonal islands. Tunneling conditions:  $U = 0.9 - 1.2$  V,  $I = 1.0$  nA.

## 5.4.2 Thickness dependent oxidation of gold films

Gold films with variable thickness were prepared on a oxygen free Ru(0001) surface, to further investigate their oxidation behavior. *Figure 5.4.2-1* shows a series of STM images of oxidized gold films depending on their former thickness after an exposure of 40 L atomic oxygen at room temperature.

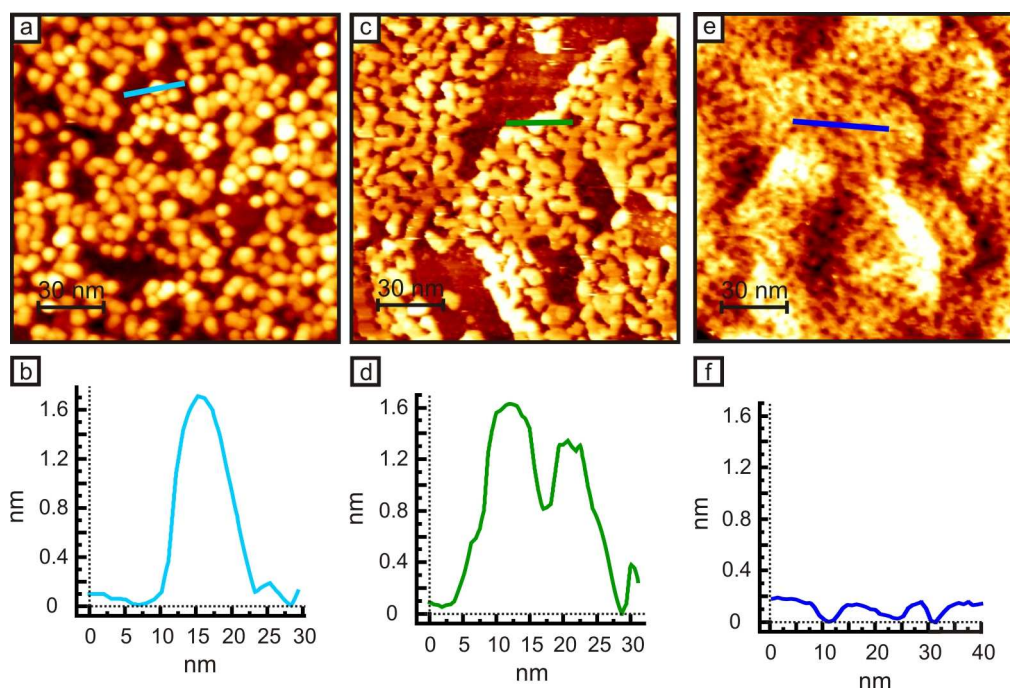


**Figure 5.4.2-1:** The STM images ( $150 \text{ nm} \times 150 \text{ nm}$ ) show the oxidation of gold films with different thickness after exposure of 40 L of atomic oxygen at 300 K. Similar to the oxidation of thin gold islands, the degree and the rate of fragmentation evidently depends on the former film thickness. For a 2 ML thick gold film the complete fragmentation into nanoparticles is visible ((a), (b)) while for a 3 ML thick gold film a network of connected particles is formed ((c), (d)). The oxidation of very thick gold islands (more than 100 layers thick) is similar to the Au(111) single crystal oxidation ((e), (f)). Tunneling conditions:  $U = 0.7 - 1.1 \text{ V}$ ,  $I = 0.2 - 1.0 \text{ nA}$ .

After the exposure of 40 L atomic oxygen to a two layered gold film (*cf. figure 5.4.2-1a*) at room temperature, separated nanoparticles are formed on the surface. In the case of a three layered gold film (*cf. figure 5.4.2-1c*) a network of connected nanoparticles is observed. The formation of separated gold nanoparticles and connected nanoparticles, due to fragmentation of a two layered and three layered gold films, respectively, is similar to the fragmentation of two and three layered gold islands. Not only are the oxidation mechanism of gold islands and films evidently the same (i.e. fragmentation and formation of small particles), in fact they show the same resulting progress in fragmentation depending on the former thickness of the metallic gold. The corresponding line scans confirm the similarities to

the oxidation of two and three layered gold islands with heights of about 17 Å after the dosage of 40 L O' (cf. figure 5.4.2-1b,d). This increase in height also indicates a shoveling process of released gold atoms to the top of the gold film. Moreover the oxidation and fragmentation of thin gold layers does not necessarily need rims or step edges. Evidently gold atoms can be released directly from the top gold layer, which leads to defect sites from whom the disruption of the gold film can proceed. The degree of fragmentation of the thin gold layers is assumed to depend on the number of such formed disrupting defect sites.

In figure 5.4.2-1e the oxidation of a very thick gold island (> 100 ML Au) is depicted. The oxidation shows the typical morphology that is observable after oxidation of a Au(111) single crystal surface.<sup>[36]</sup> For these thick Au layers, no fragmentation or particle formation occurs. Instead its surface starts to roughen by 2-3 Å (cf. figure 5.4.2-1f), which is consistent to the observed roughening of the Au(111) single crystal surface.<sup>[66]</sup>

## 5.5 Proposed mechanism for the fragmentation process of thin gold islands and films

The combined results of STM and XPS show the thickness dependent oxidation behavior of thin gold islands and films. During oxidation the gold islands fragment into nanoparticles that consist of metallic gold as well as gold oxide. As previously discussed, the formation of core-shell structures for these small nanoparticles is a possible interpretation based on the XPS data and similar interpretations in the literature for partially oxidized gold nanoparticles.<sup>[32,74]</sup> The formed gold nanoparticles, due to fragmentation of thin gold films or islands, are assumed to consist of a gold oxide shell covering the metallic core. After a completely wetting oxide shell is formed, no metallic gold is exposed to the gas phase and further oxidation by the atomic oxygen is inhibited. This is shown by the STM images where the morphology of the nanoparticles does not change further on, after a certain amount of atomic oxygen was dosed and the formation of separated nanoparticles was completed. Instead the oxidation of the ruthenium substrate is more and more favored and the Ru(0001) steps and terraces are decorated by small RuO<sub>x</sub> particles.

The STM experiments lead to the following general considerations: After an exposure of 40 L atomic oxygen at room temperature, a single *thin island* ( $\leq 3$  layers) is fragmented into several *oxidized gold nanoparticles*. In contrast, a single *thicker island* (4 layers), which contains the same amount of gold as the thinner island, is now transformed into only a *few nanoparticles* that are still connected to each other, but separate at higher dosages of atomic oxygen. Even thicker gold islands ( $\geq 5$  layers) are transformed into one single big gold nanoparticle. These nanoparticles are usually laterally larger and contain more gold than the nanoparticles formed after the fragmentation of thinner gold islands.

In the following an oxidation mechanism will be suggested to describe the thickness dependent fragmentation process. For this oxidation mechanism a mobile gold-oxygen species needs to be introduced. The existence of such a mobile AuO<sub>x</sub> precursor species is based on the literature of the Au(111) single crystal oxidation: During the oxidation of the Au(111) single crystal surface undercoordinated gold atoms are produced, leading to a roughening of the surface with ongoing oxidation.<sup>[32,38-40,51,58-61]</sup> Induced by atomic oxygen, single gold atoms are released from the gold surface to form a mobile AuO<sub>2</sub> species.<sup>[57,78]</sup> These AuO<sub>2</sub> species are determined to be the precursors, which form gold oxide structures with ongoing oxidation.<sup>[38,39,57]</sup>

Figure 5.5-1 shows a schematic illustration of the suggested thickness dependent oxidation mechanism of thin gold structures at room temperature.

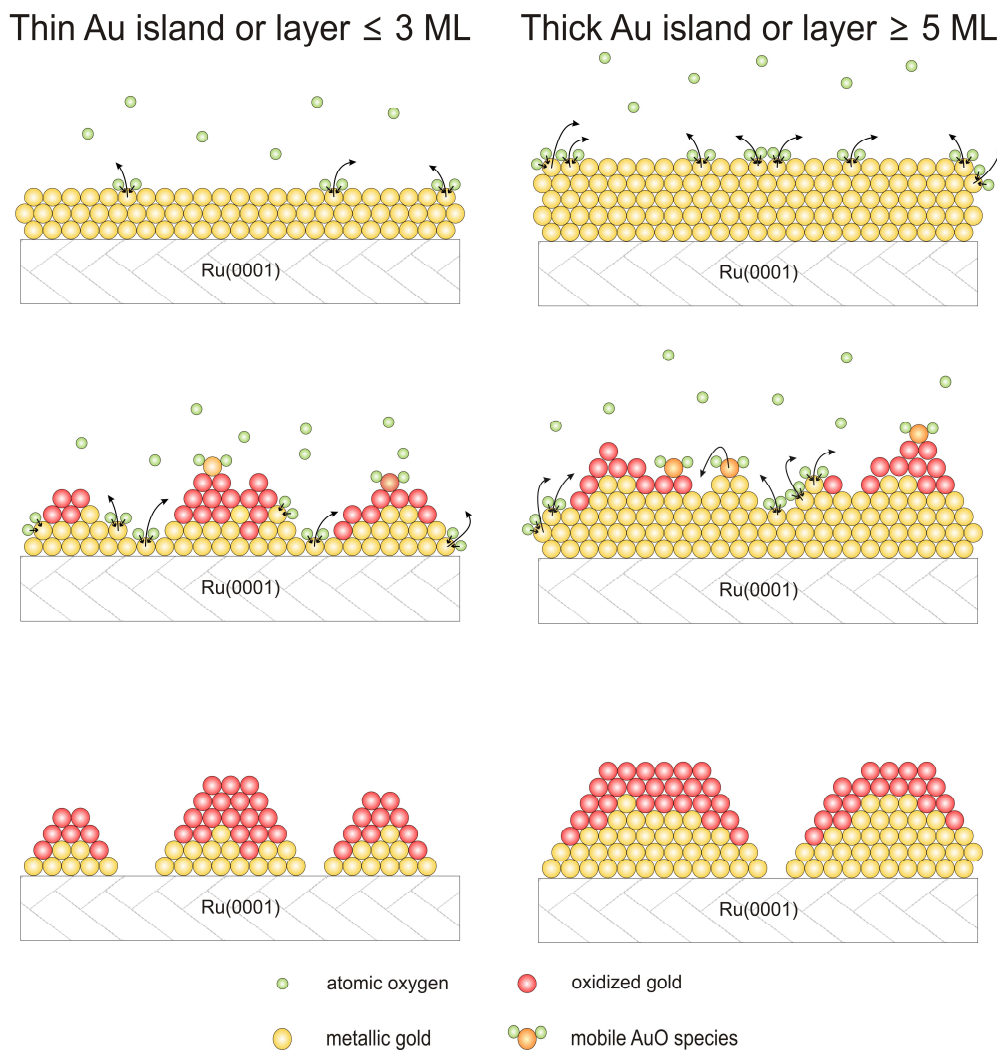


**Figure 5.5-1:** Schematic illustration of the proposed oxidation mechanism of thin gold islands (or films) by the exposure of atomic oxygen at room temperature via a shoveling process of mobile gold atoms. By adsorption of atomic oxygen at room temperature single gold atoms are released from the gold surface, thus forming a mobile  $\text{AuO}_x$  precursor species (here illustrated as  $\text{AuO}_2$ ). Several  $\text{AuO}_x$  precursors form a Au oxide, which covering metallic gold atoms. Because the mobile  $\text{AuO}_x$  precursors are assumed to be unstable on the Ru(0001) surface, oxidized gold atoms are expelled from the Au/Ru(0001) interface, which results in the fragmentation of the island. The degree of fragmentation for thin gold islands ( $\leq 3$  layers) is high because the formation of  $\text{AuO}_x$  precursors at the Au/Ru(0001) interface is more probable compared to thicker gold islands ( $> 4$  layers). With increasing thickness of the gold islands (or films) the probability of formed  $\text{AuO}_x$  precursors at the interface decreases, thus prohibiting the fragmentation.

At room temperature the atomic oxygen adsorbs on the thin gold islands. If two oxygen atoms bind to a single gold atom, the mobile  $\text{AuO}_2$  precursor species is formed and the gold atom can be released from the gold island. Generally undercoordinated gold atoms can be oxidized easier by atomic oxygen than highly coordinated gold atoms due to a higher reactivity. As a consequence the steps and defect sites of gold islands are preferentially attacked by the atomic

oxygen. By generating a defect in the flat terrace by releasing a single gold atom, additional  $\text{AuO}_x$  precursors are formed at these new defect sites by the highly reactive atomic oxygen.

These precursors are able to diffuse over the gold island surface due to its high mobility at room temperature. By a nucleation and growth process the mobile  $\text{AuO}_x$  precursors start to arrange themselves to a covering Au oxide on the metallic Au islands. In principle gold oxide could also bind to the Ru(0001) surface. But if the mobile  $\text{AuO}_x$  precursor stays on the ruthenium surface its stability is assumed to decrease dramatically. By comparing the weak Au-O binding and the strong Ru-O binding it is reasonable that the mobile  $\text{AuO}_x$  precursors should decompose rather easy on the metallic Ru(0001) surface. The instability of the  $\text{AuO}_x$  precursor on the Ru(0001) surface is assumed to be the reason for the fragmentation of the thin gold structures into oxidized gold nanoparticles. Starting from defect sites, the additional atomic oxygen induces the penetration into the island by shoveling the mobile precursors onto the upper layers of the metallic gold island (or film).

For thin gold structures the continuous shoveling of Au atoms leads to the formation of  $\text{AuO}_x$  precursors at the interface. An extreme example is the oxidation a single monolayer of gold on Ru(0001). By the exposure of atomic oxygen, the  $\text{AuO}_x$  precursors would be formed immediately at the interface. The amount of gold atoms that have to get oxidized and shoveled on top of the metallic gold islands, before  $\text{AuO}_x$  at the interface is formed, increases with increasing thickness of the gold structures. Therefore larger amounts of atomic oxygen are necessary to produce separated gold nanoparticles. This becomes evident by comparing the oxidation of two and three layered gold islands, where 40 L and 80 L  $\text{O}'$  are needed for the formation of completely separated nanoparticles, respectively. Besides the rate of fragmentation, the degree of fragmentation is also assumed to critically depend on the  $\text{AuO}_x$  formation probability at the interface. If many  $\text{AuO}_x$  precursors are formed during the oxidation the degree of fragmentation and the amount of the formed nanoparticles is higher, too. For thicker gold structures ( $\geq 5$  layers) the penetration into the gold layers is not sufficient to form  $\text{AuO}_x$  species at the interface. As a consequence the degree of fragmentation is much lower and larger particles are formed. In case of the oxidation of a thick gold island, its transformation into one big particle is more likely than a fragmentation into several smaller particles.

**So the amount of formed  $\text{AuO}_x$  precursors at the interface determines the degree of fragmentation of a single island and therefore the amount and the size of formed oxidized gold nanoparticles.**

## 5.6 Activity of the oxidized gold nanoparticles

### 5.6.1 Transient activity of the oxidized gold nanoparticles

To get a first impression about the activity of the formed gold nanoparticles, reduction experiments were performed with CO at room temperature. By these experiments a transient activity of the oxidized gold nanoparticles towards CO conversion is investigated. At first, oxidized gold nanoparticles were prepared by dosing 40 L atomic oxygen to a 2 ML thick gold film. These Au oxide/Au nanoparticles were reduced by dosing 100 L CO ( $p(\text{CO}) = 1 \cdot 10^{-7}$  mbar, 15 min) at room temperature. Usually the reduction experiments were conducted immediately after the formation of the oxidized gold nanoparticles due to the metastability of gold oxide. Chen et al. determined a half-life time of 22 hours for  $\text{Au}_2\text{O}_3$  at 22 °C in air. This slow decomposition over time is neglected for the reduction experiments by CO, which were conducted at a much shorter timescale (15 minutes).

*Figure 5.6.1-1* illustrates the reduction of the formed oxidized gold nanoparticles by the respective XPS measurements. After exposure of 100 L CO at room temperature (1<sup>st</sup> cycle) the Au 4f signals for metallic gold increase while the Au 4f gold oxide signals decrease significantly (*cf. figure 5.6.1-1*, red curve). After this reduction, a reoxidation was performed by again dosing 40 L O' to the surface (XPS spectra analogous to *figure 5.4.1-1* and therefore not presented here). Afterwards a second reduction by 100 L CO at room temperature was conducted (2<sup>nd</sup> cycle) (*cf. figure 5.6.1-1*, blue curve). This reoxidation and reduction of the gold nanoparticles is nicely observable on the basis of the shifted Au 4f signals (at 85.6 eV and 89.2 eV), which increase after treatment with atomic oxygen and decrease after exposure of CO, respectively. However the Au 4f signals after the second oxidation-reduction cycle (*cf. figure 5.6.1-1*, blue curve) differ from the Au 4f signals that were measured after the first reduction (*cf. figure 5.6.1-1*, red curve). This decrease of the total Au 4f signal intensity, with continuing oxidation and reduction cycles, can be explained by an increase of the nanoparticle thickness.

The peak deconvolution of the Au 4f signals reveals that the reduced nanoparticles may still consist of some gold oxide (signals at 85.6 eV and 89.2 eV in inlet, *cf. figure 5.6.1-1*). From literature it is known that CO reduces only the outer part of thicker gold oxide shells at room temperature, thus leaving the deeper layers of gold oxide unaffected.<sup>[32]</sup>

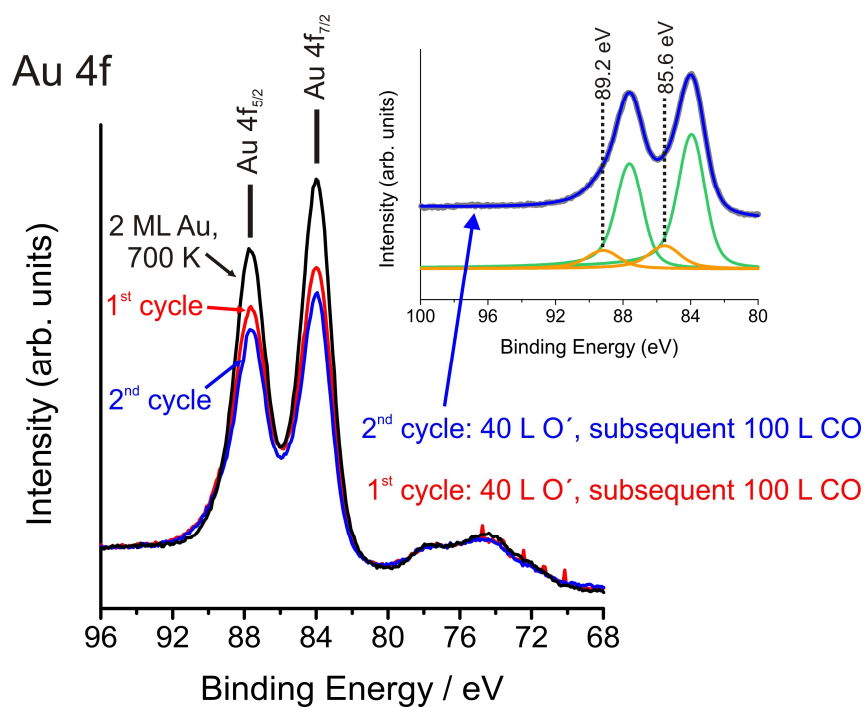


**Figure 5.6.1-1:** Au 4f XPS data of a 2 ML Au film prepared on the clean Ru(0001) surface (black curve). After the oxidation by 40 L O' at room temperature subsequent reduction by 100 L CO was done and monitored (red curve). A second cycle of oxidation (40 L O') and reduction (100 L CO) of these nanoparticles is also illustrated (blue curve). The inset shows the Au 4f peak deconvolution after the second oxidation and reduction cycle. The green peaks Au 4f signals in the inset are assigned to metallic gold while the orange signals (at 85.6 eV and 89.2 eV) can either be assigned to gold oxide or to final state effects from the nanoparticular form of the reduced gold. The overall decrease of the Au 4f signal intensity is an indication for the increase of the gold nanoparticle size.

Because the gold nanoparticles remain their shape after this reduction procedure (*cf. figure 5.6.1-2c*), these small Au 4f signals (at 85.6 eV and 89.2 eV) could also be assigned to final state effects of the nanoparticular gold. Because gold oxide is metastable, it is possible to determine if these small signals are either related to a buried oxidized gold species or to final state effects. For this the slow decomposition of gold oxide in vacuum has to be monitored with XPS for several days. However, this experiment was not done and the nature of these small signals remains elusive.

The STM measurements reveal that no obvious morphologic change appears after the exposure of 100 L CO at room temperature (*cf. figure 5.6.1-2c*) to the Au oxide/Au nanoparticles (*cf. figure 5.6.1-2a*). Evidently, the gold nanoparticles remain their overall droplet-like shape on the surface at these reduction conditions. This is explained by the low mobility of the metallic gold atoms at room temperature, which inhibits a restructuring of the reduced nanoparticles to thin gold islands or films. It is assumed that an additional annealing step to 700 K is assumed to lead to the formation of gold islands or films. The subsequent reoxidation by 40 L O' does not noticeably change the morphology of the nanoparticles (*cf. figure 5.6.1-2e*).

The STM images support the previous conclusion of reversibility between oxidized and metallic gold nanoparticles, which can be obtained without losing the dispersion by reduction and oxidation cycles at room temperature.

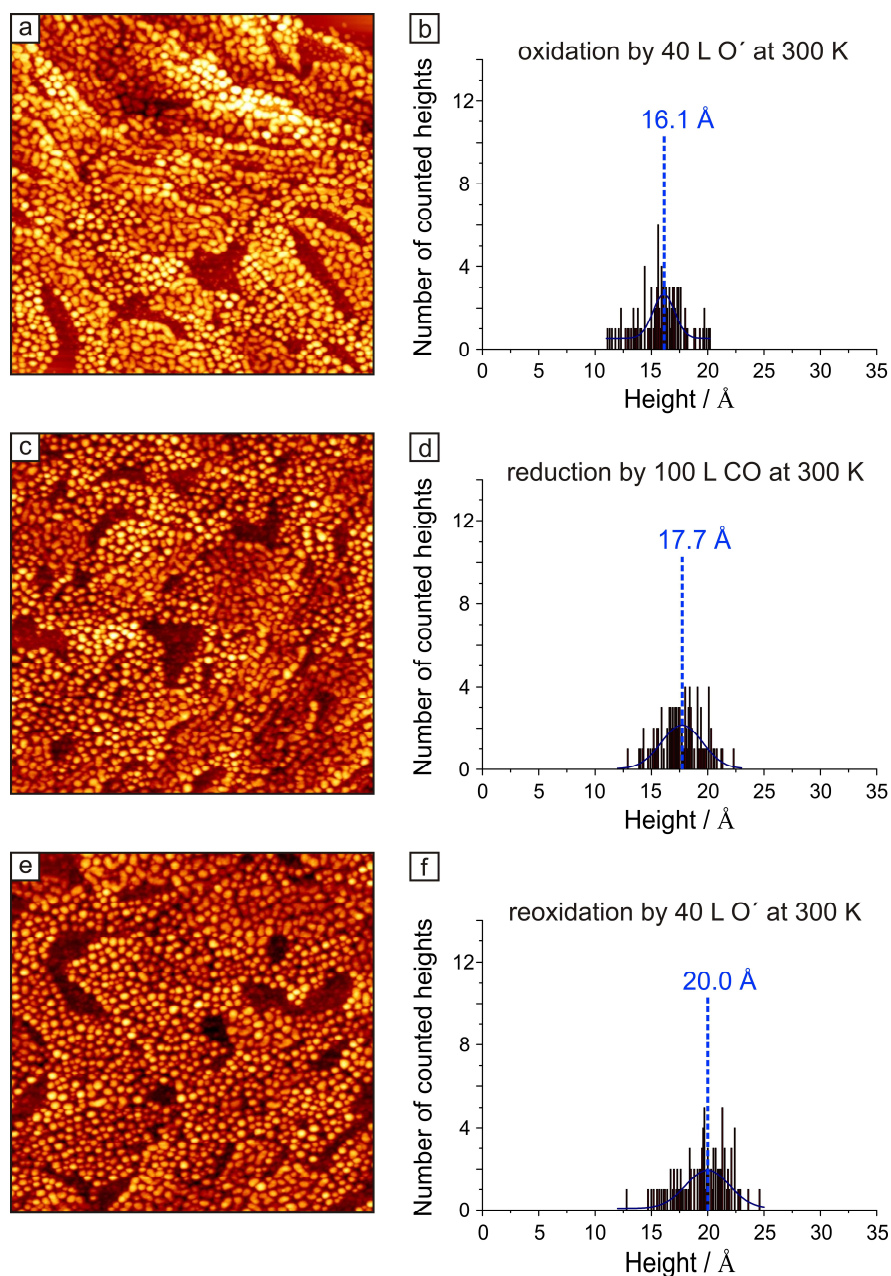


**Figure 5.6.1-2:** STM image and height distribution of formed gold nanoparticles after oxidation of a 2 ML gold film by 40 L atomic oxygen at room temperature ((a),(b)). The reduction of these nanoparticles was accomplished by dosing 100 L CO at room temperature ((c),(d)). The reoxidation of these particles was done by dosing again 40 L O' to the metallic nanoparticles ((e),(f)). The dispersity of the nanoparticles is remained by the reduction at room temperature (c). The increase in particle height (cf. (b),(d)) after reductions is assumed to be a tip effect in STM. With the different electronic structure of metallic gold and oxidized gold nanoparticles, their height is not equally described by STM. But with each oxidation cycle, the thickness of the nanoparticles increases (b),(f). This confirms the interpretation of the decreasing Au 4f total signal intensity (cf. figure 5.6.1-1). All STM images are in the range of (300 nm x 300 nm); the height distributions are determined by line scan analysis of the nanoparticles. Tunneling conditions:  $U = 0.9 - 1.1$  V,  $I = 0.8 - 1.0$  nA.

However statistical analysis reveals an increasing nanoparticle height with each oxidation and reduction cycle (*cf. figure 5.6.1-2b and 5.6.1-2f*). This slight increase in nanoparticle height confirms the previous interpretation of the decreasing Au 4f signal intensity in *figure 5.6.1-1*. With more three-dimensional gold nanoparticles on the surface, less gold is detected due to the limited depth information of XPS. The height of the reduced nanoparticles (*cf. figure 5.6.1-2d*) is unexpected, but will be explained in the following: With an average thickness of about 16.1 Å prior to the reduction (*cf. figure 5.6.1-2b*), the nanoparticle thickness increases further on to 17.7 Å after the exposure of 100 L CO (*cf. figure 5.6.1-2d*). However, the reduced metallic gold nanoparticles should be smaller than their oxidized counterpart, due to removal of oxygen from the particles and a smaller lattice constant for the metallic gold<sup>18</sup>.<sup>[80,82]</sup> Therefore this increase in height is assumed to be a tip effect. With different electronic structures for the metallic and the oxidized gold, the measured height in the line scans does not only reflect the geometric structure but also the electronic structure of the nanoparticles. Because the same tunneling conditions for the metallic and the oxidized nanoparticles were used, the influence of the electronic structure on the nanoparticle height becomes evident, i.e. the metallic nanoparticles appear higher than the formed oxidized particles, although a decrease of the nanoparticle height was expected. Therefore the overall increase in nanoparticle height is evident by comparing nanoparticles that have similar chemical nature, e.g. the oxidized nanoparticles (*cf. figure 5.6.1-2b and 5.6.1-2f*).

*Figure 5.6.1-3* schematically illustrates the morphologic changes of the gold nanoparticles with continuing oxidation and reduction cycles. The black arrows indicate the movement of the gold atoms during the oxidation, based on the previously described shoveling mechanism (*cf. chapter 5.5*).

The proposed mechanism includes the following steps: After the oxidation of a thin gold film (e.g. 2 ML) by 40 L atomic oxygen, oxidized gold nanoparticles are formed that may consist of a core(metallic Au)-shell(gold oxide) structure. The exposure of 100 L CO at room temperature induces a partial reduction, i.e. only the oxidized gold atoms exposed to CO are reduced, thus leaving gold oxide atoms from deeper layers unaffected. The reduction of the nanoparticles is related to the removal of oxygen without further diffusion of metallic gold atoms. As a consequence the nanoparticles retain their droplet like shape without rewetting the ruthenium surface during this reduction at room temperature. The reoxidation by 40 L atomic oxygen leads to even thicker nanoparticles at the expense of their lateral expansion on the Ru(0001) surface, i.e. gold atoms from the nanoparticle side are shoveled to its top. The

---

<sup>18</sup> The nearest neighbor distance between two gold atoms for fcc bulk gold is approximately 2.885 Å.[178-180] In Au<sub>2</sub>O<sub>3</sub> the Au-Au distances are elongated to 3.3 – 3.8 Å. Ref.[80,201]

subsequent reduction by CO is again considered as the removal of oxygen without further diffusion of the metallic gold atoms, thus retaining the overall dispersity of the thicker nanoparticles. By continuing such oxidation and reduction cycles at room temperature, the thickness of the nanoparticle increases steadily.

This increase may be an additional explanation for the deactivation of gold nanoparticle catalysts with ongoing oxidation reactions besides the nanoparticle sintering process.

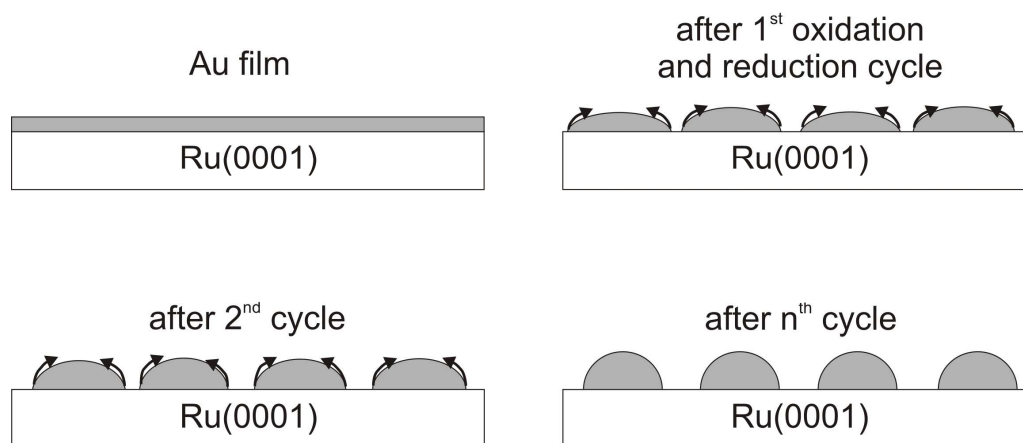


**Figure 5.6.1-3:** Schematic illustration of the proposed mechanism for the increasing thickness of the gold nanoparticles with continuing cycles of oxidation and reduction at room temperature. Within this mechanism the previously proposed shoveling mechanism (cf. chapter 5.5, page 98ff) is displayed by the diffusion of oxidized Au atoms from the Au/Ru interface to the top side of the nanoparticle. The resulting thicker particles after the n<sup>th</sup> cycle are assumed to adapt a hemispherical morphology.

## 5.6.2 CO oxidation by the oxidized gold nanoparticles

Many oxidized gold nanoparticles were prepared by exposure of 40 L atomic oxygen to a 2 ML thick gold film at room temperature (*cf. figure 5.4.1-1d*). CO oxidation was done by simultaneously dosing molecular oxygen and carbon monoxide with a ratio of 10:1 to the Au oxide/Au nanoparticles at 300 K. The CO pressure was kept constant at  $1 \cdot 10^{-7}$  mbar while oxygen was set to  $1 \cdot 10^{-6}$  mbar during the CO oxidation.

The oxidation state of the gold nanoparticles was monitored *ex situ* on the basis of the gold oxide Au 4f signals (at 85.6 eV and 89.2 eV) before and after a total exposure of 100 L, 200 L, 300 L, 400 L, 600 L, 800 L and 1500 L CO, respectively. The corresponding amounts of molecular oxygen are: 1000 L, 2000 L, 3000 L, 4000 L, 6000 L, 8000 L and 15000 L, respectively. With an O<sub>2</sub>/CO ratio of 10:1 it is expected that the gold oxide Au 4f signals remain constant if sufficient amounts of O<sub>2</sub> are activated during the catalytic oxidation of CO. As described in the literature, oxidized gold surfaces and undercoordinated gold atoms show an increased dissociation probability for O<sub>2</sub>.<sup>[36,51,54,82]</sup>

*Figure 5.6.2-1* summarizes the CO oxidation experiment by plotting the relative integrated Au 4f signal areas of the gold oxide signals (at binding energies 85.6 eV and 89.3 eV) against the exposure of CO (black squares).<sup>19</sup> For comparison the simple reduction of 1.6 nm (red hexagon) and 2.0 nm (blue cross) thick oxidized gold nanoparticles after exposure of 100 L CO at room temperature is included, too.

During CO oxidation (O<sub>2</sub>/CO ratio of 10:1) the amount of gold oxide is decreasing linearly with continuing CO and O<sub>2</sub> exposures at room temperature (*cf. figure 5.6.2-1*, black squares). A linear fit (dashed green line) for the gold oxide signal decrease during the CO oxidation is additionally plotted. A direct comparison between the CO oxidation experiment and the pure reduction by CO is possible for the gold oxide signals after a total exposure of 100 L CO. After simultaneously dosing 100 L CO and 1000 L O<sub>2</sub>, the integrated gold oxide signal decreased to 84 % of its initial integrated gold oxide signal value. For comparison, the pure reduction (100 L CO) of gold oxide nanoparticles with similar height (*cf. figure 5.6.2-1*, red hexagon) leads to a decrease to 39 % of its initial gold oxide signal value. Evidently the gold oxide layers are more stable with the excess of oxygen in the gas phase than in the pure CO environment.

---

<sup>19</sup> Despite keeping the oxidation parameters constant, there was a slight variation in the resulting gold oxide signals of the as-prepared Au oxide/Au nanoparticles. The integrated gold oxide signal areas after exposure were divided by the integrated gold oxide signal areas of the as-prepared Au oxide/Au nanoparticles to account for this fact.

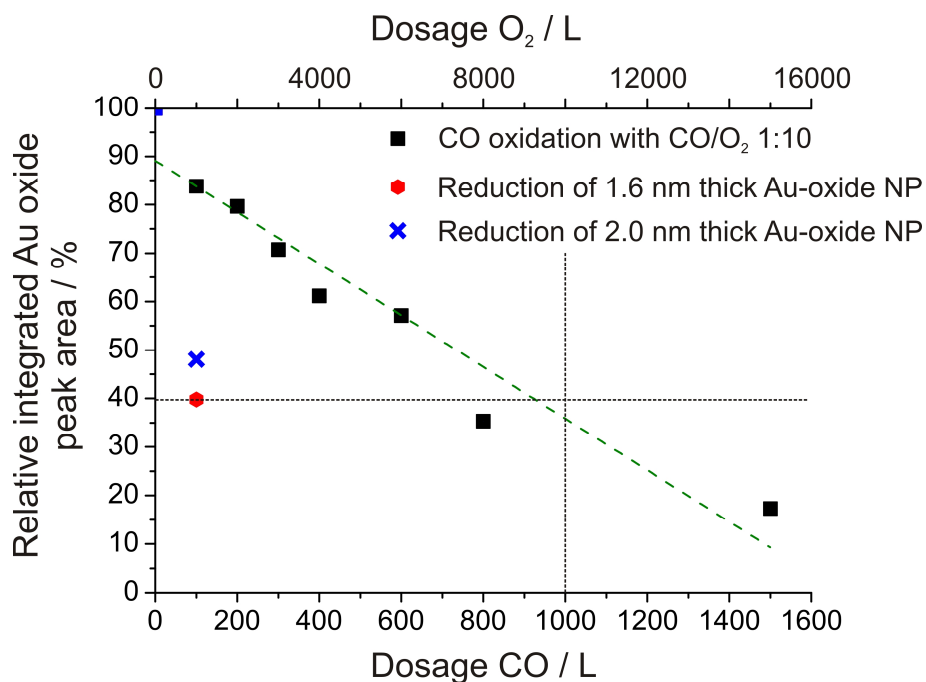


**Figure 5.6.2-1:** The decay of the integrated Au 4f gold oxide signals at 85.6 eV and 89.3 eV is plotted against the total dosage of CO and O<sub>2</sub>, respectively. For this plot the integrated gold oxide signals are compared to those of newly formed Au oxide/Au nanoparticles, i.e. the integrated gold oxide signal area of the as-prepared Au oxide/Au nanoparticles is defined as 100 %. The decrease of the gold oxide signal during CO oxidation experiment with an O<sub>2</sub>/CO ratio of 10:1 is presented (black squares). For comparison, the simple reduction experiments by 100 L CO are used as a reference (red hexagon and blue cross).

The Au 4f oxide signal decreases below 20 % of its initial value over several hours<sup>20</sup> of CO oxidation. This signal decay is even more pronounced than what was observed for the case of the pure reduction in CO. One possible explanation is that the reduction of the upper Au oxide layers by the 100 L CO at room temperature is incomplete and higher exposures of CO are necessary for a complete reduction of the gold oxide layers that are accessible by CO. The second possible explanation for this distinct decrease of the gold oxide signal would be a decomposition of the deeper gold oxide layers due to the metastability of gold oxide.<sup>[72,73]</sup> To identify the correct explanation, either CO reduction experiments with higher exposures of CO, or life-time experiments in vacuum could be conducted to investigate the metastability of gold oxide.

Considering that CO reduces the gold oxide in the CO oxidation experiment as well as in the CO reduction experiment, two explanations for the faster reduction of the gold oxide species in the pure CO environment are possible:

<sup>20</sup> The dosage of 1500 L CO was performed over a time period of 210 minutes.

- (1) The molecular oxygen from the gas phase is dissociated by the undercoordinated or oxidized gold atoms during the reaction. The dissociated oxygen then subsequently reoxidizes the gold nanoparticles. However the reduction by CO is assumed to be more favored than the reoxidation by the dissociated O<sub>2</sub>, which is consistent with the linear decrease of the Au oxide signals. Otherwise saturation to a constant Au oxide signal would have been expected.
- (2) The adsorbed O<sub>2</sub> is poisoning the surface of the catalyst, thus leaving the CO less adsorption sites to reduce the gold oxide shell, which leads to a slower reduction. In general: O<sub>2</sub> binds stronger at step regions, defect sites and undercoordinated gold atoms than on flat single crystal terraces.<sup>[25,54]</sup> Therefore the undercoordinated gold atoms of the oxidized nanoparticles facilitate the adsorption of O<sub>2</sub> while the adsorption of CO is inhibited.

With a gas ratio of 10:1 during the CO oxidation, the amount of CO adsorbing on the surface is assumed to decrease approximately by one order of magnitude, if CO and O<sub>2</sub> have similar sticking coefficients. As a result a reduction of the Au oxide/Au nanoparticles in the O<sub>2</sub>/CO gas atmosphere should show similar results to the pure reduction by 100 L CO (red hexagon), if the surface is exposed to a tenfold higher amount of CO and O<sub>2</sub> (i.e. 1000 L CO and 10000 L O<sub>2</sub>). This hypothetical decrease is presented in *figure 5.6.2-1* by the intersection point of the dotted lines. The linear fit of the gold oxide signal decrease (dashed green line) matches well to this calculated intersection point, thus indicating a decreased adsorption probability of CO. To differentiate between a possible catalytic activity of the oxidized gold nanoparticles and a poisoning effect of O<sub>2</sub> during the CO oxidation reaction, a thicker gold film (6 ML) and a Au(111) surface were both first oxidized by 40 L atomic oxygen, followed by an exposure of oxygen ( $p(\text{O}_2) = 1 \cdot 10^{-6} \text{ mbar}^{21}$ ) for several hours at room temperature. If the formed gold oxides are able to dissociate O<sub>2</sub> the Au 4f signals at 85.6 eV and 89.3 eV should either remain constant or increase over time. *Figure 5.6.2-2* shows the change of the gold oxide Au 4f signals depending on the O<sub>2</sub> exposure.

---

<sup>21</sup> The applied oxygen pressure is equal to the oxygen pressure during the CO oxidation experiments.

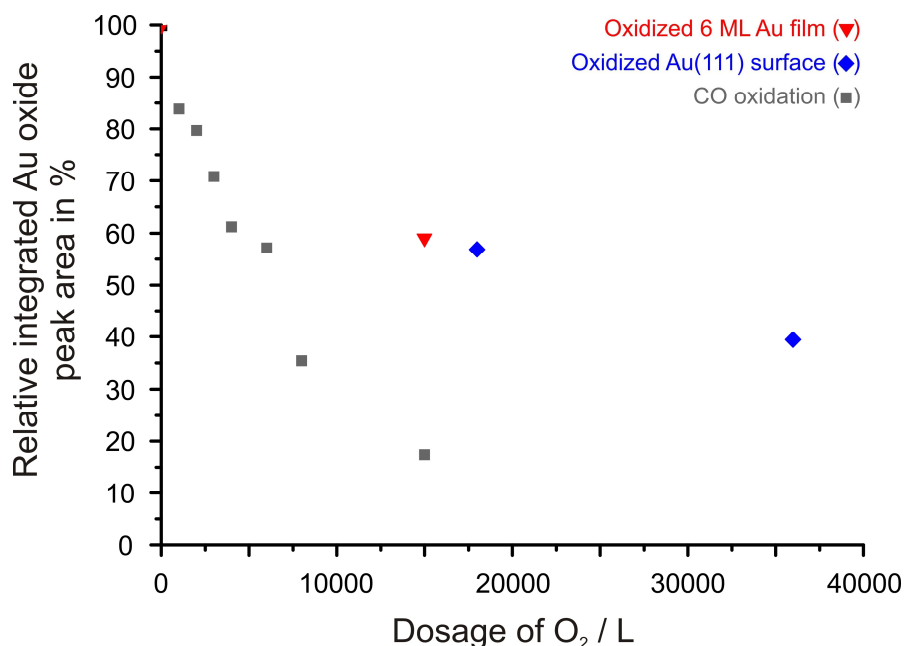


**Figure 5.6.2-2:** Change of the gold oxide signal due to exposure of O<sub>2</sub> at room temperature over time for an oxidized gold film (red triangle) and a Au(111) single crystal surface (blue rhombus). For a better comparison to the previous figure, the Au oxide signal decrease during the CO oxidation experiment (grey square) is also shown with the respective amount of dosed O<sub>2</sub>.

After keeping the gold oxide nanoparticles in 10<sup>-6</sup> mbar O<sub>2</sub> for 4 hours, the gold oxide Au 4f signals decreased significantly, thus revealing the reduction of the gold oxide. Keeping in mind that Au oxide is metastable, the reduction depicted in *figure 5.6.2-2* suggests that the partial pressure of oxygen is too low to either stabilize or reform the gold oxide by dissociated O<sub>2</sub>. A similar decrease of the Au 4f signals is observable if O<sub>2</sub> is exposed to an oxidized Au(111) surface (*cf. figure 5.6.2-2*, blue rhombus). A slow decomposition of the gold oxide in UHV over time (4 hours) may be a possible explanation for the gold oxide signal decrease. Another possibility to explain this signal decrease would be the reduction of the Au oxide/Au nanoparticles by a reducing gas component. Exchange reactions of the dosed molecular oxygen with different filaments in the chamber (ion gauges, x-ray source) and the chamber walls could have released CO and H<sub>2</sub> into the gas atmosphere, which then slowly reduced the gold oxide.

To conclude the question of a possible catalytic activity for the Au oxide/Au nanoparticles, CO oxidation experiments as well as O<sub>2</sub> dissociation experiments were conducted. Both experiments showed a linear decrease of the gold oxide Au 4f signals upon continuous exposure of CO/O<sub>2</sub> or O<sub>2</sub>, respectively. In case of the CO oxidation decrease of the gold oxide signals is proportional to the CO exposure, indicating a simple reduction of the Au oxide/Au nanoparticles. The simultaneously dosed O<sub>2</sub> does not reoxidize the gold nanoparticles, more likely a poisoning of the catalyst surface by adsorbed O<sub>2</sub> is assumed, which then extends the

needed amount of CO to reduce the gold nanoparticles. This interpretation is confirmed by the O<sub>2</sub> dissociation experiment where the gold surface was first oxidized by atomic oxygen, which was followed by the exposure of O<sub>2</sub> to further oxidize the gold by dissociation of the molecular oxygen. Although a facilitated O<sub>2</sub> dissociation over oxidized gold surfaces has been reported<sup>[36,51]</sup> this could not be confirmed for the Au oxide/Au nanoparticles presented in this work. The linear decrease of the gold oxide signal evidently illustrates the instability of the oxidized gold nanoparticles at the chosen reaction conditions.

This inactivity towards CO oxidation could be explained by the formation of a catalytic inactive gold oxide species. Generally, various gold-oxygen species can be formed upon exposure of atomic oxygen.<sup>[16,66]</sup> From these, chemisorbed oxygen atoms bound to undercoordinated metallic gold atoms are proposed to be the most active species for CO oxidation.<sup>[16,27,38,39,67]</sup> In all experiments within this work, this species has never been observed in XPS, based on its characteristic O 1s binding energy at 529.1 eV. Therefore it is assumed that the oxidative potential of thermally cracked oxygen is too high, and an inactive gold oxide (e.g. bulk like Au<sub>2</sub>O<sub>3</sub>) has been formed.

However, even with no visible catalytic activity of the formed oxidized gold nanoparticles on the ruthenium surface the morphologic changes due to oxidation of thin gold films have been presented. The systematic investigations on the morphology, during oxidation and reduction, and the presented oxidation mechanism of thin gold films and islands can be used as a guideline for further understanding of gold nanoparticle catalysts. Moreover these experiments can be used as a model for a re-dispersion of inactive gold catalysts. With sintering being one of the biggest problems in gold catalysis, the formation of thin gold films by annealing of these sintered nanoparticles and subsequent oxidation by atomic oxygen can lead to newly formed small and active gold nanoparticles. Still further investigations are necessary to find oxidation conditions to prepare catalytic active chemisorbed oxygen phase and to prevent a completely oxidized bulk like oxide structure.

## 5.7 Conclusion considering the growth and oxidation of Au on Ru(0001)

Based on the STM measurements and the corresponding XPS data for the Au/Ru(0001) system, the following conclusions are drawn:

1. Gold deposited on oxygen precovered Ru(0001) grows in a Volmer-Weber-like behavior. Separated (111) oriented gold islands are preferentially formed along the steps of the Ru(0001) surface while the oxygen overlayer on the ruthenium surface is simultaneously compressed. The thickness of the hexagonal gold islands can be controlled by the oxygen overlayer density on the Ru(0001) surface and the applied sample temperature during the gold deposition process. This growth behavior can be rationalized by Young's equation and is assumed to be mainly induced by the significant difference between the surface free energies of Au and oxygen covered Ru ( $\sigma_{Au} > \sigma_{O/Ru}$ ).
2. Gold deposition on an oxygen free Ru(0001) surface leads to the formation of a covering gold film, which shows a Stranski-Krastanov-like growth behavior. Again Young's equation and the significant difference in the surface free energies of Ru and Au in particular describe the observed growth behavior ( $\sigma_{Au} < \sigma_{Ru}$ ).
3. If gold is deposited on RuO<sub>2</sub>(110) the morphology the formed gold islands strongly depends on the position where they are formed. Gold islands formed on the flat RuO<sub>2</sub>(110) terraces are cuboid-like shaped, which indicates the growth of (100) oriented gold. At intersection areas, where different RuO<sub>2</sub>(110) domains are rotated by 120° to each other, hexagonally shaped gold islands are formed. This strongly indicates correlation between the symmetry of the underlying RuO<sub>2</sub> patches and the resulting crystallographic orientation of the growing gold islands. Therefore it is assumed that crystallographic orientation of gold on the RuO<sub>2</sub>(110) surface is determined by a complex energy relation between the strain energy of the growing islands, the interface energy and the surface free energies of RuO<sub>2</sub>(110) and the gold islands.
4. The exposure of atomic oxygen to the thin gold islands or films at room temperature lead to the formation of small oxidized gold nanoparticles, which consist of a Au<sup>3+</sup> species (most probably Au<sub>2</sub>O<sub>3</sub>) and metallic gold. The size of the

formed Au oxide/Au nanoparticles as well as their formation rate strongly depends on the former thickness of the metallic gold islands (or film). While two or three layered gold islands readily fragment into many oxidized nanoparticles, a thicker gold island ( $\geq 4$  ML) is usually transformed into very few big particles. The oxidation of the thin gold islands (or films) are explained by a proposed shoveling mechanism, which describes the diffusion of oxidized gold atoms from the perimeter sites of the Au-Ru interface to the top of the gold islands/nanoparticles.

5. The reduction of these Au oxide/Au nanoparticles under CO environment at room temperature lead to metallic gold nanoparticles, which mostly remained their shape and size. Restoration of flat and hexagonally shaped Au islands was accomplished by reduction in CO at 700 K. If the oxidized nanoparticles are thermally reduced at 700 K significantly thicker gold islands are formed, thus indicating a oxygen spillover process from the decomposing Au oxide to the Ru(0001) surface.
6. CO oxidation experiments were conducted to investigate the catalytic activity of the Au oxide/Au nanoparticles. But even under very oxidizing reaction conditions the particles were reduced to metallic gold while retaining their shape. Therefore only a transient activity but no catalytic activity for the Au oxide/Au nanoparticles could be demonstrated.

## 6. Deposition of Ru on Au(111)

In electrochemistry bimetallic anodes have gained interest as model catalyst systems for fuel cells.<sup>[202]</sup> Especially platinum based PtRu bimetallic electrodes showed higher activities than the pure platinum counterparts.<sup>[203-205]</sup> To further investigate the high activity of this PtRu bimetallic system, Ru/Au(111) was chosen as the model system due to the high nobility of gold.<sup>[206-213]</sup> With gold as the substrate reactions like the CO oxidation can be studied in more detail because the activity of the system is limited to the deposited Ru. To prepare these bimetallic Ru/Au electrodes, ruthenium was electrochemically deposited on a Au(111) surface.<sup>[206-213]</sup> The nucleation and growth of the deposited ruthenium film depends on the electrochemical conditions. It was shown that ruthenium first forms small islands which are preferentially located at the “elbow sites<sup>22</sup>” of the reconstructed Au(111) surface.<sup>[206,207,214]</sup> If the Au(111) herringbone reconstruction is lifted during the deposition process, the deposited ruthenium is preferentially located at defect sites and steps of the Au(111) surfaces. The nucleation and growth of ruthenium islands on the terraces is significantly less favored. With ongoing deposition a three-dimensional growth of hexagonally shaped ruthenium islands is observable resulting in a rough film of ruthenium.<sup>[210-212]</sup>

Quite in contrast, the deposition of ruthenium on Au(111) under UHV conditions has only been carried out by chemical vapor deposition (CVD) of  $\text{Ru}_3(\text{CO})_{12}$  so far.<sup>[89-91]</sup> By annealing the covered gold surface to 500 K the  $\text{Ru}_3(\text{CO})_{12}$ -precursors were decomposed with release and desorption of CO. By this procedure small but mobile ruthenium clusters are formed on the surface. But during the precursor decomposition, carbon impurities are formed and intercalated in the ruthenium clusters due to the dissociation of CO at the freshly deposited metal clusters. A possible simultaneous contamination by oxygen is inhibited because the underlying gold substrate induces desorption of  $\text{O}_2$ . After  $\text{Ru}_3(\text{CO})_{12}$  decomposition at 500 K, the exposed ruthenium clusters agglomerate to small and flat islands at the ordered “elbow sites” of the Au(111) herringbone pattern, which results in an ordered distribution of these small ruthenium islands on the gold surface. If higher temperatures (> 500 K) are applied, less Ru islands are formed that are larger in lateral size. Induced by the grown ruthenium islands, the herringbone patterns of the Au(111) surface get distorted, thus leading to more and more randomly distributed ruthenium islands on the surface. For lower coverages of ruthenium at 500 K, a two-dimensional aggregation of clusters to larger Ru islands is observable. A

---

<sup>22</sup> In figure 6-1 the STM picture illustrates the Au(111) herringbone structure with its unique structural properties.

temperature of 500 K was too low, so the ruthenium clusters did not rearrange to atomically flat islands, thus retaining their spherical shape in the agglomerated cluster network. For higher coverages three-dimensional growth is observable before the whole Au(111) surface is completely covered by the two-dimensional aggregation of Ru clusters.<sup>[91]</sup>

A closer inspection of the literature of the Ru/Au(111) system revealed that the deposition of pure metallic ruthenium by PVD on Au(111) in UHV has not been investigated yet.

From the knowledge of the well described growth of gold on Ru(0001)<sup>[154-167]</sup> the relationship of surface free energies has been derived:

$$\sigma_{Ru} > \sigma_{Au} > \sigma_{RuO_2}$$

Based on this order of the surface free energies the growth behavior of Ru and RuO<sub>2</sub> on Au(111) in UHV by PVD are estimated. As a first guideline, the interface energy and the strain energy are neglected at this point:

1. *Ru on Au(111)*: Deposition of metallic ruthenium on a Au(111) surface at higher temperatures with low deposition rates should lead to the formation of three-dimensional ruthenium islands on the surface due to the significantly higher surface free energy of ruthenium ( $\sigma_{Ru} > \sigma_{Au}$ ).
2. *RuO<sub>2</sub> on Au(111)*: Deposition of ruthenium in O<sub>2</sub> atmosphere on a Au(111) surface at higher temperatures with low deposition rates should lead to the formation of a wetting layer of oxidized ruthenium due to the lower surface free energy of ruthenium oxide ( $\sigma_{Au} > \sigma_{RuO_2}$ ).
3. *Oxidation of Ru/Au(111) using O<sub>2</sub> at higher temperatures*: Oxidation of the three-dimensional ruthenium islands should form a wetting layer of ruthenium dioxide on the Au(111) surface if the oxidation conditions are chosen properly. Again the morphology would be determined by the surface free energies ( $\sigma_{Au} > \sigma_{RuO_2}$ ).

It should be mentioned that for these first assumptions the interface energy is neglected completely. Also the unique structural properties of the Au(111) are not considered. But from the literature it is known that the herringbone structure strongly influences the growth of ruthenium islands, as can be seen by the preferred nucleation sites of ruthenium. Therefore the unique structure and properties of the reconstructed Au(111) surface will be briefly elucidated in the following:

Compared to other transition metals, gold has a low surface free energy, a low melting point, a low hardness and is a very ductile metal. The three single-crystalline fcc gold surfaces with

lowest miller indices (Au(111), Au(110) and Au(100)) do reconstruct in UHV. The reconstruction of the Au(111) surface is well described in literature.<sup>[178-180,215]</sup> Its most important properties are depicted in the following STM image (*cf. figure 6-1*).

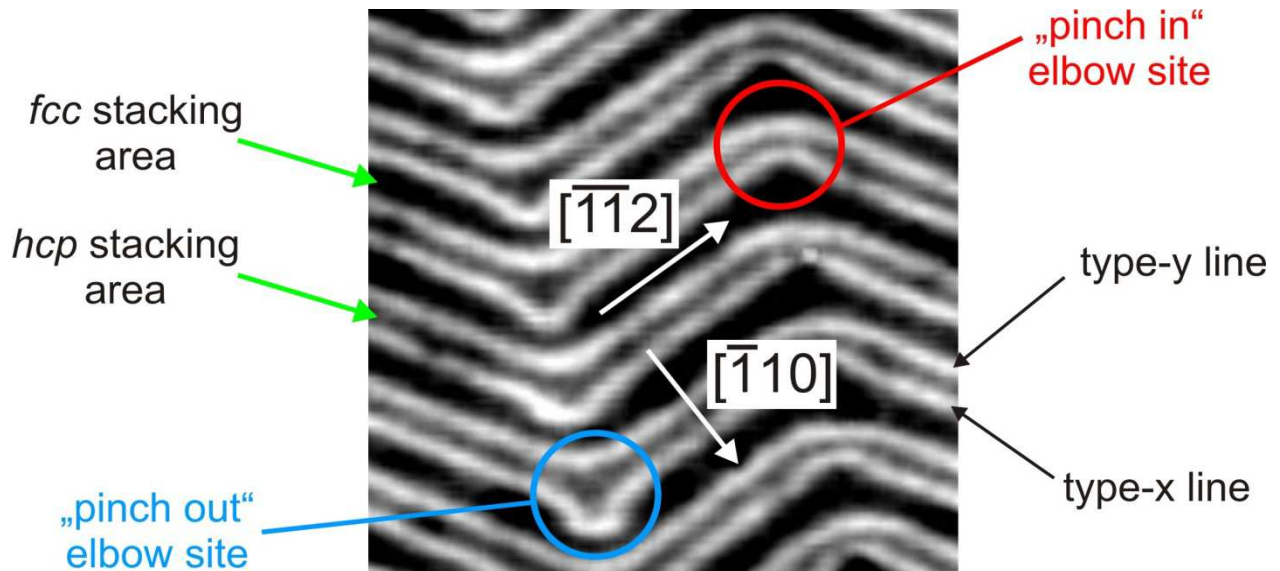


**Figure 6-1:** The STM (32 nm x 31 nm) image of the reconstructed Au(111) surface displays and summarizes the unique structural properties of this surface.  $U = 0.5$  V,  $I = 1.0$  nA. Picture taken from [216].

The so called “herringbone pattern” consists of alternating lines (the so called type-x and type-y lines) which enclose and separate the fcc and hcp stacking areas, respectively. At each bend of the herringbone pattern, point dislocations occur in the type-x line<sup>23</sup>, resulting in the formation of the so called “pinch out” and “pinch in” elbow sites. By forming this reconstruction the gold atom density is approximately 4 % higher than in the not reconstructed (1x1) Au(111) surface.<sup>[179,216]</sup>

Physical vapor deposition of many metals on gold in UHV usually leads to the formation of clusters or islands at the elbow sites of the Au(111) surface.<sup>[90,207,217-221]</sup> Via an excited atom exchange process, single gold atoms are released from the gold surface to incorporate the adsorbed metal atoms or islands at these elbow sites.<sup>[216,222,223]</sup> This place exchange of deposited metals is assumed to be possible for all metals that exhibit a significantly higher surface free energy compared to gold at elevated temperatures.<sup>[223]</sup> Using this process, surface alloys of immiscible metals<sup>24</sup> have either been prepared or predicted in the literature.<sup>[216,222-225]</sup> Within these predictions was also the possible formation of an surface alloy between

<sup>23</sup> The type-y lines are free of point dislocations.

<sup>24</sup> i.e.: Ni, Co, Mo, Ru with Au(111), respectively.

ruthenium and Au(111).<sup>[222]</sup> This subject will be discussed in the following chapter, where the investigations of the growth of Ru (by PVD) on Au(111) are presented.

## 6.1 Deposition of ruthenium on Au(111) in vacuum

In the following the growth of ruthenium on Au(111) will be presented. By physical vapor deposition (PVD) from a metallic ruthenium target a high purity of the formed ruthenium islands on the gold surface is accomplished<sup>25</sup>. During the deposition of ruthenium the Au(111) surface was kept at 620 K. The amount of deposited ruthenium was determined by quantitative STM analysis of the deposited ruthenium on the surface. XPS was used to verify the amount of the deposited ruthenium.

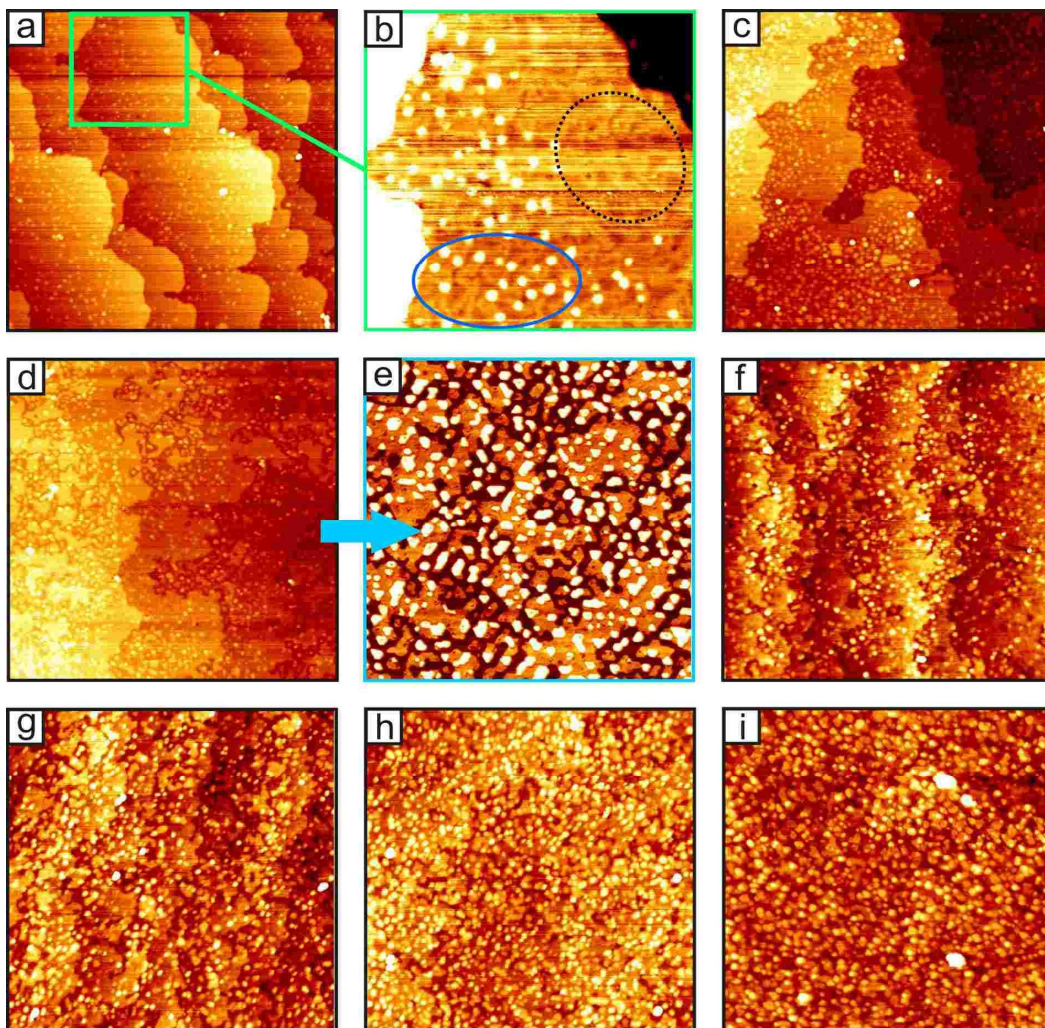


**Figure 6.1-1:** Deposition of different amounts of ruthenium on Au(111) at 620 K: (a) 0.5 ML Ru, 300 nm x 300 nm; (b) 0.5 ML Ru, 120 nm x 120 nm; (c) 1.0 ML Ru, 300 nm x 300 nm; (d) 1.5 ML Ru, 300 nm x 300 nm; (e) 1.5 ML Ru, 150 nm x 150 nm; (f) 2.0 ML Ru, 300 nm x 300 nm; (g) 3.0 ML Ru, 300 nm x 300 nm; (h) 4.0 ML Ru, 300 nm x 300 nm; (i) 10.0 ML Ru, 300 nm x 300 nm. With increasing amounts of deposited Ru the roughness of the growing film of merged ruthenium islands increases, too. Tunneling conditions:  $U = 0.5 - 1.0$  V,  $I = 0.5 - 3.5$  nA.

<sup>25</sup> For comparison, the previously described formation of metallic ruthenium islands on Au(111) by CVD of  $\text{Ru}_3(\text{CO})_{12}$  lead to carbon impurities due to decomposition of the CO molecules.[89]

Figure 6.1-1 shows a series of STM images after 0.5 ML, 1.0 ML, 1.5 ML, 2.0 ML, 3.0 ML, 4.0 ML and 10.0 ML of ruthenium have been deposited on the Au(111) surface, respectively. After deposition of 0.5 ML (*cf. figure 6.1-1a*) ruthenium, small islands are formed, which are randomly distributed over the surface. Simultaneous to the growth of ruthenium islands, the distortion of the nearby herringbone pattern (blue circle, *cf. figure 6.1-1b*) and the serration of the Au(111) steps can be observed in the STM images (*cf. figure 6.1-1a,c*). The ruthenium islands are preferentially located on the terraces, while leaving a thin area along the serrated steps where no islands are formed (dotted black circle, *cf. figure 6.1-1b*). These serrated steps also show a distorted herringbone pattern. With proceeding deposition of ruthenium, the serration of the steps increases as well as the three-dimensional growth of the ruthenium islands (*cf. figure 6.1-1c,d*). In a magnification (*cf. figure 6.1-1e*) the hexagonal shape of the deposited Ru is visible, thus indicating a hcp(0001) or fcc(111) orientation of the growing ruthenium islands. Eventually a rough ruthenium film is formed after the growing ruthenium islands merged together (*cf. figure 6.1-1h,i*). With the merging of the ruthenium islands the former step arrangement of the Au(111) substrate is not visible anymore.

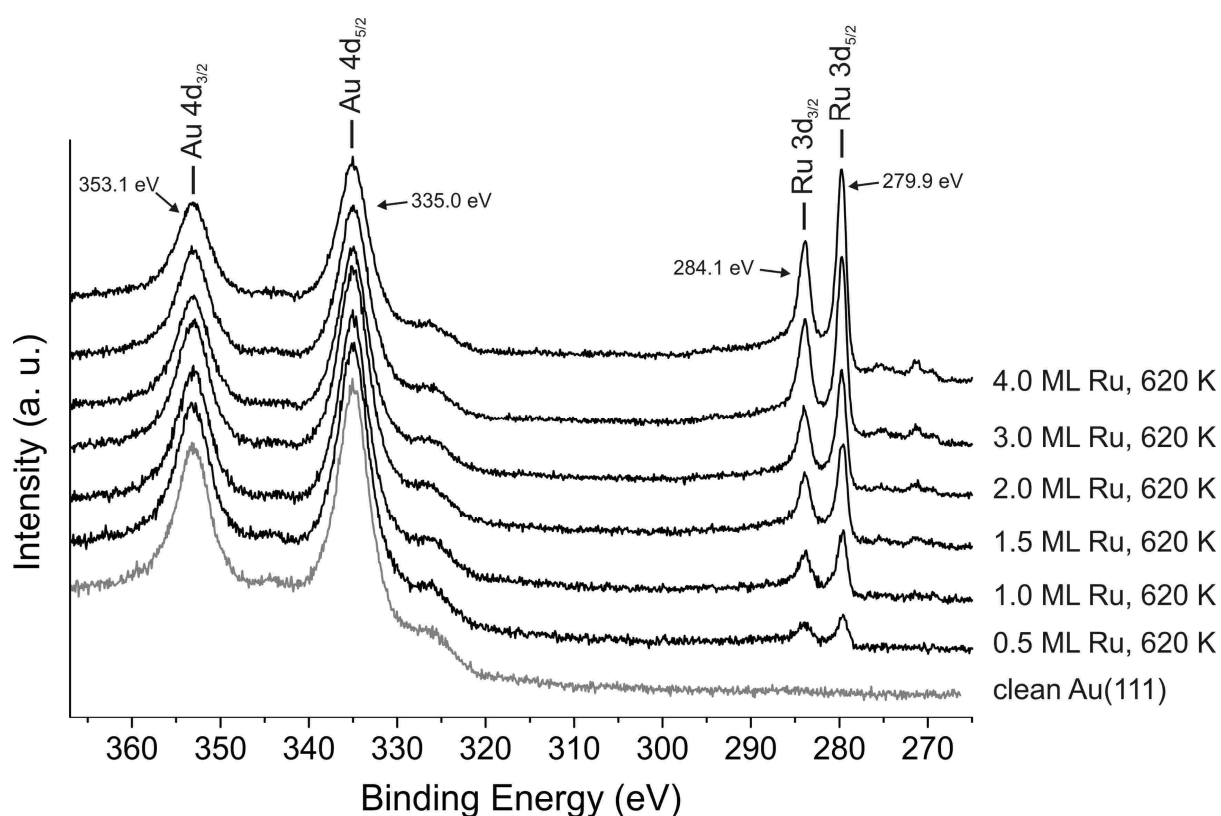


**Figure 6.1-2:** XPS data of the deposition of ruthenium on Au(111) at 620 K. The increasing thickness of the merged Ru islands is observable by the increase of the Ru 3d signals, while the Au 4d signals decrease simultaneously.

From XPS studies, an evolving Ru 3d signal is observable at 279.9 eV (Ru 3d<sub>5/2</sub>) that is assigned to the growth of metallic ruthenium (*cf. figure 6.1-2*). The steady increase of the Ru 3d signals and the simultaneous decrease of the Au 3d signals confirms that the deposited ruthenium is covering the Au(111) surface.

The growth of ruthenium on gold, presented in this work, is very similar to the growth of Mo on Au(111) described by Friend et al.<sup>[223]</sup> Similar to Ru on Au(111), small Mo islands are formed at the elbow sites of the Au(111)-surface reconstruction. Also the formation of serrated steps and the distortion of the herringbone pattern have been observed. The authors interpret these morphologic changes as the formation of a surface alloy besides the growth of metallic Mo islands on top of the Au(111) surface. It is also mentioned that the alloying process competes with the nucleation and growth of Mo islands, depending on the sample temperature. DFT calculations performed by Hrbek et al. examine the rather unusual growth of Ni, Mo and Ru on Au(111).<sup>[222]</sup> They determined that a Au/metal/Au sandwich complex would be energetically more favorable than a single monolayer of the metal on top of the Au(111) surface. Therefore the formation of a surface alloy between Ni/Au, Mo/Au and Ru/Au might be possible. However only for the Ni/Au(111) system the formation of a surface alloy has been proven so far.<sup>[225]</sup> It has to be mentioned that the interpretations for the surface alloy formation in the Mo/Au(111) system are mainly based on STM observations.<sup>[223,226]</sup> Without atomic resolution this interpretation of a surface alloy is insufficient and a final conclusion remains elusive.

The absence of Ru islands near the serrated steps and the distorted herringbone pattern structure (*cf. figure 6.1-1a,b*) is explained by the following: Nucleation and growth of the ruthenium islands at the elbow sites is accompanied by an atom exchange process of gold and ruthenium atoms, leading to incorporated ruthenium atoms and released gold atoms at the elbow sites. Due to the applied temperature of 620 K the released gold atoms are able to diffuse and agglomerate at the steps of the gold surface. This would explain both: why no ruthenium islands can be found on the upper terrace near the steps and why the steps are serrated and show a distorted herringbone structure.

The random distribution of the ruthenium islands is related to the distortion of the herringbone pattern (*cf. figure 6.1-1b*, blue circle). A similar distortion of the herringbone structure by metal deposition has been observed in literature.<sup>[90,223]</sup> The deposited ruthenium atoms nucleate at the elbow sites of the Au surface, thus forming small islands. After the formation of this ruthenium island the nearby herringbone pattern gets distorted and new point dislocations are formed in the Au(111) surface. At these new point dislocations the next

ruthenium islands are formed, which induces further distortion of the herringbone pattern. These growing islands are generally hexagonally shaped, which is induced by the *fcc* and *hcp* stacking areas of the underlying Au(111) surface.

Due to the small lattice misfit between Au(111) and Ru(0001) (+6.6 %,  $a_{\text{Au}(111)} = 2.884 \text{ \AA}$ ,  $a_{\text{Ru}(0001)} = 2.706 \text{ \AA}$ )<sup>[16,178-181]</sup>, the resulting strain energy and interface energy are assumed to be small, too. Therefore the observed three-dimensional (Volmer-Weber-like) growth of Ru islands is explainable by the significantly higher surface free energy of ruthenium compared to Au(111).<sup>26</sup>

An important question is how the ruthenium atoms are incorporated in the first Au(111) layer after the atom exchange process. The (single) ruthenium atoms may either form a surface alloy like in the case of Ni<sup>[224,225]</sup> or small ruthenium islands are formed, which were embedded into the gold surface. Such a subsurface island growth or island encapsulation has been reported for the growth of Cu on Pb(111), where entire copper islands are overgrown by Pb.<sup>[136]</sup>

With STM experiments the growth of Ru on Au(111) has been systematically investigated. The observed three-dimensional growth nicely reflects the previously stated growth behavior of metallic Ru on Au(111), which is simply based on the surface free energy relation ( $\sigma_{\text{Ru}} > \sigma_{\text{Au}}$ ). Therefore the general growth behavior is assumed to be significantly affected by the surface free energies of both metals. However, a detailed description of the growth on the atomic level cannot be given at this point. It is not possible to decide if Ru and Au(111) form an alloy in the initial growth phase or if a partial encapsulation of small Ru islands occurs. Further experiments are mandatory, to elaborate a detailed and reliable description for the initial growth of Ru on Au(111).

---

<sup>26</sup>  $\sigma_{\text{Au}} = 1.50 \text{ J/m}^2$ ,  $\sigma_{\text{Ru}} = 3.05 \text{ J/m}^2$ .<sup>[182]</sup>

## 6.2 Oxidation of ruthenium islands by molecular oxygen

### 6.2.1 Formation of a perforated ruthenium film

In the following section the exposure of  $O_2$  to the rough film of merged ruthenium islands will be presented. Typical oxidation conditions for the formation of a covering film of  $RuO_2(110)$  on  $Ru(0001)$  were chosen to oxidize 1.5 ML  $Ru/Au(111)$  and 4.0 ML  $Ru/Au(111)$ , i.e. dosing molecular oxygen ( $p(O_2) = 2 \cdot 10^{-5}$  mbar) for 30 minutes towards the gold surface that was annealed to 680 K. On the basis of STM images, the oxygen treatment of a 1.5 ML and 4.0 ML  $Ru/Au(111)$  surface is presented (*cf. figure 6.2.1-1a-c and 6.2.1-1d-f, respectively*).

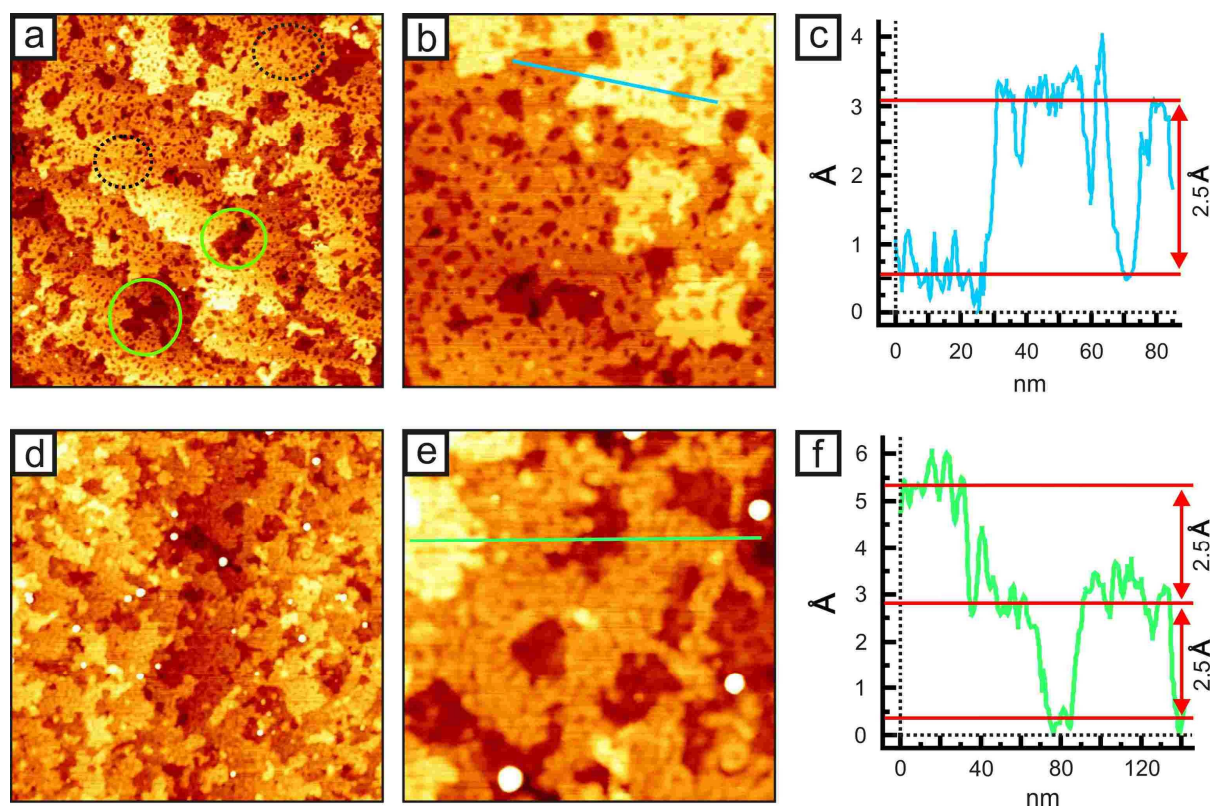


**Figure 6.2.1-1:** STM images after the oxidation of 1.5 ML (a,b) and 4.0 ML (d,e) deposited ruthenium on  $Au(111)$  by  $O_2$  at 680 K, respectively. In both cases an inhomogeneous film covers the surface, containing minor (highlighted in dotted black circles in a) and major defects (highlighted in green circles in a). An average step height of 2.5 Å for this film was determined by statistic line scan analysis (c,f). STM images: Oxidation of 1.5 ML Ru (a) 400 nm x 400 nm, (b) 150 nm x 150 nm; Oxidation of 4 ML Ru (d) 400 nm x 400 nm, (e) 150 nm x 150 nm. Tunneling conditions:  $U = 0.4 - 0.8$  V,  $I = 3.0 - 10.0$  nA.

As depicted by the STM images the morphology changed significantly for both, i.e. the former 1.5 ML and 4.0 ML thin ruthenium film, respectively. Contrary to the oxidation of a  $Ru(0001)$  single crystal surface no typical  $RuO_2(110)$  structures could be found, which should

have formed at these oxidation conditions. Instead a flat but inhomogeneous film is covering the gold surface (*cf. figures 6.2.1-1a and 6.2.1-1d*). A zoom in of the surface (*cf. figure 6.2.1-1b,e*) show that the inhomogeneous film consists of randomly distributed minor holes (dotted black circles, *figure 6.2.1-1a*) as well as larger defect areas or holes within the first several layers of the perforated film (green circles, *figure 6.2.1-1a*). In the following, the minor holes will also be referred as “minor defects” and the large holes as “major defects”.

From the major defects in the film, the structure of the underlying layers becomes visible, which also contains these minor holes, thus giving the impression of a porous structure. It should be noted that only the top film layers of this perforated structure is observable by STM. Therefore it *cannot* be determined via STM alone if this perforated structure is continuously formed between the Au(111) surface and the topmost film layer. Besides the morphologic similarities between the oxidized 1.5 ML and 4.0 ML ruthenium film, some structural differences are revealed by STM. After oxygen exposure to the 4.0 ML Ru/Au(111) surface, small clusters are formed additionally, which are located on top of the perforated film. Furthermore the lateral size of the minor defects has decreased significantly (*cf. figure 6.2.1-1e*).

But what is the chemical nature of this perforated film? In the following it will be elucidated that this film most likely consists of metallic ruthenium with a chemisorbed oxygen species. In principle an alloy between gold and ruthenium could also be responsible for this rather unique structure, too. But this assumption is refuted by the following considerations: At first, even if a surface alloy was initially formed between metallic ruthenium and metallic gold by the incorporation of ruthenium atoms in the first Au(111) layer, the exposure of oxygen leads to the formation of rather strong ruthenium-oxygen bindings compared to the weaker ruthenium-gold bindings. Therefore the oxygen treatment induces the release of the ruthenium atoms from the first gold layers, regardless of the former structure, i.e. a Au-Ru surface alloy or embedded small ruthenium islands in the first layer. This oxygen induced de-alloying between two metals has been reported for the Mo/Au(111) system, too.<sup>[223]</sup> Secondly the complimentary system (Au/Ru(0001)) has never shown the formation of a surface alloy. The assumption of a surface alloy between metallic gold and ruthenium was only made on the basis of the STM images where ruthenium is incorporated in the first layer of the Au(111) surface. However this is not the case for the Au/Ru(0001) system, where the ruthenium surface is too rigid and gold atoms are not incorporated. So if the perforated film may consist of a gold-ruthenium alloy, gold atoms from the Au(111) surface have to get incorporated into the rough ruthenium film of merged islands, which seems rather unlikely, especially if the

rough film is thicker (e.g. 4 ML). Based on this argumentation, the perforated film is considered to consist solely of ruthenium with no gold incorporated. A ultimate conclusion would be possible by depth profiling via a high resolution XPS or time of flight secondary ion mass spectrometry (TOF-SIMS).

An explanation for the perforated structure is attempted, based on the assumption that the ruthenium film is gold free. The minor defects are most probably induced by the lattice misfit between the ruthenium film and the Au(111) surface, thus leading to a lateral strain in the growing film. If the strain is too large the attachment of an additional ruthenium atom is energetically not favorable and defects or holes are formed to release the lateral strain. The observed decrease of the lateral size of these holes, with increasing thickness of the former rough film of merged ruthenium islands, corroborates this view.

The major defects can be explained by the mobility of the diffusing ruthenium atoms on the surface. Considering that oxidized ruthenium wants to form a covering film on the Au(111) surface (due to the lower surface free energy), ruthenium atoms have to diffuse from the top layers of the three-dimensional islands to the gold surface. If the amount of diffusing ruthenium atoms is significantly higher than the mean free pathway or the mobility of these atoms, a rougher film with more and larger defects will be formed due to a higher nucleation rate.

The formation of clusters after the oxygen treatment of the 4 ML Ru may be an indication for the beginning of the RuO<sub>2</sub> formation (*cf. figure 6.2.1-1d,e*). It is known in literature that the gas phase oxidation of Ru(0001) leads to the formation of RuO<sub>2</sub>(110) via an nucleation and growth mechanism.<sup>[190]</sup> The observed clusters on the perforated ruthenium film might be similar to the critical nuclei that are formed in the initial gas phase oxidation process on Ru(0001). However the chemical nature of these clusters has not been determined yet. But it is assumed that these clusters consist of a RuO<sub>x</sub> structure.<sup>[92,200]</sup>

An average step height of 2.5 Å was determined by line scan analysis for this porous ruthenium layers (*cf. figures 6.2.1-1c and 6.2.1-1f*), which rather fits to the step height of metallic ruthenium (2.2 Å) than to RuO<sub>2</sub>(110) (3.2 Å).<sup>[185]</sup> The corresponding XPS measurements of the O 1s, and the Ru 3d signal areas are presented in *figure 6.2.1-2*.

After oxygen treatment an O 1s signal at 530.2 eV is observable as well as the simultaneous decrease of the neighboring Au 4p<sub>3/2</sub> signal (*cf. figure 6.2.1-2b*). The Ru 3d<sub>5/2</sub> signals do a slight shift from 279.9 eV (black curve, ruthenium prior to oxidation) to 280.2 eV (blue curve, after oxidation) upon the oxygen exposure, and again the decrease of the neighboring gold signals (Au 4d) is visible (*cf. figure 6.2.1-2a*).

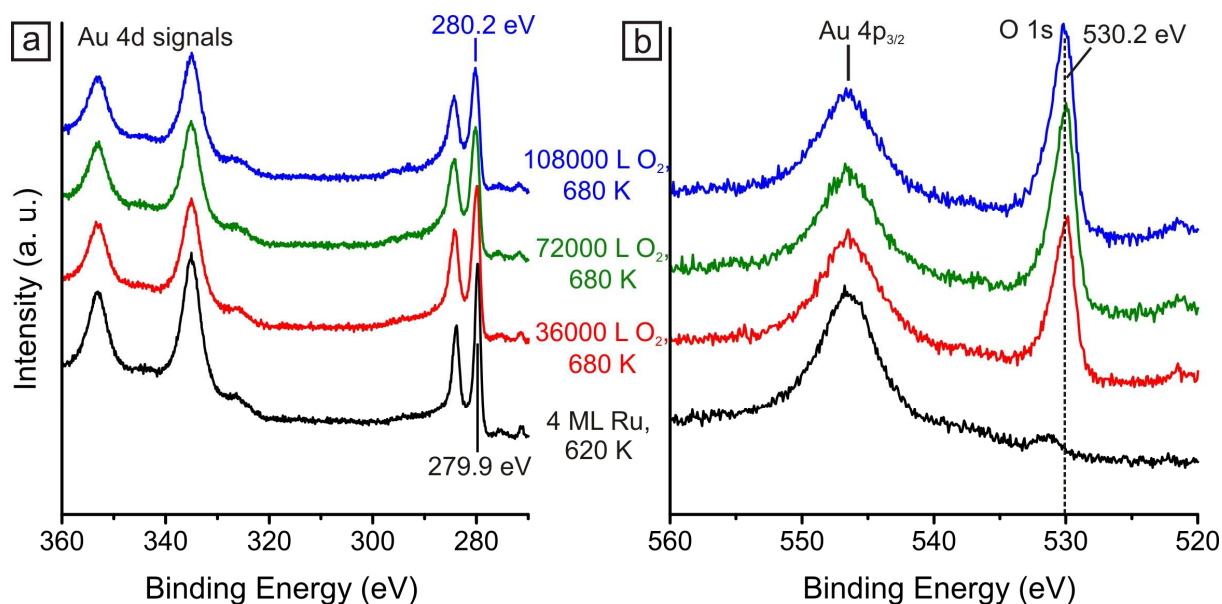


**Figure 6.2.1-2:** XPS spectra of the Ru 3d and O 1s signal regions illustrate the oxidation of a 4 ML ruthenium film by  $O_2$  at 680 K. The XPS data for the exposure of 36000 L  $O_2$  (red curves) corresponds to the STM images from figure 6.2.1-1d,e. The O 1s signal at 530.2 eV and the slightly shifted Ru 3d signals (by 0.3 eV to higher binding energies) evidently show the oxygen evolution on the surface and the formation of Ru-O bonds.

The observed decrease of the Au signals (Au 4d and 4p) can be explained by the morphologic changes of the deposited ruthenium. After the deposition of 4 ML Ru, gold is either still exposed at the surface or is only slightly overgrown where the ruthenium islands just merged together. By oxidation a more and more continuous and covering perforated Ru film with a rather uniform height is formed, thus attenuating the Au signals due to the limited depth resolution of XPS.

The interpretation of the Ru 3d signals and the O 1s signal is more complicated. The chemical shift of the Ru 3d signals by 0.3 eV to higher binding energies can be assigned to the loss of electron density of ruthenium after the oxygen exposure due to the formation of Ru-O bindings.<sup>[227]</sup> However, discrimination between the formation of a ruthenium oxide or a chemisorbed phase on ruthenium on the basis of the Ru 3d signals is difficult. In principle these species are discriminable, but the differences of the binding energies are very low ( $\leq 0.3$  eV for  $RuO_2(110)$  or  $RuO_2(100)$  vs.  $(1 \times 1)O-Ru(0001)$ ).<sup>[8,227]</sup> The energy resolution of the used XPS spectrometer is too low ( $\sim 0.5$  eV) to reliably differentiate between ruthenium oxide or chemisorbed oxygen phase. But a differentiation between  $RuO_2$  or a chemisorbed oxygen phase on the basis of the O 1s signal is more reliable due to a larger binding energy difference ( $> 0.6$  eV) and a significant higher peak intensity for  $RuO_2$ , compared to a chemisorbed oxygen phase. During the oxygen treatment and the ruthenium film formation the O 1s signal stays at 530.2 eV and does not shift to lower binding energies (*cf.* figure 6.2.1-2b). This

strongly indicates the formation of a chemisorbed oxygen phase on metallic ruthenium. For comparison: the O 1s binding energies for RuO<sub>2</sub>(110) or a (1x1)O phase on Ru(0001) are 529.5 eV or 530.1 eV, respectively.<sup>[8]</sup> Also the O 1s signal intensity (*cf. figure 6.2.1-2b*, red curve) is qualitatively comparable to a (1x1)O phase on Ru(0001). The slight increase in height for further dosages is assigned to the formation of the RuO<sub>x</sub> clusters (*cf. figure 6.2.1-1d,e*).

In conclusion, the exposure of O<sub>2</sub> to the rough film of merged Ru islands ( $\leq 4$  ML Ru) with typical oxidation conditions ( $p(\text{O}_2) = 2 \cdot 10^{-5}$  mbar, 680 K) did not lead to the formation of RuO<sub>2</sub>. Instead a perforated inhomogeneous film is formed that consists of metallic ruthenium with chemisorbed oxygen. The transformation of three-dimensional metallic ruthenium islands to a rather two-dimensional wetting film is facilitated by the chemisorbed oxygen. The oxygen evidently reduces the surface free energy of ruthenium so significantly that the energy relation from Young's equation is now in favor of a two-dimensional film instead of the three-dimensional islands ( $\sigma_{Au} > \sigma_{O/Ru}$ ). The question, why no RuO<sub>2</sub> has been formed under these typical oxidation conditions, will be elucidated in the next section.

## 6.2.2 Formation of RuO<sub>2</sub>(110) by oxidation of 10 ML Ru/Au(111)

Although a first indication for the oxidation of the 4 ML film of merged Ru islands is visible on the basis of the formed clusters (*cf. figure 6.2.1-1d,e*), it is still unclear why flat RuO<sub>2</sub> layers have not been formed by using the typical Ru(0001) single crystal oxidation conditions. With a (0001) orientation of the 4 ML deposited ruthenium, its oxidation is assumed to be similar. In literature, the thickness of a growing ultrathin RuO<sub>2</sub>(110) is determined to be at least 3 to 4 layers.<sup>[145,190,191]</sup> While the interface is well defined in the RuO<sub>2</sub>/TiO<sub>2</sub>(110) system, the binding the oxide and the metallic substrate at the interface is unknown for the RuO<sub>2</sub>/Ru(0001) system. In case of the oxygen treatment of the 4 ML Ru/Au(111) surface, a hypothetical 3 to 4 layered RuO<sub>2</sub> would either bind directly to the Au(111) substrate surface or only a very thin layer of metallic ruthenium would be located at the interface between the oxide and the gold substrate. Due to the weak interactions between oxygen and the gold surface it is assumed that RuO<sub>2</sub> structures are not stable on or near the Au(111) surface. This raises the question how much deposited Ru is necessary on the Au(111) surface before it can readily be oxidized to RuO<sub>2</sub>. To investigate this question, larger amounts of ruthenium (10 ML) were evaporated to the Au(111) surface to increase the thickness of the film of merged Ru islands and to create a “buffer” layer of metallic Ru on which RuO<sub>2</sub> can be formed.

At first 7000 L molecular oxygen were dosed to the 10 ML Ru/Au(111) surface at room temperature to form a chemisorbed oxygen phase on the merged ruthenium islands, which have (0001) orientation. Generally, at room temperature the oxidation of Ru(0001) by O<sub>2</sub> is prevented and only a chemisorbed oxygen layer with a coverage up to 0.5 ML can be formed by this procedure.<sup>[174]</sup> Afterwards the 10 ML Ru were oxidized by annealing the surface to 680 K in an oxygen environment of  $p(\text{O}_2) = 2 \cdot 10^{-5}$  mbar for 30, 50 and 80 minutes. By the exposure of these high dosages of O<sub>2</sub> on the 10 ML Ru/Au(111) surface, the oxidation and formation of a RuO<sub>2</sub>(110) film was facilitated. The corresponding XPS data of this oxidation are presented in *figure 6.2.2-1*.

The XP spectrum of the as-prepared 10 ML ruthenium film shows a small and broad O 1s signal with its maximum at ~ 531.0 eV (*cf. figure 6.2.2-1*, black curve a). The subsequent exposure of 7000 L O<sub>2</sub> at room temperature towards the rough ruthenium film leads to an increase of the O 1s signal without any measurable chemical shift (*cf. figure 6.2.2-1*, purple curve). Upon oxidation, the O 1s signal has increased significantly and is shifted to lower binding energies from 530.1 eV after 30 minutes of oxygen exposure (*cf. figure 6.2.2-1*, green curve c) to 529.8 eV after 80 minutes of oxygen exposure (*cf. figure 6.2.2-1*, blue curve e).

STM images are presented in *figure 6.2.2-2* to illustrate the surface after 80 minutes of oxidation.

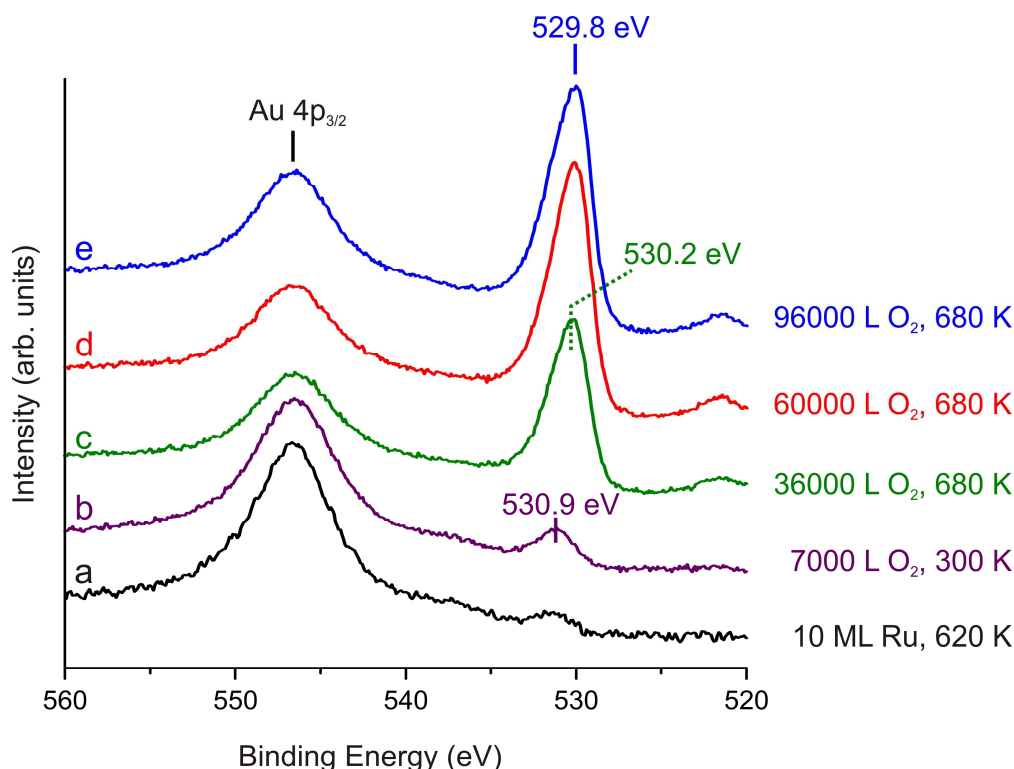


**Figure 6.2.2-1:** XPS spectra of the O 1s signal after exposure of O<sub>2</sub> on the 10 ML ruthenium film of merged islands at room temperature and the subsequent oxidation at 680 K with increasing amounts of oxygen (c,d,e). The shift to lower binding energies and the increase of the O 1s signal indicates the formation of RuO<sub>2</sub>.

The STM images evidently display the formation of flat RuO<sub>2</sub>(110) islands (*c.f. figure 6.2.2-2a,b*). Magnification of the flat RuO<sub>2</sub>(110) terraces reveals the typical oxygen bridge rows with its interatomic distance of 6.3 Å (*cf. figure 6.2.2-2e*). The thickness of the oxide is determined by line scan analysis (*cf. figure 6.2.2-2c*). With a height of 16.5 Å and 19.9 Å, a thickness of five and six layers can be assigned to the formed RuO<sub>2</sub>(110) patches, respectively. The stripe-like patches of RuO<sub>2</sub>(110) seen in *figure 6.2.2-2b* show two distinct rotational domains, that are rotated by 120° with respect to each other. This growth behavior is analogous to RuO<sub>2</sub>(110) grown on Ru(0001). For the Ru(0001) single crystal surface, the formation of three rotational domains results from the transition of the higher symmetry of the underlying Ru substrate (3-fold) to the lower symmetry of the rectangular unit cell of RuO<sub>2</sub>(110) (2-fold).<sup>[192]</sup> When applying this information to the STM pictures from *figure 6.2.2-2*, it can be concluded that the substrate below the RuO<sub>2</sub>(110) patches must also exhibit 3-fold symmetry.

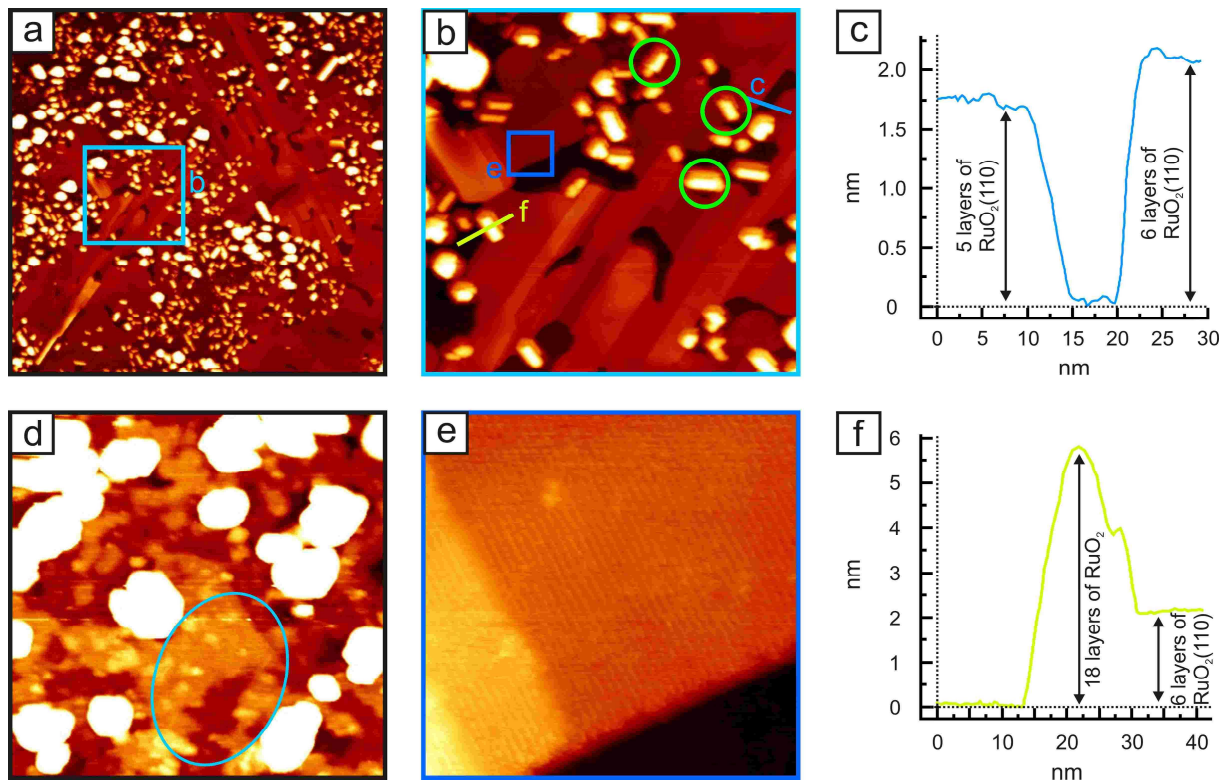


**Figure 6.2.2-2:** STM images of the oxidized 10 ML ruthenium film after a total exposure of 96000 L  $O_2$  at 680 K. (a)  $1.0 \mu\text{m} \times 1.0 \mu\text{m}$  scan of the oxidized surface; (b)  $200 \text{ nm} \times 200 \text{ nm}$  magnification of an area with grown  $\text{RuO}_2(110)$  patches (marked blue in (a)); (c) The line scan analysis illustrates the thickness of the formed  $\text{RuO}_2(110)$  film (d) magnified  $120 \text{ nm} \times 120 \text{ nm}$  area where no  $\text{RuO}_2(110)$  islands are present on the surface; (e)  $30 \text{ nm} \times 30 \text{ nm}$  magnification of the  $\text{RuO}_2(110)$  patches, showing atomic resolution of the oxygen bridges; (f) line scan analysis illustrates the height of one formed  $\text{RuO}_2$  crystallite. Tunneling conditions:  $U = 1.2 - 1.5 \text{ V}$ ,  $I = 0.8 - 1.0 \text{ nA}$ .

Besides the flat  $\text{RuO}_2(110)$  films very high islands or clusters are formed, too, which are also rotated by  $120^\circ$  with respect to each other (cf. green circles in *figure 6.2.2-2b*). With regard to the symmetry relations between the  $\text{RuO}_2(110)$  domains and the underlying film in *figure 6.2.2-2b*, this indicates a faceted oxide structure for these rotated islands. Line scan analysis reveals that these clusters and islands are significantly thicker ( $\sim 6 \text{ nm}$ ) than the flat oxide patches ( $< 2 \text{ nm}$ ) (cf. *figure 6.2.2-2f*). But with no atomic resolution the exact structure of these faceted islands remains elusive. The magnification shown in *figure 6.2.2-2d* depicts the morphology of the surface to which these faceted islands are binding. A closer inspection of the underlying surface reveals an inhomogeneous film with many larger defects in its top layer (cf. *figure 6.2.2-2d*, light blue circle). From the morphology of this film, its similarities towards the previously described perforated ruthenium film are evident (cf. *figure 6.2.1-1*). But due to the very big height differences ( $> 6 \text{ nm}$ ) on the surface, a better resolution of the underlying substrate was not achieved. Therefore the typical minor defects or holes could not be resolved and a firm assignment is not possible. But from the rotation domains of the grown

faceted islands, the symmetry of the underlying film can be determined to be either trigonal or hexagonal, which supports the interpretation of the underlying perforated ruthenium film.

By comparing the observed structures in the STM images to the corresponding XPS data, further interpretations of the O 1s signals are possible. The O 1s signal with a high intensity and a binding energy 529.8 eV (*cf. figure 6.2.2-1*, blue curve e) is now clearly assigned to the formation of flat RuO<sub>2</sub>(110) structures. For comparison the O 1s signal after 30 minutes of oxygen treatment has a binding energy of 530.2 eV. Its intensity and binding energy is comparable to the O 1s spectra of the perforated film with many clusters located on top of it. Therefore the exposure of O<sub>2</sub> at these conditions is related to the so-called nucleation phase of the Ru(0001) oxidation mechanism, where small RuO<sub>x</sub> clusters are formed from which the growth of RuO<sub>2</sub>(110) is enabled.<sup>[190]</sup> The binding energy difference between the perforated ruthenium film and the grown oxide (~ 0.4 eV) patches is comparable to the binding energy difference for a chemisorbed oxygen phase and a formed RuO<sub>2</sub>(110) on the Ru(0001) single crystal surface (0.6 eV)<sup>27</sup>.

The interpretation of the O 1s signal after exposure of 7000 L O<sub>2</sub> at room temperature is elusive. By this preparation a chemisorbed oxygen phase with coverages up to 0.5 ML on the rough ruthenium film should be formed. While the O 1s signal intensity is in principle comparable to a (2x2)O overlayer structure on Ru(0001), the binding energy difference towards the RuO<sub>2</sub> O 1s signal (*cf. figure 6.2.2-1*, at 529.8 eV) is too large ( $\geq 1.1$  eV). Therefore a clear assignment for this oxygen species is not possible at this point and an interpretation would be speculative.

In conclusion, the oxidation behavior of a rough ruthenium film on the Au(111) surface (*cf. figure 6.1-1*) has significantly changed by increasing the amount of deposited Ru. Due to the weak gold-oxygen binding, RuO<sub>2</sub> bound directly to the Au(111) surface is assumed to be unstable. But RuO<sub>2</sub>(110) can readily be formed if the rough Ru film thickness on the Au(111) substrate is increased, e.g. by deposition of 10 ML Ru on the Au surface. This evidently proves that the Au(111) substrate significantly inhibits the oxidation of the deposited ruthenium. If the amount of deposited Ru is too low ( $\leq 4$  ML), only a reconstruction of the rough ruthenium film of merged islands to an oxygen stabilized, flat and perforated film on the Au(111) surface is observed. Although the formation of RuO<sub>2</sub> has only been proven for the oxidation of 10 ML Ru/Au(111) surface, it is assumed that about 6 ML of Ru might already be sufficient, so a three layered RuO<sub>2</sub> can be formed on a 3 ML thick metallic ruthenium buffer layer. As already shown, the oxygen treatment of the 4 ML Ru/Au(111) surface leads

---

<sup>27</sup> O 1s binding energies: for chemisorbed oxygen on Ru(0001) 530.07 eV; for RuO<sub>2</sub>(110) on Ru(0001) 529.5 eV.[8]

to the formation of critical nuclei on top of the perforated ruthenium film. Starting from these nuclei the formation of thin (3 layered)  $\text{RuO}_2$  film may occur, which is partially covering the metallic ruthenium, if the amount of deposited ruthenium is sufficient ( $\geq 6$  ML in total). However this threshold value for the critical amount of deposited ruthenium, which can readily be oxidized, needs to be verified. Oxidation experiments of rough ruthenium films with stepwise increasing amounts of deposited Ru (e.g. 5 ML, 6 ML, 7 ML, etc.) are one possibility to clarify this question. Also the influence of the Au(111) surface on the deposited ruthenium is still unclear. It evidently inhibits the oxidation capability of the (0001) oriented rough ruthenium film. Evidently 1 ML of metallic ruthenium, acting as a buffer layer, is not sufficient to stabilize the formation of a three layered  $\text{RuO}_2$  film at the chosen oxidation conditions (cf. the oxygen treatment of the 4 ML Ru/Au(111) surface, chapter 6.2.1). Theoretical investigations (e.g. DFT calculations) as well as thickness dependent STS measurements are one possibility to examine the influence of the underlying Au(111) substrate on the electronic structure of the (0001) oriented rough ruthenium film.

### 6.2.3 Thermal stability of the perforated ruthenium film

Besides the described STM and XPS measurements of the oxidation of Ru deposited on Au(111), further studies are mandatory for a better understanding of the chemical nature and properties of the perforated ruthenium film. One of these questions is related to the influence of the chemisorbed oxygen on the film morphology: *If the oxygen is removed, is it possible to restore the three-dimensional structure of hexagonal metallic ruthenium islands on the Au(111) surface?*

The following experiment addresses this question by investigating the thermal stability of the perforated ruthenium film. The series of STM images presented in *figure 6.2.3-1* illustrates the morphologic changes by annealing the ruthenium film to 750 K in vacuum.

Starting from the rough ruthenium film (4 ML) formed on Au(111) at 620 K (*cf. figure 6.2.3-1a*), a perforated but flat ruthenium film (*cf. figure 6.2.3-1b*) can already be prepared by exposure of 2000 L O<sub>2</sub> ( $p(\text{O}_2) = 2 \cdot 10^{-5}$  mbar) at 680 K. By STM the typical smaller and larger holes in the film are visible. However this film consists of a rather flat morphology with wide terraces, which is different to the previously described morphology of the perforated ruthenium films (*cf. figure 6.2.1-1*) that have been prepared at higher exposures of oxygen (36000 L O<sub>2</sub>). Further oxygen exposure of 12000 L O<sub>2</sub> to the rather flat perforated ruthenium film led to an increase of its overall roughness, i.e. the terrace size decreased while the serration of the step edges increased (*cf. figure 6.2.3-1c*). These STM images evidently show that the formation of the perforated ruthenium film is fast and low dosages of O<sub>2</sub> (~2000 L) are already sufficient for its preparation.

The thermal decomposition of the porous ruthenium film was achieved by annealing in vacuum to 750 K for 30 min (*cf. figure 6.2.3-1d*). The ruthenium film is still covering the Au(111) surface, but its structure has changed. On the one hand the roughness has slightly decreased, while on the other hand the top layer of the ruthenium film rearranges to more hexagonally shaped islands (*cf. figure 6.2.3-1d*, blue circles). This change is intensified by further annealing in vacuum for additional 90 minutes (*cf. figure 6.2.3-1e*). After this second annealing step, connected hexagonal ruthenium islands are clearly visible by STM. Line scan analysis revealed that these ruthenium islands are very high, i.e. up to 4 layers (*cf. figure 6.2.3-1f*). Although the perforated film has rearranged to hexagonal islands, the morphology is significantly different to the as-prepared Ru islands by PVD (*cf. figure 6.2.3-1a*). The hexagonal structure of the rearranged Ru islands is better pronounced and the top layer terrace width is much larger.

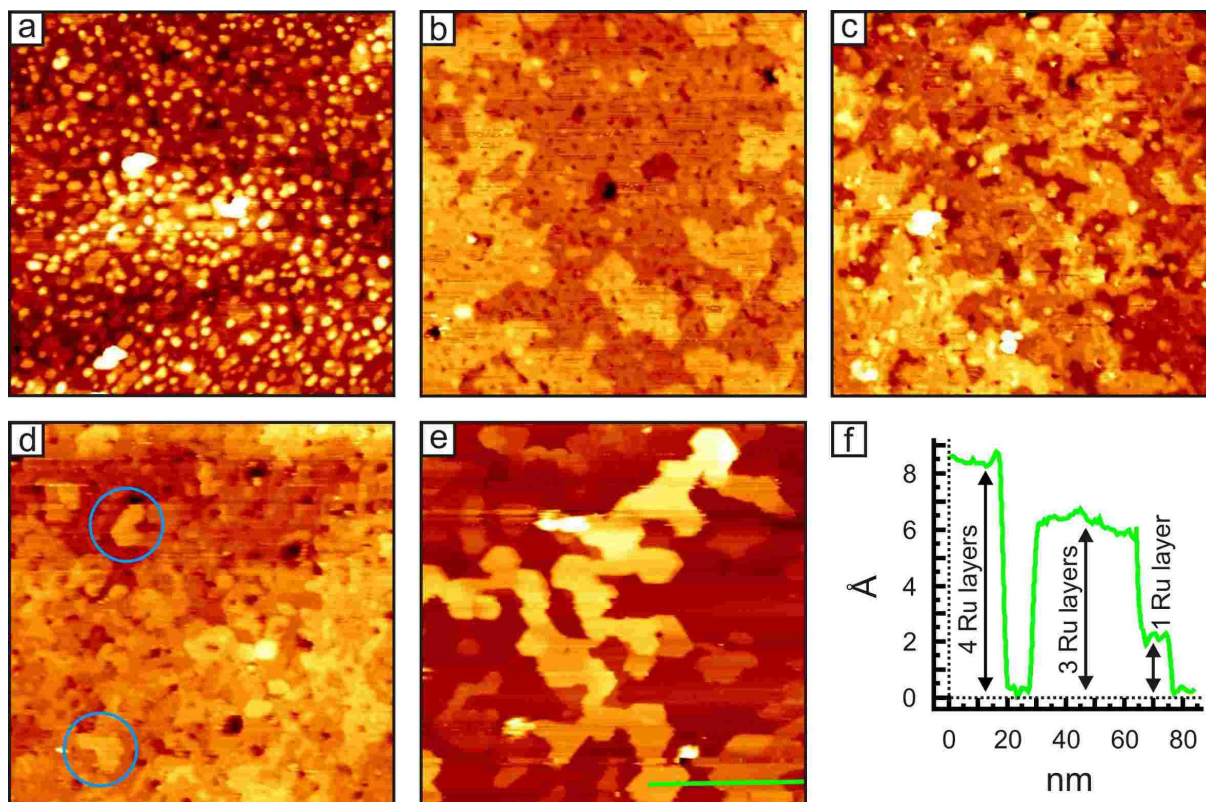


**Figure 6.2.3-1:** Thermal decomposition of the porous oxidized ruthenium film. (a) 4 ML Ru deposited at 620 K (200 nm x 200 nm); (b) Oxidation by 2000 L O<sub>2</sub> ( $p(\text{O}_2) = 2 \cdot 10^{-5}$  mbar) at 680 K (200 nm x 200 nm); (c) Additional dosage of 12000 L O<sub>2</sub> ( $p(\text{O}_2) = 2 \cdot 10^{-5}$  mbar, 680 K) (200 nm x 200 nm); (d) Annealing in vacuum: 750 K, 30 min (200 nm x 200 nm); (e) Annealing in vacuum: 750 K, additional 90 min (200 nm x 200 nm); (f) Line scan analysis of the reduced porous ruthenium shows the formation of thick ruthenium islands (up to 4 layers). Tunneling conditions:  $U = 0.9 - 1.3$  V,  $I = 1.0 - 8.0$  nA.

As previously described (cf. chapter 6.2.1), the rearrangement of the merged Ru islands to the rather flat perforated ruthenium film is accomplished by the diffusion of a mobile ruthenium species (RuO<sub>x</sub>) from the top layers of the Ru islands to the Au(111) surface. *Figure 6.2.3-1b* evidently illustrates the high formation rate of the perforated film. This leads to the assumption that the mobile RuO<sub>x</sub> species is formed rather easily so the rearrangement from the rough three-dimensional ruthenium islands to the flat (perforated) ruthenium film occurs quickly. The increase in overall roughness of the perforated ruthenium film with increasing exposures of O<sub>2</sub> (cf. *figure 6.2.3-1c*) is assumed to stem from the continuous formation, diffusion, agglomeration and decomposition of RuO<sub>x</sub> precursors. By comparing the morphology of this roughened film (cf. *figure 6.2.3-1c*) to the morphology of the underlying substrate beneath the RuO<sub>x</sub> clusters and the RuO<sub>2</sub>(110) patches (cf. *figure 6.2.2-2d*, blue circle), the similarities are evident. Thus the observed corrosion indicates an onset of the oxidation of the perforated ruthenium film.

But the most important information of this experiment is the applied temperature of 750 K, where the thermal decomposition of the perforated ruthenium film is visualized by STM. Although this decomposition was confirmed *ex situ* after annealing in vacuum for 120 minutes, this temperature is a first set point for the thermal stability of the porous ruthenium layer. Based on the STM images, the restoration of three-dimensional ruthenium islands on the Au(111) surface is assumed to occur between 30 minutes (*cf. figure 6.2.3-1d*) and 120 minutes (*cf. figure 6.2.3-1e*) of annealing in vacuum. A precondition for this island reformation is the loss of chemisorbed oxygen, which is assumed to stabilize the two-dimensional spreading of ruthenium on the Au(111) surface. However the applied temperature of 750 K in vacuum is below the measured desorption temperatures for ruthenium-oxygen species from the Ru(0001) surface in literature.<sup>[185]</sup> The thermal decomposition of RuO<sub>2</sub>(110)/Ru(0001) and the resulting O<sub>2</sub> desorption of this decomposition process is observable around 1040 K. If chemisorbed oxygen phases (e.g. the (1x1)O) were present on Ru(0001), the desorption maximum of O<sub>2</sub> occurs above 1100 K. In recent studies a ruthenium-oxygen species was prepared whose decomposition and O<sub>2</sub> desorption is observable around 750 K to 800 K.<sup>[197]</sup> Herd et al. suggested that this O<sub>2</sub> desorption signal stems from the thermal decomposition of the critical RuO<sub>x</sub> nuclei from which the formation of RuO<sub>2</sub>(110) starts.<sup>[92,197]</sup> This shows that ruthenium-oxygen species exist that have a lower stability in vacuum than the well known RuO<sub>2</sub>(110) or chemisorbed oxygen phase on the Ru(0001) surface. This leads to assumption that the perforated ruthenium film is also a less stable ruthenium-oxygen structure that can readily decompose at temperatures below 800 K due to a partial loss of chemisorbed oxygen by O<sub>2</sub> desorption.

However, it has to be emphasized that within the mentioned TDS experiments from literature the high temperatures are usually reached by steep heating ramps (several K/s). Therefore the mentioned O<sub>2</sub> desorption temperatures for the different ruthenium-oxygen species ( $\geq 1040$  K)<sup>[185]</sup> cannot be compared directly to the thermal decomposition temperature of the perforated ruthenium film. For a better comparison of the thermal stability of the perforated ruthenium film to the literature, TDS experiments and a series of *ex situ* thermal decomposition experiments, which are monitored by XPS and STM, are mandatory.

### 6.3 Proposed mechanism for the formation of the perforated ruthenium film

The oxygen treatment of the merged Ru islands leads to the formation of a covering perforated ruthenium film. To explain the unique structure of this film a mechanism for its formation is proposed. A schematic illustration is given in *figure 6.3-1* by a top and side view on the different atomic processes that are included in the mechanism. This proposed mechanism is solely focusing on the oxidation of the ruthenium islands and the formation of the perforated ruthenium film by mobile ruthenium atoms. The distortion of the Au(111) herringbone structure is not shown within this mechanism.

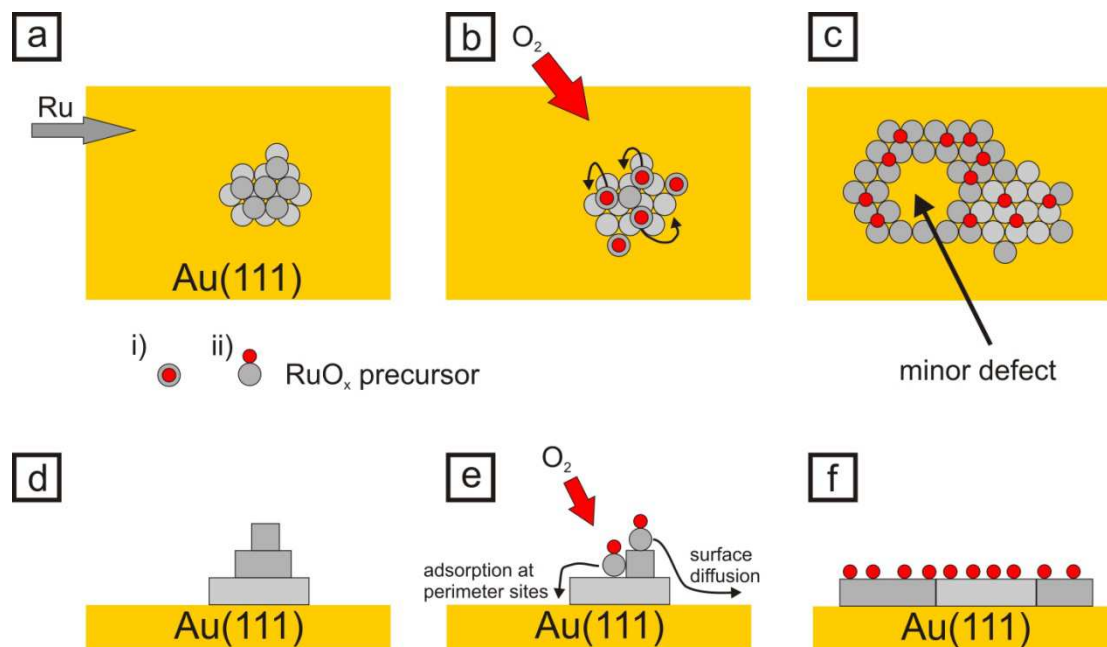


**Figure 6.3-1:** Schematic illustration of the proposed mechanism for the formation of the perforated ruthenium film on Au(111) by oxygen exposure to the rough ruthenium film. Top view (a-c) and side view (d-f). The changes of the Au(111) herringbone reconstruction are not included in this schematic illustration, because the proposed mechanism for the perforated ruthenium film solely concentrates on the oxidation of the Ru islands and the rearrangement of the Ru atoms on the surface. (a,d) Physical vapor deposition of Ru on the Au(111) surface at higher temperatures (e.g. 620 K) leads to the formation of ruthenium islands. (b,d) Exposure of oxygen to the Ru/Au(111) surface induces the dissociative adsorption of  $O_2$  exclusively on the ruthenium islands with the subsequent formation of the mobile  $RuO_x$  precursors. The  $RuO_x$  precursors diffuse downwards to the Au(111) surface where they either get stuck at the perimeter sites or they diffuse on the Au(111) surface. (c,f) Further attachment of diffusing  $RuO_x$  precursors causes the formation of a covering ruthenium film with oxygen bound on top of it. The mobile  $RuO_x$  precursors are assumed to bind to certain perimeter sites but not others, due to increasing local strain in the ruthenium film. This leads to small areas where no ruthenium atoms are attached, i.e. the so-called minor defects or holes.

After the deposition of ruthenium on the Au(111) surface at 620 K, small and isolated ruthenium islands are formed (*cf. figure 6.3-1a,d*). From the hexagonal shape of the islands, a hcp(0001) orientation for the deposited ruthenium is assumed. On these small islands the exposed O<sub>2</sub> can adsorb dissociatively thus forming mobile RuO<sub>x</sub> precursors at 650 K (*cf. figure 6.3-1b,e*). The formation of such mobile RuO<sub>x</sub> precursors was proposed in literature for the initial oxidation of Ru(0001) single crystal surface by O<sub>2</sub>.<sup>[190]</sup> With the same crystallographic orientation of the grown Ru islands on Au(111), it is also expected that a similar mobile RuO<sub>x</sub> species is involved in this oxidation process<sup>28</sup>. Due to the nobility of gold, the dissociative adsorption of O<sub>2</sub> on the Au(111) surface is very unlikely, especially at a temperature of 680 K, where every known gold-oxygen species should be decomposed immediately (*cf. TDS data in table 1.2-1*). The formed mobile RuO<sub>x</sub> precursors are diffusing downwards from the top of the Ru islands towards the Au(111) surface (*cf. figure 6.3-1b,e*). Depending on the stability and mobility of the RuO<sub>x</sub> precursors on the gold substrate, either further diffusion over the Au(111) surface is possible or the attachment of the precursors at the perimeter sites of the Ru island and the Au substrate occurs (*cf. figure 6.3-1e*). The continuous formation of RuO<sub>x</sub> precursors on the top ruthenium layers induces the attachment of more and more ruthenium atoms at the perimeter sites by the downward diffusion precursors, thus leading to a wetting ruthenium film with adsorbed oxygen bound on top of it (*cf. figure 6.3-1c,f*). The chemisorbed oxygen on the flat and perforated ruthenium film is very important for its wetting behavior. While metallic ruthenium rather tends to grow three-dimensional to islands in absence of oxygen, this is different if chemisorbed oxygen is available. By significantly decreasing the surface free energy of ruthenium<sup>[187]</sup> the chemisorbed oxygen phase facilitates the two-dimensional spreading on the Au(111) surface. The porosity of the wetting ruthenium film is induced by local strain. A similar effect of a inhibited lateral attachment of atoms at perimeter sites has been reported for the system of Ag nanoparticles on CeO<sub>2-x</sub>(111).<sup>[137]</sup> Campbell et al. pointed out that the local strain maximizes at the Ag nanoparticle island edges, which prohibits further agglomeration of Ag atoms at these nanoparticles. They also stated that these local strain effects are very important for the morphology and the nucleation and growth of deposited metals. Adapted from this model of local strain, the formation of the small holes in the perforated ruthenium film is assumed to stem from a similar effect of local strain within the ruthenium film. It is assumed that not all perimeter sites are energetically equal for the attachment of RuO<sub>x</sub> precursors due to increasing strain with increasing lateral expansion of the wetting film. Accordingly the precursors

---

<sup>28</sup> Keeping in mind that the oxidation conditions for the oxidation of the hexagonally shaped Ru islands on Au(111) are the same as in the Ru(0001) single crystal oxidation.

preferentially bind to perimeter sites where the local strain is not too big. As a consequence, small (minor) holes in the ruthenium film are formed at the perimeter sites, where the local strain is too high for the attachment of RuO<sub>x</sub> precursors.

With this mechanism it is also possible to describe the presence of the larger holes in the perforated ruthenium film (*cf. figure 6.2.1-1*, green circles). The exposure of O<sub>2</sub> to the surface results in the formation of tremendously high amounts of RuO<sub>x</sub> precursors on the surface. For these many RuO<sub>x</sub> precursors, their mean free pathway for surface diffusion is significantly reduced, which results in a higher nucleation rate and therefore a higher density of smaller islands. If these islands do not merge together completely, larger holes in upper layers of the perforated film structure are formed.

In principle this high nucleation rate is comparable to an epitaxially growing material which is deposited on a surface with very high deposition rates. For instance: In the FvdM-growth a single covering adlayer is formed, before the next layer starts to grow. This can be achieved if lower deposition rates are applied, so the deposited atoms can freely diffuse on the surface and no nucleation on top of the formed layer occurs. But if the deposition rate is strongly increased, nucleation of the deposited atoms on top of the already formed layer gets more and more pronounced. As a result a rough film of merged islands will be formed instead of a flat and homogeneous film.

This simplified mechanism describes the formation and the morphology of the perforated ruthenium film. However the disadvantages of this proposed mechanism are also revealed. By excluding the morphologic changes of the substrate (e.g. the loss of the herringbone overstructure and the reformation of the primitive Au(111)-1x1 surface) the important influence of the supporting substrate on the resulting morphology of the ruthenium film is not considered, yet. Additionally the interface between the ruthenium film and the Au(111) substrate is unknown. Therefore the local strain and its influence on the porosity of the ruthenium film needs to be proven by experiments or theoretical investigations. Generally, this mechanism is used as a first guideline to describe and understand the formation of the perforated ruthenium film and its morphology. An adoption of this mechanism on the basis of conducted experiments in the future will be mandatory.

## 6.4 Conclusion considering the growth and oxidation of Ru on Au(111)

Based on the STM measurements and the corresponding XPS data for the Ru/Au(111) system, the following conclusions can be drawn:

1. Ruthenium deposited by PVD on the Au(111) surface grows three-dimensional in a Volmer-Weber-like behavior, thus forming islands with hexagonal symmetry. This observed growth nicely reflects the expected growth behavior of metallic ruthenium on Au(111) based on the huge differences of their surface free energies ( $\sigma_{Ru} > \sigma_{Au}$ ). Simultaneous to the growth of Ru is the distortion and rearrangement of the gold herringbone reconstruction. The observable amount of Ru in the STM images is lower than the expected amount of Ru that was calculated on the basis of the deposition rate. This indicates an insertion of ruthenium into the top Au(111) layer by forming either a ruthenium-gold surface alloy or partially embedded ruthenium islands.
2. Oxygen exposure to the ruthenium islands leads to a perforated ruthenium film, which is covering the Au(111) surface. The porosity stems from small holes and larger holes or defects within the first layers of the ruthenium film. The small holes are formed to release strain of the ruthenium film, which is induced by the lattice misfit between Au(111) and the ruthenium film. The larger holes or defects in the first layers are explainable by the formation of too many mobile ruthenium atoms that nucleate to new islands instead of attaching to an already formed island step edge. By this high nucleation rate, a complete defect free growing film by merging of these growing islands is not formed. This is similar to the principle of deposition rate in epitaxial growth: A high deposition rate can lead to low mean free pathway of diffusing atoms and a high nucleation rate. As a result a rough film of merged islands would be formed instead of a well grown two-dimensional film (in case of FvdM-like growth behavior).
3. The characterization by XPS was done by preparing the well known RuO<sub>2</sub>(110) film on the Au(111) surface and using its O 1s signal as a reference value for the oxygen treated Ru/Au(111) system. With assigning the O 1s binding energy of 529.8 eV to the formed RuO<sub>2</sub>(110), a binding energy of 530.2 eV is assigned to the

perforated ruthenium film. This shift by  $\sim 0.4$  eV to higher binding energies indicates a chemisorbed oxygen phase on metallic ruthenium. Also the O 1s signal intensity of the perforated ruthenium film is comparable to a (1x1)O phase on the Ru(0001) single crystal surface. The formed chemisorbed oxygen phase is assumed to stabilize the perforated metallic ruthenium film. By the formation of ruthenium-oxygen bindings, the surface free energy of Ru is assumed to be lowered ( $\sigma_{O/Ru} < \sigma_{Au}$ ) that the formation of a two-dimensional film covering the Au(111) surface is favored.

4. The influence of the underlying Au(111) substrate on the grown ruthenium islands becomes evident by taking a closer look on the critical amount of Ru, which is necessary for the formation of RuO<sub>2</sub>(110) on the gold surface. Compared to the Ru(0001) single crystal surface, higher dosages of O<sub>2</sub> are necessary to form RuO<sub>2</sub>(110) from the hexagonally shaped ruthenium islands. Also the amount of Ru, deposited on the Au(111) surface, for the oxide formation is crucial. In the Ru(0001) single crystal oxidation RuO<sub>2</sub>(110) grows to a minimum thickness of about three to five layers, which spread laterally over the surface without significant further increase in oxide thickness. With only 4 ML Ru deposited on the Au(111) surface, most of the ruthenium would be needed for the formation of an oxide with equal thickness. Therefore the oxide would bind either directly to the Au(111) surface, or only a single layer of ruthenium would be at the interface separating the oxide from the gold. Due to the weak oxygen gold interaction, RuO<sub>2</sub>(110) bound to the Au(111) surface is assumed to be not stable. This becomes evident by the oxidation of 10 ML Ru/Au(111) where RuO<sub>2</sub>(110) is readily formed, thus supporting the assumption of a critical thickness (or amount) of ruthenium, which acts as a buffer layer between the Au(111) surface and the RuO<sub>2</sub>(110).
5. The thermal stability of the porous ruthenium film was investigated by annealing to 750 K in vacuum for 120 minutes. By STM a complete rearrangement to hexagonally shaped Ru islands is observable, thus evidently revealing the decomposition of the perforated ruthenium film.

The presented experiments are the first systematic growth and oxidation investigations on the Ru/Au(111) system under UHV conditions. Similar to the complimentary Au/Ru(0001) system, the exposure of oxygen significantly changes the morphology of the deposited

metallic Ru film. The growth behavior and resulting morphologies of both systems (with or without the presence of oxygen) can be described qualitatively by Young's equation, with the surface energy relation between ruthenium and gold being the main driving force.

Although various results have been obtained yet, further XPS and STM experiments as well as a combination of TDS and LEED experiments have to be performed to further investigate and clarify the structural properties of the perforated ruthenium film on the one hand, and its redox behavior on the other hand. Moreover the unique structural morphology of the perforated ruthenium calls for intercalation experiments of different molecules. For instance, it could be used as a template for water intercalation and the preparation of hydrous ruthenium oxide under UHV conditions.

## 7. Inhibition of the Ru(0001) oxidation by gold islands

As described in chapter 5.1.1 the deposition of gold (0.5 ML) on Ru(0001)-(2x1)O at 700 K induces the growth of hexagonal gold islands along the step edges as well as at the high coordination sites of the surface. Coincidentally at these high coordination sites, critical nuclei<sup>29</sup> are formed, from which the growth of RuO<sub>2</sub>(110) starts during the initial oxidation of the Ru(0001) surface.<sup>[190]</sup> Due to the nobility of bulk gold towards O<sub>2</sub>, the formation of the rather large hexagonal gold islands at these nucleation sites is assumed to inhibit the formation of the critical nuclei and the further oxidation of the Ru(0001) surface. Comparable experiments have been carried out by Chorkendorff et al. where the dissociative adsorption of N<sub>2</sub> on the Ru(0001) surface was inhibited by the deposition of gold.<sup>[228]</sup>

*Figure 7-1* schematically illustrates the critical steps for the formation of the critical nuclei in the initial gas phase oxidation of Ru(0001) by O<sub>2</sub>.

- a) Schematic illustration of a nucleation site on the Ru(0001) surface. The numbers in brackets represent the difference in layers towards the lowest terrace (*cf. figure 7-1a*, indicated by 0). The double- or multistep is highlighted by a thicker line while the single step is depicted by a thin line.
- b) Dissociative adsorption of O<sub>2</sub> and surface diffusion of chemisorbed oxygen.
- c) Mobile RuO<sub>x</sub> precursor formation and diffusion along the double- or multi-steps towards the nucleation sites.
- d) Formation and growth of the critical nucleus by the agglomeration of RuO<sub>x</sub> precursors at the nucleation site as well as the one-dimensional corrosion of the steps to form more mobile precursors.
- e) Growth of a two-to-four layered RuO<sub>2</sub>(110) film initiated by the active clusters at the nucleation sides.

To achieve the inhibition of the Ru(0001) single crystal oxidation, 0.5 ML Au were deposited on the Ru(0001)-(2x1)O surface at 700 K. Afterwards 27000 L molecular oxygen ( $p(\text{O}_2) = 3 \cdot 10^{-5}$  mbar) at 680 K were dosed to induce the oxidation. By these oxidation conditions usually many critical nuclei and a partially covering thin film of RuO<sub>2</sub>(110) is formed on the bare Ru(0001) surface.<sup>[92,190]</sup>

---

<sup>29</sup> The critical nuclei, which are formed in the initial gas phase oxidation, are also simply called (critical) clusters in the recent publications.<sup>[92,190]</sup>

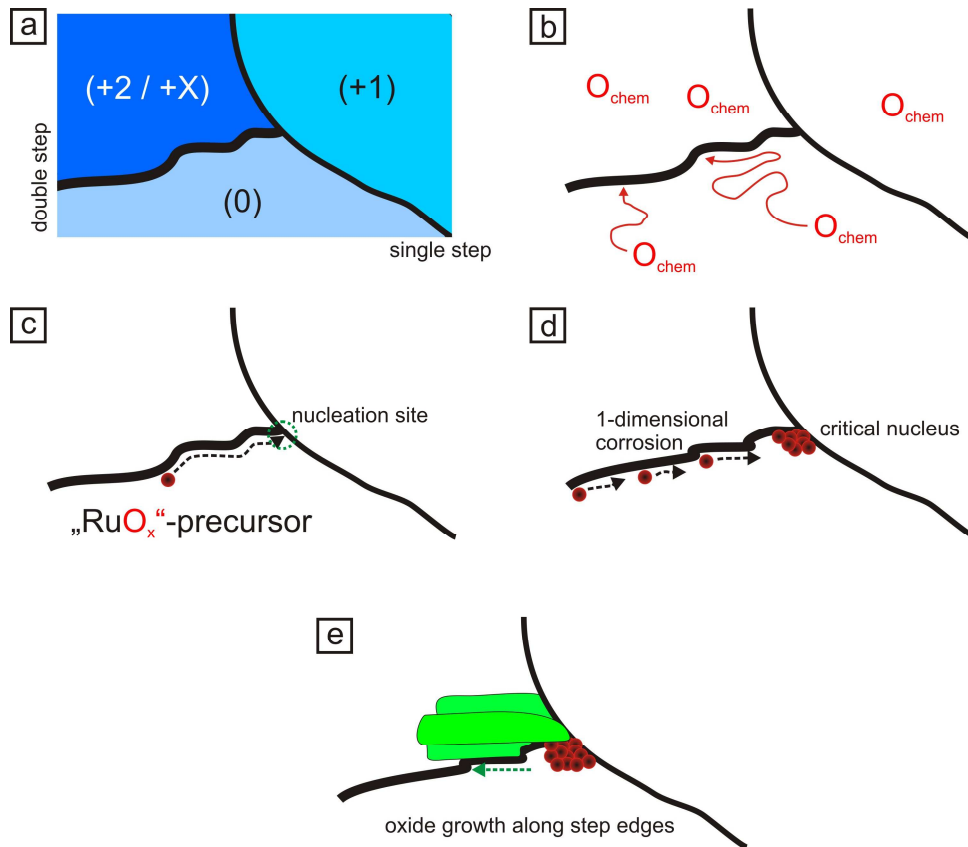


**Figure 7-1:** Summarized initial gas phase oxidation of the Ru(0001) single crystal surface near the nucleation site. (a) Schematic illustration of the nucleation site; (b) dissociative adsorption of  $O_2$  and surface diffusion of chemisorbed oxygen; (c) formation of the mobile  $RuO_x$  precursors as well as their diffusion along the steps to the nucleation site; (d) agglomeration of  $RuO_x$  precursors induces the formation of the critical nucleus; (e) growth of a thin  $RuO_2(110)$  film (2 to 4 layer thick) along the neighboring step edges.

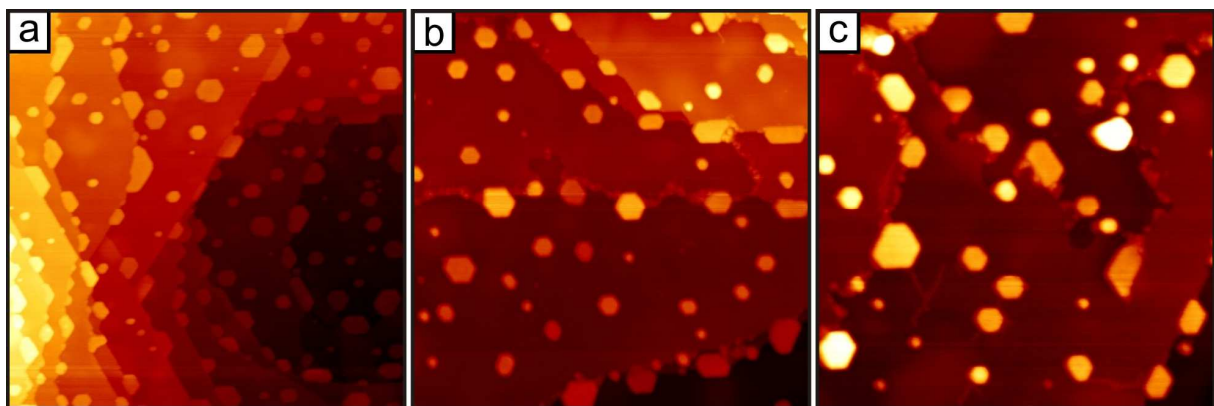


**Figure 7-2:** This series of STM images illustrates the influence of deposited gold on the oxidation process of the Ru(0001) surface by typical oxidation conditions:  $p(O_2) = 3 \cdot 10^{-5}$  mbar, 680 K. Image a) (300 nm x 300 nm) displays a larger area of the surface before the exposure of 27000 L  $O_2$ . The images b) (200 nm x 200 nm) and c) (150 nm x 150 nm) shows the strong corrosion at the Ru steps while the Au islands remain unharmed upon the oxygen treatment. Tunneling conditions:  $U = 1.2$  V,  $I = 1.0$  nA.

Figure 7-2 shows STM pictures of the Ru(0001)-(2x1)O surface with deposited gold (0.5 ML at 700 K, cf. figure 7-2a) and the subsequent oxygen treatment of this Au/Ru(0001) surface

by exposure of 27000 L O<sub>2</sub> at 680 K (cf. figure 7-2b,c). The STM images give no indication for the formation of RuO<sub>2</sub>(110) or critical nuclei during this preparation. The grown gold islands are blocking most of the step edges and especially the intersections between single steps and double (or multiple) steps (cf. figure 7-2a). Instead of the Ru(0001) single crystal oxidation, a strong corrosion of the steps is observable (cf. figure 7-2b,c). This is insofar noteworthy because such a corrosion of the ruthenium surface has only been observed for the oxidation by atomic oxygen.<sup>[197,200]</sup> The gold islands retained their hexagonal shape and are not attacked by the exposed O<sub>2</sub> (cf. figure 7-2b,c). This is confirmed by the corresponding Au 4f XPS signals (cf. figure 7-3a), which give no indication for the oxidation of the gold islands. The slight increase of the O 1s signal at 530.1 eV (cf. figure 7-3b) can be assigned to the formation of a more dense oxygen overlayer. Both, the O 1s signal intensity and its binding energy confirm that no covering film of RuO<sub>2</sub>(110) is formed on the surface.<sup>30</sup>

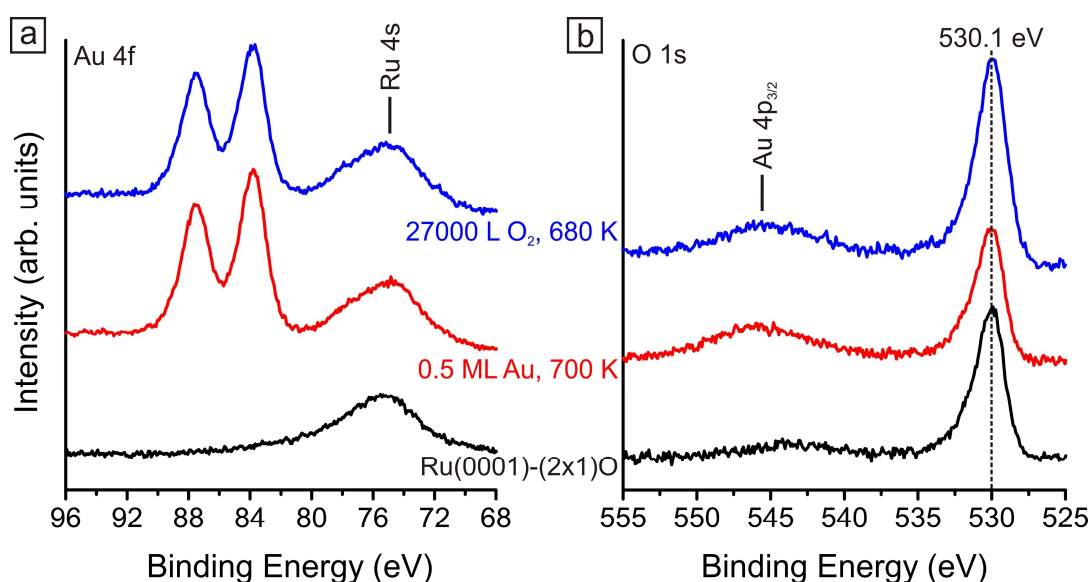


**Figure 7-3:** The inhibited oxidation of the Ru(0001) surface is illustrated on the basis of Au 4f (a) and O 1s (b) spectra. After deposition of 0.5 ML gold on a (2x1) oxygen precovered Ru(0001) surface, the formation of metallic gold islands is confirmed by the Au 4f signals at 84.0 eV and 87.7 eV. After the deposition of gold, 27000 L O<sub>2</sub> were exposed to the Au/Ru(0001) surface at 680 K for the formation of RuO<sub>2</sub>(110). However, the O 1s signal in (b) evidently shows that no RuO<sub>2</sub>(110) is formed by this oxygen treatment. The slight increase of the O 1s signal intensity at the binding energy of 530.1 eV, is assigned to the formation of a (1x1)O chemisorbed oxygen phase. For the formation of a RuO<sub>2</sub>(110) film, a significant shift to lower binding energies ( $\geq 0.6$  eV) of the O 1s signal is expected. The unchanged Au 4f signals in (a) indicate that the gold islands are not attacked during the O<sub>2</sub> treatment.

A more careful analysis of magnified STM images reveals a selective corrosion of certain steps while other steps remain mostly unaffected (cf. figure 7-4). Line scans of corroded (cf. line scan 7-4b) and unaffected steps (cf. line scans 7-4a and 7-4c) show that only the single

<sup>30</sup> The O 1s binding energy of RuO<sub>2</sub>(110) on Ru(0001) is 529.5 eV.

steps of the Ru(0001) surface are attacked upon the O<sub>2</sub> exposure. However, the corrosion of the single steps has never been observed in the initial gas phase oxidation of Ru(0001) upon O<sub>2</sub> exposure.<sup>[190]</sup>

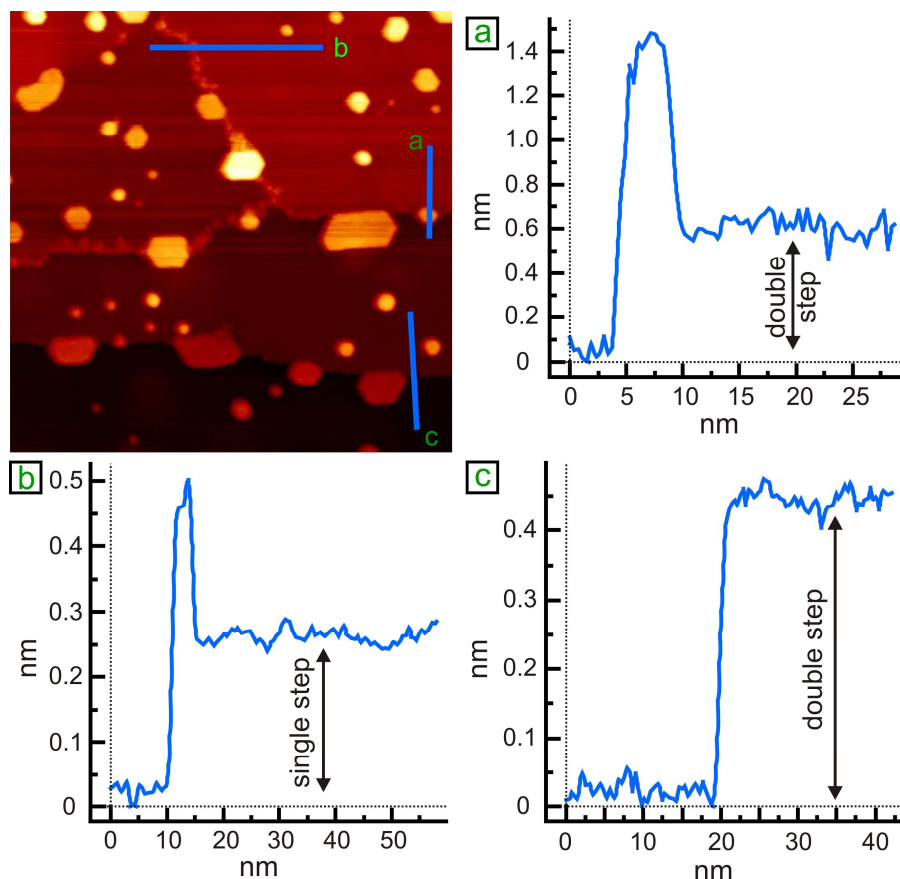


**Figure 7-4:** A STM picture shows the selective behavior of corrosion on the Au/Ru(0001) surface. Using line scans at certain positions on the surface the single steps (line scans b) were identified to corrode during the exposure of O<sub>2</sub>, while the double or multi steps remain mostly unharmed (line scans a and c). Tunneling conditions:  $U = 1.2$  V,  $I = 1.0$  nA.

Therefore the deposited gold islands may change the extraction process of ruthenium atoms from the steps: Instead of the double steps of the Ru(0001) surface, the single steps are attacked by the dosed O<sub>2</sub>. Upon oxygen exposure a two-dimensional corrosion into the terraces of Ru(0001) and the agglomeration of the RuO<sub>x</sub> precursors along the corroded steps is visible (*cf. figure 7-2b,c*). At this point it cannot be determined if the oxidation of the Ru(0001) surface is only inhibited or completely prevented. It is possible that the oxidation starts at (significantly) higher exposures of molecular oxygen. Long term oxidation experiments are a possibility to clarify this issue.

Statistical analysis (*cf. figure 7-5*) of the agglomerated RuO<sub>x</sub> precursors reveals no clear structure information. For a direct comparison to literature, the height of metallic ruthenium

layers and bulk RuO<sub>2</sub> are indicated by the blue and green dotted lines, respectively.<sup>31</sup> The broad height distribution ranges from 1.8 Å to 8.0 Å. Therefore no reliable assignment is possible, neither to metallic ruthenium nor to RuO<sub>2</sub>(110).

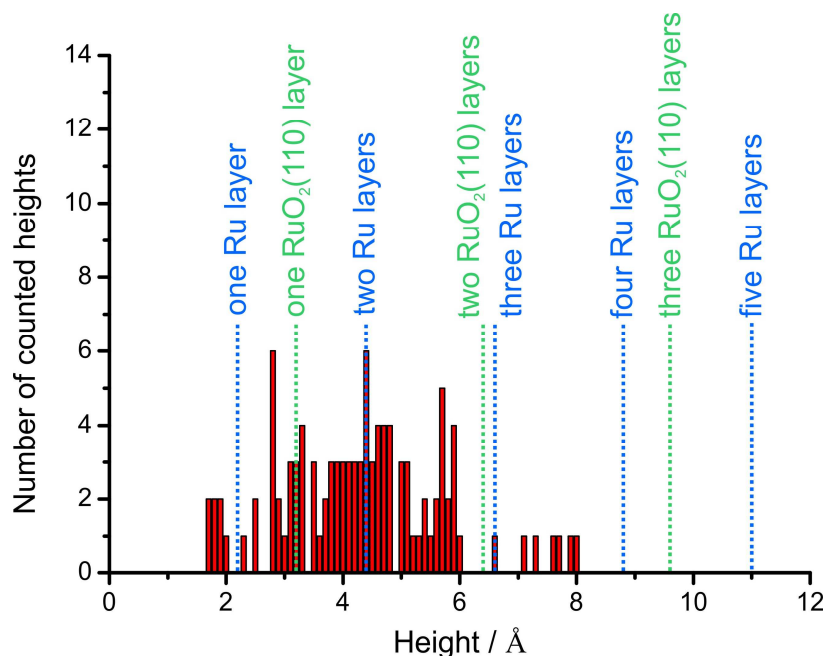


**Figure 7-5:** Statistical height analysis of the agglomerated deposit along the Ru steps shows a broad distribution, ranging between 1.8 Å and 8.0 Å. Marked by the blue and green dotted lines are the thickness of single or multiple layer spacings of bulk Ru(0001) or bulk RuO<sub>2</sub>, respectively. Compared to these reference values no clear assignment to one of these ruthenium species is possible by this statistical height distribution.

Herd et al. recently suggested that the activation of O<sub>2</sub> on the Ru(0001) surface solely appears at double or multi steps and not at single steps.<sup>[92,200]</sup> During O<sub>2</sub> exposure at higher temperatures a dense (1x1)O overlayer is formed on the Ru(0001) surface.<sup>[177,229]</sup> On this (1x1)O precovered ruthenium surface the dissociative adsorption of additional O<sub>2</sub> molecules becomes improbable as can be seen by the sticking coefficient of O<sub>2</sub>.<sup>[230]</sup> On the oxygen free Ru(0001) surface the sticking coefficient is estimated to be approximately 1, i.e. every O<sub>2</sub> molecule that hits the surface is immediately bound and not reflected back into the gas phase. On the Ru(0001)-(2x1)O surface the sticking coefficient already decreased to  $\sim 10^{-3}$  and for the (1x1)O overlayer it even drops to  $\sim 10^{-6}$ .<sup>[8,168,230]</sup> Also the O-Ru binding energy, with respect to a free oxygen atom, displays a similar trend. Due to repulsive interactions between the oxygen atoms in the overlayer structure the binding energy between ruthenium and oxygen decreases with increasing oxygen coverage.<sup>[8,187]</sup> Table 7-1 summarizes the correlation between the oxygen coverage and O<sub>2</sub> adsorption properties on Ru(0001).

<sup>31</sup> The height of a single metallic Ru(0001) and RuO<sub>2</sub> layer are 2.2 Å and 3.2 Å, respectively.<sup>[92,190,231]</sup>

**Table 7-1:** Adsorption properties for the dissociative adsorption of O<sub>2</sub> on Ru(0001) depending on the oxygen coverage. Values taken from ref. [8,168,230]

| Chemisorbed oxygen phase on Ru(0001) | Oxygen coverage | O-Ru binding energy with respect to free oxygen atoms | Sticking coefficient of O <sub>2</sub> |
|--------------------------------------|-----------------|---|--|
| (2x2)O                               | 0.25 ML         | 5.55 eV   | ~ 1                                    |
| (2x1)O                               | 0.5 ML          | 5.10 eV   | ~ 10 <sup>-3</sup>                     |
| (2x2)3O                              | 0.75 ML         | 5.28 eV   | -                                      |
| (1x1)O                               | 1.0 ML          | 4.84 eV   | < 10 <sup>-6</sup>                     |

Considering that O<sub>2</sub> activation occurs only at the double or multi steps of the Ru(0001) during its oxidation, the micro faceting of the ruthenium surface is assumed to become crucial. Generally adsorption and activation of O<sub>2</sub> at undercoordinated ruthenium atoms is favored due to the change in the local density of states (LDOS) of the d-orbitals.<sup>[232]</sup> However this is not the key factor for O<sub>2</sub> activation during the oxidation of Ru(0001) because otherwise O<sub>2</sub> may also be activated at single steps, too. More likely at the micro faceted double or multi steps, two neighboring adsorption sites are available for the O<sub>2</sub> activation.<sup>[200]</sup>

In case of the exposure of atomic oxygen in the Ru(0001) surface, the adsorption properties change significantly. It is assumed that the adsorption probability of atomic oxygen on the Ru(0001)-(1x1)O surface is significantly higher than the adsorption of O<sub>2</sub>.<sup>[92,197]</sup> If high local density of chemisorbed oxygen atoms is necessary for the release of ruthenium atoms from the steps, the formation of RuO<sub>x</sub> precursors at single steps by exposure of atomic oxygen can be explained: Hammer et al. calculated chemisorbed oxygen phases at the single steps of the Ru(0001) surface thus depicting that the ruthenium atoms at the step edges are slightly lifted at very high oxygen coverages.<sup>[233]</sup> Such a lifting of ruthenium atoms is assumed to occur due to adsorption of atomic oxygen on the ruthenium surface and especially at the single steps. In principle the local density of chemisorbed oxygen at all ruthenium steps should be increased by the adsorption of atomic oxygen. However the formation RuO<sub>x</sub> precursors upon exposure of atomic oxygen predominantly occurs at the single steps, and only at higher dosages of atomic oxygen the double and multi steps are attacked, too.<sup>[197]</sup> This indicates a kinetic limitation for the RuO<sub>x</sub> precursor formation at the faceted double or multi steps upon exposure of atomic oxygen.

In conclusion, these observations confirm the importance of faceted double or multi steps for O<sub>2</sub> activation on the Ru(0001) surface. With a negligible adsorption probability at single

steps, the dosed molecular oxygen can increase the local oxygen coverage only at the micro faceted multi or double steps where the dissociative adsorption of  $O_2$  is possible.

The question within this context is now: *How do the formed gold islands on the Ru(0001)-(2x1)O surface change the location for the  $RuO_x$  precursor formation from double to single steps?*

The formation of the  $RuO_x$  precursors at the single steps and their corrosion by exposure of  $O_2$  is assumed to be induced by the deposited Au. In the STM images the shape and size of separated gold islands is visible. One could think that a very thin line of gold is attached at the double and multi steps of the Ru(0001) surface. But this has never been observed by STM. As has been presented in the previous experiments, dosed atomic oxygen predominantly attacks the deposited gold. If a thin line of gold is formed along the steps of the ruthenium surface, then the formation of small gold nanoparticles along these steps is expected due to the preferred oxidation of gold. But this has never been observed by STM. Instead only the fragmentation of the hexagonal gold islands into clusters has been monitored, thus indicating that these islands contain all of the deposited gold. Therefore a specific passivation of double or multi steps by a thin gold line is rather unlikely.

This leads to the assumption that the activation process of  $O_2$  may have changed due to the deposited gold. Many studies investigated the binding and activation of  $O_2$  on gold nanoparticles.<sup>[25,26,37,41,42,44-49,56]</sup>  $O_2$  activation on the Au nanoparticles itself is hard to achieve due to the weak oxygen–gold binding. Instead  $O_2$  predominantly adsorbs at the triple phase boundary (tpb) by binding one oxygen atom to the substrate and the other binding to the gold island, if a reducible oxide is used as a support.<sup>[41,46,49]</sup> The  $O_2$  readily dissociates at the tpb so one oxygen atom can strongly bind to the support while the other oxygen atom, which is bound to the gold atom, is assumed to participate in oxidation reactions, e.g. the CO oxidation reaction.<sup>[41,45,46,49]</sup> This active atomic oxygen species is proposed to even oxidize the gold atoms at the interface.<sup>[41,49]</sup> Based on these investigations it is assumed that the activation process of  $O_2$  on the Au/Ru(0001) surface may be similar. Instead of the exclusive activation at the double or multisteps  $O_2$  it is possible that molecular oxygen adsorbs at the perimeter sites of the gold islands with one oxygen atom bound to the ruthenium surface and the other bound to the gold island. The activation of  $O_2$  at these sites then induces the formation of the  $RuO_x$  precursors at single steps instead of double steps. However, due to lacking knowledge of the  $O_2$  activation mechanism on bare Ru(0001), the change in oxidation behavior when introducing gold cannot be explained conclusively.

In conclusion, the influence of the deposited gold on the oxidation of Ru(0001) is schematically illustrated in figure 7-6<sup>32</sup>.

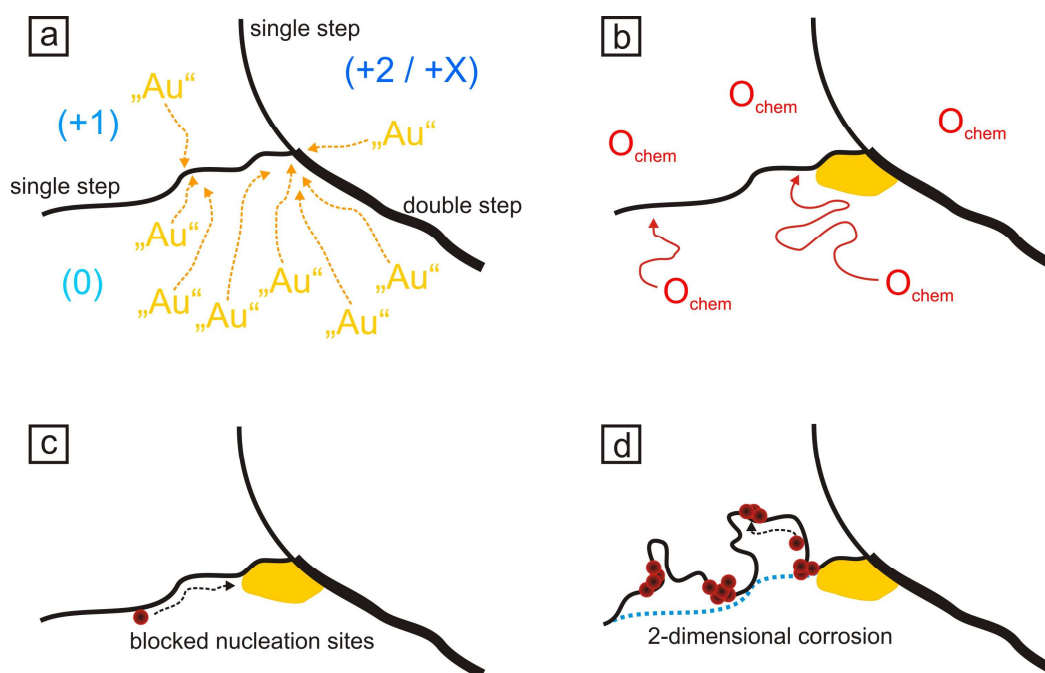


**Figure 7-6:** Summarized steps of the initial gas phase oxidation of Ru(0001) with previously formed gold islands at the nucleation sites: (a) Gold deposition leads to surface diffusion of gold islands on the oxygen precovered ruthenium surface towards the nucleation sites; (b) dissociative adsorption of O<sub>2</sub> at 680 K as well as surface diffusion of chemisorbed oxygen; (c) formation of mobile RuO<sub>x</sub> precursors exclusively at single steps and their diffusion along these steps; (d) due to the blocked nucleation sites the formation of critical nuclei at these positions and the subsequent formation of RuO<sub>2</sub>(110) is inhibited. Instead more and more mobile RuO<sub>x</sub> precursors are formed at the single steps, thus resulting in a two-dimensional corrosion and the agglomeration of RuO<sub>x</sub> deposits.

The inhibition of the RuO<sub>2</sub>(110) formation and the observed two-dimensional corrosion of the ruthenium single steps are summarized in the following:

- Gold deposition and its diffusion to the nucleation sites forms hexagonally shaped (mostly) three layered islands at the chosen growth conditions (0.5 ML Au on (2x1)O precovered Ru(0001) at 700 K).
- Dissociative adsorption of O<sub>2</sub> and surface diffusion of chemisorbed oxygen.
- RuO<sub>x</sub> precursor formation and diffusion along the single steps towards the blocked nucleation sites.
- Due to the blocked nucleation sites no RuO<sub>2</sub> clusters are formed. Instead more and more RuO<sub>x</sub> precursor species are formed, leading to a two-dimensional corrosion of the gold free ruthenium single steps.

<sup>32</sup> Please note that (although this graphic looks similar to the one from figure 7-1) the nomenclature of the steps and the terraces has changed. The double and single steps are exchanged and the higher lying terrace is now the right one.

## 8. Brief survey about growth behaviors in the literature

The growth mechanism of a deposited material on a substrate surface on the atomic level is usually very complex and includes many variables that influence the growth behavior substantially. Therefore a detailed prediction for the growth behavior of a particular system is usually not reliable. Experimental and theoretical investigations are mandatory before an interpretation of the growth is reasonable.

Based on the general model for nucleation theory and epitaxial growth, it is possible to qualitatively describe and explain the observed growth behavior: By using Young's equation an explanation for the observed growth morphology can be given. The tables 8-1 and 8-2 give a brief overview of growth behaviors for various systems in literature. General assumptions can be concluded by these observed growth behaviors.

**Table 8-1:** *Growth on metal surfaces*

| System  | Growth conditions   | Growth behavior  | Reference |
|---|---|--|-----------|
| MoO <sub>3</sub> / Au(111)                                  | PVD of Mo in vacuum with subsequent annealing in O <sub>2</sub>                           | 2 D film growth  | 234       |
| MgO / Mo(100)   | PVD of Mg in background O <sub>2</sub> with subsequent annealing in vacuum                | 2 D film growth: at 700 K flat film with dislocations, at 1000 K flat film with Moiré pattern  | 235       |
| Fe <sub>x</sub> Si <sub>1-x</sub> O <sub>2</sub> / Ru(0001) | PVD of Si and Fe in background O <sub>2</sub> with subsequent annealing in O <sub>2</sub> | 2 D growth of ultrathin Fe-doped silicate films with Moiré pattern   | 236       |
| ZnO / Pt(111)   | PVD of ZnO in background O <sub>2</sub> with subsequent annealing in O <sub>2</sub>       | 2 D layer by layer growth  | 237       |
| ZnO / Au(111)   | PVD of ZnO in background O <sub>2</sub> with subsequent annealing in O <sub>2</sub>       | 2 D film growth with Moiré pattern   | 238       |
| FeO and Fe <sub>3</sub> O <sub>4</sub> / Pt(111)            | PVD of Fe in vacuum with subsequent annealing in O <sub>2</sub>                           | Fe deposition: 300 K 3 D VW growth, at 520 K wetting of the Pt(111)<br>Oxidation: FeO and Fe <sub>3</sub> O <sub>4</sub> 2 D film growth | 239,240   |

**Table 8-1: Growth on metal surfaces, continued from previous page**

| System   | Growth conditions  | Growth behavior   | Reference   |
|--|--|---|-------------|
| Au NP /<br>CeO <sub>2</sub> (111) /<br>Ru(0001)                                    | CeO <sub>2</sub> : PVD of Ce in background O <sub>2</sub> with subsequent annealing in O <sub>2</sub><br><br>Au NP: PVD of Au at low temperatures  | CeO <sub>2</sub> : 2 D film growth with small free areas due to O-overlayer on Ru(0001)<br><br>Au: 3 D cluster growth | 241         |
| Ag NP /<br>CeO <sub>2-x</sub> (111) /<br>Pt(111)                                   | CeO <sub>2</sub> : PVD of Ce in background O <sub>2</sub> with subsequent annealing in O <sub>2</sub><br><br>Ag NP: pulsed atomic beam from high temperature effusion cell<br><br>Ag NP: MBE evaporation in vacuum | CeO <sub>2</sub> : 2 D film growth<br><br>Ag: 3 D cluster growth  | 137,242,243 |
| Au NP / TiO <sub>2</sub> /<br>Ru(0001)   | TiO <sub>2</sub> : PVD of Ti in background O <sub>2</sub> with subsequent annealing in O <sub>2</sub><br><br>Au NP: PVD in vacuum with subsequent annealing  | TiO <sub>2</sub> : 2 D island coalescence SK growth<br><br>Au: 3 D cluster growth                                     | 244,245     |
| MgO / Mo(100)  | PVD of Mg in background O <sub>2</sub> with subsequent annealing in vacuum   | 2 D ultrathin film growth   | 246         |
| NaCl / Al(111) or<br>Al(100)   | PVD of NaCl in vacuum  | 3 D island growth   | 247         |
| Cr / Ru(0001)  | PVD of Cr in vacuum  | 0.25 ML, 300 K: 2 D island growth<br><br>2 ML, 300 K: 3 D island growth<br><br>2 ML anneal to 500 – 700 K: SK growth  | 248         |
| Oxidation of Cu-9at% Al(111) (Cu-Al alloy)   | Al segregation and oxidation at 680 °C using O <sub>2</sub>  | Formation of a wetting thin Al <sub>2</sub> O <sub>3</sub> film   | 249         |
| TiO <sub>x</sub> / Mo(112)<br>and TiO <sub>x</sub> / SiO <sub>2</sub> /<br>Mo(112) | TiO <sub>x</sub> : PVD of Ti in vacuum with subsequent oxidation   | 2 D growth of ultrathin TiO <sub>x</sub> layer  | 250         |

**Table 8-1: Growth on metal surfaces, continued from previous page.**

| System                            | Growth conditions   | Growth behavior   | Reference |
|-----------------------------------|---|---|-----------|
| TiO <sub>2</sub> / Pt(100)        | 1. PVD of Ti in vacuum with subsequent oxidation using atomic oxygen<br>2. PVD of Ti in background O <sub>2</sub> with subsequent annealing | SK growth: 2 D film growth of the first layer. Afterwards 3 D island formation. | 251       |
| CeO <sub>2</sub> (111) / Ru(0001) | MBE of Ce in oxygen atmosphere with subsequent annealing in oxygen  | 3 D island VW growth  | 252-254   |
| Au / TiO <sub>x</sub> / Mo(112)   | PVD of Au in vacuum with subsequent annealing   | 2 D film SK growth. 3 D island growth at 2.5 ML Au                              | 20,21     |
| h-BN / Rh(111)                    | CVD of borazine in vacuum   | 2 D film growth with Moiré pattern  | 255-257   |
| h-BN / Ru(0001)                   | CVD of borazine in vacuum   | 2 D film growth with Moiré pattern  | 258-260   |
| Au / h-BN / Ru(0001)              | PVD of Au in vacuum with subsequent annealing   | 3 D cluster growth with additional flat 2 D island formation                    | 261       |
| Graphene / Me (overview)          | CVD of various carbon containing molecules  | 2 D film growth with Moiré pattern  | 262       |

**Table 8-2: Growth on oxide surfaces.**

| System                                    | Growth conditions   | Growth morphology   | Reference |
|---|---|---|-----------|
| Au NP / CeO <sub>2</sub> (111) / Ru(0001) | CeO <sub>2</sub> : PVD of Ce in background O <sub>2</sub> with subsequent annealing in O <sub>2</sub><br>Au NP: PVD of Au at low temperatures | CeO <sub>2</sub> : 2 D film growth with small free areas due to O-overlayer on Ru(0001)<br>Au: 3 D cluster growth | 241       |
| Cu / ZnO(0001)                            | PVD of Cu in vacuum   | At low T: Cu islands covering the surface.<br>Annealing leads to dewetting and 3 D island formation               | 263-265   |

**Table 8-2: Growth on oxide surfaces, continued from previous page.**

| System   | Growth conditions  | Growth morphology   | Reference   |
|--|--|---|-------------|
| Pd / $\alpha$ -Al <sub>2</sub> O <sub>3</sub> (0001)                   | PVD of Pd in vacuum  | At 300 K: initially 2 D cluster growth with a transition to 3D growth at 0.25 ML<br>Annealing to 1000 K induces sintering and 3 D cluster formation | 266         |
| Ag NP /<br>CeO <sub>2-x</sub> (111) /<br>Pt(111)                       | CeO <sub>2</sub> : PVD of Ce in background O <sub>2</sub> with subsequent annealing in O <sub>2</sub><br>Ag NP: pulsed atomic beam from high temperature effusion cell<br>Ag NP: MBE evaporation in vacuum | CeO <sub>2</sub> : 2 D film growth<br>Ag: 3 D cluster growth  | 137,242,243 |
| Au / TiO <sub>2</sub>  | PVD of Au in vacuum  | Initially 2 D island growth with a 2 D to 3 D transition at a temperature dependent critical coverage   | 267         |
| Pd and Co /<br>NiAl(110) (thin<br>Al <sub>2</sub> O <sub>3</sub> film) | PVD of Pd and Co in vacuum   | Co and Pd 300 K: 3 D cluster growth   | 268         |
| TiO <sub>2</sub> / Pt(100)   | 1. PVD of Ti in vacuum with subsequent oxidation using atomic oxygen<br>2. PVD of Ti in background O <sub>2</sub> with subsequent annealing  | SK growth: 2 D film growth of the first layer. Afterwards 3 D island formation.   | 251         |
| Au / TiO <sub>2</sub> (110)  | PVD of Au in vacuum with subsequent annealing  | 3 D growth of Au clusters at 300 K and sintering at higher temperature. Higher amounts of Au induces formation of rough films by island coalescence | 23,269,270  |
| Pt / TiO <sub>2</sub> (110)  | PVD of Pt in vacuum with subsequent annealing  | 3 D growth of Pt clusters   | 271         |

**Table 8-2: Growth on oxide surfaces, continued from previous page.**

| System                                     | Growth conditions  | Growth morphology   | Reference   |
|--|--|---|-------------|
| Me / TiO <sub>2</sub> (110)<br>(overview)  | PVD of various metals with subsequent annealing  | 3 D cluster formation of metals with low reactivity towards O<br><br>2 D film growth of metals with low reactivity towards O. Simultaneous reduction of TiO <sub>2</sub> and oxidation of adsorbed Me | 108,270,272 |
| RuO <sub>2</sub> / TiO <sub>2</sub> (110)  | MBE of Ru in oxygen plasma   | 2 D layer by layer growth   | 273         |
| RuO <sub>2</sub> / TiO <sub>2</sub> (110)  | CVD of Ru <sub>3</sub> (CO) <sub>12</sub> in O <sub>2</sub> atmosphere with subsequent annealing in O <sub>2</sub> | 3 D VW like island growth   | 274         |
| RuO <sub>2</sub> NP / P25-TiO <sub>2</sub> | RuO <sub>2</sub> NP deposited on P25-TiO <sub>2</sub> by impregnation from acidic RuCl <sub>3</sub> solution       | 3 D NP redistribute during deacon process at 300 °C forming a wetting 2 D layer   | 275         |
| RuO <sub>2</sub> / TiO <sub>2</sub> (110)  | CVD of Ru <sub>3</sub> (CO) <sub>12</sub> with subsequent annealing in O <sub>2</sub>                              | 1 D wire formation covering the surface for lower RuO <sub>2</sub> amounts<br><br>Annealing to 800 K reduces the oxide and forms 3 D metallic particles   | 276         |
| RuO <sub>2</sub> /TiO <sub>2</sub> (110)   | PVD of Ru in O <sub>2</sub> atmosphere   | Formation of 3 D square shaped islands ( $\leq 4$ ML RuO <sub>2</sub> ) followed by 2 D step flow multilayer growth ( $\geq 6$ ML RuO <sub>2</sub> )  | 145         |

Metal oxides usually have significant lower surface free energies compared to pure metal surfaces. Near thermodynamic equilibrium the growth of an oxide on a metal surface is assumed to result in the formation of a covering two-dimensional film, if the contribution of the interface energy and the strain energy are negligible for the growth behavior. Vice versa,

the deposition of a metal on an oxide surface mostly leads to the formation of either clusters or three-dimensional islands on the surface. As can be seen by various examples given in table 8-1 the growing oxide usually tends to cover the metal surface in a Stranski-Krastanov-like or Frank-van-der-Merwe-like growth. In table 8-2 examples for the deposition of metals on oxide surfaces are listed for which three-dimensional Volmer-Weber-like growths are mainly observed. Besides the general growth behavior of these systems (two-dimensional vs. three-dimensional growth), their structures on the nanoscale are strongly influenced by the interface energy and strain energy. The introduction of defects or the formation of a moiré pattern is often observed for covering films, where the interface between the adsorbate and the substrate determines the structure of the growing material.<sup>[235,236,238]</sup>

In cases where the interface energy and strain energy become more decisive, the growth behavior changes substantially. Although a lower surface free energy of the adsorbate would induce a two-dimensional growth, a dominant interface energy can lead to a three-dimensional growth. A good example for this strong influence of the interface energy is the growth of CeO<sub>2</sub> on Ru(0001).<sup>[252-254]</sup> Instead of a flat covering oxide, triangularly shaped isolated CeO<sub>2</sub> islands are growing on the Ru(0001) surface. Another example is the growth of Ag deposited on CeO<sub>2-x</sub>.<sup>[137]</sup> By deposition of Ag, nanoparticles are formed on the CeO<sub>2-x</sub> surface, whose increase in size is limited due to local strain effects between the nanoparticles and the oxide substrate. For both examples the effect of strain has a strong influence on the resulting morphology.

To elucidate the general applicability and limitations of the simplified model of heterogeneous nucleation and epitaxial growth, three intensively studied systems will be described in more detail, i.e. the formation of metal clusters on TiO<sub>2</sub>, the growth of RuO<sub>2</sub> on TiO<sub>2</sub>(110) and the formation of RuO<sub>2</sub>(110) by oxidation of a Ru(0001) surface.

## 8.1 Deposition of metals on TiO<sub>2</sub>

Since the discovery of high activity and selectivity of gold nanoparticles on reducible metal oxide surfaces by Haruta et al. manifold research was performed in the field of gold catalysis, with TiO<sub>2</sub> used as the underlying substrate surface.<sup>[12-19]</sup> As already summarized by Diebold et al. the deposition of metals on TiO<sub>2</sub> surfaces generally leads to the formation of three-dimensional clusters on the surface.<sup>[108,272,277]</sup> This is confirmed by the simplified model of epitaxial growth, i.e. the energy relation given by Young's equation (cf. equation 3.2-1, chapter 3.2). Generally TiO<sub>2</sub> has a significant lower surface free energy than the most metals, which facilitates the three-dimensional growth of such a deposited metal.<sup>[108,272,277]</sup> However for metals with a high reactivity towards oxygen (e.g. Na or Hf) the formation of flat films has been observed.<sup>[272]</sup>

By using surface sensitive low-energy ion scattering (LEIS)<sup>33</sup> the decrease of the Ti signal due to deposition of the adsorbate was measured. In *figure 8.1-1* the normalized Ti intensities are plotted against the overlayer thickness of the deposited metal. For Hf, the Ti LEIS intensity decreases linearly and reaches zero when about 1 ML of Hf was deposited on the surface. Due to the higher surface free energy of Hf a three-dimensional growth would have been expected. As a consequence one could assume that the interface energy significantly changed the growth behavior of Hf on TiO<sub>2</sub>. But further investigations revealed that during the deposition of Hf the top TiO<sub>2</sub> layers are reduced to metallic Ti while simultaneously the adsorbed Hf is oxidized. This observation is again consistent with Young's equation due to the higher surface free energy of the metallic Ti surface compared to the formed Hf-oxide layer. In case of Cu deposition the LEIS signal for Ti decreases parabolically and is still observable, even for high amounts of deposited Cu. A three-dimensional growth of Cu clusters or islands on the TiO<sub>2</sub> surface explains this parabolic pattern. These examples show the importance of understanding the chemical processes, which may occur during the deposition and growth of a metal on an oxide surface.

---

<sup>33</sup> In LEIS, ions (usually from a noble gas) with a low energy are directed towards the targeted surface. By applying energies below 10 keV the ions are scattered at the top layer of the surface. By either transferring energy to or from the surface atoms during the scattering process, the noble gas ions change their velocity in vacuum. This changed velocity is usually monitored by a time-of-flight analyzer coupled with a microchannel plate detector or electron multiplier. By the characteristics of the noble gas beam and geometric setup of the different components of the ion scattering system, information about the surface species can be obtained due to the element specific scattering process.<sup>[278,279]</sup>

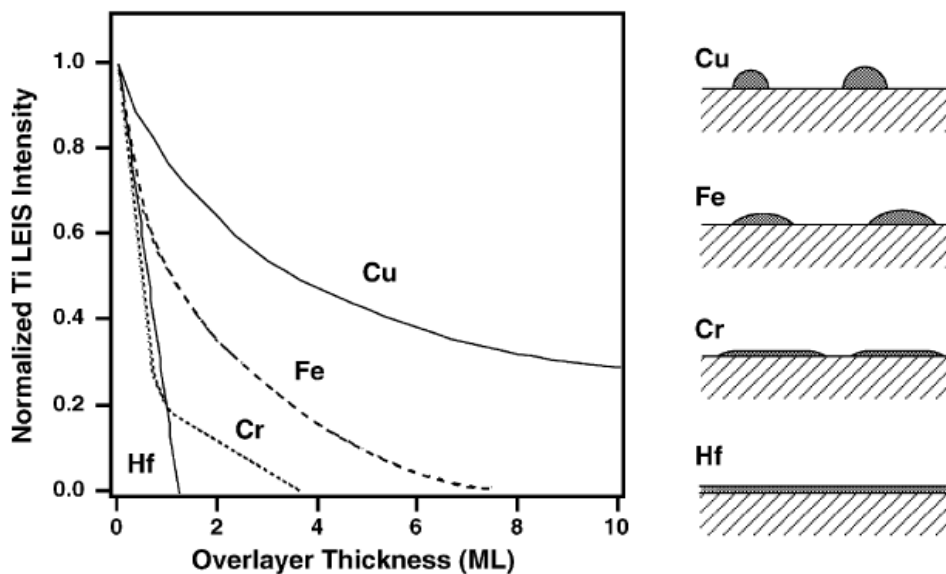


**Figure 8.1-1:** Trends for the attenuation of the Ti LEIS signal for four different deposited metallic species (Cu, Fe, Cr and Hf) on  $\text{TiO}_2(110)$  (left). Corresponding schematic illustrations of these metals visualize the early growth stages, i.e. three-dimensional cluster formation (Cu), flat island formation (Fe), two-dimensional flat island formation followed by three-dimensional cluster growth (Cr) and the formation of a flat wetting film (Hf). Figure taken from [272].

Another good example is the deposition of gold on  $\text{TiO}_2$ : While gold deposition on  $\text{TiO}_2(110)$  single crystal surfaces leads to the formation of three-dimensional clusters on the surface,<sup>[23,269,270]</sup> the morphology of gold deposited on ultrathin  $\text{TiO}_2$  films changed to thin gold layers, which are wetting the surface.<sup>[20,21]</sup> How can this contradiction be explained? The formation of three-dimensional gold clusters on the  $\text{TiO}_2(110)$  single crystal surface confirms that the growth is induced by the surface free energies of the involved materials ( $\sigma_{\text{Au}} > \sigma_{\text{TiO}_2}$ ). As a consequence, the ultrathin  $\text{TiO}_2$  film must have different chemical and physical properties than bulk  $\text{TiO}_2(110)$ , thus inducing the two-dimensional growth of gold. This change of the chemical and physical properties of a ultrathin film will be elucidated on the basis of the Rh/Ru(0001) system: It is known for Rh deposited on Ru(0001) that the first layer adopts the lattice constants and continues the hcp stacking of the Ru(0001) substrate, although Rh is an fcc metal.<sup>[280,281]</sup>  $\text{O}_2$  exposure at 535 K leads to the formation of a (1x1)O overlayer on 1 ML Rh. This is insofar interesting that on the Rh(111) single crystal surface the formation of the (1x1)O overlayer cannot be achieved by molecular oxygen. Therefore the first layer of Rh is not only continuing the Ru(0001) stacking, more likely the (chemical) properties of the underlying ruthenium are adopted, too.<sup>[280,281]</sup> In recent studies on the properties of thin oxide films formed on metal substrates, it was shown that charge transfer through ultrathin films occurs, which changes the properties of such oxide/metal systems.<sup>[246]</sup>

Similar effects probably change the properties of the ultrathin TiO<sub>2</sub> film formed on Mo(112), thus forcing the deposited gold to wet the TiO<sub>2</sub> layer instead of forming three-dimensional islands or clusters. By comparing the surface free energies of gold (1.5 J/m<sup>2</sup>) and Mo (2.9-3.0 J/m<sup>2</sup>), a two-dimensional growth of gold on bare Mo(112) is expected.<sup>[182,183]</sup> By considering that ultrathin layers can adopt the properties of the underlying substrate, the two-dimensional growth for gold on the TiO<sub>2</sub>/Mo(112) surface becomes comprehensible.

## 8.2 Growth of RuO<sub>2</sub> on TiO<sub>2</sub>(110)

The system of RuO<sub>2</sub> on rutile TiO<sub>2</sub>(110) has gained major interest for the HCl oxidation. While Cl<sub>2</sub> formation from HCl is usually performed by electrolysis, Sumitomo chemicals offered an alternative and more energy efficient approach for the gas phase chlorine formation, using the RuO<sub>2</sub>/TiO<sub>2</sub>(110) system as the active catalyst.<sup>[282-284]</sup> Due to its unique properties and a well defined structure with a atomically sharp interface, the system of RuO<sub>2</sub>/TiO<sub>2</sub>(110) can be used as a photocatalyst, too.<sup>[285]</sup> The grown RuO<sub>2</sub> acts as a cocatalyst while TiO<sub>2</sub>(110) is the photoabsorber. Their synergy enhances the photocatalytic activity, making it a suitable model catalyst for reactions like the water splitting.

With versatile applications in electrochemistry, heterogeneous catalysis and photocatalysis, in-depth understanding of the RuO<sub>2</sub>/TiO<sub>2</sub>(110) system is desirable. Recent studies presented the importance of the morphology of the RuO<sub>2</sub>/TiO<sub>2</sub>(110) system and its related catalytic properties.<sup>[275]</sup> The growth of RuO<sub>2</sub> on rutile TiO<sub>2</sub>(110) has been done by CVD and PVD.<sup>[273-276]</sup> For multilayer thick films (> 40 layers) of RuO<sub>2</sub> on TiO<sub>2</sub>(110), the growth was determined to be FvdM- or layer-by-layer like.<sup>[273]</sup> For smaller amounts of deposited Ru, different morphologies have been reported, i.e. flat one-dimensional RuO<sub>x</sub> row-like structures as well as small three-dimensional islands of RuO<sub>2</sub>.<sup>[274,276]</sup> In a recent STM work, the growth of RuO<sub>2</sub>(110) on rutile TiO<sub>2</sub>(110) near thermodynamic equilibrium has been visualized by systematic STM investigations (*cf. figure 8.2-1*).<sup>[145]</sup> To form RuO<sub>2</sub>(110) on TiO<sub>2</sub>(110), metallic ruthenium was evaporated in an oxygen atmosphere ( $p(\text{O}_2) = 1 \cdot 10^{-6}$  mbar) to the titania surface, which was kept at 600 K. In the initial stage of the RuO<sub>2</sub>(110) growth ( $\leq 2$  ML RuO<sub>2</sub>), square islands are predominantly formed at the steps of the TiO<sub>2</sub>(110) surface (*cf. figure 8.2-1b,c*). Significantly fewer RuO<sub>2</sub> islands are formed on the terraces, indicating the importance of defect sites for the nucleation of RuO<sub>2</sub> on the TiO<sub>2</sub> surface. By increasing the number of defects on the TiO<sub>2</sub>(110) terraces the amount of formed RuO<sub>2</sub> islands on these terraces increases, and the islands are more homogeneously distributed on the TiO<sub>2</sub>(110) surface. Line scan analysis revealed a critical thickness of 3-4 ML for the square-shaped islands. This thickness is largely maintained during subsequent growth of RuO<sub>2</sub>, thus leading mainly to the lateral growth of the islands until they coalesce to complete a wetting film of RuO<sub>2</sub>(110) (*cf. figure 8.2-1d-g*). This wetting film flattened with ongoing deposition of ruthenium in O<sub>2</sub> atmosphere leading to large terraces of RuO<sub>2</sub>. Further growth of RuO<sub>2</sub>(110) ( $\geq 6$  ML) continues via the typical step flow mechanism, i.e. newly formed RuO<sub>2</sub> are exclusively attached at the steps and no nucleation on the terraces occurs.

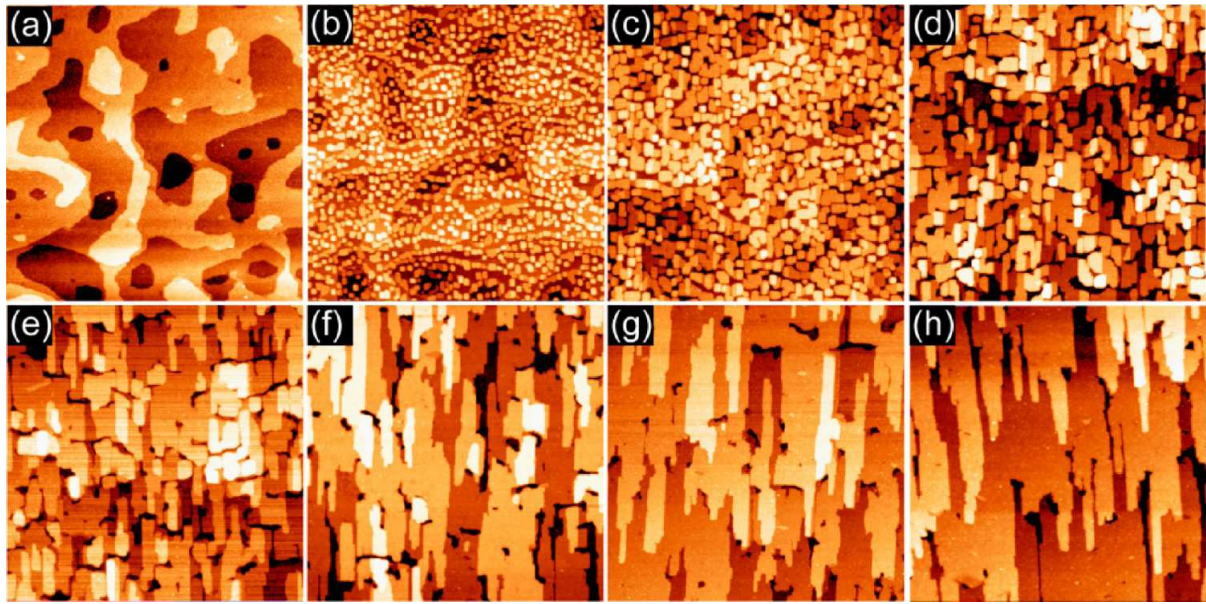


**Figure 8.2-1:** STM images ( $300 \text{ nm} \times 300 \text{ nm}$ ) for  $\text{RuO}_2$  islands and films grown on  $\text{TiO}_2(110)$  at 600 K with increasing amounts of deposited Ru: (a) clean  $\text{TiO}_2(110)$ , (b) 1 ML, (c) 2 ML, (d) 3 ML, (e) 4 ML, (f) 5 ML, (g) 6 ML, and (h) 7 ML. Figure taken from [145].

The step flow growth of  $\text{RuO}_2$  fits very well to the reported layer-by-layer growth for thick  $\text{RuO}_2$  films on  $\text{TiO}_2(110)$ .<sup>[273]</sup> This growth behavior is consistent with several assumptions that can be made for the growth of  $\text{RuO}_2$  on  $\text{TiO}_2(110)$ : Rutile bulk  $\text{RuO}_2(110)$  and  $\text{TiO}_2(110)$  have similar lattice parameters<sup>34</sup>, leading to a rather small lattice misfit and small lateral strain. Therefore a pseudomorph growth behavior occurs with a sharp interface between both oxides, i.e. their atomic structure is well defined.

The surface free energy of  $\text{TiO}_2$  and  $\text{RuO}_2$  are approximately equal.<sup>[286]</sup> With such a small difference of the surface free energies, the interface energy or the strain are very important for the initial growth. The formation of square-shaped islands strongly indicates an important role of the strain energy. From the rectangular unit cell of  $\text{RuO}_2(110)$  a preferred growth direction and rectangular islands would be assumed. The formation of square-shaped islands could be explained by the different lateral strain in the  $\text{RuO}_2$  layer, i.e. compressive strain by  $\sim 4.8 \%$  in the  $[001]$  direction and tensile strain by  $\sim 2.4 \%$  in the  $[1-10]$  direction.<sup>[145]</sup> To elaborate on the square-shaped morphology of the  $\text{RuO}_2$  islands further temperature dependent investigations are required.

Although the square-shaped island structure cannot be completely explained at this point, it confirms and visualizes the previously reported growth of three-dimensional  $\text{RuO}_2$  clusters or islands on  $\text{TiO}_2(110)$  for small deposition amounts of ruthenium.<sup>[274]</sup> Besides this square-shaped morphology the sharp height distribution of 3-4 ML in particular is of interest. By

<sup>34</sup>  $\text{RuO}_2(110)$ : (6.35 Å x 3.11 Å),  $\text{TiO}_2(110)$ : (6.50 Å x 2.96 Å).[145]

keeping the surface at 600 K during the growth, no kinetic barriers are assumed to occur. That the RuO<sub>2</sub>/TiO<sub>2</sub>(110) system is near thermodynamic equilibrium at these growth conditions can be confirmed by the following observations from STM: (i) No nucleation on top of the atomically flat RuO<sub>2</sub> islands or terraces occurs, indicating diffusion limitations have been overcome at 600 K; (ii) the observed step flow growth, for RuO<sub>2</sub> multilayers, is typical for homoepitaxial growth very close to thermodynamic equilibrium. With the RuO<sub>2</sub>/TiO<sub>2</sub>(110) system being at thermodynamic equilibrium the formation of three-dimensional islands would in principle implicate that the surface free energy of RuO<sub>2</sub>(110) is (slightly) higher compared to TiO<sub>2</sub>(110). However the three-dimensional growth stops after 3-4 ML of RuO<sub>2</sub> are reached, leading to an exclusive lateral expansion of these islands with continuing growth. *Why does the three-dimensional growth stop after the 3<sup>rd</sup> (or 4<sup>th</sup>) layer of RuO<sub>2</sub>?*

The formation of such thin 3-4 ML layers of RuO<sub>2</sub> on TiO<sub>2</sub> under HCl reaction conditions or thermal treatment have been reported, but without deeper explanation.<sup>[275]</sup> In Wang's work, 2 nm RuO<sub>2</sub> nanoparticles, impregnated in mesoporous TiO<sub>2</sub>, were transformed to 1 nm thick (~ 3 ML) film of RuO<sub>2</sub> at 300 °C. Assuming that this system was also near thermodynamic equilibrium the transformation from the 2 nm thick nanoparticles to 3 ML thin RuO<sub>2</sub> films strongly indicates a further structural stabilization. Interestingly at similar temperatures (580 K) the oxidation of Ru(0001) by O<sub>2</sub> leads to the formation of ultrathin RuO<sub>2</sub>(110) films covering the ruthenium surface.<sup>[190,191]</sup> The thickness of such thin oxides has been determined to be ≤ 3 ML. Again the thickness of approximately 3 ML is achieved rather fast, but then the three-dimensional growth of RuO<sub>2</sub>(110) is negligible compared to the lateral expansion over the Ru(0001) surface. This also indicates a stabilization of thin three-layered RuO<sub>2</sub>(110) structures. But further experiments and theoretical investigations are necessary to elucidate a possible structural stabilization mechanism for 3-4 ML thick RuO<sub>2</sub> films or islands.

### 8.3 Formation of RuO<sub>2</sub>(110) by oxidation of Ru(0001)

The system of RuO<sub>2</sub>(110) grown on Ru(0001) is known to be an active catalyst for oxidation reactions even at ambient pressures. Due to its well defined structure, RuO<sub>2</sub>(110) is used as a model catalyst in various research fields.<sup>[8]</sup> With various possible coexisting surface orientations for rutile RuO<sub>2</sub> (e.g. RuO<sub>2</sub>(110), RuO<sub>2</sub>(100) and RuO<sub>2</sub>(101)) the conditions for oxidation are crucial to predominantly grow a certain ruthenium oxide and simultaneously preventing the formation of the other oxide orientations.<sup>[191,287-289]</sup> During the gas phase oxidation of the Ru(0001) single crystal surface by O<sub>2</sub> mainly RuO<sub>2</sub>(110) is formed. Due to the reduction in symmetry from the Ru(0001) substrate (C<sub>3</sub>)<sup>35</sup> to the RuO<sub>2</sub>(110) (C<sub>2</sub>) three energetically equal oxide domains are formed on the surface rotated by 120°.<sup>[8]</sup>

Recent studies by Herd et al. gave insight into the initial gas phase oxidation of Ru(0001) using molecular oxygen.<sup>[92,190]</sup> The formation of RuO<sub>2</sub>(110) on Ru(0001) by gas phase oxidation using O<sub>2</sub> is induced by a heterogeneous nucleation and growth process.<sup>[190]</sup> He et al. already showed an Avrami like growth behavior for RuO<sub>2</sub>(110) on Ru(0001) by SXRD, which was confirmed and further investigated by recent LEEM, LEED and SXRD studies.<sup>[191,288-291]</sup> The growth consists of a *induction time* (or *nucleation phase*), where RuO<sub>2</sub> nuclei are formed along the steps of the ruthenium surface, which act as starting points for the growth of flat RuO<sub>2</sub>(110) patches. The nucleation phase is followed by the *growth phase* where the oxide spreads two-dimensionally over the surface leading to a ultrathin (2-4 layers) RuO<sub>2</sub>(110) film covering the Ru(0001) surface. The final *saturation phase* is reached after a thickness of ~ 5 layers of RuO<sub>2</sub>(110) on Ru(0001) where the further thickness growth of the oxide occurs very slowly.<sup>[190,191,288-291]</sup>

For the oxidation of Ru(0001), a threshold pressure and temperature were determined. If either the temperature or the pressure are below 550 K or p(O<sub>2</sub>) = 1·10<sup>-5</sup> mbar, the oxidation is strongly inhibited and RuO<sub>2</sub>(110) is formed very slowly.<sup>[190,191]</sup> For comparison, a completely covering film of RuO<sub>2</sub>(110) on the Ru(0001) surface is formed after 60 minutes, if the temperature and oxygen pressure are set to 630 K and p(O<sub>2</sub>) = 1·10<sup>-5</sup> mbar, respectively.<sup>[288]</sup> It should be mentioned that the growth of RuO<sub>2</sub>(110) can be continued at pressures below 10<sup>-5</sup> mbar, if some nuclei are already available on the surface.<sup>[190,291,292]</sup> This can be explained by nucleation theory, where the stability of a formed oxide nucleus is related to the applied oxygen pressure. If the O<sub>2</sub> pressure is too low (e.g. p(O<sub>2</sub>) = 1·10<sup>-7</sup> mbar), the

---

<sup>35</sup> For simplification the symmetry only refers to the top layer and not to the real symmetry groups of bulk Ru(0001) and RuO<sub>2</sub>(110).

formation of critical clusters is strongly inhibited.<sup>[92,190]</sup> But if the oxide nuclei have already been formed, the growth can readily continue at this low pressure because the growth of the patches itself is not as pressure dependent as the cluster formation.<sup>[290]</sup> The threshold temperature simply reflects the activated oxidation process of Ru(0001) by O<sub>2</sub>.<sup>[92]</sup>

Recent studies showed that the growth of RuO<sub>2</sub>(110) on the mesoscale can vary significantly by changing the applied temperature and O<sub>2</sub> pressures.<sup>[191,291]</sup> By increasing the temperature during the oxidation the lateral size of the RuO<sub>2</sub>(110) flakes increases, while the roughness of the oxide film decreases.<sup>[189]</sup> *Figure 8.3-1* shows the temperature dependent morphology change of the RuO<sub>2</sub>(110) flakes after a Ru(0001) single crystal surface was oxidized by dosing 10<sup>6</sup> L O<sub>2</sub> at 650 K (a), 700 K (b), 800 K (c) and 900 K (d).

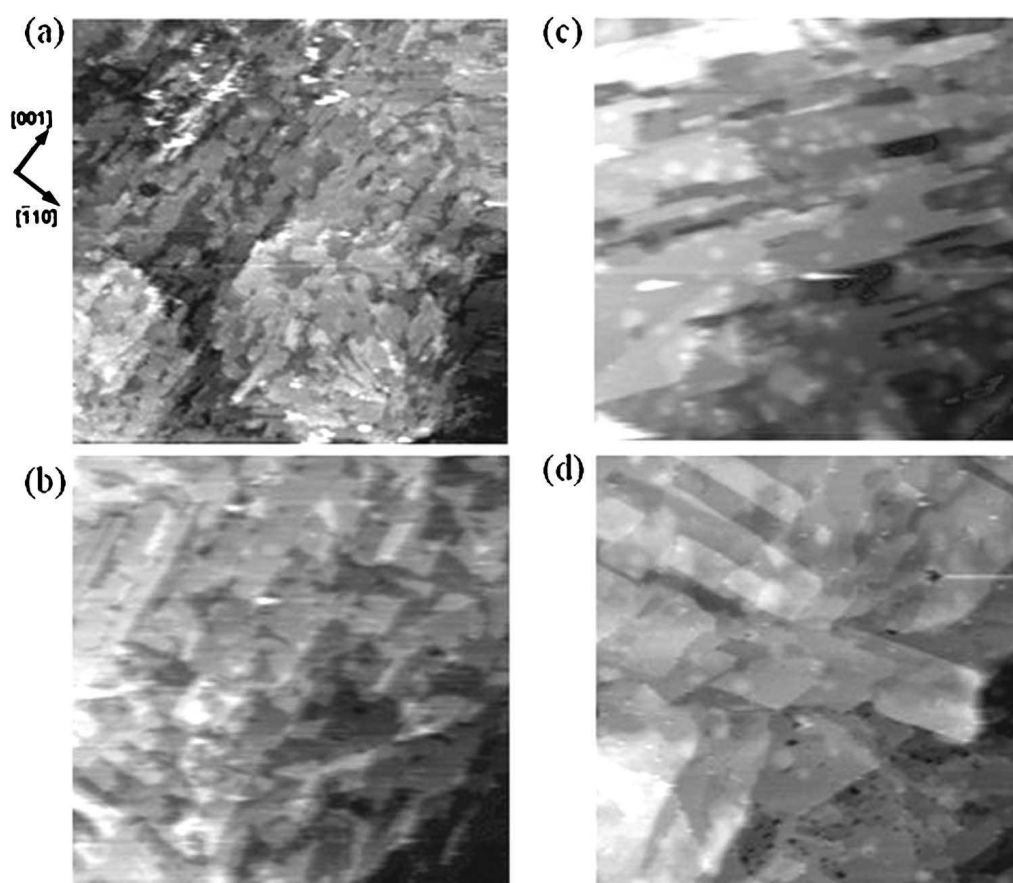


**Figure 8.3-1:** STM images of the morphology of the RuO<sub>2</sub>(110) oxide film grown at various preparation temperatures  $T_{prep}$  on the mesoscale.  $T_{prep}$  = (a) 650 K, (b) 700 K, (c) 800 K, and (d) 850 K. With increasing temperature the terrace width of the grown oxide patches increases, too.  $V = -0.6$  V;  $I = 2.2$  nA; STM image area: 270 nm x 270 nm. Figure taken from [189].

Comparing the calculated surface free energies of the different coexisting surface orientations for RuO<sub>2</sub>, i.e. RuO<sub>2</sub>(110) (0.114 J/m<sup>2</sup>), RuO<sub>2</sub>(100) (0.139 J/m<sup>2</sup>) and RuO<sub>2</sub>(101) (0.123 J/m<sup>2</sup>), with the surface free energy of the Ru(0001) single crystal surface (3.050 J/m<sup>2</sup>) the wetting behavior of RuO<sub>2</sub> can readily be explained.<sup>[182,193]</sup> Due to the different symmetry and lattice

parameters of RuO<sub>2</sub> and Ru(0001) the growth is incommensurate, although it is not known in detail how the RuO<sub>2</sub>(110) binds to the Ru(0001) surface on the atomic level.<sup>[8,92]</sup> But it is assumed that the interface and the resulting interface energy has a major impact on the morphology of the formed RuO<sub>2</sub>(110) on Ru(0001).

The formation of two-to-three layered RuO<sub>2</sub>(110) islands and its two-dimensional spreading over the surface with ongoing oxidation is of further interest. The formation of such ultrathin RuO<sub>2</sub> films has been confirmed by Freund et al., too.<sup>[293]</sup> This supports the interpretation that a stabilization for two-to-four layered RuO<sub>2</sub>(110) structures occurs, which calls for future theoretical investigations to elucidate this interesting observation.

After completing a covering film of two-to-four layered RuO<sub>2</sub>(110), STM shows that the oxide film is not atomically flat. It consists of many flake like patches or islands with different heights, which merged during the growth, thus leading to a rough RuO<sub>2</sub>(110) surface.<sup>[92,189,191,289]</sup> LEEM measurements illustrate that the film grows over the surface starting from several nucleation points.<sup>[191,289]</sup> Evidently the growth of RuO<sub>2</sub>(110) and the resulting morphology cannot be described by one of the ideal growth modes<sup>36</sup>. More likely this rough RuO<sub>2</sub>(110) carpet is the result of a complex interplay of various energy contributions at the interface. The conclusion that the interface determines the resulting morphology becomes more evident by comparing ultrathin RuO<sub>2</sub>(110) grown on the Ru(0001) surface to equal thin films formed on TiO<sub>2</sub>(110). In the previously described system of RuO<sub>2</sub>(110)/TiO<sub>2</sub>(110) significantly larger terraces of RuO<sub>2</sub> are formed, which are also atomically flat. By considering that in both systems an ultrathin film of RuO<sub>2</sub>(110) with equal thickness is formed, the importance how the RuO<sub>2</sub>(110) binds to the underlying substrate becomes evident.

Because the formation process of these both systems cannot be compared directly (epitaxial growth of RuO<sub>2</sub> on TiO<sub>2</sub> versus the oxidation of Ru(0001)), ruthenium was evaporated to the Ru(0001) in oxygen atmosphere to grow RuO<sub>2</sub> at the same conditions as in the RuO<sub>2</sub>/TiO<sub>2</sub>(110) system, i.e. same deposition rate (1 ML Ru / 4 min), substrate temperature (620 K) and oxygen pressure ( $p(\text{O}_2) = 1 \cdot 10^{-6}$  mbar).<sup>[294]</sup> By using these growth conditions the deposited ruthenium atoms attach to the step edges of the Ru(0001) surface and an oxygen overlayer is formed. Both, STM and XPS showed that no oxide was formed on the Ru(0001) surface. By this experiment, the importance of the substrate that induces the rutile structure of RuO<sub>2</sub> on the one hand and has a well defined interface on the other hand becomes evident for the epitaxial growth of RuO<sub>2</sub> by deposition of ruthenium in an oxygen atmosphere.

---

<sup>36</sup> Frank-van-der-Merwe growth; Volmer-Weber growth; Stranski-Krastanov growth.

As mentioned before an increase in temperature also increases the flatness and size of the  $\text{RuO}_2(110)$  terraces. The decrease of the  $\text{RuO}_2$  film roughness can be explained by a simple mind game. With increasing temperature the amount of formed  $\text{RuO}_2$  clusters decreases from which the formation of the flat  $\text{RuO}_2(110)$  film starts.<sup>[190,191]</sup> If, for instance, only one cluster is formed on the surface from which the oxidation starts, then no oxide intersection areas should occur, thus reducing the overall roughness of the oxide film. But experiments showed that the oxidation process is far more complex and the resulting morphology cannot be explained by the nucleation rate alone. Oxidation of  $\text{Ru}(0001)$  by  $\text{O}_2$  at temperatures above 740 K leads to the simultaneous formation of  $\text{RuO}_2(110)$ ,  $\text{RuO}_2(100)$  and  $\text{RuO}_2(101)$ .<sup>[289,295]</sup> Additionally recent studies demonstrated that at higher temperatures ( $> 680$  K) new rotational domains of  $\text{RuO}_2(110)$  begin to appear. With respect to the high symmetry direction of  $\text{RuO}_2$  on the  $\text{Ru}(0001)$  substrate, these new  $\text{RuO}_2(110)$  domains are slightly rotated by up to  $20^\circ$ .<sup>[191]</sup> The formation of differently oriented  $\text{RuO}_2$  as well as occurrence of the rotated  $\text{RuO}_2(110)$  increases the overall roughness of the growing oxide film. The influence of the temperature on the growth behavior has been further visualized by LEEM measurements (*cf. figure 8.3-2*).<sup>[191]</sup>

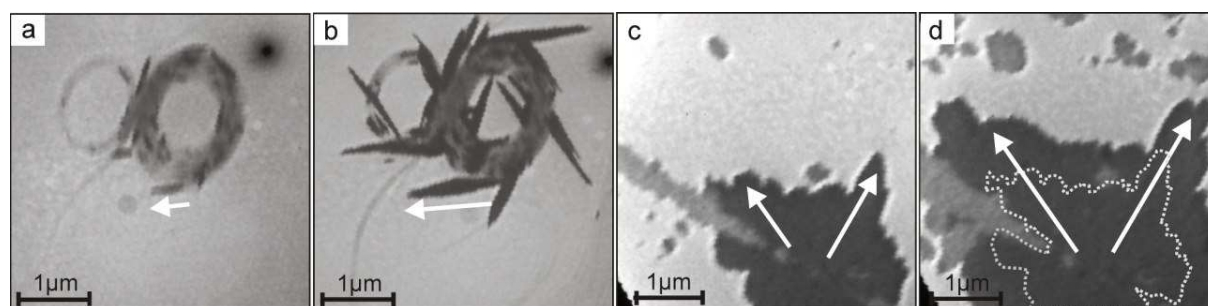


**Figure 8.3-2:** Low energy electron microscopy images obtained during the oxidation of  $\text{Ru}(0001)$  by  $p(\text{O}_2) = 4 \cdot 10^{-5}$  mbar at 580 K after an exposure time of 25 min (a) und 37 min (b) and at 680 K after an exposure time of 25 min (c) and 37 min (d), respectively. While at 580 K (a,b) the  $\text{RuO}_2$  domains grow needle like, i.e. predominantly in the  $[001]$  direction of the oxide, which is also along the main symmetry direction of the  $\text{Ru}(0001)$  substrate (white arrows). The width growth of the oxide is inhibited. At 680 K (c,d) broad oxide islands appear, which grow discoidal over the surface. Again the oxide grows along the high symmetry direction of the substrate with their oxide width being increased. But the growth behavior changed from a merging of separated needles to a disc-like spreading over the  $\text{Ru}(0001)$  surface. Figure taken from [191].

At temperatures around 580 K narrow, needle like  $\text{RuO}_2(110)$  patches are formed, which are mainly growing along the high symmetry directions of the  $\text{Ru}(0001)$  surface (*cf. figure 8.3-2a,b*). From the needle-like shape it is concluded that the oxide grows preferentially in its  $[001]$ <sup>37</sup> direction while the growth in the  $[-110]$  direction is inhibited. By increasing the

<sup>37</sup> This direction is referred to the growing  $\text{RuO}_2(110)$  film and not to the underlying  $\text{Ru}(0001)$  substrate.

temperature to 680 K the growth of the RuO<sub>2</sub> patches changes (*cf. figure 8.3-2c,d*). Instead of many separated needles, which grow simultaneously on the surface and form a covering film of RuO<sub>2</sub>(110) by merging together, at temperatures  $\geq 680$  K the RuO<sub>2</sub>(110) seems to grow more uniformly and discoidal over the Ru(0001) surface starting from one nucleation point. With micro LEED the growth directions of different RuO<sub>2</sub>(110) domains are visible (indicated by the white arrows in *figure 8.3-2c,d*).

The width of the growing oxide patches increased with increasing temperature. Also the oxide patches are still growing predominantly along the [001] direction. It is still unclear if the oxide solely grows one-dimensionally in its [001] direction, or if also a (significantly) slower growth in the [-110] direction occurs. It is therefore not possible to discriminate if the oxide grows two-dimensional on the surface or if a one-dimensional growth of continuously formed needles along an already existing RuO<sub>2</sub>(110) patch occurs.<sup>[191]</sup>

The temperature depending broadening of the RuO<sub>2</sub>(110) terraces (*cf. STM images from figure 8.3-1*) has been further investigated by SXR measurements, where the oxide width at temperatures between 590 K and 680 K has been determined (*cf. figure 8.3-3*).<sup>[290,291]</sup>

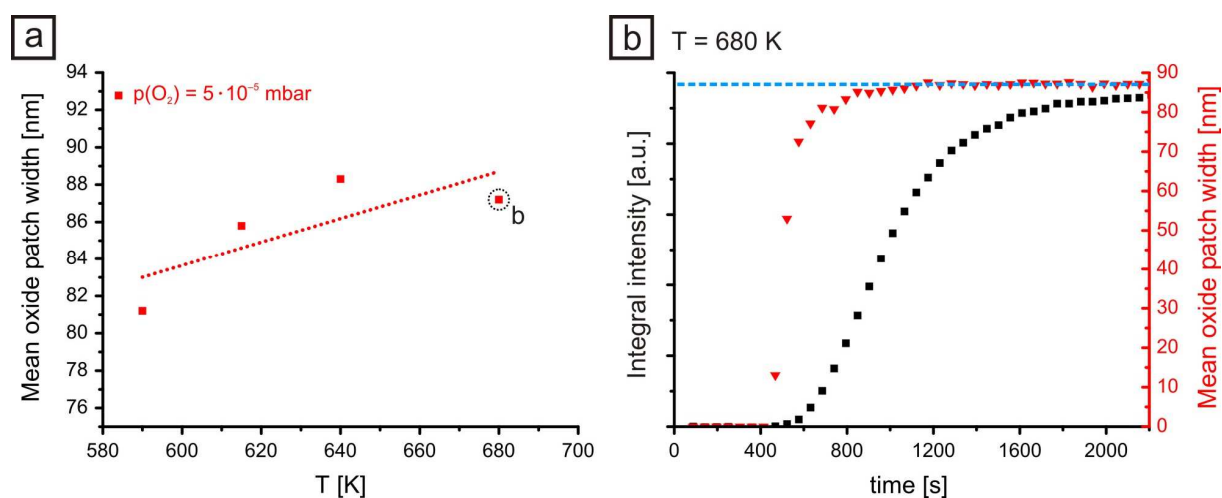


**Figure 8.3-3:** Illustration of the temperature dependent mean oxide patch width, derived from SXR measurements. (a) Oxidation of the Ru(0001) surface in the temperature range of 590 K to 680 K with an applied oxygen pressure of  $5 \cdot 10^{-5}$  mbar. With increasing temperature during oxidation, the mean oxide patch width increases, too. The values of these oxide widths are derived after the saturation of the mean oxide patch width signal (dashed blue line in b). (b) Time dependent growth of the mean oxide patch width (red triangles) and the corresponding overall growth of RuO<sub>2</sub>(110) on the surface (black squares) at 680 K. The mean oxide patch width saturates earlier than the corresponding overall growth signal for the RuO<sub>2</sub> formation on the surface. After reaching a particular width, the growth of RuO<sub>2</sub> in its [-110] direction is inhibited. Therefore the lateral spreading over the surface is done by the growth in the [001] direction of the oxide, which induces the needle-like morphology of RuO<sub>2</sub>(110) on the surface. Figure modified from [290].

The mean oxide patch width is plotted against the temperature. For each temperature the surface was oxidized at  $p(\text{O}_2) = 5 \cdot 10^{-5}$  mbar. The mean oxide patch widths are derived after its saturation is monitored by SXR (cf. *figure 8.3-3b*, dashed blue line).

The mean oxide width of the  $\text{RuO}_2(110)$  patches increases with increasing temperature. This is consistent with the previous interpretation of the STM images. The relatively large deviation between the linear fit and the data points in *figure 8.3-3a* can be explained by the  $\text{RuO}_2(110)$  morphology in this temperature region (cf. *figure 8.3-1a*). In STM, a broad distribution of  $\text{RuO}_2$  patch widths is observable. With SXR, a mean oxide patch width from all grown  $\text{RuO}_2(110)$  patches with the same growth direction were derived. Therefore, this broad distribution is assumed to be one of the main reasons for the deviation between the linear fit and the data points.

By plotting the increase of the mean oxide patch width (red triangles) together with the overall growth of  $\text{RuO}_2(110)$  (black squares) against the time, the kinetics of the oxide growth at 680 K are presented (cf. *figure 8.3-3b*).<sup>[291]</sup> The plots for the other temperatures (590 K, 615 K and 640 K) show a similar Avrami-like curve progression and are not presented here, because only the time scale is different and the interpretation of the growth kinetics is not in the focus within this work. Because the oxide is spreading as a two-to-four layered film two-dimensionally over the surface, the Avrami curve combines the growth of the mean oxide width in  $[-110]$  direction as well as the mean oxide length in  $[001]$  direction. The comparison of the two curves evidently illustrates, that the mean oxide width is reached very fast, compared to the overall lateral growth of the oxide on the  $\text{Ru}(0001)$  surface. This means that the growth in the  $[-110]$  oxide direction is very fast at the beginning but then inhibited. The lateral growth over the surface is then accomplished by the growth of the oxide in the  $[001]$  direction. The LEEM experiments confirm this explanation, where the formation of needles is observable (cf. *figure 8.3-2*), which also predominantly grow in the  $[001]$  direction while their width increases very slowly. Furthermore, by comparing the observed growth behavior by LEEM and by SXR for the whole temperature range (590 K – 680 K), the oxide width always saturates before the overall lateral expansion over the surface has been accomplished. This shows that even for the uniformly growing discoidal carpet of  $\text{RuO}_2$  observed by LEEM (cf. *figure 8.3-2c,d*) the increase of mean oxide width is inhibited, thus indicating that new  $\text{RuO}_2(110)$  patches are continuously formed at the sides of already grown  $\text{RuO}_2(110)$ .

The main question derived by all the presented experiments is: What determines the overall morphology of the covering  $\text{RuO}_2(110)$  film on the  $\text{Ru}(0001)$  substrate? Can the rather simplified model for heterogeneous nucleation and epitaxial growth describe the temperature

dependent morphology and growth behavior of RuO<sub>2</sub>(110) on the Ru(0001) surface? Evidently the complex growth of RuO<sub>2</sub>(110) on Ru(0001) exposes the limitations of the simplified epitaxial growth model at the current level of understanding for the RuO<sub>2</sub>(110)/Ru(0001) system. Although the two-dimensional spreading of RuO<sub>2</sub>(110) over the ruthenium substrate is nicely explainable by the surface free energy relations ( $\sigma_{\text{RuO}_2} \ll \sigma_{\text{Ru0001}}$ )<sup>[182,193]</sup>, the resulting overall morphology and the temperature dependent broadening of the oxide patches cannot be explained that easily. With no information about the RuO<sub>2</sub>/Ru(0001) interface and no explanation of the atomic processes during the RuO<sub>2</sub>(110) growth over the surface, the resulting (temperature depending) morphology cannot be described at this point and descriptions about the growth mechanism on the atomic level are speculative. This evidently shows the importance of a better understanding of the growth mechanism of RuO<sub>2</sub>(110) on Ru(0001) on the one hand and the binding at the interface between the oxide and the substrate on the other hand. Although the resulting morphology cannot be explained without further information of the oxidation mechanism on the atomic scale, the description of the temperature dependent morphologies might become helpful to understand the growth behavior and therefore be another important piece of the overall picture of the oxidation of the Ru(0001) single crystal surface by O<sub>2</sub>.

## 8.4 Summary and conclusions

The previously presented model of heterogeneous nucleation and epitaxial growth (cf. chapter 3) is widely used in surface science. Many observed growth behaviors and the resulting morphologies can be explained qualitatively, only on the basis of the relation between the surface free energies, the interface energy and the strain energy (cf. tables 8-1 and 8-2).

Generally, epitaxially growing materials can be qualitatively described by the surface free energy relation between the deposited material and the substrate. For many systems the difference of a two-dimensional growth or three-dimensional growth is assumed to be determined by the surface energy relation. For a system, where the deposited species has a significantly larger surface free energy than the substrate, a three-dimensional Volmer-Weber-like growth of islands or clusters is expected. Vice versa a system, with the deposited species having a significantly lower surface free energy than the substrate, is expected to form wetting film structures by either a two-dimensional Frank-van-der-Merwe-like layer-by-layer or by a Stranski-Krastranov-like layer-plus-island growth. However these general assumptions are only valid for systems with significantly different surface free energies and only small contributions from the interface energy and the strain energy due to a small lattice misfit between the deposited material and the substrate. But even if a two-dimensional growth is observable due to significantly higher surface free energy of the substrate, the more complex structures at the atomic level (e.g. moiré pattern) of the grown film can only be explained if the interface energy and the strain energy are included into the model.

Moreover other parameters might strongly influence the general growth behavior. This was shown on the basis of the changing oxidation state during metal deposition on the  $\text{TiO}_2$  surface. For this  $\text{Me/TiO}_2$  system the redox chemistry between the deposited material and the substrate substantially changes the growth behavior and the resulting morphologies.<sup>[272]</sup>

Therefore the applicability of the heterogeneous nucleation and epitaxial growth model presented in chapter 3 to predict the growth behavior for any given system is only possible with strong reservations. Even if the overall morphology and growth behavior can be roughly estimated, the real structure (especially on the atomic level) cannot be predicted. Predictions are only reliable if sufficient knowledge about the system has already been gathered. For instance, the temperature dependent growth behavior for any given system can be estimated for a certain temperature range if the growth behavior for this system for another temperature range has already been investigated.

The applicability of the epitaxial growth theory on a transformation process, like the transformation of the Ru(0001) surface to RuO<sub>2</sub>(110) via oxidation, is basically possible. But usually the oxidation of a surface (especially on the atomic level) is so complex, that knowledge of the oxidation mechanism is mandatory so the model can be adapted and improved to describe certain observed morphologies or the growth behavior itself.

In conclusion, the epitaxial growth and heterogeneous nucleation theories are a first guideline to qualitatively explain and conditionally predict the growth behavior and morphologies of well defined systems. This becomes evident by the presented systems within this dissertation. The growth of Au on oxygen free and oxygen precovered Ru(0001) can be well described based on Young's equation. And even the oxidation of the thin gold islands (or films) and the resulting fragmentation is described by the proposed shoveling mechanism for which general assumptions on the basis of Young's equation were done.

The complimentary system of Ru deposited on Au(111) is, however, conditionally describable. The Au(111) surface with its unique herringbone reconstruction significantly influences the growth of the deposited ruthenium. In a first approach, the general growth behavior of metallic Ru on Au(111) and the formation of the perforated Ru film under oxygen exposure can be described qualitatively on the basis of Young's equation. However, several issues like the discrimination between a Au-Ru surface alloy and embedded Ru islands in the first Au(111) layers remains elusive. Evidently for this more complex system the applicability of Young's equation reaches its limitations and further knowledge of the Ru/Au(111) system is mandatory to adequately explain the observed morphologies and the growth behavior.

## 9. References

- [1] Competence Network Catalysis (ConNeCat) DECHEMA e.V., *Katalyse eine Schlüsseltechnologie für nachhaltiges Wirtschaftswachstum – Roadmap der deutschen Katalysatorforschung*. **2006**, 2 Auflage.
- [2] U.S. Climate Change Technology Program, *Technology Options for the Near and Long Term*. August **2005** – 1.4-9
- [3] G. H. Zhu, J. Y. Han, D. Y. Zernlyanov, F. H. Ribeiro, *J. Phys. Chem. B* **2005**, *109*, 2331-2337.
- [4] J. F. Weaver, *Chem. Rev.* **2013**, *113*, 4164-4215.
- [5] R. M. Heck, R. J. Farrauto, *Appl. Catal. A* **2001**, *221*, 443-457.
- [6] Y. Nishihata, J. Mizuki, T. Akao, H. Tanaka, M. Uenishi, M. Kimura, T. Okamoto, N. Hamada, *Nature* **2002**, *418*, 164-167.
- [7] M. Ziauddin, G. Veser, L. D. Schmidt, *Catal. Lett.* **1997**, *46*, 159-167.
- [8] H. Over, *Chem. Rev.* **2012**, *112*, 3356-3426.
- [9] F. Zaera, *J. Phys. Chem. B* **2002**, *106*, 4043-4052.
- [10] G. A. Somorjai, J. Y. Park, *Angew. Chem. Int. Ed.* **2008**, *47*, 9212-9228.
- [11] G. A. Somorjai, C. J. Kliewer, *React. Kinet. Catal. Lett.* **2009**, *96*, 191-208.
- [12] M. Haruta, *Chem. Record* **2003**, *3*, 75-87.
- [13] M. Haruta, *Gold Bulletin* **2004**, *37*, 27-36.
- [14] M. Haruta, N. Yamada, T. Kobayashi, S. Iijima, *J. Catal.* **1989**, *115*, 301-309.
- [15] J. Gong, *Chem. Rev.* **2012**, *112*, 2987-3054.
- [16] B. K. Min, C. M. Friend, *Chem. Rev.* **2007**, *107*, 2709-2724.

- [17] R. Meyer, C. Lemire, Sh. K. Shaikhutdinov, H.-J. Freund, *Gold Bulletin* **2004**, *37*, 72-124.
- [18] G. C. Bond, D. T. Thompson, *Catal. Rev.-Sci. Eng.* **1999**, *41*, 319-388.
- [19] A. Stephen, K. Hashmi, G. J. Hutchings, *Angew. Chem. Int. Ed.* **2006**, *45*, 7896-7936.
- [20] M. S. Chen, D. W. Goodman, *Science* **2004**, *306*, 252-255.
- [21] M. S. Chen, Y. Cai, Z. Yan, D. W. Goodman, *J. Am. Chem. Soc.* **2005**, *128*, 6341-6346.
- [22] M. S. Chen, D. W. Goodman, *Acc. Chem. Res.* **2006**, *39*, 739-746.
- [23] M. Valden, X. Lai, D. W. Goodman, *Science* **1998**, *281*, 1647-1650.
- [24] T. S. Kim, J. D. Stiehl, C. T. Reeves, R. J. Meyer, C. B. Mullins, *J. Am. Chem. Soc.* **2003**, *125*, 2018-2019.
- [25] M. Mavrikakis, P. Stoltze, J. K. Nørskov, *Catal. Lett.* **2000**, *64*, 101-106.
- [26] N. López, J. K. Nørskov, *J. Am. Chem. Soc.* **2002**, *124*, 11262-11263.
- [27] T. Herranz, X. Deng, A. Cabot, P. Alivisatos, Z. Liu, G. Soler-Illia, M. Salmeron, *Catal. Today* **2009**, *143*, 158-166.
- [28] M. S. Chen, D. W. Goodman, *Catal. Today* **2006**, *111*, 22-33.
- [29] M. S. Chen, D. W. Goodman, *Top. Catal.* **2007**, *44*, 41-47.
- [30] E. D. Park, J. S. Lee, *J. Catal.* **1999**, *186*, 1-11.
- [31] L. Delannoy, N. Weiher, N. Tsapatsaris, A. M. Beesley, L. Nchari, S. L. M. Schroeder, C. Louis, *Top. Catal.* **2007**, *44*, 263-273.
- [32] L. K. Ono, B. R. Cuenya, *J. Phys. Chem. C* **2008**, *112*, 4676-4686.
- [33] J. A. van Bokhoven, C. Louis, J. T. Miller, M. Tromp, O. V. Safonova, P. Glatzel, *Angew. Chem. Int. Ed.* **2006**, *45*, 4651-4654.

- [34] N. Weiher, A. M. Beesley, N. Tsapatsaris, L. Delannoy, C. Louis, J. A. van Bokhoven, S. L. M. Schroeder, *J. Am. Chem. Soc.* **2007**, *129*, 2240-2241.
- [35] A.-F. Lamic-Humblot, P. Barthe, G. Guzman, L. Delannoy, C. Louis, *Thin Sol. Films* **2013**, *527*, 96-101.
- [36] B. K. Min, A. R. Alemozafar, M. M. Biener, J. Biener, C. M. Friend, *Top. Catal.* **2005**, *36*, 77-90.
- [37] G. Mills, M. S. Gordon, H. Metiu, *J. Chem. Phys.* **2003**, *118*, 4198-4205.
- [38] T. A. Baker, C. M. Friend, E. Kaxiras, *J. Chem. Theory Comput.* **2010**, *6*, 279-287.
- [39] T. A. Baker, X. Liu, C. M. Friend, *Phys. Chem. Chem. Phys.* **2011**, *13*, 34-46.
- [40] J. Gong, C. B. Mullins, *Acc. Chem. Res.* **2009**, *42*, 1063-1073.
- [41] J. G. Wang, B. Hammer, *Top. Catal.* **2007**, *44*, 49-56.
- [42] G. C. Bond, D. T. Thompson, *Gold Bulletin* **2000**, *33*, 41-50.
- [43] D. Widmann, Y. Liu, F. Schüth, R. J. Behm, *J. Catal.* **2010**, *276*, 292-305.
- [44] N. López, T. V. W. Janssens, B. S. Clausen, Y. Xu, M. Mavrikakis, T. Bligaard, J. K. Nørskov, *J. Catal.* **2004**, *223*, 232-235.
- [45] T. Fujitani, I. Nakamura, *Angew. Chem. Int. Ed.* **2011**, *50*, 10144-10147.
- [46] Z.-P. Liu, X.-Q. Gong, J. Kohanoff, C. Sanchez, P. Hu, *Phys. Rev. Lett.* **2003**, *91*, 266102.
- [47] A. Sanchez, S. Abbet, U. Heiz, W.-D. Schneider, H. Häkkinen, R. N. Barnett, U. Landman, *J. Phys. Chem. A* **1999**, *103*, 9573-9578.
- [48] M. Kotobuki, R. Leppelt, D. A. Hansgen, D. Widmann, R. J. Behm, *J. Catal.* **2009**, *264*, 67-76.
- [49] D. Widmann, R. J. Behm, *Angew. Chem. Int. Ed.* **2011**, *50*, 10241-10245.
- [50] J. M. Gottfried, K. Christmann, *Surf. Sci.* **2004**, *566-568*, 1112-1117.

- [51] X. Deng, B. K. Min, A. Guloy, C. M. Friend, *J. Am. Chem. Soc.* **2005**, *127*, 9267-9270.
- [52] C. Lemire, R. Meyer, S. Shaikhutdinov, H.-J. Freund, *Angew. Chem. Int. Ed.* **2004**, *43*, 118-121.
- [53] C. Lemire, R. Meyer, Sh. K. Shaikhutdinov, H.-J. Freund, *Surf. Sci.* **2004**, *552*, 27-34.
- [54] Y. Xu, M. Mavrikakis, *J. Phys. Chem. B* **2003**, *107*, 9298-9307.
- [55] I. Nakamura, A. Takahashi, T. Fujitani, *Catal. Lett.* **2009**, *129*, 400-403.
- [56] J. Kim, E. Samano, B. E. Koel, *Surf. Sci.* **2006**, *600*, 4622-4632.
- [57] T. A. Baker, B. Xu, X. Liu, E. Kaxiras, C. M. Friend, *J. Phys. Chem. C* **2009**, *113*, 16561-16564.
- [58] B. Koslowski, H.-G. Boyen, C. Wilderotter, G. Kästle, P. Ziemann, R. Wahrenberg, P. Oelhafen, *Surf. Sci.* **2001**, *475*, 1-10.
- [59] J. J. Pireaux, M. Liehr, P. A. Thiry, J. P. Delrue, R. Gaudano, *Surf. Sci.* **1984**, *141*, 221-232.
- [60] A. E. Baber, D. Torres, K. Müller, M. Nazzarro, P. Liu, D. E. Starr, D. J. Stacchiola, *J. Phys. Chem. C* **2012**, *116*, 18292-18299.
- [61] J. Biener, M. M. Biener, T. Nowitzki, A. V. Hamza, C. M. Friend, V. Zielasek, M. Bäumer, *ChemPhysChem* **2006**, *7*, 1906-1908.
- [62] M. A. Chesters, G. A. Somorjai, *Surf. Sci.* **1975**, *52*, 21-28.
- [63] L. Huang, P. Zeppenfeld, J. Chevrier, G. Comsa, *Surf. Sci.* **1996**, *352-354*, 285-289.
- [64] P. Jiang, S. Porsgaard, F. Borondics, M. Köber, A. Caballero, H. Bluhm, F. Besenbacher, M. Salmeron, *J. Am. Chem. Soc.* **2010**, *132*, 2858-2859.
- [65] A. G. Sault, R. J. Madix, C. T. Campbell, *Surf. Sci.* **1986**, *169*, 347-356.
- [66] B. K. Min, A. R. Alemozafar, D. Pinnaduwege, X. Deng, C. M. Friend, *J. Phys. Chem. B* **2006**, *110*, 19833-19838.

- [67] R. A. Ojifinni, J. Gong, D. W. Flaherty, T. S. Kim, C. B. Mullins, *J. Phys. Chem. C* **2009**, *113*, 9820-9825.
- [68] J. M. Gottfried, N. Elghobashi, S. L. M. Schroeder, K. Christmann, *Surf. Sci.* **2003**, *523*, 89-102.
- [69] J. M. Gottfried, K. J. Schmidt, S. L. M. Schroeder, K. Christmann, *Surf. Sci.* **2002**, *511*, 65-82.
- [70] K. Dumbuya, G. Cabailh, R. Lazzari, J. Jupille, L. Ringel, M. Pistor, O. Lytken, H.-P. Steinrück, J. M. Gottfried, *Catal. Today* **2012**, *181*, 20-25.
- [71] N. Saliba, D. H. Parker, B. E. Koel, *Surf. Sci.* **1998**, *410*, 270-282.
- [72] E. Irissou, M.-C. Denis, M. Chaker, D. Guay, *Thin Sol. Films* **2005**, *472*, 49-57.
- [73] H. Tsai, E. Hu, K. Perng, M. Chen, J.-C. Wu, Y.-S. Chang, *Surf. Sci.* **2003**, *537*, L447-L450.
- [74] H.-G. Boyen, G. Kästle, F. Weigl, B. Koslowski, C. Dietrich, P. Ziemann, J. P. Spatz, S. Riethmüller, C. Hartmann, M. Möller, G. Schmid, M. G. Garnier, P. Oelhafen, *Science* **2002**, *297*, 1533-1536.
- [75] D. C. Lim, Y. D. Kim, *Appl. Surf. Sci.* **2006**, *253*, 2984-2987.
- [76] D. C. Lim, I. Lopez-Salido, R. Dietsche, M. Bubek, Y. D. Kim, *Chem. Phys.* **2006**, *330*, 441-448.
- [77] K. M. Cook, G. S. Ferguson, *J. Phys. Chem. C* **2011**, *115*, 22976-22980.
- [78] K. Sun, M. Kohyama, S. Tanaka, S. Takeda, *J. Phys. Chem. A* **2012**, *116*, 9568-9573.
- [79] K. A. Davis, D. W. Goodman, *J. Phys. Chem. B* **2000**, *104*, 8557-8562.
- [80] H. Shi, R. Asahi, C. Stampfl, *Phys. Rev. B* **2007**, *75*, 205125.
- [81] P. G. Jones, H. Rumpel, E. Schwarzmann, G. M. Sheldrick, H. Paulus, *Acta Cryst.* **1979**, *B35*, 1435-1437.

- [82] H. Shi, C. Stampfl, *Phys. Rev. B* **2007**, *76*, 075327.
- [83] N. D. S. Canning, D. Outka, R. J. Madix, *Surf. Sci.* **1984**, *141*, 240-254.
- [84] T. Hayashi, K. Tanaka, M. Haruta, *J. Catal* **1998**, *178*, 566-575.
- [85] K. J. Stowers, R. J. Madix, C. M. Friend, *J. Catal.* **2013**, *308*, 131-141.
- [86] B. Xu, R. J. Madix, C. M. Friend, *Acc. Chem. Res.* **2014**, *47*, 761-772.
- [87] X. Deng, B. K. Min, X. Liu, C. M. Friend, *J. Phys. Chem. B* **2006**, *110*, 15982-15987.
- [88] X. Deng, C. M. Friend, *J. Am. Chem. Soc.* **2005**, *127*, 17178-17179.
- [89] T. Cai, Z. Song, Z. Chang, G. Liu, J. A. Rodriguez, J. Hrbek, *Surf. Sci.* **2003**, *538*, 76-88.
- [90] T. Cai, Z. Song, J. A. Rodriguez, J. Hrbek, *J. Am. Chem. Soc.* **2004**, *126*, 8886-8887.
- [91] F. M. Hoffmann, Y. S. Hoo, T. H. Cai, M. G. White, J. Hrbek, *Surf. Sci.* **2012**, *606*, 1906-1913.
- [92] B. Herd, *Die initiale Gasphasenoxidation von Ru(0001) unter Verwendung von molekularem und atomarem Sauerstoff*. Ph.D. thesis, Justus-Liebig-Universität Gießen, **2013**.
- [93] Y. Zhang, J. R. G. Evans, S. Yang, *J. Chem. Eng. Data* **2011**, *56*, 328-337.
- [94] K. S. S. Harsha, *Principles of Physical Vapor Deposition of Thin Films*, Elsevier Great Britain **2006**.
- [95] H. von Wartenberg, *Z. anorg. allg. Chem.* **1938**, *238*, 299-304.
- [96] Oxford Applied Research, *TC50 Universal Thermal Cracker for Surface Science* **2000**, <http://www.oaresearch.co.uk/oaresearch/brochures/TCSeries.pdf>, retrieved August 2015.
- [97] Oxford Applied Research, *Thermal Cracker Application Note* **2008**, <http://www.oaresearch.co.uk/oaresearch/brochures/TC50ApplicationNotes.pdf>, retrieved August 2015.

- [98] Pfeiffer Vacuum, *Operating Instructions Prisma Plus QMG 220, Compact Mass Spectrometer System*, <https://www.pfeiffer-vacuum.com/en/products/analysis-equipment/>, retrieved August 2015.
- [99] Oxford Instruments, *Full Range of Electron Beam Evaporators for all Kind of Deposition* **2013**, <http://www.omicron.de/en/products/efm-3-/instrument-concept>, retrieved August 2015.
- [100] tectra GmbH Physikalische Instrumente, *Electron Beam Evaporator* **2010**, <http://www.tectra.de/e-flux.pdf>, retrieved August 2015.
- [101] G. Binning, H. Rohrer, C. Gerber, E. Weibel, *Appl. Phys. Lett.* **1982**, *40*, 178-180.
- [102] G. Binning, H. Rohrer, C. Gerber, E. Weibel, *Phys. Rev. Lett.* **1982**, *49*, 57-61.
- [103] G. Binning, H. Rohrer, *Angew. Chem.* **1987**, *99*, 622-631.
- [104] G. Binning, H. Rohrer, *Rev. Mod. Phys.* **1999**, *71*, S324.
- [105] F. Besenbacher, *Rep. Prog. Phys.* **1996**, *59*, 1737-1802.
- [106] J. Tersoff, D.R. Hamann, *Phys. Rev. Lett.* **1983**, *50*, 1998-2001.
- [107] J. Tersoff, D. R. Hamann, *Phys. Rev. B* **1985**, *31*, 805-813.
- [108] U. Diebold, *Surf. Sci. Rep.* **2003**, *48*, 53-229.
- [109] K. Siegbahn, *Nobel lecture* **1981**.
- [110] E. Mutoro, B. Luerßen, S. Günther, J. Janek, *Bunsen-Magazin* **2007**, *9*.
- [111] K. Levsen, *Chemie in unserer Zeit* **1976**, *10*, 48-53.
- [112] W. F. Moulder, P. E. Strickle, K. D. Sobol, *Handbook of X-ray Photoelectron Spectroscopy* Physical Electronics Inc. **1995**.
- [113] K. Christmann, *Introduction to Surface Physical Chemistry* Steinkopf-Verlag Darmstadt, Springer-Verlag New York **1991**.

- [114] G. Ertl, J. Knoppers, *Low Energy Electron and Surface Chemistry*, Verlag-Chemie **1985**.
- [115] T. Koopmans, *Physica* **1934**, *1*, 104-113.
- [116] S. Hüfner, *Photoelectron Spectroscopy-Principles and Applications*, Springer-Verlag, Berlin Heidelberg New York **2003**.
- [117] M. P. Seah, W. A. Dench, *Surf. Interface Anal.* **1979**, *1*, 2-11.
- [118] I. V. Markov, *Crystal Growth for Beginners*, World Scientific Publishing, Singapore New Jersey London HongKong **1995**.
- [119] M. Ohring, *Materials Science of Thin Films*, Academic Press, San Diego **2002**.
- [120] T. Michely, J. Krug, *Islands, Mounds and Atoms*, Springer-Verlag, Berlin Heidelberg New York **2004**.
- [121] A. P. Sutton, R. W. Balluffi, *Interfaces in Crystalline Materials*, Oxford University Press Oxford New York **1995**.
- [122] K. W. Kolasinski, *Surface Science – Foundations of Catalysis and Nanoscience*, Wiley-VCH Verlag New Jersey Weinheim **2012**.
- [123] G. A. Somorjai, Y. Li, *Introduction to Surface Chemistry and Catalysis*, Wiley-VCH Verlag New Jersey Weinheim **2010**.
- [124] D. A. King, D. P. Woodruff, *The Chemical Physics of Solid Surfaces – Growth and Properties of Ultrathin Epitaxial Layers*, Elsevier Science Amsterdam New York **1997**.
- [125] M. Bäumer, H.-J. Freund, *Prog. Surf. Sci.* **1999**, *61*, 127-198.
- [126] S. A. Chambers, *Surf. Sci. Rep.* **2000**, *39*, 105-180.
- [127] S. A. Chambers, *Adv. Mater.* **2010**, *22*, 219-248.
- [128] C. T. Campbell, *Surf. Sci. Rep.* **1997**, *27*, 1-111.
- [129] Q. Fu, T. Wagner, *Surf. Sci. Rep.* **2007**, *62*, 431-498.

- [130] B. R. Cuenya, *Thin Sol. Films* **2010**, *518*, 3127-3150.
- [131] M. Brune, *Surf. Sci. Rep.* **1998**, *31*, 121-229.
- [132] M. Opel, *J. Phys. D* **2012**, *45*, 1-31.
- [133] W. D. Nix, *Metall. Trans.* **1989**, *20*, 2217-2245.
- [134] E. Bauer, *Appl. Surf. Sci.* **1982**, *11/12*, 479-494.
- [135] H. Brune, *Surf. Sci. Rep.* **1998**, *31*, 121-229.
- [136] C. Nagl, E. Platzgummer, M. Schmid, P. Varga, S. Speller, W. Heiland, *Phys. Rev. Lett.* **1995**, *75*, 2976-2979; Erratum *Phys. Rev. Lett* **1996**, *76*, 3240
- [137] J. A. Farmer, C. T. Campbell, *Science* **2010**, *329*, 933-936.
- [138] W. A. Jesser, D. Kuhlmann-Wilsdorf, *Phys. Stat. Sol.* **1967**, *19*, 95-105.
- [139] J. H. Van Der Merwe, *J. Appl. Phys.* **1963**, *34*, 117-122.
- [140] J. H. Van Der Merwe, *J. Appl. Phys.* **1963**, *34*, 123-127.
- [141] N. Cabrera, *Surf. Sci.* **1964**, *2*, 320-345.
- [142] N. H. Fletcher, *J. Appl. Phys.* **1964**, *35*, 234-240.
- [143] A. Farkas, G. C. Mellau, H. Over, *J. Phys. Chem. C* **2009**, *113*, 14341-14355.
- [144] A. Farkas, *In situ IR spectroscopic studies of the CO oxidation reaction over a ruthenium model catalyst*. Ph.D. thesis, Justus-Liebig-Universität Gießen, **2008**.
- [145] Y. He, D. Langsdorf, L. Li, H. Over, *J. Phys. Chem. C* **2015**, *119*, 2692-2702.
- [146] J. A. Venables, *Surf. Sci.* **1994**, *299/300*, 798-817.
- [147] R. L. Schwoebel, E. J. Shipsey, *J. Appl. Phys.* **1966**, *37*, 3682-3686.
- [148] G. Ehrlich, F. G. Hudde, *J. Chem. Phys.* **1966**, *44*, 1039-1049.

- [149] D. A. Reed, G. Ehrlich, *Surf. Sci.* **1981**, *102*, 588-609.
- [150] G. L. Kellog, *Surf. Sci. Rep.* **1994**, *21*, 1-88.
- [151] M. Bowker, D. A. King, *Surf. Sci.* **1978**, *71*, 583-598.
- [152] M. Bowker, D. A. King, *Surf. Sci.* **1978**, *72*, 208-212.
- [153] B. K. Min, X. Deng, D. Pinnaduwege, R. Schalek, C. M. Friend, *Phys. Rev. B* **2005**, *72*, 121410.
- [154] R. Q. Hwang, J. Schröder, C. Günther, R. J. Behm, *Phys. Rev. Lett.* **1991**, *67*, 3279-3282.
- [155] G. Pötschke, J. Schröder, C. Günther, R. Q. Hwang, R. J. Behm, *Surf. Sci.* **1991**, *251/252*, 592-596.
- [156] R. Q. Hwang, C. Günther, J. Schröder, S. Günther, E. Kopatzki, R. J. Behm, *J. Vac. Sci. Tech. A* **1992**, *10*, 1970-1980.
- [157] J. Schröder, C. Günther, R. Q. Hwang, R. J. Behm, *Ultramicroscopy* **1992**, *42-44*, 475-482.
- [158] J. Hrbek, A. K. Schmid, M. C. Bartelt, R. Q. Hwang, *Surf. Sci.* **1997**, *385*, L1002-L1009.
- [159] W. L. Ling, J. C. Hamilton, K. Thürmer, G. E. Thayer, J. de la Figuera, R.Q. Hwang, C. B. Carter, N. C. Bartelt, K. F. McCarty, *Surf. Sci.* **2006**, *600*, 1735-1757.
- [160] S. Poulston, M. Tikhov, R. M. Lambert, *Surf. Sci.* **1995**, *331-333*, 818-823.
- [161] S. Poulston, M. Tikhov, R. M. Lambert, *Langmuir* **1997**, *13*, 5356-5361.
- [162] I. J. Malik, J. Hrbek, *J. Vac. Sci. Technol. A* **1991**, *9*, 1737-1741.
- [163] I. J. Malik, J. Hrbek, *J. Vac. Sci. Technol. A* **1991**, *9*, 1806-1809.
- [164] M. Kuhn, J. A. Rodriguez, J. Hrbek, A. Bzowski, T. K. Sham, *Surf. Sci.* **1995**, *341*, L1011-L1018.

- [165] Q. Wu, J. Hrbek, *Surf. Sci.* **2005**, 588, 117-126.
- [166] A. Steltenpohl, N. Memmel, E. Taglauer, T. Fauster, J. Onsgaard, *Surf. Sci.* **1997**, 382, 300-309.
- [167] O. Stein, J. Ankri, M. Asscher, *Phys. Chem. Chem. Phys.* **2013**, 15, 13506-13512.
- [168] T. E. Madey, H. A. Engelhardt, D. Menzel, *Surf. Sci.* **1975**, 48, 304-328.
- [169] M. Lindroos, H. Pfnür, G. Held, D. Menzel, *Surf. Sci.* **1989**, 222, 451-463.
- [170] J. Winterlin, J. Trost, S. Renisch, R. Schuster, T. Zambelli, G. Ertl, *Surf. Sci.* **1997**, 394, 159-169.
- [171] S. L. Parrot, G. Praline, B. E. Koel, J. M. White, T. Taylor, *J. Chem. Phys.* **1979**, 71, 3352-3354.
- [172] H. Pfnür, G. Held, M. Lindroos, D. Menzel, *Surf. Sci.* **1989**, 220, 43-58.
- [173] C. Corriol, F. Calleja, A. Arnau, J. J. Hinarejos, A. L. Vázquez de Parga, W. A. Hofer, R. Miranda, *Chem. Phys. Lett.* **2005**, 405, 131-135.
- [174] K. L. Kostov, M. Gsell, P. Jakob, T. Moritz, W. Widdra, D. Menzel, *Surf. Sci.* **1997**, 394, L138-L144.
- [175] Y. D. Kim, S. Wendt, S. Schwegmann, H. Over, G. Ertl, *Surf. Sci.* **1998**, 418, 267-272.
- [176] P. Jakob, M. Gsell, D. Menzel, *J. Chem. Phys.* **2001**, 114, 10075-10085.
- [177] C. Stampfl, S. Schwegmann, H. Over, M. Scheffler, G. Ertl, *Phys. Rev. Lett.* **1996**, 77, 3371-3374.
- [178] J. V. Barth, H. Brune, G. Ertl, R. J. Behm, *Phys. Rev. B* **1990**, 42, 9307-9318.
- [179] A. R. Sandy, S. G. J. Mochrie, D. M. Zehner, K. G. Huang, D. Gibbs, *Phys. Rev. B* **1991**, 43, 4667-4687.
- [180] S. Narasimhan, D. Vanderbilt, *Phys. Rev. Lett.* **1992**, 69, 1564-1567; Erratum *Phys. Rev. Lett.* **1992**, 69, 2455-2456.

- [181] Y. D. Kim, S. Schwegmann, A. P. Seitsonen, H. Over, *J. Phys. Chem. B* **2001**, *105*, 2205-2211.
- [182] L. Vitos, A. V. Ruban, H. L. Skriver, J. Kollár, *Surf. Sci.* **1998**, *411*, 186-202.
- [183] F. Aqra, A. Ayyad, *Appl. Surf. Sci.* **2011**, *257*, 6372-6379.
- [184] G. D. Barmparis, I. N. Remediakis, *Phys. Rev. B* **2012**, *86*, 085457.
- [185] Y. D. Kim, A. P. Seitsonen, S. Wendt, J. Wang, C. Fan, K. Jacobi, H. Over, G. Ertl, *J. Phys. Chem. B* **2001**, *105*, 3752-3758.
- [186] H. Bludau, M. Skottke, B. Pennemann, P. Mrozek, K. Wandelt, *Vacuum* **1990**, *41*, 1106-1108.
- [187] C. Stampfl, H. J. Kreuzer, S. H. Payne, H. Pfnür, M. Scheffler, *Phys. Rev. Lett.* **1999**, *83*, 2993-2996.
- [188] W. L. Ling, T. Giessel, K. Thürmer, R. Q. Hwang, N. C. Bartelt, K. F. McCarty, *Surf. Sci.* **2004**, *570*, L297-L303.
- [189] S. H. Kim, J. Wintterlin, *J. Chem. Phys.* **2009**, *131*, 064705.
- [190] B. Herd, M. Knapp, H. Over, *J. Phys. Chem. C* **2012**, *116*, 24649-24660.
- [191] J. C. Goritzka, B. Herd, P. P. T. Krause, J. Falta, J. I. Flege, Herbert Over, *Phys. Chem. Chem. Phys.* **2015**, *17*, 13895-13903.
- [192] H. Over, A. P. Seitsonen, E. Lundgren, M. Schmid, P. Varga, *Surf. Sci.* **2000**, *515*, 143-156.
- [193] H. Over, M. Knapp, E. Lundgren, A. P. Seitsonen, M. Schmid, P. Varga, *Chem. Phys. Chem.* **2004**, *5*, 167-174.
- [194] G. K. Wertheim, S. B. DiCenzo, S. E. Youngquist, *Phys. Rev. Lett.* **1983**, *51*, 2310-2313.
- [195] C. C. Chusuei, X. Lai, K. Luo, D. W. Goodman, *Top. Catal.* **2001**, *14*, 71-83.

- [196] H. Over, A. P. Seitsonen, E. Lundgren, M. Wiklund, J. N. Anderson, *Chem. Phys. Lett.* **2001**, *342*, 467-472.
- [197] Benjamin Herd, Jan C. Goritzka, and Herbert Over, *J. Phys. Chem. C* **2013**, *117*, 15148-15154.
- [198] A. Krozer, M. Rodahl, *J. Vac. Sci. Tech. A* **1997**, *15*, 1704-1709.
- [199] E. A. Willneff, C. Klanner, S. L. M. Schroeder, *Chem. Commun.* **2003**, 258–259.
- [200] B. Herd, H. Over, *Surf. Sci.* **2014**, *622*, 24-34.
- [201] N. Weiher, E. A. Willneff, C. Figulla-Kroschel, M. Jansen, S. L. M. Schroeder, *Solid State Comm.* **2003**, *125*, 317-322.
- [202] J. Lipkowski, P. N. Ross, *Electrocatalysis*, Wiley-VHC, New York **1998**.
- [203] W. F. Lin, T. Iwasita, W. Vielstich, *J. Phys. Chem. B* **1999**, *103*, 3250-3257.
- [204] W. F. Lin, M. S. Zei, M. Eiswirth, G. Ertl, T. Iwasita, W. Vielstich, *J. Phys. Chem. B* **1999**, *103*, 6968-6977.
- [205] M. Watanabe, S. Motoo, *Electroanal. Chem. Interf. Electrochem.* **1975**, *60*, 267-273.
- [206] F. Maroun, S. Morin, A. Lachenwitzer, O. M. Magnussen, R. J. Behm, *Surf. Sci.* **2000**, *460*, 249-263.
- [207] S. Strbac, F. Maroun, O. M. Magnussen, R. J. Behm, *J. Electroanal. Chem.* **2001**, *500*, 479-490.
- [208] O. Mann, W. Freyland, O. Raz, Y. Ein-Eli, *Chem. Phys. Lett.* **2008**, *460*, 178-181.
- [209] C. Thambidurai, Y.-G. Kim, J. L. Stickney, *Electrochim. Acta* **2008**, *53*, 6157-6164.
- [210] S. Strbac, R. J. Behm, A. Crown, A. Wieckowski, *Surf. Sci.* **2002**, *517*, 207-218.
- [211] S. Strbac, C. M. Johnston, G. Q. Lu, A. Crown, A. Wieckowski, *Surf. Sci.* **2004**, *573*, 80-99.
- [212] S. Strbac, C. M. Johnston, A. Wieckowski, *Russ. J. Electrochem.* **2006**, *42*, 1244-1250.

- [213] S. Strbac, M. A. Ivic, *Electrochim. Acta* **2009**, *54*, 5408-5412.
- [214] S. Strbac, O. M. Magnussen, R. J. Behm, *Phys. Rev. Lett.* **1999**, *83*, 3246-3249.
- [215] R. J. Needs, M. Mansfield, *J. Phys. Condens. Matter* **1989**, *1*, 7555-7563.
- [216] W. G. Cullen, P. N. First, *Surf. Sci.* **1999**, *420*, 53-64.
- [217] S. Helveg, J. V. Lauritsen, E. Lægsgaard, I. Stensgaard, J. K. Nørskov, B. S. Clausen, H. Topsøe, F. Besenbacher, *Phys. Rev. Lett.* **2000**, *84*, 951-954.
- [218] D. D. Chambliss, R. J. Wilson, S. Chiang, *J. Vac. Sci. Tech. B* **1991**, *9*, 933-937.
- [219] D. D. Chambliss, R. J. Wilson, S. Chiang, *Phys. Rev. Lett.* **1991**, *66*, 1721-1724.
- [220] B. Voigtländer, G. Meyer, N. M. Amer, *Phys. Rev. B* **1991**, *44*, 10354-1357.
- [221] J. A. Stroschio, D. T. Pierce, R. A. Dragoset, P. N. First, *J. Vac. Sci. Tech. A* **1992**, *10*, 1981-1985.
- [222] P. Liu, J. A. Rodriguez, J. T. Muckerman, J. Hrbek, *Phys. Rev. B* **2003**, *67*, 155416.
- [223] M. M. Biener, J. Biener, R. Schalek, C. M. Friend, *Surf. Sci.* **2005**, *594*, 221-230.
- [224] P. Allongue, L. Cagnon, C. Gomes, A. Gündel, V. Costa, *Surf. Sci.* **2004**, *557*, 41-56.
- [225] F. Lecadre, F. Maroun, I. Braems, F. Berthier, C. Goyhenex, P. Allongue, *Surf. Sci.* **2013**, *607*, 25-32.
- [226] I. Song, C. Park, M. Hong, J. Baik, H.-J. Shin, H. C. Choi, *Angew. Chem. Int. Ed.* **2014**, *53*, 1266-1269.
- [227] S. Lizzit, A. Baraldi, A. Groso, K. Reuter, M. V. Ganduglia-Pirovano, C. Stampfl, M. Scheffler, M. Stichler, C. Keller, W. Wurth, D. Menzel, *Phys. Rev. B* **2001**, *63*, 205419.
- [228] S. Dahl, E. Törnqvist, I. Chorkendorff, *J. Catal.* **2000**, *192*, 381-390.
- [229] C. Stampfl, M. Scheffler, *Phys. Rev. B* **1996**, *54*, 2868-2872.
- [230] A. Böttcher, H. Niehus, *Phys. Rev. B* **1999**, *60*, 14396-14404.

- [231] Y. D. Kim, A. P. Seitsonen, H. Over, *Surf. Sci.* **2000**, *465*, 1-8.
- [232] T. Zambelli, J. Wintterlin, J. Trost, G. Ertl, *Science* **1996**, *273*, 1688-1690.
- [233] Ž. Šljivančanin, B. Hammer, *Phys. Rev. B* **2010**, *81*, 121413.
- [234] S. Guimond, D. Göbke, J. M. Sturm, Y. Romanyshyn, H. Kuhlenbeck, M. Cavalleri, H.-J. Freund, *J. Phys. Chem. C* **2013**, *117*, 8746-8757.
- [235] S. Benedetti, P. Torelli, and S. Valeri, H. M. Benia and N. Nilius, G. Renaud, *Phys. Rev. B* **2008**, *78*, 195411.
- [236] R. Włodarczyk, J. Sauer, X. Yu, J. A. Boscoboinik, B. Yang, S. Shaikhutdinov, H.-J. Freund, *J. Am. Chem. Soc.* **2013**, *135*, 19222-19228.
- [237] Y. Martynova, B.-H. Liu, M. E. McBriarty, I. M. N. Groot, M. J. Bedzyk, S. Shaikhutdinov, H.-J. Freund, *J. Catal.* **2013**, *301*, 227-232.
- [238] F. Stavale, L. Pascua, N. Nilius, H.-J. Freund, *J. Phys. Chem. C* **2013**, *117*, 10552-10557.
- [239] A. Sala, H. Marchetto, Z.-H. Qin, S. Shaikhutdinov, T. Schmidt, H.-J. Freund, *Phys. Rev. B* **2012**, *86*, 155430.
- [240] W. Weiss, M. Ritter, *Phys. Rev. B* **1999**, *59*, 5201-5213.
- [241] Y. Pan, Y. Cui, C. Stiehler, N. Nilius, H.-J. Freund, *J. Phys. Chem. C* **2013**, *117*, 21879-21885.
- [242] J. A. Farmer, J. H. Baricuatro, C. T. Campbell, *J. Phys. Chem. C* **2010**, *114*, 17166-17172.
- [243] P. Luches, F. Pagliuca, S. Valeri, F. Illas, Gloria Preda, G. Pacchioni, *J. Phys. Chem. C* **2012**, *116*, 1122-1132.
- [244] A. Männig, Z. Zhao, D. Rosenthal, K. Christmann, H. Hoster, H. Rauscher, R. J. Behm, *Surf. Sci.* **2005**, *576*, 29-44.

- [245] Z. Zhao, T. Diemant, D. Rosenthal, K. Christmann, J. Bansmann, H. Rauscher, R. J. Behm, *Surf. Sci.* **2006**, *600*, 4992-5003.
- [246] S. Prada, L. Giordano, G Pacchioni, *J. Phys. Chem. C* **2012**, *116*, 5781-5786.
- [247] W. Hebenstreit, J. Redinger, Z. Horozova, M. Schmid, R. Podloucky, P. Varga, *Surf. Sci.* **1999**, *424*, L321-L328.
- [248] M. P. Engelhardt, M. Schmid, A. Biedermann, R. Denecke, H.-P. Steinrück, P. Varga, *Surf. Sci.* **2005**, *578*, 124-135.
- [249] E. Napetschnig, M. Schmid, P. Varga, *Surf. Sci.* **2008**, *602*, 1750-1756.
- [250] M. S. Chen, W. T. Wallace, D. Kumar, Z. Yan, K. K. Gath, Y. Cai, Y. Kuroda, D. W. Goodman, *Surf. Sci.* **2005**, *581*, 115-121.
- [251] T. Matsumoto, M. Batzill, S. Hsieh, B. E. Koel, *Surf. Sci.* **2004**, *572*, 127-145.
- [252] B. Kaemena, S. D. Senanayake, A. Meyer, J. T. Sadowski, J. Falta, J. I. Flege, *J. Phys. Chem. C* **2013**, *117*, 221-232.
- [253] J. I. Flege, B. Kaemena, S. D. Senanayake, J. Höcker, J. T. Sadowski, J. Falta, *Ultramicroscopy* **2013**, *130*, 87-93.
- [254] J. I. Flege, B. Kaemena, A. Meyer, J. Falta, S. D. Senanayake, J. T. Sadowski, R. D. Eithiraj, E. E. Krasovskii, *Phys. Rev. B* **2013**, *88*, 235428.
- [255] M. Corso, W. Auwärter, M. Muntwiler, A. Tamai, T. Greber, J. Osterwalder, *Science* **2004**, *303*, 217-220.
- [256] D. Martoccia, S. A. Pauli, T. Brugger, T. Greber, B. D. Patterson, P. R. Willmott, *Surf. Sci.* **2010**, *604*, L9-L11.
- [257] R. Laskowski, P. Blaha, T. Gallauner, K. Schwarz, *Phys. Rev. Lett.* **2007**, *98*, 106802.
- [258] S. Berner, M. Corso, R. Widmer, O. Groening, R. Laskowski, P. Blaha, K. Schwarz, A. Goriachko, H. Over, S. Gsell, M. Schreck, H. Sachdev, T. Greber, J. Osterwalder, *Angew. Chem. Int. Ed.* **2007**, *46*, 5115-5119.

- [259] A. Goriachko, Y. He, M. Knapp, H. Over, M. Corso, T. Brugger, S. Berner, J. Osterwalder, T. Greber, *Langmuir* **2007**, *23*, 2928-2931.
- [260] D. Martoccia, T. Brugger, M. Björck, C. M. Schlepütz, S. A. Pauli, T. Greber, B. D. Patterson, P. R. Willmott, *Surf. Sci.* **2010**, *604*, L16-L19.
- [261] A. Goriachko, Y. B. He, H. Over, *J. Phys. Chem. C* **2008**, *112*, 8147-8152.
- [262] J. Wintterlin, M.-L. Bocquet, *Surf. Sci.* **2009**, *603*, 1841-1852.
- [263] K. H. Ernst, A. Ludviksson, R. Zhang, J. Yoshihara, and C. T. Campbell, *Phys. Rev. B* **1993**, *47*, 13782-13796.
- [264] J. Yoshihara, J. M. Campbell, C. T. Campbell, *Surf. Sci.* **1998**, *406*, 235-245.
- [265] J. Yoshihara, S. C. Parker, C. T. Campbell, *Surf. Sci.* **1999**, *439*, 153-162.
- [266] S. L. Tait, L. T. Ngo, Q. Yu, S. C. Fain Jr., C. T. Campbell, *J. Chem. Phys.* **2005**, *122*, 064712.
- [267] S. C. Parker, A. W. Grant, V. A. Bondzie, C. T. Campbell, *Surf. Sci.* **1999**, *441*, 10-20.
- [268] E. Napetschnig, M. Schmid, P. Varga, *Surf. Sci.* **2007**, *601*, 3233-3245.
- [269] L. Zhang, F. Cosandey, R. Persaud, T. E. Madey, *Surf. Sci.* **1999**, *439*, 73-85.
- [270] L. Zhang, R. Persaud, T. E. Madey, *Phys. Rev. B* **1997**, *56*, 10549-10557.
- [271] S. Bonannia, K. Aït-Mansour, M. Hugentobler, H. Brune, W. Harbich, *Eur. Phys. J. D* **2011**, *63*, 241-249.
- [272] U. Diebold, J.-M. Pan, T. E. Madey, *Surf. Sci.* **1995**, *331-333*, 845-854.
- [273] Y. J. Kim, Y. Gao, S. A. Chambers, *Appl. Surf. Sci.* **1997**, *120*, 250-260.
- [274] G. A. Rizzi, A. Magrin, G. Granozzi, *Surf. Sci.* **1999**, *443*, 277-286.
- [275] G. Xiang, X. Shi, Y. Wu, J. Zhuang, X. Wang, *Sci. Rep.* **2012**, *2*, 801.

- [276] F. Yang, S. Kundu, A. B. Vidal, J. Graciani, P. J. Ramírez, S. D. Senanayake, D. Stacchiola, J. Evans, P. Liu, J. F. Sanz, J. A. Rodriguez, *Angew. Chem. Int. Ed.* **2011**, *50*, 10198-10202.
- [277] S. H. Overbury, P. A. Bertrand, G. A. Somorjai, *Chem. Rev.* **1975**, *75*, 547-560.
- [278] E. Hulpke, *Helium Atom Scattering from Surfaces*, Springer-Verlag, Berlin Heidelberg **1992**.
- [279] H. Niehus, W. Heiland, E. Taglauer, *Surf. Sci. Rep.* **1993**, *17*, 213-303.
- [280] Y. He, A. P. Seitsonen, H. Over, *Phys. Rev. B* **2005**, *72*, 075432.
- [281] Y. He, A. P. Seitsonen, H. Over, *J. Chem. Phys.* **2006**, *124*, 034706.
- [282] J. P. Hofmann, *Structural Dynamics of Chlorinated Ruthenium Dioxide Model Catalysts under Reaction Conditions*. Ph.D. thesis, Justus-Liebig-Universität Gießen, **2009**.
- [283] S. F. Rohrlack, *HCl-Oxidation über RuO<sub>2</sub>-Modellkatalysatoren*. Ph.D. thesis, Justus-Liebig-Universität Gießen, **2012**.
- [284] K. Iwanaga, K. Seki, T. Hibi, K. Issoh, T. Suzuta, M. Nakada, Y. Mori, T. Abe, *Sumitomo Kagaku* **2004**, *I*, 1–11.
- [285] A. L. Linsebigler, G. Lu, J. T. Yates Jr., *Chem. Rev.* **1995**, *95*, 735-758.
- [286] W. Wei, T. Jakob, *unpublished DFT calculations*, Institut für Elektrochemie, Universität Ulm, **2013**.
- [287] Y. D. Kim, H. Over, G. Krabbes, G. Ertl, *Top. Catal.* **2001**, *14*, 95-100.
- [288] Y. B. He, M. Knapp, E. Lundgren, H. Over, *J. Phys. Chem. B* **2005**, *109*, 21825-21830.
- [289] J. I. Flege, B. Herd, J. Goritzka, H. Over, E. E. Krasovskii, J. Falta, *ACS Nano* **2015**, DOI: 10.1021/acsnano.5b03393.
- [290] J. Goritzka, unpublished results **2015**.

- [291] J. Goritzka, D. Langsdorf, A. Farkas, B. Herd, H. Over, O. Balmes, unpublished SXRD experiments, ESRF Grenoble, **2011**.
- [292] J. Goritzka, S. Rohrlack, A. Pietzsch, J. Schnadt, E. Lundgren, H. Over, unpublished high pressure XPS experiments, MAX-lab Lund, **2011**.
- [293] Y. Martynova, S. Shaikhutdinov, H.-J. Freund, *Chem. Cat. Chem.* **2013**, 5, 2162-2166.
- [294] B. Herd, H. Over, unpublished STM and XPS results, Justus-Liebig-Universität Gießen, **2014**.
- [295] M. Delheusy, A. Stierle, S. Zweidinger, H. Over, H. Dosch, unpublished SXRD experiments of the low temperature oxidation of Ru(0001), Karlsruhe, **2011**.
- [296] P. Müller, A. Saúl, *Surf. Sci. Rep.* **2004**, 54, 157-258.

## 10. Appendices

### A: Theory of heterogeneous nucleation

The formation of a liquid droplet on a solid surface can be described by a spherical cap or spherical dome. To derive the critical radius and the Gibbs free energy of a stable droplet on the solid surface, the volume and the total surface area has to be described. *Figure A1-1* shows the schematic illustration of the spherical cap.

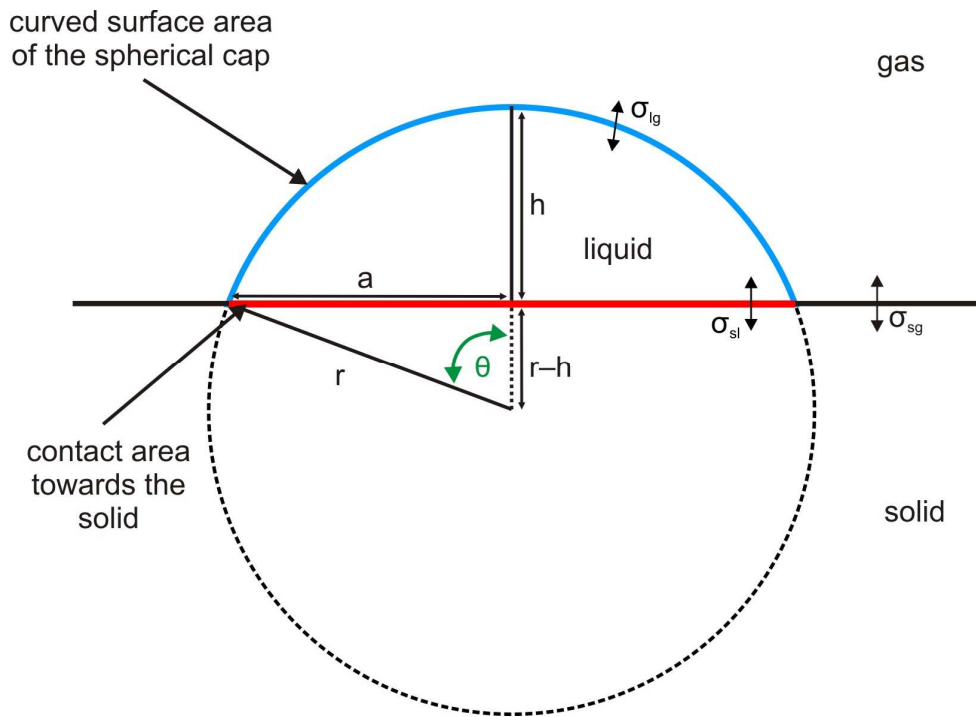


**Figure A1-1:** Two-dimensional illustration of a spherical cap, which describes the form of a droplet on a solid surface. The curved surface area of the spherical cap is marked by the blue line. The contact area at the liquid solid interface is highlighted by the red line.

The curved surface area of the spherical cap is given by:

$$A_{\text{curved}} = 2\pi \cdot r \cdot h \quad (\text{A1})$$

By inserting the angular dependency of the radius from *figure A1-1*

$$\cos(\theta) = \frac{r-h}{r} \Leftrightarrow h = r \cdot (1 - \cos(\theta)) \quad (\text{A2})$$

into equation (A1), the expression of the curved surface area changes to:

$$A_{\text{curved}} = 2\pi \cdot r^2 \cdot (1 - \cos(\theta)) \quad (\text{A3})$$

The contact area (between the droplet and the solid surface) of the spherical cap is given by:

$$A_{\text{contact}} = \pi \cdot a^2 \quad (\text{A4})$$

By inserting

$$\sin(\theta) = \frac{a}{r} \Leftrightarrow a = r \cdot \sin(\theta) \quad (\text{A5})$$

into (A4), the expression of the contact area changes to:

$$A_{\text{contact}} = \pi \cdot r^2 \cdot \sin^2(\theta) \quad (\text{A6})$$

The volume of the spherical ( $V_{sc}$ ) cap is given by:

$$V_{sc} = \frac{\pi \cdot h^2}{3} \cdot (3r - h) \quad (\text{A7})$$

By inserting (A2) into (A7), the volume of the spherical gap changes to:

$$V_{sc} = \frac{\pi \cdot [r \cdot (1 - \cos(\theta))]^2}{3} \cdot (3r - r \cdot (1 - \cos(\theta)))$$

$$V_{sc} = \frac{\pi \cdot r^2}{3} \cdot (1 - \cos(\theta))^2 \cdot r(2 + \cos(\theta))$$

$$V_{sc} = \frac{4}{3} \pi \cdot r^3 \cdot \frac{(1 - \cos(\theta))^2 \cdot (2 + \cos(\theta))}{4}$$

$$V_{sc} = \frac{4}{3} \pi \cdot r^3 \cdot \frac{(1 - 2\cos(\theta) + \cos^2(\theta)) \cdot (2 + \cos(\theta))}{4}$$

$$V_{sc} = \frac{4}{3} \pi \cdot r^3 \cdot \frac{2 - 4\cos(\theta) + 2\cos^2(\theta) + \cos(\theta) - 2\cos^2(\theta) + \cos^3(\theta)}{4}$$

$$V_{sc} = \frac{4}{3} \pi \cdot r^3 \cdot \frac{2 - 3\cos(\theta) + \cos^3(\theta)}{4} = \frac{4}{3} \pi \cdot r^3 \cdot S(\theta) \quad (\text{A8})$$

The term of equation (A8) that contains the angular dependency of the spherical cap volume is called as the wetting function or the catalytic factor  $S(\theta)$ .

$$S(\theta) = \frac{(1 - \cos(\theta))^2 \cdot (2 + \cos(\theta))}{4} = \frac{2 - 3\cos(\theta) + \cos^3(\theta)}{4} \quad (\text{A9})$$

This function describes the tendency for the formation of nuclei instead of a wetting film on the substrate.

The total Gibbs free energy of the droplet formation consists of two summands: One that describes the formation of the bulk, and another that describes the formation of the surface.

$$\Delta G_{total,het} = -nRT \cdot \ln\left(\frac{p}{p_{eq}}\right) + \sum (A_i \cdot \sigma_i) \quad (A10)$$

By introducing the molar volume ( $V_{m,sc}$ ), equation (A8) can be expressed by the amount of substance:

$$n = \frac{4}{3} \cdot \frac{\pi}{V_{m,sc}} \cdot r^3 \cdot S(\theta) \quad (A11)$$

To derive the summand of the surface formation of the spherical droplet, the curved surface area and the contact area are both multiplied by the corresponding surface free energy terms, which are shown in *figure A1-1*.

$$\sum (A_i \cdot \sigma_i) = A_{curved} \cdot \sigma_{lg} + A_{contact} \cdot (\sigma_{sl} - \sigma_{sg}) \quad (A12)$$

By substituting  $(\sigma_{sl} - \sigma_{sg})$  with  $-\sigma_{lg} \cdot \cos(\theta)$ <sup>38</sup> and inserting (A3) and (A6), equation (A12) changes to:

$$\begin{aligned} \sum (A_i \cdot \sigma_i) &= 2\pi \cdot r^2 \cdot (1 - \cos(\theta)) \cdot \sigma_{lg} + \pi \cdot r^2 \cdot \sin^2(\theta) \cdot (-\sigma_{lg} \cdot \cos(\theta)) \\ &= \pi \cdot r^2 \cdot \sigma_{lg} \cdot [2(1 - \cos(\theta)) - \sin^2(\theta) \cdot \cos(\theta)] \\ &= 4\pi \cdot r^2 \cdot \sigma_{lg} \cdot \frac{2 - 2\cos(\theta) - [\cos(\theta) \cdot (1 - \cos^2(\theta))]}{4} \\ &= 4\pi \cdot r^2 \cdot \sigma_{lg} \cdot \frac{2 - 2\cos(\theta) - \cos(\theta) + \cos^3(\theta)}{4} \\ &= 4\pi \cdot r^2 \cdot \sigma_{lg} \cdot \frac{2 - 3\cos(\theta) + \cos^3(\theta)}{4} \\ &= 4\pi \cdot r^2 \cdot \sigma_{lg} \cdot S(\theta) \end{aligned} \quad (A13)$$

---

<sup>38</sup> Rearrangement of Young's equation:  $\sigma_{sg} = \sigma_{sl} + \sigma_{lg} \cdot \cos(\theta) \Leftrightarrow (\sigma_{sl} - \sigma_{sg}) = -\sigma_{lg} \cdot \cos(\theta)$

Inserting (A11) and (A13) into (A10), the total Gibbs free energy for the formation of a droplet can be described by:

$$\Delta G_{total,het} = -\frac{4}{3} \cdot \frac{\pi}{V_{m,sc}} \cdot r^3 \cdot S(\theta) \cdot RT \cdot \ln\left(\frac{p}{p_{eq}}\right) + 4\pi \cdot r^2 \cdot \sigma_{lg} \cdot S(\theta) \quad (A14)$$

Analogous to the homogeneous nucleation, in case of the heterogeneous nucleation the critical radius of the droplet on the solid surface can be calculated by differentiation of  $\Delta G_{total}$  (A14) with respect to the radius:

$$\frac{\partial(\Delta G_{total,het})}{\partial r} = -4 \cdot \frac{RT}{V_{m,sc}} \cdot \pi \cdot r^2 \cdot \ln\left(\frac{p}{p_{eq}}\right) \cdot S(\theta) + 8 \cdot \pi \cdot r \cdot \sigma_{lg} \cdot S(\theta) \quad (A15)$$

When the total free energy reaches its maximum ( $\partial(\Delta G_{total,het})/\partial r = 0$ ),  $r$  describes the *critical radius* of a stable droplet. Solving equation (A15) for the critical radius leads to:

$$r_{critical} = \frac{2 \cdot \sigma_{lg} \cdot V_{m,sc}}{RT \cdot \ln\left(\frac{p}{p_{eq}}\right)} \quad (A16)$$

or by inserting the Clausius-Clapeyron relation:

$$r_{critical} = -\frac{2 \cdot \sigma_{lg} \cdot V_{m,sc} \cdot T_{eq}}{\Delta H_m \cdot (T_{eq} - T)} \quad (A17)$$

By inserting equation (A16) into (A14) the Gibbs free energy of a stable droplet with its critical radius can be derived:

$$\begin{aligned}
\Delta G_{\max,het} &= -\frac{4}{3} \cdot \pi \cdot r_{critical}^3 \cdot \frac{RT \cdot \ln\left(\frac{P}{P_{eq}}\right)}{V_{m,sc}} \cdot S(\theta) + 4\pi \cdot r_{critical}^2 \cdot \sigma_{lg} \cdot S(\theta) \\
&= -\frac{4}{3} \cdot \pi \cdot r_{critical}^3 \cdot 2\sigma_{lg} \cdot \frac{RT \cdot \ln\left(\frac{P}{P_{eq}}\right)}{2\sigma_{lg} \cdot V_{m,sc}} \cdot S(\theta) + 4\pi \cdot r_{critical}^2 \cdot \sigma_{lg} \cdot S(\theta) \\
&= -\frac{4}{3} \cdot \pi \cdot r_{critical}^3 \cdot 2\sigma_{lg} \cdot \frac{RT \cdot \ln\left(\frac{P}{P_{eq}}\right)}{2\sigma_{lg} \cdot V_{m,sc}} \cdot S(\theta) + 4\pi \cdot r_{critical}^2 \cdot \sigma_{lg} \cdot S(\theta) \\
&= -\frac{8}{3} \cdot \pi \cdot r_{critical}^2 \cdot \sigma_{lg} \cdot S(\theta) + 4\pi \cdot r_{critical}^2 \cdot \sigma_{lg} \cdot S(\theta) \\
&= \frac{4}{3} \cdot \pi \cdot r_{critical}^2 \cdot \sigma_{lg} \cdot S(\theta) \tag{A18}
\end{aligned}$$

To derive the temperature dependence of the Gibbs free energy of the heterogeneous nucleation (A17) is inserted:

$$\Delta G_{\max,het} = \frac{16\pi \cdot \sigma_{lg}^3 \cdot T_{eq}^2}{3 \cdot (\Delta H_m)^2} \cdot \left( \frac{1}{(T_{eq} - T)^2} \right) \cdot S(\theta) \tag{A19}$$

For better comparison to the homogeneous nucleation, the equation (A19) can be simplified if the surface free energy of a droplet on the surface ( $\sigma_{lg}$ ) is assumed to be equal to surface free energy of a droplet ( $\sigma$ ) from the homogeneous nucleation. By this assumption, the Gibbs free energy of a stable droplet in homogeneous nucleation (cf. equation (3.1-10)) can be inserted and the well known relation is derived:

$$\Delta G_{\max,het} = \Delta G_{\max,hom} \cdot S(\theta) \tag{A20}$$

Depending on the wetting angle, the catalytic factor  $S(\theta)$  has values ranging between 0 ( $\theta = 0^\circ$ , full wetting) and 1 ( $\theta = 180^\circ$ , no wetting) (cf. figure 3.2-2, page 33). With the contact angle of  $180^\circ$  the nucleation process can be described by homogeneous nucleation because the substrate surface becomes irrelevant in the nucleation process.

From equation (A20) it becomes evident that  $\Delta G_{\max,het} \leq \Delta G_{\max,hom}$  and therefore nucleation on a surface is always more favored than the corresponding homogeneous nucleation process, if the critical radius in both cases is equal.

## Appendix B: Basic elastic theory - strain energy and dislocation energy

In the following the formation of dislocations in a growing film will be described, which are induced by the lattice misfit between the growing film and the underlying substrate. Within this section several quantities from elasticity theory and continuum mechanics are used and therefore explained:

- Stress (mechanics):  $\tau = \frac{F}{A}$  (B1)

The mechanical stress is defined as the force per unit area that is put on an area or surface. Stress is classically divided into two categories: If the applied force is perpendicular to the surface ( $F \perp A$ ), the corresponding stress is usually named as *normal stress* (cf. figure B1-1a). Depending on the direction of the force the stress is more classified to *compressive stress* (force directed towards the area) or *tensile stress* (force directed away from the area). If the applied force is parallel to the surface, the ( $F \parallel A$ ) the corresponding stress is called *shear stress* (cf. figure B1-1b).

- Strain (deformation):  $\varepsilon = \frac{\Delta l}{l}$  (B2)

The strain is defined as the deformation of a stressed material. Depending on the direction of the deformation, the strain is further classically divided into *tensile strain*, *compressive strain* (for deformation perpendicular to the area, cf. figure B1-1a) or *shear strain* (for deformation parallel to the area, cf. figure B1-1b).

- Young's modulus:  $Y = \frac{\text{stress}}{\text{strain}} = \frac{F \cdot l}{A \cdot \Delta l}$  (B3)

Young's modulus is defined as the ratio of normal stress to normal strain. It describes the material's response a uniaxial stress and therefore its stiffness. The larger  $Y$  is the bigger is the inelasticity of the material. A typical example for a linear deformation is shown in figure B1-1a.

- Shear modulus:  $\mu = \frac{\text{shear stress}}{\text{shear strain}} = \frac{Y}{2(1 + \nu)}$  (B4)

The shear modulus is defined as the ratio of shear stress to the shear strain. It describes the material's response to shear stress. Analogous to Young's modulus, the elasticity

of a material is described, but the direction of the applied force is different (*cf. figure B1-1b*).

- Poisson's ratio:  $\nu = -\frac{d\epsilon_{trans}}{d\epsilon_{axial}}$  (B5)

The Poisson's ratio is defined as the negative ratio of the transverse strain to the axial strain. *Figure B1-1c* gives an example for the linear tension of a rod. Due to the linear extension of the rod, its transverse section decreases to maintain the overall volume of the rod.

- Burgers vector:  $\|b\| = \frac{a_0}{2} \cdot \sqrt{h^2 + k^2 + l^2}$  (B6)

The Burgers vector represents the magnitude and direction of the atomic displacement resulting from a formed dislocation in the crystal lattice. It quantifies the difference between the distorted lattice around the formed dislocation and the perfect lattice. In many metals the absolute value of the Burgers vector is approximately equal to the lattice parameter of the respective metal (*cf. figure B1-1d*).

- Lattice mismatch or misfit (strain):  $\underline{f} = \frac{a_0(S) - a_0(A)}{a_0(A)}$  (B7)

The lattice misfit strain describes the quantity of strain that occurs in a pseudomorph growing film due to different lattice parameters and the resulting compression or expansion of the binding length between the adlayer atoms. Therefore it displays how good (or bad) two crystallographic lattices fit to each other based on their unstrained lattice parameters  $a_0(S)$  and  $a_0(A)$  (lattice parameters of the substrate  $S$  and the adsorbate film  $A$ , respectively). For simplification, the substrate is assumed to be rigid and no strain occurs in its top layers. *Figure B1-1e* illustrates the derivation of the lattice misfit for a growing film with tensile strain. For positive  $\underline{f}$  values, the first growing layers are stretched under tensile strain. Vice versa, for negative  $\underline{f}$  values the growing layers are under compressive strain.

Note that the convention for the lattice misfit strain can differ, depending on the derivation. If the lattice misfit is derived for a growing film with compressive strain, the numerator from (B7) changes to  $a_0(A) - a_0(S)$ . As a consequence the definition for  $\underline{f}$  changes: Now negative  $\underline{f}$  values describe a tensile strain of the growing film and positive  $\underline{f}$  values a compressive strain. Both conventions are used in literature:

$a_0(A) - a_0(S)$ <sup>[118,122,124,132]</sup> and  $a_0(S) - a_0(A)$ <sup>[119,133,296]</sup>. Within this work the equation (B7) will be used.

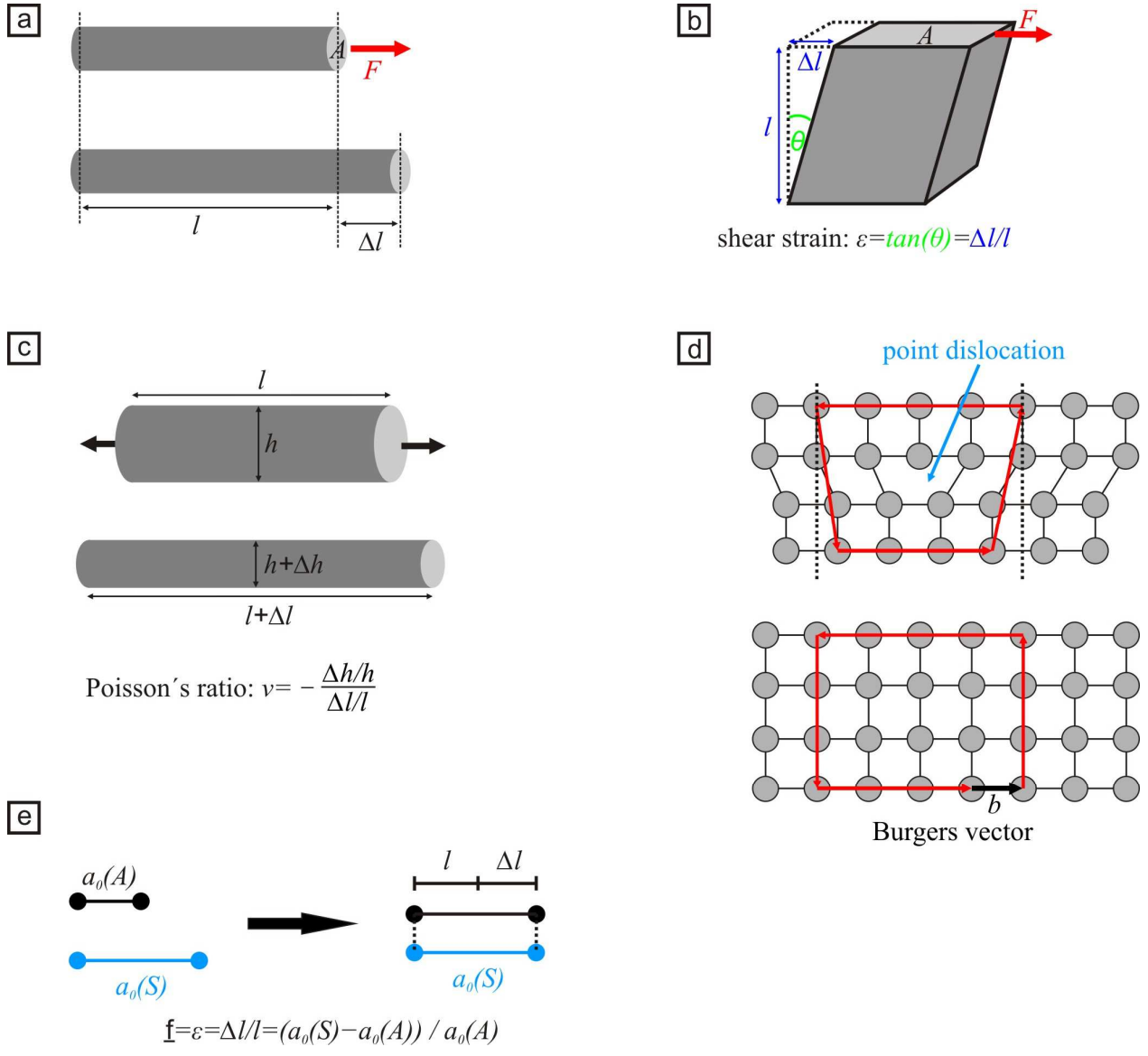


**Figure B1-1:** Schematic illustration of different quantities from basic elastic theory: (a) basic stress and strain, (b) shear stress and strain, (c) Poisson's ratio from a linear deformation, (d) point dislocation in a crystal lattice and the derivation of the corresponding Burgers vector, (e) lattice tensile strain of the growing film and the derivation of the lattice misfit.

For simplification it is assumed that the shear modulus and Young's modulus of the adsorbate film and the substrate are equal, meaning both materials have the same deformation properties and the strain energy therefore is only related to the different lattice parameters.

At the initial film growth ( $d < d_{c,disl}$ ) the elastic strain energy of the wetting film is given by:

$$E_{el} = \frac{1}{(1-\nu)} \cdot Yd\varepsilon^2 \quad (\text{B8})$$

$\varepsilon$  : *biaxial strain*

$\nu$  : *Poisson's ratio*

$Y$  : *Young's modulus*

With increasing film thickness  $d$  the elastic strain energy increases linearly as can be seen in equation (B8). Beneath a critical film thickness  $d_{c,disl}$  no dislocations occur in the growing film. To form a dislocation energy is needed, the dislocation energy. So even if the formation of the dislocation releases strain and reduces the strain energy, the total (strain) energy of the system might still get higher after the formation of the dislocation due to the dislocation energy. Beneath the critical film thickness ( $d < d_{c,disl}$ ), the increase in the total energy by the gain of dislocation energy is larger than the simultaneous decrease of the strain energy. Therefore dislocations only appear if the sum of the dislocation energy and the strain energy of a film with formed dislocations is lower than the total energy of an equal thick film without dislocations.

If the growing film reaches the critical thickness ( $d > d_{c,disl}$ ), dislocations are formed to reduce the strain energy. *Figure B1-2* illustrates schematically the formation of dislocations depending on the film thickness.

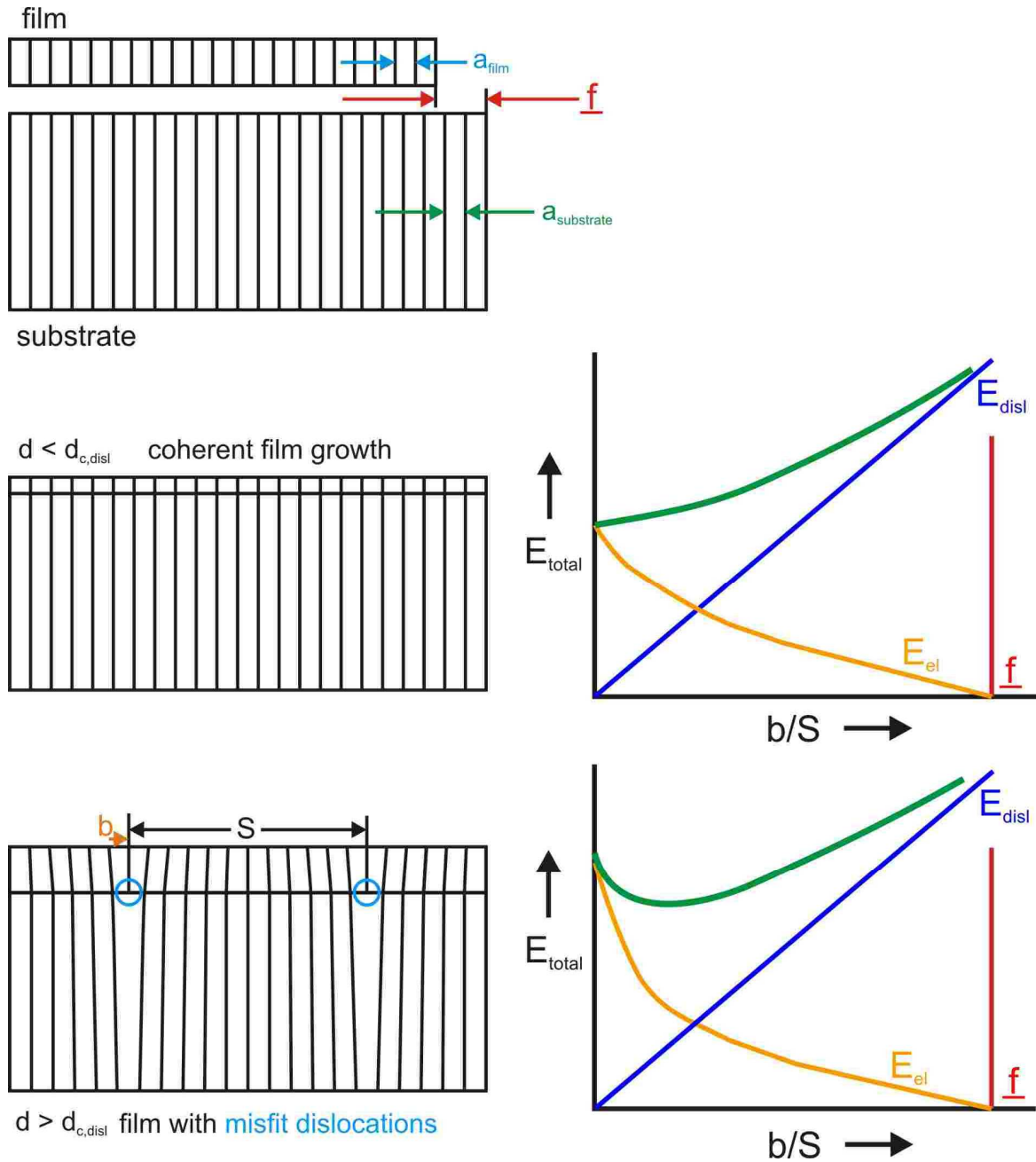


**Figure B1-2:** Illustration of the Matthews-Blakeslee equilibrium theory of misfit-dislocation formation. For  $d < d_{c,disl}$  the coherent film growth is shown with corresponding dependence of the dislocation number  $b/S$  towards the total strain energy  $E_{total}$ . For  $d > d_{c,disl}$  film growth with misfit dislocation and the corresponding energy diagram are shown. Figure modified from [133].

To describe the reduction of the strain in the film by the formation of dislocations in *figure B1-2*, the dislocation number  $b/S$  is introduced:

$$\varepsilon = \underline{f} - \frac{b}{S} \quad (\text{B9})$$

Dislocations are formed at somewhat regular distances of  $\mathbf{S}$  at the interface (*cf. figure B1-2*, left bottom). The dislocation number is the quotient of Burgers vector and the distance between the formed dislocations and represents the density of formed dislocations. The strain at the interface is reduced by the formation of dislocations and it disappears if the dislocation number is equal to the lattice misfit ( $\underline{f} = \frac{b}{S}$ ). By introducing the dislocation number in equation (B8) the elastic strain energy changes to:

$$E_{el} = \frac{1}{(1-\nu)} \cdot Yd \left( \underline{f} - \frac{b}{S} \right)^2 \quad (\text{B10})$$

By introducing the dislocation energy,

$$E_{disl} = \frac{\mu \cdot b^2}{2\pi(1-\nu) \cdot S} \cdot \ln \left( \frac{\beta \cdot d}{b} \right) \quad (\text{B11})$$

$\beta$ : numerical constant

it is possible to describe the total strain energy of the growing film:

$$E_{total} = E_{el} + E_{disl} = \frac{1}{(1-\nu)} \cdot Yd \cdot \left( \underline{f} - \frac{b}{S} \right)^2 + \frac{\mu \cdot b^2}{2\pi(1-\nu) \cdot S} \cdot \ln \left( \frac{\beta \cdot d}{b} \right) \quad (\text{B12})$$

In *figure B1-2* the total strain energy is plotted versus the dislocation number for the coherent or pseudomorph film growth beneath the critical film thickness (*cf. figure B1-2*, middle right) and for a grown film with formed dislocations above the critical film thickness (*cf. figure B1-2*, bottom right). As described in equation (B12) the dislocation energy increases linearly with increasing dislocation density (blue curve). Similarly the elastic strain energy is reduced with increasing number of formed dislocations at the interface until  $\underline{f} = \frac{b}{S}$  (orange curve). The sum of both curves represents the total strain energy of the film and is illustrated by the green curve.

Beneath the critical film thickness ( $d < d_{c,disl}$ ) the total strain energy continuously increases with increasing formation of dislocations. Therefore no dislocations are formed during the initial growth phase because the total strain energy is minimal if  $b/S = 0$ .

Above the critical film thickness ( $d > d_{c,disl}$ ) a minimum occurs for the total strain energy. This means that with a certain number of dislocations it is possible to reduce the strain in an energetically favorable way and therefore reducing the total strain energy, if the critical film thickness is obtained.

To calculate the critical thickness of the growing film it is necessary to determine the minimum of the total strain energy. Therefore the total strain energy is derived with respect to the dislocation number:

$$\frac{\partial E_{total}}{\partial \left(\frac{b}{S}\right)} = -2 \frac{Yd}{(1-\nu)} \cdot \left(\underline{f} - \frac{b}{S}\right) + \frac{\mu b}{2\pi(1-\nu)} \cdot \ln\left(\frac{\beta \cdot d}{b}\right) = 0 \quad (\text{B13})$$

It is assumed that at the critical thickness of the film ( $d_{c,disl}$ ) no dislocations have been formed yet ( $b/S = 0$ ), but their formation starts immediately with the next growing layer. If the thickness  $d$  is not exchanged by the critical thickness  $d_{c,disl}$ , equation (B13) changes to:

$$0 = -2 \frac{Yd_{c,disl}}{(1-\nu)} \cdot (\underline{f}) + \frac{\mu b}{2\pi(1-\nu)} \cdot \ln\left(\frac{\beta \cdot d_{c,disl}}{b}\right) \quad (\text{B14})$$

By rearranging equation (B14) the critical thickness of the film can be obtained:

$$\begin{aligned} \Leftrightarrow 2 \frac{Yd_{c,disl}}{(1-\nu)} \cdot (\underline{f}) &= \frac{\mu b}{2\pi(1-\nu)} \cdot \ln\left(\frac{\beta \cdot d_{c,disl}}{b}\right) \\ \Leftrightarrow d_{c,disl} &= \frac{(1-\nu)}{2Y(\underline{f})} \cdot \frac{\mu b}{2\pi(1-\nu)} \cdot \ln\left(\frac{\beta \cdot d_{c,disl}}{b}\right) \\ \Leftrightarrow d_{c,disl} &= \frac{\mu b}{4\pi \cdot Y \cdot \underline{f}} \cdot \ln\left(\frac{\beta d_{c,disl}}{b}\right) \end{aligned} \quad (\text{B15})$$

If the shear modulus ( $\mu = \frac{Y}{2(1+\nu)}$ ) is inserted in equation (B15), the expression for the critical film thickness changes to:

$$d_{c,disl} = \frac{b}{8\pi \cdot (1+\nu) \cdot \underline{f}} \cdot \ln\left(\frac{\beta d_{c,disl}}{b}\right) \quad (\text{B16})$$

With the approximation done before, all the deformation parameters<sup>39</sup> are set as constant for both materials during the growth. This leads to the important inverse proportion of the critical film thickness and the lattice misfit between both materials:

$$d_{c,dist} \sim \frac{1}{\underline{f}} \quad (\text{B17})$$

In conclusion the total strain energy of the growing film is related to the lattice misfit and the film thickness. From this follows that if the lattice misfit is low the total strain energy is low and the growth is mostly determined by the surface free energies of the materials in case that the interface energy is not influenced by other effects (e.g. charging). If, in principle, the lattice misfit between the adsorbate and the substrate is zero a homoepitaxial FvdM growth occurs. However in heteroepitaxial growth the lattice misfit between two different materials usually is not zero. Even for well-fitting materials it usually is only a question of the film thickness until defects need to be introduced to release the strain of the growing film. This can vary from  $\leq 1$  layer for a bigger lattice misfit to  $\geq 50$  layers for nearly equal lattice parameters between both materials.

---

<sup>39</sup> Shear modulus  $\mu$  and Young's modulus  $Y$  are constant: Both materials have the same deformation properties.

## C: Blueprint of the used Ru(0001) and Au(111) single crystals

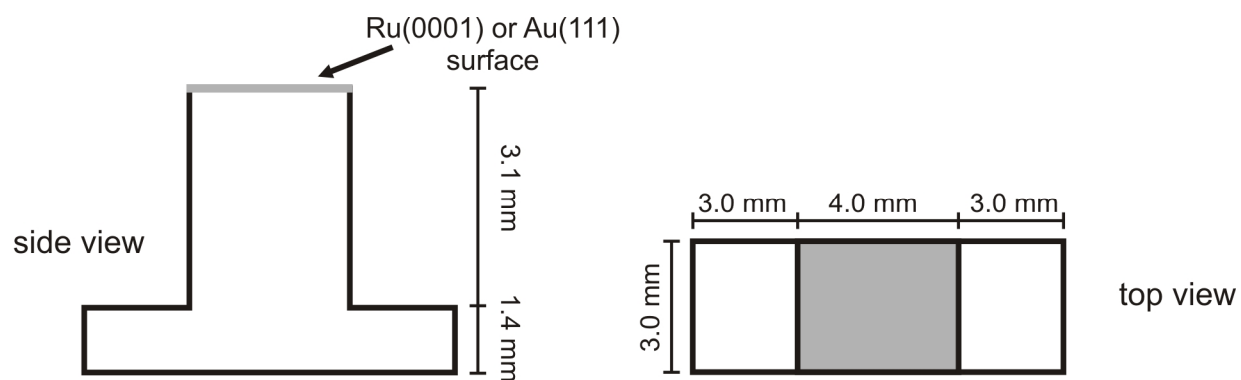


**Figure C1-1:** Blueprint of the Ru(0001) and Au(111) single crystals from top and side view, with the respective length specification. The used single crystal surfaces are highlighted in grey.

## D: Danksagung

Im Folgenden möchte ich mich bei allen Menschen bedanken, welche die Entstehung dieser Arbeit ermöglicht und mich auf meinem Weg dorthin begleitet und unterstützt haben.

An erster Stelle möchte ich mich bei Prof. Dr. Herbert Over für die intensive Betreuung in den letzten Jahren bedanken. Außerdem möchte ich Ihm für die Möglichkeit danken, diese Arbeit in seiner Arbeitsgruppe anfertigen zu können. An Prof Dr. Bernd Smarsly geht ein großer Dank für die Anfertigung des Zweitgutachtens.

Ein weiterer großer Dank geht an Dr. Benjamin Herd, der, neben Prof. Over, immer mein erster Ansprechpartner war. Bei offenen Fragen oder Interpretation von Messergebnissen stand er mir stets mit Rat und Tat zur Seite. Des Weiteren möchte ich mich auch ganz besonders bei allen Mitgliedern der Arbeitsgruppe von Prof. Dr. Over bedanken, die alle einen Teil zu der Vollendung dieser Arbeit beitrugen. Besonderer Dank geht hierbei an die Korrektoren meiner Dissertation. Wiederum ist hier Dr. Benjamin Herd zu nennen, der einen Großteil meiner Arbeit Korrektur gelesen hat und dessen unermüdliche Hilfe einen erheblichen Beitrag zu deren Anfertigung gewesen ist. Des Weiteren bedanke ich mich vielfach bei Franziska Hess, die immer ein offenes Ohr für mich hatte und viele Stunden mit mir über meine Ergebnisse diskutierte, obwohl sie gleichzeitig mit dem Schreiben ihrer eigenen Dissertation beschäftigt war. Gleiches gilt auch für Jan Goritzka, der nicht nur mit einer Engelsgeduld meine Dissertation verfeinerte, sondern mir auch Abseits der Arbeit immer ein sehr guter Freund ist. Ich bedanke mich vielfach bei Prof. Yunbin He für die vielen Stunden der Zusammenarbeit, die mir einen neuen Blickwinkel auf meine Ergebnisse ermöglicht haben. Ich bedanke mich bei dem Rest der Arbeitsgruppe für die vielen fachlichen Diskussionen und Rückkopplungen zu meinen Ergebnissen und das schöne Gemeinschaftsgefühl auch außerhalb der Arbeitszeiten. Ich werde die vielen gemeinsamen Gruppenaktivitäten sehr vermissen.

Außerdem danke ich den Mitgliedern des Physikalisch-Chemischen Instituts für die gute kollegiale Atmosphäre, die die Grundbasis für die erfolgreiche Zusammenarbeit ist.

Weiter möchte ich mich bei allen Mitarbeitern der institutseigenen Werkstätten (Feinmechanikwerkstatt sowie Elektronikwerkstatt) bedanken, die mir immer bei technischen Problemstellungen bezüglich An- und Umbauten an den in dieser Arbeit genutzten UHV-Kammern mit Rat und Tat zur Seite standen.

Des Weiteren bedanke ich mich bei der Deutschen Forschungsgemeinschaft für die finanzielle Unterstützung.

Ich bedanke mich bei meinen Kommilitonen für die gemeinsame Zeit während des Chemiestudiums und danach. Die vielen anstrengenden und spaßigen Jahre unseres Studiums haben uns stark zusammengeschweißt, was an den wöchentlichen Treffen zum Semesteressen deutlich wird.

Meinen Freunden danke ich für die gemeinsame Zeit abseits der Universität, wo sie es immer wieder schafften mich auf positive Weise abzulenken.

Zu guter Letzt möchte ich meiner Familie danken, allen voran meinen Eltern, meinen Geschwistern und meinen Großeltern, die mich von Anfang an mit all ihren Möglichkeiten unglaublich unterstützt haben.